Low Velocity Impact Response of a Novel Class of Fiber Metal Laminates Consisting of a 3D Fiberglass Fabrics

by

Zohreh Asaee

Submitted in partial fulfilment of the requirements
for the degree of Doctor of Philosophy

at

Dalhousie University
Halifax, Nova Scotia
November 2017

In memory of my father

To my mother
the strongest one in my life and my real-life hero

with love and eternal appreciation.

Table of Contents

List of Tables

List of Figures

Abstract

The most important concern in automobiles collision is their crashworthiness. From an engineering point of view, the term "crashworthiness" provides a metric of the abilities of a vehicle and its components to prevent the extent of injury to vehicle's occupants during a crash event. The Canadian motor vehicle collision statistics reported by Transport Canada reveal the importance of crashworthiness. For instance, in 2012, Canada witnessed over 2,077 deaths, 10,656 serious injuries and 152,439 minor injuries resulted from automobile collisions.

The above facts and the recent challenge posed to the automotive industry to lower green-house gas emission of vehicles have sparked renewed activities in synthesizing lighter-weight materials to form various components of vehicles. However, there are basic requirements for rendering a material acceptable for use in manufacturing automobiles' shells and enhancing their crashworthiness. Materials must have the sufficient strength, and preferably have controllable deformations under a suddenly applied load. Over the last six decades, a great volume of mass-produced vehicle panels has been manufactured mainly by metallic alloys (with steel constituting the majority of them), and in recent years, with some fiber-reinforced plastic composites (FRP). It is however believed that one can take advantage of the synergistic marriage of both metals and FRP, and develop lighter-weight and more resilient materials for use in fabrication of various components of a vehicle.

The main aim of the research carried out and presented in this dissertation has therefore been to develop an innovative and effective hybrid material configuration for production of vehicle panels, with the main goals of providing comparatively optimal crashworthiness, as well as reduced weight and cost. The proposed hybrid material, referred to as 3D fiber metal laminates (3DFML), is comprised of light-weight magnesium alloy sheets and a truly 3D fiberglass fabric with its cavities filed with a foam.

In this thesis, the behavior of various configurations of the developed 3DFML is systematically examined under both static and impact loading conditions. The low-velocity impact (LVI) response and failure modes of the 3DFMLs are investigated, and their performance is compared with that of conventional FML. Furthermore, computational simulations and experimental investigations are conducted to evaluate the influence of the stacking sequence on the low-velocity impact response of various configurations of 3DFML. The most optimal configuration is established based on the strength, weight and cost criteria. The level of enhancement that could be attained by using different fabric types (i.e., fiberglass and carbon) to reinforce 3DFML was also established. Furthermore, a numerical model is developed, using a commercial software (ABAQUS/Explicit), for predicting the analysis of impact response of the FMLs and assessment of their failure modes. Attempts are made to improve the interface strength by inclusion of inexpensive graphene nanoplatelets (GNP) in the interface resin. A mechanistic model is developed for estimating the strength of 3DFGFs subjected to out-of-plane compressive loading. The contribution of each constituents of fabric in carrying the load is investigated. Finally, a general practical analytical model is presented by which the impact capacity of 3DFMLs can be predicted. The developed analytical model is modified and generalized based on various configurations of the 3DFML, as well as impactor's geometry.

List of Abbreviations and Symbols Used

3DFG	3D-fiberglass
3DFGF	3D Fiberglass Fabric
C3D8R	8-node solid element
DLVDT	Dynamic Linear Variable Differential Transformer
ERC	Energy Restitution Coefficient
ESP	Electronic Stability Program
FE	Finite Element
FEA	Finite-Element Analysis
FML	Fiber-Metal Laminate
FRP	Fiber-Reinforced Plastic Composite
GLARE	GLAss laminate aluminum-REinforced epoxy
GNP	Graphene Nanoplatelets
LVDT	Linear Variable Differential Transformer
LVI	Low-Velocity Impact
MgAs	magnesium alloys
PP	Polypropylene
S4R	4-node shell element
SEM	Scanning Electron Microscope
USDOE	United States Department of Energy

VUMAT	user-defined material model
wt%	weight percentage
a	Distance between pillars of 3D fiberglass fabric
a_c	Radius of contact region
A_{foam}	net cross-sectional areas of the foam
C_d	Reduced damaged stiffness matrix
D	Damage index
D_{11}	Bending stiffness of laminate
D_{66}	Flexural stiffness of laminate
E_0	Initial energy of impactor
E_1	Young's Modulus in 1-direction
E_2	Young's Modulus in 2-direction
E_3	Young's Modulus in 3-direction
$E_{absorbed}$	Absorbed impact energy
E_b	Absorbed energy due to bending deformation of target
E_{bs}	Absorbed impact energy due to shear and bending deformations
E_c	Absorbed energy due to the indentation in the local contact region of impactor and target
E_f	Flexural modulus
E_{Impact}	Initial impactor Energy
E_m	Absorbed energy due to membrane stretching of target

E_s	Absorbed energy due to shear deformation of target
$F_1^{(0)}$	Impact force corresponding to the first damage mode of baseline 3DFML
F_{fLC}	Compressive failure index of fiber
F_{fLT}	Tensile failure index of fiber
F_{foam}	Force in the foam core
$F_{fT(Z)c}$	Combined compressive and shear failure index of fiber (through the thickness direction)
$F_{fT(Z)t}$	Combined tensile and shear failure index of fiber (through the thickness direction)
$F_{mt,c}$	Tensile and compressive failure index of matrix
F_{pillar}	Force in the pillars of 3D fiberglass fabric
G_o	Initial strain energy release rate
G_{12}	Shear modulus in 1-2 direction
G_{23}	Shear modulus in 2-3 direction
G_{31}	Shear modulus in 3-1 direction
G_C	Critical strain energy release rate
G_n	Strain energy release rate in the normal direction
G_s	Strain energy release rate in the first shear direction
G_t	Strain energy release rate in the second shear direction
I	Second moment of area
K	Stiffness matrix of the interface material

K_b	Bending stiffness of plate
K_{bs}	Effective stiffness due to the combined shear and bending effects
K_{eq}	Equivalent stiffness value of a plate subjected to the out-of-plane displacement
K_{IC}	Mode I fracture toughness
K_{IIC}	Mode II fracture toughness
K_s	Shear stiffness of plate
L	Length of specimen
m_1	Impactor mass
r	Radius of impactor
R	Radius of circular plate
S_{12}	Laminate shear strength in 1-2 direction
S_{23}	Laminate shear strength in 2-3 direction
S_{31}	Laminate shear strength in 3-1 direction
t	Thickness of specimen
t_0	Initial thickness of a cohesive element
t_c	Core thickness of sandwich plate
T_{eff}	Effective Traction
t_f	Face-sheet thickness of sandwich plate
$\bar{t}_n$	Predicted traction stress in the normal direction without considering the damage effects

$\bar{t}_s$	Predicted traction stress in the first shear direction without considering the damage effects
$\bar{t}_t$	Predicted traction stress in the second shear direction without considering the damage effects
t_n	Traction stress in the normal direction
t_s	Traction stress in the first shear direction
t_t	Traction stress in the second shear direction
V_0	Initial velocity of impactor
V_{Impact}	Impactor velocity before impact
$V_{Rebound}$	Impactor velocity after impact
w	Width of specimen
w_{max}	Maximum out of plane deflection of a plate
X^C	Compressive strength in longitudinal direction
X^T	Tensile strength in longitudinal direction
Y^C	Compressive strength in transverse direction
Y^T	Tensile strength in transverse direction
Z^C	Out-of-plane compressive strength
Z^T	Out-of-plane tensile strength
α_{max}	Maximum indentation depth
ρ	Material density
ν_{12}	Poisson's ratio in 1-2 direction

v_{23}	Poisson's ratio in 2-3 direction
v_{31}	Poisson's ratio in 3-1 direction
δ_A	Axial displacement of pillar
δ_{eq}^{f}	Equivalent displacement at the fully-damaged state
δ_{eq}	Equivalent displacement
δ_{eq}^{0}	Equivalent displacement at the onset of failure initiation
δ_n	Separation counterparts in the normal direction
δ_s	Separation counterparts in the first shear direction
δ_t	Separation counterparts in the second shear direction
δW_{ext}	External work done by the surface and body forces
δW_{int}	Strain energy of system
δW_{spring}	Strain energy stored in springs
σ	Flexural strength
σ_{foam}	Compressive stress in the foam
$\sigma_{C,foam}$	Crushing strength of foam
Φ_i	Energy stored in the i^{th} torsional springs
Δ_{max}	Maximum centre location deflection at the mid-surface of the plate
w_{max}	Total displacement of impactor

Acknowledgement

First and foremost, I would like to express my sincere gratitude to my supervisor, Professor Farid Taheri, for his intellectual and scientific support throughout my PhD program. He greatly supported and encouraged me through all the challenging steps and helped me to expand and hone my abilities. My discussions with Prof. Taheri deeply broadened my vision towards my research goals and provided me with numerous innovative ideas to explore. I appreciate all his contributions of time, ideas and energy to make my PhD experience productive and stimulating.

As well, I wish to extend my appreciation to Dr. Jeremy Laliberte of Carleton University and Profs. Noubar Yemenidjian and Dr. Tamunoiyala Koko of Dalhousie University for reviewing my PhD thesis and providing technical feedback.

My gratitude also extends to Mr. Mark MacDonald, Mr. Angus MacPherson, Mr. Albert Murphy, Mr. Brian Kennedy, Mr. Blair Nickerson and Mr. Jesse Keane, skillful technicians at Dalhousie University's Mechanical Engineering Department and Civil and Resource Engineering Department. Their assistance and technical support throughout my experimental work was greatly appreciated.

In addition, I gratefully acknowledge the funding sources that made my PhD work possible. The financial support I received through the National Science and Engineering Research Council of Canada (NSERC) in support of this study is deeply appreciated. I am also thankful to Killam Trust for my Doctoral Killam Scholarship, the Government of Nova Scotia for the Nova Scotia Research and Innovation Graduate Scholarship, and Zonta International for the Amelia Earhart Fellowship awarded to only 35 women around the globe pursuing a doctoral degree in aerospace science or related fields of engineering.

I also owe a great debt of gratitude to my colleagues, Dr. Shahin Shadlou and Dr. Babak Ahmadi, who helped me during the initial stages of my research. My gratitude extends as well to my friends and colleagues who collaborated with me during the different stages of my research at Dalhousie, including but not limited to Dr. Meisam Asgari, Davide De Cicco, Mbarka Mohamed and Sadman Soumik.

Last but not least, I would like to express my sincere and heartful gratitude to my family for their love and encouragement: To my parents, who raised me with a love of learning and greatly sacrificed to give me the life that I have; to my brother, Hassan, who is always the first to support me when times get tough, even when I am thousands of miles away; to my sister, Tahereh, my role model who taught me to be a strong woman, to never give up on my dreams, and to fight to achieve them; and most of all, to my brother, Rasoul, my best friend who stayed by my side during all the ups and downs of my academic life, providing me with intellectual, emotional and technical support to help me deal with challenges I faced over the past four years. Thank you all for supporting me not just during my studies but throughout the years leading to now. I could never have achieved this milestone without you.

Chapter 1: Introduction

1.1 Fiber Metal Laminates

The most important concern in automobiles collision is their crashworthiness, which can be described as the ability to prevent the extent of injury to the occupants of automobiles in an event of a collision. From an engineering point of view, the term “crashworthiness” provides a metric of the vehicle and its components in protecting the occupants in crashes. The Canadian motor vehicle collision statistics reported by Transport Canada reveal the importance of the crashworthiness - In 2012, Canada witnessed over 2,077 deaths, 10,656 serious injuries and 152,439 injuries in automobile collisions. The economic impact of the fatalities and injuries, including the lost wages, insurance payouts and property damage, is to the tune of over $10 billion a year. Consequently, auto industry stakeholders are continually developing new technologies (e.g., Electronic Stability Program (ESP), Collision Warning System, etc.), in order to improve an automobile's crashworthiness, thereby minimizing the number of fatalities and injuries and mitigate the loss of billions of dollars. Notwithstanding the existing efforts for inhibiting car crashes, the reported statistics indicate that the number of victims suffering from serious injuries or fatalities is still large, which implies that irrespective of new technologies, many people still suffer catastrophic loses.

As a means to improve crashworthiness, the basic requirements for acceptable materials used to construct automobile shells include sufficient strength and controlled deformations under suddenly applied loads, so to absorb the crash induced impact energy. Moreover, the post-crash behavior of the material(s) should still provide adequate survivable space to the

occupants (i.e., the component should not deform excessively). In addition, the overall structure should be lightweight, thus reducing fuel consumption. The abstractly stated reduction in weight would in turn increase sustainability of the energy and would also address climate-change issues by decreasing emission of carbon dioxide (CO_2). According to the United States Department of Energy (USDOE), automotive industry plays a special role in consumption of energy, consuming 71% of fuel in the US, almost 30% of total energy (U.S.D.O.E 2017).

A great volume of the mass-produced vehicle bodies over the last six decades has been manufactured from mainly metallic alloys (with steel constituting the majority of them), and some fiber-reinforced plastic composites (FRP) in the recent years. Table 1-1 presents the advancement of materials used in the automotive industry to reduce the weight. The competition among metals and FRP is, however, quite significant in today's automotive industry, especially where the drive for lighter-weight and fuel efficiency is the strongest.

Table 1-1. Mass reduction and relative cost for different materials used on the vehicles (Powers 2000)

Materials resulting in lighter weight	Material replaced	Mass reduction	Relative cost (per part, High strain steel = 1)
High strength steel	Mild steel	10 – 25	1
Aluminum	Steel, cast iron	40 – 60	1.3 – 2
Magnesium	Steel or cast iron	60 – 75	1.5 – 2.5
Magnesium	Aluminum	25 – 35	1 – 1.5
Glass FRP composites	Steel	25 – 35	1 – 1.5
Carbon FRP composites	Steel	50 – 60	2 – 10+
Al matrix composites	Steel or cast iron	50 – 65	1.5 – 3+
Titanium	Alloy steel	40 – 55	1.5 – 10+
Stainless steel	Carbon steel	20 – 45	1.2 – 1.7

Figure 1-1 presents the comparison of metal and composite materials in terms of weight and cost of vehicles. As seen, composite materials can reduce the weight of a vehicle by 20% to 40%. The relatively large specific-strength and stiffness and remarkable fatigue and corrosion endurance of FRPs have rendered them as effective materials for automotive applications. However, they are considerably costlier than conventional steel; therefore, it is strongly believed that the future will see neither metals, nor composites predominating, but instead, a synergistic marriage of both of these materials, in form of optimized hybrid materials. This would enable manufacturers to produce light-weight and resilient structures in the most cost-effective manner.

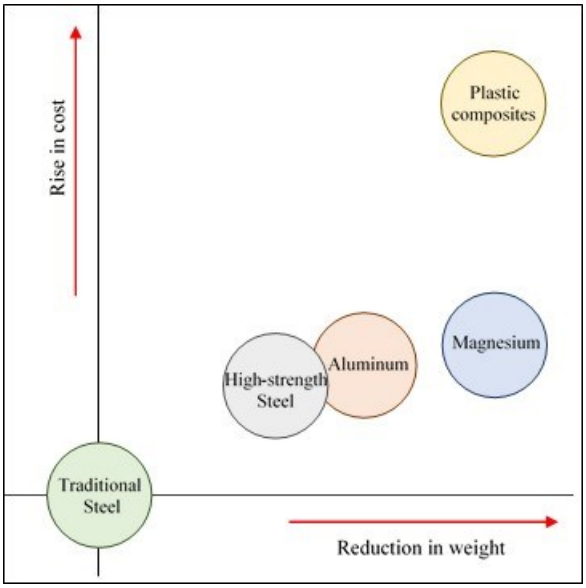

Figure 1-1. Cost comparison of plastic composites with traditional metals (Agrawal 2014)

This class of hybrid materials, referred to as fiber-metal laminates (FMLs), are formed by combining thin metallic sheets with layers of FRP. Each layer of this hybrid material would possess its own unique properties, which collectively would yield the final desired structural properties. In addition to the excellent impact resistance and enhanced crashworthiness, FMLs provide improved specific strength and stiffness, as well as

excellent performance under fatigue in comparison to their metallic and FRP counterparts (Sadighi, Alderliesten et al. 2012).

This technology was originally developed by two professors in mid-70s at the Delf University of Technology in the Netherlands (Vlot, Vogelesang et al. 1999). The most commonly used FML is the GLARE (GLAss laminate aluminum-REinforced epoxy), whereby several thin sheets of aluminum are interspersed with layers of prepreg E-glass/epoxy FRP. To further enhance the impact resistance of this FML, a variation of it was developed by the same inventors, by replacing the unidirectional glass layers of the GLARE with aramid fibers, referred thereafter to ARALL.

1.2 Impact Loading

Vehicles experience different levels of impact loadings during their life-spans. Therefore, when a FML is desired to be used in an automobile or other forms of transport vehicles, then understanding of its behavior under impact loading takes a precedent for design engineers. In general, impact loading is categorized as “low-velocity” or “intermediate-velocity” or “high-velocity (ballistic)” impact. Low-velocity impact (LVI) is usually caused by impact of a relatively large mass in velocities below 10 m/sec. Intermediate and high-velocity impacts occur in the 10 m/sec - 50 m/sec and 50 m/sec – 1000 m/sec velocities, respectively. Figure 1-2 presents the relative responses of the three different types of impact loadings. From the perspective of response, a high-velocity impact is dominated by stress wave propagation through thickness of the target. In this regime, contact time is extremely small, and the target does not have any time to respond. In contrast and comparatively, in low-velocity impact events, the contact time is relatively

long; therefore, the impact response of the target would depend on the geometry, stiffness and boundary conditions of the target.

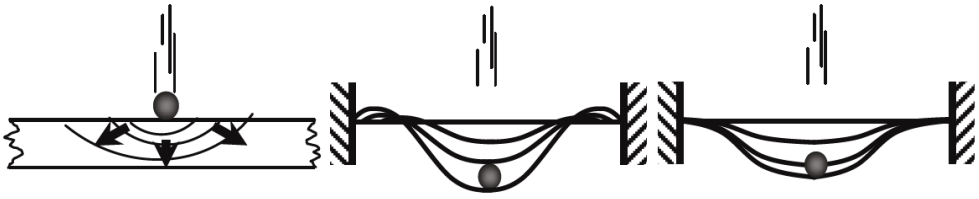

Figure 1-2. Relative Reponses of a target subject to different impact velocities; (a) High-velocity impact, (b) Intermediate-velocity impact and (c) Low-velocity impact (Abrate 2011)

It should be noted that LVI is the most common type of impact occurring in vehicles. To characterize the impact response of vehicles, impact tests are conducted at various levels of components, as pictorially illustrated in Figure 1-3. There are four main levels, as illustrated in the figure. The required testing effort decreases by increasing the level of complexity (Barnes, Coles et al. 2010). For most cases, many numbers and categories of tests are performed for the first level on the pyramid; subsequently, the results from this step will be used to perform finite element analysis of the components noted in the upper levels, with the aim of obtaining acceptable accuracy of the results. It should be noted that the level of tests performed in this research fits to the first level of the pyramid.

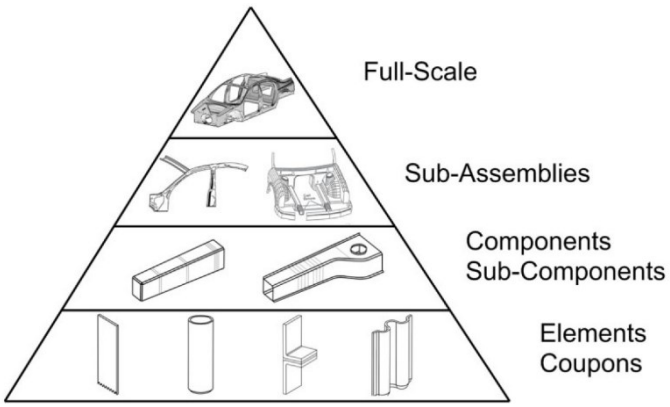

Figure 1-3. Pyramid of levels of tests performed on vehicles (Barnes, Coles et al. 2010)

1.3 Motivations and Objectives

Development of a new class of fiber metal laminates that could offer a lighter weight alternative to current materials used in automotive industry, with the same or preferably improved crashworthiness, is the primary aim of the present research. The novel class of FML introduced in this study is developed using a new generation of 3D fiberglass fabric (3DFGF). 3DFGFs are a new generation of fiberglass woven/braided fabrics that offer significant potential for use in different demanding structural applications such as those involved in automotive, aerospace, marine, and other industries. Their superior specific bending stiffness and strength, light weight, high-energy absorption capacity under impact loading, excellent thermal insulation and acoustic damping are some of the notable features of this new class of materials. 3DFGFs consist of two bi-directional woven glass-fabrics, knitted together by a series of vertical glass fibers, referred hereafter as “pillars”. Therefore, this unique configuration mitigates the delamination issue that is known to be the Achilles' heel of 2D-FRPs (Asaee, Shadlou et al. 2015). As a result, the above-mentioned positive attributes render this unique class of fabrics as an effective alternative constituent in fabrication of FMLs.

As mentioned earlier, 3DFGFs have been recently introduced to the market; therefore, to the best of author’s knowledge, there has been basically no investigation carried out into exploring the performance of FMLs made of 3DFGF under low-velocity impact applications. Moreover, no one had ever explored the response of 3DFMLs either under static or impact loading conditions. Therefore, in brief, the main objective of the present research is to introduce a new class of FML, formed by sandwiching foam-filled 3DFGF

in between thin sheets of magnesium alloy, and to investigate the low-velocity impact (LVI) response and failure modes of various configurations of the FML.

The following major tasks were carried out during the course of development of the 3DFML and characterization of its response under impact loading:

- Investigation of LVI response and assessment of failure modes of the 3DFML and comparison of the response with that of conventional FML.
- Examination of LVI response of various configurations of 3DFML and identification of the most optimum 3DFML configuration based on two design factors (i.e., total weight and cost).
- Enhancement of LVI performance of 3DFML by reinforcing the face sheet with different fabrics and identification of the most efficient reinforcing scheme based on the impact strength, and overall weight and cost.
- Development of a semi-empirical model for evaluation of the impact strength of reinforced-3DFMLs.
- Development of a finite element model to simulate 3DFMLs impact response, using commercial software ABAQUS/Explicit. This software is quite capable of handling highly nonlinear problems as the one considered in this thesis in an efficient manner. Moreover, our research group has had over twenty years of experience with this FE code. It is, however, acknowledges that LS-Dyna FE code has been traditionally used (especially by the automotive sector) to solve impact problems; notwithstanding, this fact does not diminish the capability of ABAQUS in handling such problems in an effective and efficient manner.
- Investigation of the buckling behavior of GNP-reinforced 3DFML.

- Development of an analytical model for assessing the contribution of each constituent of the 3DFGF in carrying load.
- Finally, development of a practical analytical model for predicting the impact response of 3DFML under LVI conditions.

1.4 Thesis Layout

This dissertation has been divided into nine chapters, including the present chapter, which explains the subject of the research, the motivation, objectives and organization of the thesis.

Chapter 2 presents a summary of the literature reviewed in regard to development of fiber metal laminates (FMLs), specifically in regard to their low-velocity impact response (LVI). Different types of FMLs, based on the materials used to form them, are introduced. The chapter also covers the literature pertinent to finite element approaches used to simulate FMLs' response under various loading conditions. Chapter 2 also outlines the studies conducted to investigate the mechanical properties of 3DFGF.

Chapter 3 presents an investigation into the low-velocity impact (LVI) response and failure modes of 3DFMLs, comparing their performance to those of conventional FMLs. The impact characteristics of all panels are also further examined by evaluating and comparing their energy absorption capacity, residual deformation and maximum deformation due to LVI. The mechanical characteristics of the 3D glass fabric are also discussed, and its positive attributes and limitations, in comparison to its conventional woven 2D fabrics are highlighted.

Chapter 4 provides details of a computational study, and an experimental investigation carried out to evaluate the influence of the stacking sequence on the low-velocity impact response of 3DFMLs. In particular, the stiffness, strength, energy absorption and failure modes of various configurations of 3DFMLs are evaluated and compared. To make the comparison unbiased, the impact capacities of the 3DFMLs are normalized with respect to their weight and cost, which are the two most important design selection criteria. In addition to the experiments, a finite-element model is constructed using the commercial finite-element code ABAQUS/Explicit, in conjunction with development of a robust VUMAT to facilitate the analysis of impact response of the FMLs and assessment of their failure modes.

Chapter 5 outlines the details of an experimental and computational investigation that is carried out to explore the level of enhancement could attain by using different fabric types (i.e., fiberglass and carbon) to reinforce 3DFMLs. The numerical results are validated by comparison against experimental results. Moreover, a semi-empirical equation is developed for evaluation of the impact capacity of such reinforced panels, capable of accounting for the reinforcing fabric type. Finally, the efficiency of these reinforced 3DFMLs are rated based on their impact strength with respect to their overall weight and cost.

Experimental observations have revealed that the metallic/FRP interfaces are the weakest link in these 3DFMLs. Therefore, attempts are also made to improve the interface strength by inclusion of inexpensive graphene nanoplatelets (GNP) in the interface resin. Chapter 6 provides the details of the attempts, including the associated experimental and numerical studies carried out to characterize the delamination buckling behavior of resulting GNP-

reinforced 3DFMLs. In total, four groups of specimens with four different delamination lengths and four GNP contents are considered to investigate the effects of GNP on the performance of 3DFMLs under axially applied compressive loading. In addition, the delamination buckling response of the 3DFMLs is investigation using nonlinear finite element analysis. The numerically obtained critical buckling capacities and failure modes are compared to the experimental results.

Chapter 7 presents details of a mechanistic model developed for estimating the strength of 3DFGFs subjected to an out-of-plane compressive loading. The developed model accounts for the strength of every constituent of the fabric (i.e., the woven fabric layers, fiberglass pillars and foam). The contribution of each constituent in carrying load is investigated. In addition, the response of four different configurations of the 3DFGF subjected to a flatwise compression loading is investigated experimentally. Finally, a finite element (FE) model is constructed to analyze the compressive response of the panels.

Chapter 8 provides details of a practical analytical model developed for predicting the static (indentation) and low-velocity impact responses of 3DFMLs. The developed analytical model is modified and generalized based on various configurations of the 3DFML, as well as impactor's geometry. The integrity of the proposed analytical model is verified by comparison of its results against results obtained through experiments and numerical simulations.

Finally, Chapter 9 presents a summary of the results and the overall conclusions established based on the analyses outlined above. Moreover, some recommendations for future research are also offered, aiming at the future development and applications of 3DFMLs.

It should be noted that some chapters may contain materials that could have been contained in other chapters of the thesis. This is due to the optional “paper-based” format of this thesis, an option allowed by Dalhousie University’s Faculty of Graduate Studies.

1.5 References

Abrate, S. (2011). Impact engineering of composite structures, Springer Science & Business Media.

Agrawal, A. (2014). Planning to profit from opportunity: preparing for future demand Global steel 2014, Ernst & Young

Asaee, Z., S. Shadlou and F. Taheri (2015). "Low-velocity impact response of fiberglass/magnesium FMLs with a new 3D fiberglass fabric." Composite Structures 122: 155-165.

Barnes, G., I. Coles, R. Roberts, D. O. Adams and D. M. Garner (2010). Crash safety assurance strategies for future plastic and composite intensive vehicles (PCIVs), US Department of Transportation, Research and Innovative Technology Administration, National Transportation Systems Center.

Powers, W. F. (2000). "Automotive materials in the 21st century." Advanced materials and processes 157(5): 38-42.

Sadighi, M., R. Alderliesten and R. Benedictus (2012). "Impact resistance of fiber-metal laminates: a review." International Journal of Impact Engineering 49: 77-90.

U.S.D.O.E (2017). U.S. Energy and Employment Report | Department of Energy.

Vlot, A., L. Vogelesang and T. De Vries (1999). "Towards application of fibre metal laminates in large aircraft." Aircraft Engineering and Aerospace Technology 71(6): 558-570.

Chapter 2: Literature Review

This chapter aims at summarizing the developments related to fiber metal laminates, and specifically, reviewing the literature related to the low velocity impact response of FMLs. Different classes of FMLs based on the type of metal and fabric used in their formation are reviewed. This chapter also reviews the finite element approaches used for simulating the response of FMLs. Moreover, the studies conducted on assessing the mechanical properties of 3D fiberglass fabric are also investigated.

2.1 Background

The first generation of FML was developed by Fokker Aerostructures of Netherlands in 1950, to prevent the rapid fatigue crack growth observed in the monolithic materials (Chai and Manikandan 2014). It was determined that bonded hybrid laminated structures showed a better performance than the monolithic materials. However, the main progress on the development of FML was achieved by the Delf University of Technology in mid-70's. The first generation of FMLs consisted of Aluminum 2024-T3 sheets and layers of aramid fiber-epoxy prepreg in between (Vlot, Vogelesang et al. 1999). The main applications of the developed FML were in aircraft wings and cargo doors. FMLs provide excellent specific strength and stiffness, superior fatigue performance, excellent impact response, low density and adequate corrosion resistance property. In addition, they also present some of the positive attributes of isotropic metallic materials, such as the elastic-plastic response, durability characteristics and impact resistance, and easily adoptable in repairs (Wu and Yang 2005, Sinmazçelik, Avcu et al. 2011). Figure 2-1 illustrates the superior behavior of FMLs under fatigue loading, illustrating their fiber bridging attribute.

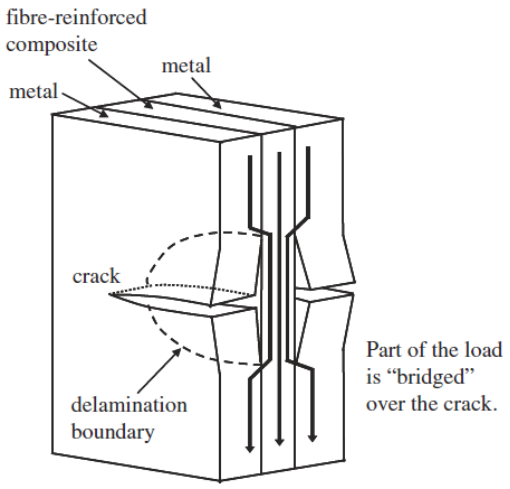

Figure 2-1. Fiber bridging attribute of FMLs resisting crack propagation (Khan, Alderliesten et al. 2009)

FMLs offer remarkable resistance against impact due to the combined presence of metal and fiber-reinforced polymer composite (FRP) materials. The ductile metallic constituent absorbs the impact energy by accommodating relatively large strains prior to failure. In contrast, the FRP constituent, being generally brittle in nature, can only withstand the impact energy within its elastic regime. The lack of plastic deformation and inherent low through-thickness shear capacity of FRPs result in their premature delamination, thus reducing their overall strength. Therefore, the combination of metal and FRP in the form of a FML enhances the impact response of the resulting hybrid material. Figure 2-2 represents the possible failure modes in a typical FML panel.

2.1.1 Aluminum-Based Fiber Metal Laminates

The most commonly used FML in the aerospace industry is the GLARE (GLAss laminate aluminum-REinforced epoxy), whereby several thin sheets of aluminum are interspersed with layers of prepreg E-glass/epoxy FRP. A variation of the GLARE was also developed by the same inventors, who replaced the unidirectional glass layers of the GLARE with

aramid fibers or carbon fibers, referred to as the ARALL and CARALL, respectively. Figure 2-3 and Table 2-1 describe the different standard grades of these FMLs.

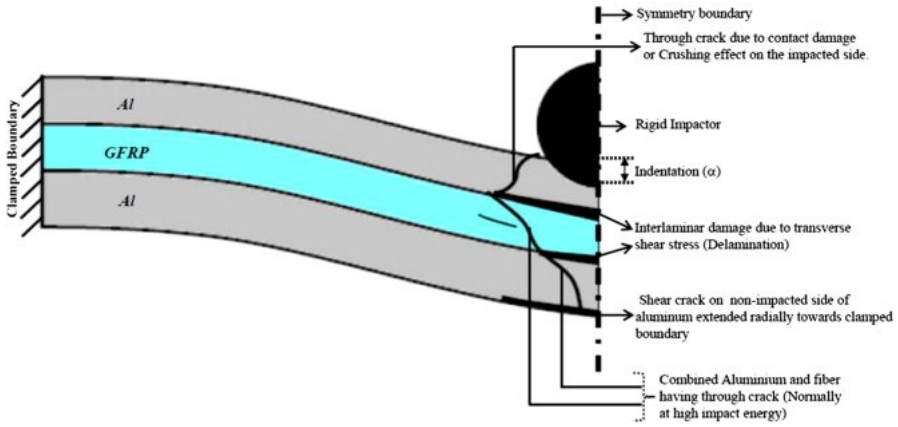

Figure 2-2. Failure modes of clamped a typical FML panel under low velocity impact loading (Chai and Manikandan 2014)

A considerable volume of research works has been conducted on characterizing the impact response of FMLs made of aluminum (Sun, Dicken et al. 1993, Abdullah and Cantwell 2006, Wu, Yang et al. 2007, Carrillo and Cantwell 2008, Liu and Liaw 2010, Payeganeh, Ghasemi et al. 2010, Fan, Cantwell et al. 2011, Fan, Guan et al. 2011, Fan, Guan et al. 2011, Seyed Yaghoubi, Liu et al. 2011, Tsartsaris, Meo et al. 2011, Moriniere, Alderliesten et al. 2012, Periasamy, Manickam et al. 2012, Sadighi, Pärnänen et al. 2012, Seyed Yaghoubi and Liaw 2012, Tan and Akil 2012, Zhu and Chai 2012, Morinière, Alderliesten et al. 2013, Starikov 2013, Tooski, Alderliesten et al. 2013, Vo, Guan et al. 2013, Zhu and Chai 2013, Múgica, Aretxabaleta et al. 2014, Taheri-Behrooz, Shokrieh et al. 2014, Zhang, Gn et al. 2014). For instance, Seyed Yaghoubi et al. (Seyed Yaghoubi, Liu et al. 2011) investigated the effects of FML thickness and impactor's mass on the impact response of glass-reinforced GLARE5 FMLs. They concluded that specimen thickness had a significant effect on the failure modes of FMLs (i.e., fiber critical or metal critical

behavior). They found that an increase in their panel thickness significantly enhanced the energy absorption capacity of their FMLs.

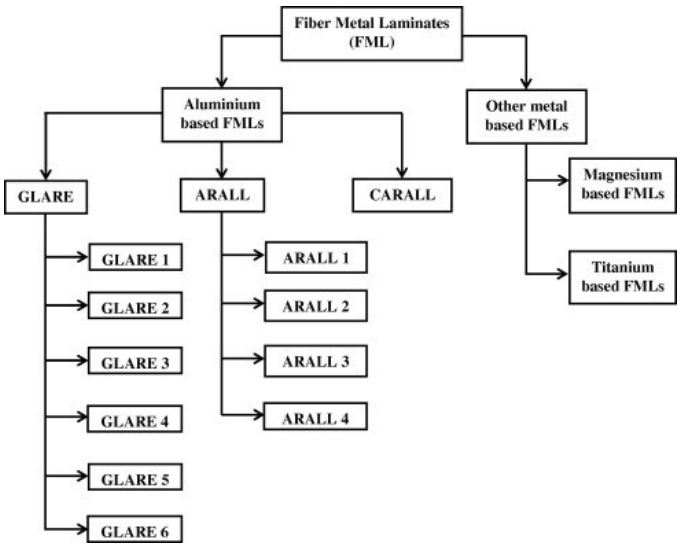

Figure 2-3. Various Classes of FML (Chai and Manikandan 2014)

Fan et al. (Fan, Cantwell et al. 2011) investigated the low-velocity impact response of a GLARE type FML in comparison to plain glass-epoxy FRP material. The results demonstrated that their FMLs could offer greater resistance to perforation than FRP could. Failure mechanisms of the FML were investigated by examining the cross-section of specimens. The failure mechanisms include plastic deformation and fracture of aluminum layers, delamination within the FRP plies and FRP/metal interfaces and fiber fracture. In addition, it was observed that an increase in target size and projectile diameter, and number of metallic and FRP layers increased perforation resistance of the target.

Zhu et al. (Zhu and Chai 2012) conducted research on impact dynamic response and failure modes of FMLs subjected to low velocity impact. The tested specimens consisted of aluminum alloy and two types of fiber-reinforced plastics: woven and unidirectional. They reported the maximum contact force, contact duration and corresponding failure modes for

the two types of FMLs. The results revealed that the impact resistance of FML made with unidirectional fiber was greater than the one made with woven fabric; since UD resulted in perforation type failure.

Table 2-1. Commercially available GLARE and ARALL laminates (Botelho, Silva et al. 2006, Sinmazçelik, Avcu et al. 2011, Sadighi, Alderliesten et al. 2012)

FML grade	Metal layers		Prepreg layers		Specific characteristics
	Al alloy type	Thickness (mm)	Fiber-orientation (°)	Thickness (mm)	
GLARE					
GLARE 1	7475-T761	0.3-0.4	0/0	0.25	Fatigue, strength, yield stress
GLARE 2A	2024-T3	0.2-0.5	0/0	0.25	Fatigue, strength
GLARE 2B	2024-T3	0.2-0.5	90/90	0.25	Fatigue, strength
GLARE 3	2024-T3	0.2-0.5	0/90	0.25	Fatigue, Impact
GLARE 4A	2024-T3	0.2-0.5	0/90/0	0.375	Fatigue, strength in 0° direction
GLARE 4B	2024-T3	0.2-0.5	90/0/90	0.375	Fatigue, strength in 90° direction
GLARE 5	2024-T3	0.2-0.5	0/90/90/0	0.5	Impact, shear, off-axis properties
GLARE 6A	2024-T3	0.2-0.5	45/-45	0.5	Shear, off-axis properties
GLARE 6B	2024-T3	0.2-0.5	-45/45	0.5	Shear, off-axis properties
ARALL					
ARALL 1	7075-T6	0.3	0/0	0.22	Fatigue, strength
ARALL 2	2024-T3	0.3	0/0	0.22	Fatigue, damage tolerant
ARALL 3	7475-T761	0.3	0/0	0.22	Fatigue, toughness
ARALL 4	2024-T8	0.3	0/0	0.22	Fatigue, elevated temperature prop.

2.1.2 Magnesium-Based Fiber Metal Laminates

With respect to light metallic alloys, the use of magnesium alloys in various engineering applications has been increasing steadily in the recent years, especially in the automotive industry. One of the primary reasons behind this trend is due to the alloy's low density (roughly a quarter of that of steel, and 35% lower than that of aluminum), which makes the

weight of magnesium alloy structural components closely comparable to that of FRPs. Similar to FRPs, they possess high strength to weight ratio, improved electromagnetic shielding capability, and superior corrosion resistance, and they cost less than aluminum alloys, (Laliberte, Poon et al. 2000, Botelho, Silva et al. 2006, Sadighi, Alderliesten et al. 2012). However, there are a very limited number of studies investigating the response of FMLs consisting of magnesium sheets (Cortes and Cantwell 2004, Cortes and Cantwell 2006, Pärnänen, Alderliesten et al. 2012, Sadighi, Pärnänen et al. 2012). An example of the few studies available in the literature is the work of Pärnänen et al. (Pärnänen, Alderliesten et al. 2012), who investigated the applicability of AZ31B-H24 magnesium alloy in production of FMLs, and the effect of the number of magnesium layers on their impact response. They compared the magnesium-based FMLs with 2024-T3 Al-based GLARE5 under two different scenarios: (i) FMLs having equal laminate thickness (ii) FMLs having equal bending stiffness. The results revealed that the impact resistance of magnesium-based FMLs were lower than that of GLARE5 when damage in form of cracking of magnesium plates was taken as the failure criterion. However, when comparing the perforation limit, the specific impact energy of the magnesium-based FMLs was observed to be approximately equal to GLARE5.

Despite the somewhat unfavorable results noted in the abovementioned studies, which discouraged the use of magnesium alloys in fabrication of FMLs, several advantages have been illustrated by other researchers (Cortes and Cantwell 2006). For instance, Sadighi et al. (Sadighi, Pärnänen et al. 2012) investigated the fracture response of a magnesium-based FML with woven carbon cloth. They found that the use of magnesium alloy offered a number of advantages, such as the relative lower density, superior corrosion resistance and

excellent electromagnetic shielding attributes in comparison to the conventional FMLs. Their results also revealed that the specific tensile strength of magnesium-based FMLs was higher than that of aluminum-based FMLs. Cortes et al. (Cortes and Cantwell 2004) investigated the fracture properties of fiber metal laminates, including a magnesium alloy-based woven carbon fiber reinforced plastic FML. The results revealed that the specific tensile strengths of their magnesium-based FMLs were higher than that of 2024-T0 aluminum alloy-based FMLs. They also reached to the conclusion that the relatively lower elastic modulus and fracture properties exhibited by their magnesium-based FMLs could be mitigated by selection of an appropriate volume fraction of the FRP constituent.

Alderliesten et al. (Alderliesten, Rans et al. 2008) explored the application of magnesium alloys in FMLs for applications in aerospace structures, by monitoring the overall behavior of FMLs. The overall weight of FMLs decreases due to the lower density of magnesium; however, the lower fatigue properties of magnesium contributes to use a thicker laminate to compensate the deficiency. Therefore, a decrease in the properties may lead to changes in the structure, which could most likely counterbalance the weight saving one could attain for the whole structure. The application of magnesium in fatigue-sensitive parts is not recommended. Moreover, concerns have also been raised in regard to their buckling response.

2.2 Finite Element Simulations of Fiber Metal Laminates

Numerical simulation of the dynamic, nonlinear and transient behavior of composite laminates, particularly FMLs subjected to impact loading is a complex task due to the damage mechanism involved. Fiber breakage, delamination, matrix cracking and large

plastic deformations of the constituents are some of the issues that add complexities to such analysis.

Guan et. al (Guan, Cantwell et al. 2009) simulated the intermediate velocity impact response of a FML, which included polypropylene (PP) fiber/PP matrix composite, formed with two grades of aluminum alloy. The PP-based composite was simulated as an isotropic material with a specified cut-off stress, in order to define the damage mechanism of the composite. Since the Tsai-Wu criterion cannot be used in conjunction with ABAQUS' tensile failure criterion, a tensile failure criterion, which included a specific tensile cut-off stress, was used to simulate the composite's failure. Furthermore, the aluminum plate was defined as an elastic-plastic material in conjunction with a specific plane stress shear and a tensile cutoff stress. The FEA results of their impact simulations, and predicted failure modes of their FML were validated by comparing them against experimental results, which proved remarkable agreements.

Linde et al. (Linde, Pleitner et al. 2004) simulated the low-velocity impact response of GLARE using ABAQUS software. Solid elements were used in the simulation. Failure modes of glass fiber reinforced epoxy such as matrix cracking, and fiber failure was predicted by UMAT subroutine. Furthermore, the delamination between metal layers and fiber-reinforced epoxy was described using the subroutine UINTER, which includes an optional contact definition and failure criterion for delamination. Their simulation included three different approaches. First, a micro-level approach was used, by which individual fibers and fiber-matrix interfaces were studied. Then, a meso-level characterization was used, by which the response of individual plies was simulated, accounting also for

fiber/matrix failure and interlaminar delamination. Finally, a macro-level approach was used to evaluate the effect of completely homogenized laminate.

Sadighi et al. (Sadighi, Pärnänen et al. 2012) simulated response of a FML under low velocity impact loading, using two different approaches. The main aim of the study was to predict the overall behavior of the target under impact loading without the requirement for any detailed failure analysis. The first approach employed solid elements for modelling of both metal and composite layers. Aluminum alloy and composite layers were defined using elastic-plastic material with a rate-dependent behavior and isotropic material, respectively. Both shear and tensile failure criteria were used to simulate the aluminum failure. Failure behavior of the composite layers was defined using the tensile failure criteria. In the second approach, aluminum alloy and composite layers were simulated using the 8-node solid element and 8-node shell element, respectively. Hashin damage criterion was applied for simulation of damage in the composite material. FE results revealed that due to the inherent nature of shell elements, the interface interaction of metal and composite and its subsequent failure due to the impact load could not be predicted. However, comparison of the experimental and FE results produced by solid element model could capture a more accurate prediction of FML's behavior, even with using an incorrect failure criterion. They concluded that a detailed FE model, incorporating a suitable failure criterion must be used if one wants to analyze outcome of a high impact energy impact event leading to development of damage in fabric.

Fan et al. (Fan, Guan et al. 2011) developed a finite element model using ABAQUS software to simulate impact response of FMLs with woven glass fiber-reinforced polymer composite and 2024 aluminum. The focus of study was on evaluating the perforation

threshold and associated failure mechanisms. In addition, the influences of target size, projectile size and striking location on the resulting perforation response were studied. The load-displacement traces of FMLs and perforation threshold of FMLs were predicted successfully.

2.3 3D Fiber Glass Fabric

3D-fiberglass (3DFG) fabric is a newly developed fiberglass woven/braided fabric, consisting of two bi-directional woven fabrics, knitted together by vertical braided glass fiber pillars (see Figure 2-4). Beside the glass fibers, carbon and even basalt fibers, as well as hybridizations of these fibers, have been used in manufacturing 3D clothes. The unique configuration of 3DFG fabrics has been claimed to provide excellent impact resistance. However, since these 3DFGs have been very recently introduced into the market, the number of investigations and studies exploring their mechanical performance are quite limited (Vaidya, Vaidya et al. 2008, Karahan, Gul et al. 2013, Fan, Chen et al. 2014, Hosseini, Sadighi et al. 2015). To the best of author's knowledge, basically no investigation had ever explored the performance of FMLs made of these fabrics under low-velocity impact applications.

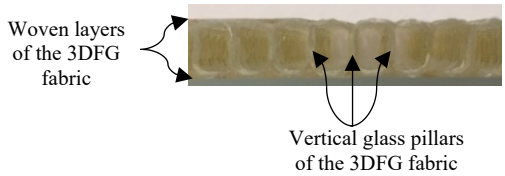

Figure 2-4. The 3D fiberglass fabric (3DFGF)

Vaidya et al. (Vaidya, Hosur et al. 2000) described the advantages of an integrated hollow (space) E-glass/epoxy core sandwich composites as being their relatively lighter weight, and greater bending stiffness. Moreover, the hollow core could be advantageous, in that

wire/rods could be routed though the core region, electronic assemblies could be embedded in the cavities, and that the core cavities could accommodate fuel and fire redundant foams. They also investigated the impact response of hollow core sandwich composite panels with three different thicknesses. It was also demonstrated that the peak forces attained under static compression and low velocity impact tests could be predicted by Euler's column buckling equation. Hosseini et al. (Hosseini, Sadighi et al. 2015) examined the experimental and numerical response of the 3D woven hollow core sandwich composite panels under low velocity impact loading. The impact test was carried out under three different energy levels and different thicknesses of the fabric. The fabric impact response was characterized by means of monitoring the damage modes, perforation loads, load-time and energy-time curves, contact time, and force-displacement relationship. The results indicated that the contact stiffness and perforation load decreased with an increase of panel thickness. In addition, the behavior of the 3D sandwich composite under impact loading was simulated using ABAQUS/Explicit finite element software. The 3D structure of the fiber and the surrounding epoxy resin were modeled via CATIA software, and subsequently exported into ABAQUS/Explicit software for analysis.

Hosur et al. (Hosur, Abdullah et al. 2004) carried out a research on the low velocity impact of 3D hollow integrated with and without additional face sheets of plain weave S2-glass and twill weave carbon fabric. The face sheets were configured on both surfaces of the panels. The results of impact tests conducted with three levels of energy were compared in terms of the peak load, time to peak load, deflection at peak load and absorbed energy. In addition, failure modes were studied by sectioning the specimens and observing their damage extent and mode under optical microscope. The results indicated that the provision

of additional face sheets enhanced the overall damage resistance of the FML markedly. In a study conducted by Asaee et al. (Asaee and Taheri 2015), the mechanical behavior and impact response of 3DFGF were experimentally investigated. They performed three-point bending, compression and impact tests on two different thicknesses of 3DFGF. Moreover, in order to enhance the mechanical performance of the fabric, the fabrics' core cavities were filled with a polyurethane foam. The results demonstrated that foam-filled 3DFGFs with smaller thickness exhibited greater bending and compression strengths. Furthermore, it was shown that the foam-filled fabric exhibited improved performance under impact loading. Moreover, the response of the fabric under low-velocity impact generated by different sizes of impactors was also investigated (Asaee and Taheri 2016). The most interesting attribute of the fabric under impact was observed to be the absence of any delamination, which is quite significant from structural mechanics' perspective.

2.4 References

Abdullah, M. and W. Cantwell (2006). "The impact resistance of polypropylene-based fibre–metal laminates." Composites science and technology 66(11): 1682-1693.

Alderliesten, R., C. Rans and R. Benedictus (2008). "The applicability of magnesium based Fibre Metal Laminates in aerospace structures." Composites Science and Technology 68(14): 2983-2993.

Asaee, Z. and F. Taheri (2015). Characterization of the Mechanical and Impact Response of a New-Generation 3D Fiberglass Fabric. American Society of Composites-30th Technical Conference.

Asaee, Z. and F. Taheri (2016). Experimental Studies on the Impact Response of 3D Fiberglass Fabric Subject to Different Size Impactors. Proceedings of the American Society for Composites: Thirty-First Technical Conference.

Botelho, E. C., R. A. Silva, L. C. Pardini and M. C. Rezende (2006). "A review on the development and properties of continuous fiber/epoxy/aluminum hybrid composites for aircraft structures." Materials Research 9(3): 247-256.

Carrillo, J. and W. J. Cantwell (2008). "Scaling effects in the low velocity impact response of fiber-metal laminates." Journal of Reinforced Plastics and Composites 27(9): 893-907.

Chai, G. B. and P. Manikandan (2014). "Low velocity impact response of fibre-metal laminates–A review." Composite Structures 107: 363-381.

Cortes, P. and W. Cantwell (2004). "Fracture properties of a fiber-metal laminates based on magnesium alloy." Journal of materials science 39(3): 1081-1083.

Cortes, P. and W. Cantwell (2006). "The fracture properties of a fibre–metal laminate based on magnesium alloy." Composites Part B: Engineering 37(2): 163-170.

Fan, H., H. Chen, L. Zhao, J. Zhou, F. Jin, J. Zheng and N. Kuang (2014). "Flexural failure mechanisms of three-dimensional woven textile sandwich panels: Experiments." Journal of Composite Materials 48(5): 609-620.

Fan, J., W. Cantwell and Z. Guan (2011). "The low-velocity impact response of fiber-metal laminates." Journal of Reinforced Plastics and Composites 30(1): 26-35.

Fan, J., Z. Guan and W. Cantwell (2011). "Numerical modelling of perforation failure in fibre metal laminates subjected to low velocity impact loading." Composite structures 93(9): 2430-2436.

Fan, J., Z. Guan and W. Cantwell (2011). "Structural behaviour of fibre metal laminates subjected to a low velocity impact." Science China Physics, Mechanics and Astronomy 54(6): 1168-1177.

Guan, Z., W. Cantwell and R. Abdullah (2009). "Numerical modeling of the impact response of fiber–metal laminates." Polymer Composites 30(5): 603-611.

Hosseini, S. A., M. Sadighi and R. Maleki Moghadam (2015). "Low-velocity impact behavior of hollow core woven sandwich composite: Experimental and numerical study." Journal of Composite Materials 49(26): 3285-3295.

Hosur, M., M. Abdullah and S. Jeelani (2004). "Manufacturing and low-velocity impact characterization of hollow integrated core sandwich composites with hybrid face sheets." Composite Structures 65(1): 103-115.

Karahan, M., H. Gul, N. Karahan and J. Ivens (2013). "Static behavior of three-dimensional ıntegrated core sandwich composites subjected to three-point bending." Journal of Reinforced Plastics and Composites 32(9): 664-678.

Khan, S., R. Alderliesten and R. Benedictus (2009). "Post-stretching induced stress redistribution in fibre metal laminates for increased fatigue crack growth resistance." Composites Science and Technology 69(3): 396-405.

Laliberte, J., C. Poon, P. Straznicky and A. Fahr (2000). "Applications of fiber-metal laminates." Polymer composites 21(4): 558-567.

Linde, P., J. Pleitner, H. de Boer and C. Carmone (2004). Modelling and simulation of fibre metal laminates. ABAQUS Users' conference.

Liu, Y. and B. Liaw (2010). "Effects of constituents and lay-up configuration on drop-weight tests of fiber-metal laminates." Applied Composite Materials 17(1): 43-62.

Moriniere, F., R. Alderliesten and R. Benedictus (2012). "Development of fibre-metal laminates for improved impact performance." The European Physical Journal-Special Topics 206(1): 79-88.

Morinière, F., R. Alderliesten, M. Sadighi and R. Benedictus (2013). "An integrated study on the low-velocity impact response of the GLARE fibre-metal laminate." Composite Structures 100: 89-103.

Múgica, J., L. Aretxabaleta, I. Ulacia and J. Aurrekoetxea (2014). "Impact characterization of thermoformable fibre metal laminates of 2024-T3 aluminium and AZ31B-H24 magnesium based on self-reinforced polypropylene." Composites Part A: Applied Science and Manufacturing 61: 67-75.

Pärnänen, T., R. Alderliesten, C. Rans, T. Brander and O. Saarela (2012). "Applicability of AZ31B-H24 magnesium in fibre metal laminates–an experimental impact research." Composites Part A: Applied Science and Manufacturing 43(9): 1578-1586.

Payeganeh, G., F. A. Ghasemi and K. Malekzadeh (2010). "Dynamic response of fiber–metal laminates (FMLs) subjected to low-velocity impact." Thin-Walled Structures 48(1): 62-70.

Periasamy, M., B. Manickam and K. Hariharasubramanian (2012). "Impact properties of aluminium-glass fiber reinforced plastics sandwich panels." Materials Research 15(3): 347-354.

Sadighi, M., R. Alderliesten and R. Benedictus (2012). "Impact resistance of fiber-metal laminates: a review." International Journal of Impact Engineering 49: 77-90.

Sadighi, M., T. Pärnänen, R. Alderliesten, M. Sayeaftabi and R. Benedictus (2012). "Experimental and numerical investigation of metal type and thickness effects on the impact resistance of fiber metal laminates." Applied Composite Materials 19(3-4): 545-559.

Seyed Yaghoubi, A. and B. Liaw (2012). "Thickness influence on ballistic impact behaviors of GLARE 5 fiber-metal laminated beams: Experimental and numerical studies." Composite Structures 94(8): 2585-2598.

Seyed Yaghoubi, A., Y. Liu and B. Liaw (2011). "Low-velocity impact on GLARE 5 fiber-metal laminates: influences of specimen thickness and impactor mass." Journal of Aerospace Engineering 25(3): 409-420.

Sinmazçelik, T., E. Avcu, M. Ö. Bora and O. Çoban (2011). "A review: Fibre metal laminates, background, bonding types and applied test methods." Materials & Design 32(7): 3671-3685.

Starikov, R. (2013). "Assessment of impact response of fiber metal laminates." International Journal of Impact Engineering 59: 38-45.

Sun, C., A. Dicken and H. Wu (1993). "Characterization of impact damage in ARALL laminates." Composites Science and Technology 49(2): 139-144.

Taheri-Behrooz, F., M. Shokrieh and I. Yahyapour (2014). "Effect of stacking sequence on failure mode of fiber metal laminates under low-velocity impact." Iranian Polymer Journal 23(2): 147-152.

Tan, C. and H. M. Akil (2012). "Impact response of fiber metal laminate sandwich composite structure with polypropylene honeycomb core." Composites Part B: Engineering 43(3): 1433-1438.

Tooski, M. Y., R. Alderliesten, R. Ghajar and S. Khalili (2013). "Experimental investigation on distance effects in repeated low velocity impact on fiber–metal laminates." Composite Structures 99: 31-40.

Tsartsaris, N., M. Meo, F. Dolce, U. Polimeno, M. Guida and F. Marulo (2011). "Low-velocity impact behavior of fiber metal laminates." Journal of Composite Materials 45(7): 803-814.

Vaidya, A., U. Vaidya and N. Uddin (2008). "Impact response of three-dimensional multifunctional sandwich composite." Materials Science and Engineering: A 472(1): 52-58.

Vaidya, U., M. Hosur, D. Earl and S. Jeelani (2000). "Impact response of integrated hollow core sandwich composite panels." Composites Part A: Applied Science and Manufacturing 31(8): 761-772.

Vlot, A., L. Vogelesang and T. De Vries (1999). "Towards application of fibre metal laminates in large aircraft." Aircraft Engineering and Aerospace Technology 71(6): 558-570.

Vo, T. P., Z. Guan, W. Cantwell and G. Schleyer (2013). "Modelling of the low-impulse blast behaviour of fibre–metal laminates based on different aluminium alloys." Composites Part B: Engineering 44(1): 141-151.

Wu, G. and J.-M. Yang (2005). "The mechanical behavior of GLARE laminates for aircraft structures." Jom 57(1): 72-79.

Wu, G., J.-M. Yang and H. T. Hahn (2007). "The impact properties and damage tolerance and of bi-directionally reinforced fiber metal laminates." Journal of materials science 42(3): 948-957.

Zhang, H., S. Gn, J. An, Y. Xiang and J. Yang (2014). "Impact behaviour of GLAREs with MWCNT modified epoxy resins." Experimental Mechanics 54(1): 83-93.

Zhu, S. and G. B. Chai (2012). "Low-velocity impact response of fibre–metal laminates–Experimental and finite element analysis." Composites Science and Technology 72(15): 1793-1802.

Zhu, S. and G. B. Chai (2013). Impact of aluminum, CFRP laminates, fibre-metal laminates and sandwich panels. Composite Materials and Joining Technologies for Composites, Volume 7, Springer: 199-205.

Chapter 3: Low-velocity Impact Response of Fiberglass/Magnesium FMLs with a New 3D Fiberglass Fabric

Zohreh Asaee, Shahin Shadlou and Farid Taheri

Published in Composite Structures, Volume 122, PP 155-165, 2015

Zohreh Asaee is the principal author of this article. As a part of her PhD program, she conducted the underpinning research noted in the article. She performed the experimental works while receiving guidance from Shahin Shadlou, who was a postdoctoral fellow within the research group. Moreover, she analyzed the experimental results, conducted all numerical simulations, and prepared the draft of the article and applied the necessary revisions prior to publication of the articles, all under supervision and guidance of her supervisor, Prof. Farid Taheri.

3.1 Abstract

A new fiber metal laminate (FML), formed by sandwiching a 3D fiberglass fabric in between thin sheets of magnesium alloy, is introduced in this study. In particular, the low-velocity impact (LVI) response and failure modes of this new FML composite are investigated experimentally and computationally. The performance of this new FML is compared against the conventional FMLs, made with various layers of biaxial woven fabrics in place of the 3D fabric. The failure modes of the specimens are characterized based on quantitative measurements of shape, type, and extent of damage on the FMLs' constituents. The characteristics of the new 3D-glass fabric are discussed, and its positive attributes and limitations, in comparison to woven fabrics, are highlighted. The results would reveal that the new FML exhibits remarkable impact absorption capacity. Moreover, in order to simulate the response of such complex structures, a finite-element analysis (FEA) framework is constructed using the commercial finite-element code ABAQUS. Good agreement between the experimental and computational results is obtained, indicating that the framework can be used for future examinations of various configurations

of the FML and the resulting response under different loading situations, as well as their optimization.

3.2 Introduction

The fiber-reinforced polymer (FRP) composite materials have been extensively utilized in various industries in the recent years. The relatively large specific-strength and stiffness and remarkable fatigue and corrosion endurance of FRPs have rendered them as effective materials for automotive applications. The weakest link in FRPs is their interlaminar shear capacity, which makes them susceptible to impact loading. Therefore, several researchers have tried to develop various means to improve the impact response of FRPs throughout the past few decades. One of the most effective means for improving the impact response of FRPs has been the incorporation of thin sheets of metals to form the so-called fiber-metal laminates (FMLs). This technology was originally developed by two professors in mid-70s at the Delf University of Technology in the Netherlands. The most commonly used FML is the GLARE (glass laminate aluminum reinforced epoxy), whereby several thin sheets of aluminum are interspersed with layers of prepreg E-glass/epoxy FRP. In addition to excellent impact resistance, FMLs provide improved specific strength and stiffness, as well as excellent fatigue performance in comparison to their FRP counterparts. To further enhance the impact resistance of FML, a variation of the GLARE was developed by the same inventors, by replacing the unidirectional glass layers of the GLARE with aramid fibers, referred to as the ARALL.

A considerable volume of research has been conducted on the impact characterization of FMLs made of aluminum (Zhu and Chai 2012, Lee, Morillo et al. 2013, Morinière, Alderliesten et al. 2013, Starikov 2013, Tooski, Alderliesten et al. 2013, Dursun and Soutis

2014, Zhu and Chai 2014). For instance, Seyed Yaghoubi et al. (Seyed Yaghoubi, Liu et al. 2011) investigated the effects of FML thickness and impactor's mass on the impact response of glass-reinforced GLARE5 FMLs. They concluded that the specimen thickness had a significant effect on the failure modes of FMLs (i.e., fiber critical or metal critical behavior). They found that an increase in their panel thickness significantly enhanced the energy absorption capacity of their FMLs.

With respect to light metallic alloys, the use of magnesium alloys in various engineering applications has been increasing steadily in the recent years, especially in the automotive industry. One of the primary reasons for this trend is due to the alloys' low density (roughly a quarter of that of steel, and 35% lower than that of aluminum), which makes the weight of magnesium alloy structural components very comparable to that of FRPs. Similar to FRPs, they possess high strength to weight ratio, improved electromagnetic shielding capability, lower cost compared to aluminum, and superior corrosion resistance (Laliberte, Poon et al. 2000, Botelho, Silva et al. 2006, Sadighi, Alderliesten et al. 2012). However, there are very limited number of studies investigating the response of FMLs made of magnesium sheets (Alderliesten, Rans et al. 2008). An example of the few studies available in the literature is the work of Pärnänen et al. (Pärnänen, Alderliesten et al. 2012), who investigated the applicability of AZ31B-H24 magnesium in production of FMLs, and the effect of the number of magnesium layers on their impact response. They compared the magnesium-based FMLs with Al 2024-T3-based GLARE5 for two different scenarios: (i) FMLs with equal laminate thickness (ii) FMLs with equal bending stiffness. The results revealed that the impact resistance of magnesium based FMLs were lower than that of GLARE5 when damage in form of cracking of magnesium plates was taken as the failure

criterion. However, when comparing the perforation limit, the specific impact energy of the magnesium-based FMLs was observed to be approximately equal to GLARE5.

Despite the somewhat unfavorable results noted in the abovementioned studies, which discouraged the use of magnesium alloys in fabrication of FMLs, several advantages have been illustrated by other researchers (Cortes and Cantwell 2006). For instance, Sadighi et al. (Sadighi, Pärnänen et al. 2012) investigated the fracture response of a magnesium-based FML with woven carbon cloth. They found that the use of magnesium alloy offered a number of advantages, such as the relative lower density, superior corrosion resistance and excellent electromagnetic shielding attributes in comparison to the conventional FMLs. Their results also revealed that the specific tensile strength of magnesium-based FMLs was higher than that of aluminum-based FMLs. Cortes et al. (Cortes and Cantwell 2004) investigated the fracture properties of fiber metal laminates including a magnesium alloy-based woven carbon fiber reinforced plastic FMLs. The results of their tensile tests revealed that the specific tensile strengths of their magnesium-based FMLs were higher than that of 2024-T0 aluminum alloy-based FMLs. They also reached to the conclusion that the relatively lower elastic modulus and fracture properties exhibited by their magnesium-based FMLs could be mitigated by selection of an appropriate volume fraction of the composite's constituents.

3D-fiberglass (3DFG) fabric is a newly developed fiberglass woven/braided fabric, consisting of two bi-directional woven fabrics, knitted together by vertical braided glass fiber pillars (see Figure 3-1). Besides glass fibers, carbon and even basalt fibers, as well as hybridizations of these fibers, could be used to form 3D clothes. The unique configuration of fibers in 3DFG has been claimed to provide excellent impact resistance. However, since

these 3DFG has been very recently introduced to the market, to the best of authors' knowledge, there has been basically no investigation into exploring the performance of FMLs made of these fabrics under low-velocity impact applications.

The main objective of the present study is, therefore, to introduce a new class of FMLs, formed by sandwiching light-weight foam filled 3DFG, in between thin (0.8 mm) sheets of magnesium alloy, and to investigate the low-velocity impact (LVI) response and failure modes of the new composite. In addition, three other FML configurations are also investigated, namely FMLs whose FRPs are composed of 4, 7, and 16 layers of biaxial woven fabrics, respectively. Moreover, the flexural strength and stiffness of all specimens were evaluated by three point-bend tests.

Figure 3-1. The 3D fiberglass fabric (3DFG)

The lack of numerical and simulation methods for predicting the behavior of 3D-fiber response is the major weakness in the current state-of-the-art research. Sadighi et al. (Sadighi and Hosseini 2013) conducted an investigation into the mechanical behavior of a 3D fiberglass composite. They employed a 3D finite element model consisting of glass fabric and the surrounding epoxy resin matrix for predicting the mechanical response of their complex system. The 3D fiberglass fabric was modeled by the CATIA software, and subsequently the model was imported into the ABAQUS commercial finite element analysis (FEA) software. They obtained good agreement between their FEA and experimental results.

In the present study, the simulation of the response of the developed 3DFG-FMLs is carried out using the ABAQUS/Explicit FEA software. The conventional 4-node shell elements and 8-node solid elements are employed to simulate the response of the complex material system examined here. The required mechanical properties of 3D fiberglass fabric are extracted from the results of 3-point bending, edgewise and flatwise compression tests. The simulation results are compared to the experimental results and validated.

3.3 Experimental Work

The magnesium alloy used to form the FMLs investigated in this study are light-weight AZ31B magnesium alloy sheets with a thickness of 0.8 mm, supplied by M&B MAG Ltd (Toronto, ON). Two different types of fabrics were used to manufacture the specimens; (i) a 3DFG fabric, and (ii) a biaxial woven glass fabric. The 3DFG fabric with thickness of 10 mm was acquired through China Beihai Fiberglass Co. Ltd. (Jiujiang City, China). In order to enhance the impact response of 3DFG, the space within the 3DFG fabric (see Figure 3-1) was filled with an 8-lbs density pour-type urethane foam supplied by the U.S. Composites (West Palm Beach, FL 33407). Araldite LY 564 (Bisphenole-A) epoxy resin was used throughout this study along with Aradur 2954 (cycloaliphatic polyamine) hardener. This epoxy system is available through Huntsman Co. (West Point, GA).

FMLs fabricated by the biaxial woven glass fabrics had three different layups - four, seven and sixteen layers of fabrics, respectively. Prior to laying up the FMLs, the surfaces of the magnesium alloy plates were manually sanded with 100 grit sandpaper with an equal number of passes. Compressed air was used to clean the surface dust, and the surfaces were then wiped clean with acetone. At that stage, specimens that included the 3D fabric were fabricated in the following order. First, resin was applied to the 3D fabric; the resin

impregnation encourages the fiber connecting the top and bottom cloth of the fabric to expand through-the-thickness direction (in other words, the resin "wakes" those the through-thickness fibers), creating spacing in the core of the fabric, as seen in Figure 3-1. Subsequently, the foam is injected in the core cavity and let cure (which takes all of five minutes). The FML panels were then assembled by sandwiching the foam impregnated and resin cured 3DFG in between magnesium plates, using a two-part acrylic epoxy adhesive. Fabrication of the FML panels, including the woven fabric followed the same procedure, with two exceptions: (i) no foam was used in these FML panels, and (ii) the FRPs were constructed following the standard vacuum-bagging procedure.

The panels were subsequently cut into 110 mm × 110 mm size specimens. Details of the stacking sequence of the four fiberglass-based FMLs are summarized in Table 3-1. The bending stiffness of the FMLs was determined by conducting 3-point bending test as per ASTM-D790 standard (ASTM-D790 1997), using an Instron servo-hydraulic test machine (model 8500+) equipped with a 25 kN load-cell.

Table 3-1. Specifics of the different FMLs

Specimen ID	Overall Thickness (mm)	Overall Density (g/mm^3)	Reinforcement Fabric type	Number of layers of fabrics
3DF-FML	14.40	0.047	3DFGF	1
4-layer FML	4.87	0.093	biaxial woven	4
7-layer FML	6.53	0.163	biaxial woven	7
16-layer FML	10.16	0.372	biaxial woven	16

Low-velocity impact tests of the FMLs were carried out using a modified Charpy impact test equipment (see Figure 3-2-(a)). The equipment consisted of a swinging pendulum, an impactor, and a fixture for holding the specimen. The fixture used to hold the specimens consisted of two thick steel plates with an 80-mm diameter hole in their center (See Figure

3-2-(b)). The Charpy impact test machine was also fitted with a computer-controlled dynamic load cell and linear variable differential transformer sensor (LVDT), which were used for measuring the impact load and displacement of the impact location of the specimen, respectively. The data obtained from the load cell, and LVDT was recorded using a digital data-acquisition system. Moreover, a code was developed in the MATLAB environment to analyze the data and extract the desired properties. Therefore, the impact characteristics, such as the absorbed impact energy, contact time, maximum force and deformation were extracted from the force-displacement time history.

The energy levels used in testing the specimens were selected such to generate damage: (i) on the impacted surface; (ii) damage to the reverse surface, and finally (iii) damage in the form of full perforation through the specimen. These damage modes will be referred to as Mode 1, 2 and 3, respectively, hereafter.

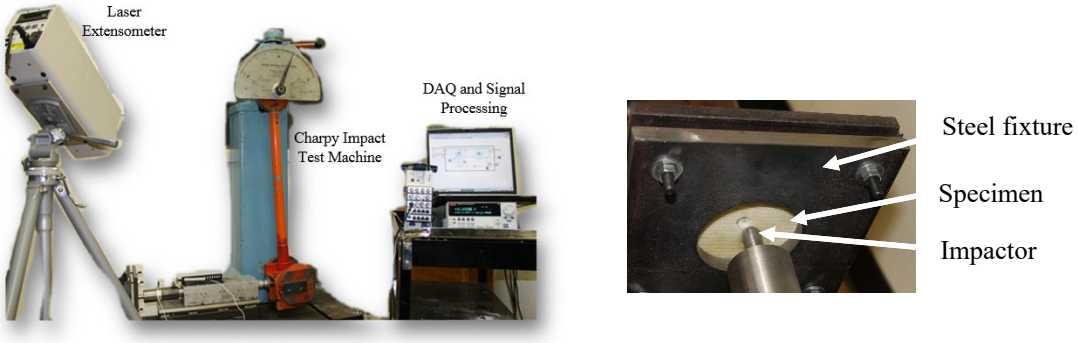

(a) (b)

Figure 3-2. (a) The Impact test equipment, (b) specimen holding fixture

3.4 Finite Element Analysis

In our preliminary search of literature related to this topic, it was discovered that there is a notable paucity of research work on numerical (simulation) methods that could accurately

predict the behavior of FMLs in general, and in particular, be capable of simulating the response of 3D-fiber-reinfoced composites (Sadighi and Hosseini 2013). Therefore, attempts have been made in the present study to investigate the impact response of 3DFG-FMLs using the finite element method by incorporating the ABAQUS/Explicit commercial FE code.

As it was mentioned earlier, the 3DFG consists of two bi-directional woven fabrics connected in a uniform specific distance by vertical columns-like fibers. In the case of our investigation, the hollow section was filled with a foam. To start the FE simulation, the woven fabrics on the top and bottom of the fabric were modeled as an orthotropic elastic material, defined with the appropriate engineering constants. The core part of the 3DFG, which was filled with foam was simulated as a crushable foam, using the average results of hardening curves obtained through a series of compression tests conducted on square blocks of foam-injected 3DFG fabric. In other words, it was assumed that the compression force was resisted by the combined foam and glass fiber columns, in an aggregate and homogeneous manner, while the bending induced stresses where endured by the top and bottom layer woven fabrics. The mechanical properties of the foam and woven fabrics of 3DFG are presented in Table 3-2 and Table 3-3, respectively. These properties were selected as the baseline and were calibrated for 3DFGF based on the results obtained from three-point bending, compression and impact tests. The magnesium alloy was modeled as an elastic-plastic material with consideration of this alloy's rate-dependency. Figure 3-3 depicts the true stress-strain curve of the alloy at different strain rates. The two 3DFGF composites and magnesium layers were modeled using the conventional 4-node shell elements, (S4R in the ABAQUS). Hashin's failure criterion was used to establish initiation

of damage in the woven fabric (Hashin 1983). This criterion is capable of identifying four damage initiation mechanisms, namely, tensile and compressive failure modes in fibers and matrix, respectively. Moreover, the onset of damage in the magnesium layers was simulated based on the ductile damage criterion available in the ABAQUS.

Table 3-2. Mechanical properties of FRP composite (Taheri-Behrooz, Shokrieh et al. 2014)

Elastic Modulus (GPa)			Poisson's Ratio			Shear Modulus (GPa)		
E_{11}	E_{22}	E_{33}	υ_{12}	υ_{13}	υ_{23}	G_{12}	G_{13}	G_{23}
37	8.5	8.5	0.254	0.254	0.428	4.7	4.7	3.28

Compressive Strength (MPa)			Tensile Strength (MPa)			Shear Strength (MPa)		
X^C	Y^C	Z^C	X^T	Y^T	Z^T	S_{12}	S_{13}	S_{23}
750	44	40	780	44	40	30	30	30

Table 3-3. Mechanical properties of the foam used in this study evaluated based on ASTM C364 and C365 (ASTM-C364 2006, ASTM-C365 2010)

Density (kg/m^3)	Compressive Modulus (MPa)	Compressive Strength (MPa)	Compressive Fracture Strain (mm/mm)	Fracture Energy ($N\text{-}mm/mm^2$)
128	435	7.0	0.055	0.326

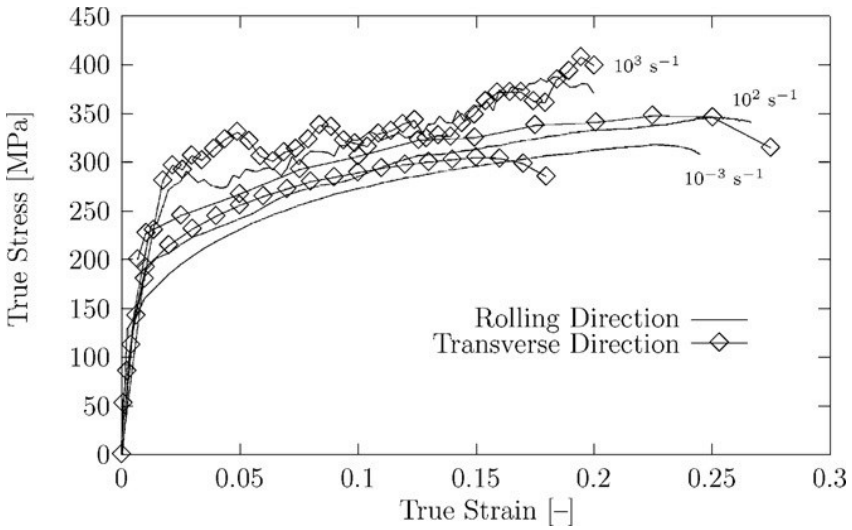

Figure 3-3. True stress-strain curve of AZ31B magnesium at different strain rates (Ulacia, Salisbury et al. 2011)

The foam core of 3DFG was simulated using C3D8R element of the ABAQUS, which is the conventional 8-node solid element, but with a reduced integration scheme. A ductile damage criterion in conjunction with shear damage criterion were utilized for simulation of damage initiation in the crushable foam (Hibbitt 2002). The development of damage was simulated using an energy based model based on the fracture energy. The fracture energy and fracture strain of the model was determined using the flatwise, edgewise compressive and three-point bending tests as per ASTM C365 (ASTM-C365 2010), ASTM C364 (ASTM-C364 2006) and ASTM C393 (ASTM-C393 2000), respectively.

The impactor was modeled as a rigid body, since, the stiffness and mass of the impactor is considerably greater than those of the 3DFG-FML. The tested specimens, including their boundary conditions, are symmetric along two-axis (i.e., x and y axis); therefore, only a quarter symmetry of the system had to be discretized.

The shell elements forming the bi-directional woven fabrics were tied to the crushable foam solid elements using shell-to-solid coupling feature available in ABAQUS. The specimen/impactor interface was model using the general contact algorithm of the ABAQUS/Explicit. The contact algorithm accounts for normal contact, with its tangential component simulated by assuming a friction coefficient of $\mu=0.2$.

Convergence analyses were performed by varying the mesh density within the plane and through the thickness of the model. Figure 3-4 presents the results of convergence analysis carried out to reach an optimal mesh density. The optimal mesh was selected based on convergent in value of the strain energy of the system produced by various mesh densities. The isometric and plan views of the final FE model are depicted in Figure 3-5. It should be noted that one of the parameters that had a significant effect on the trial mesh densities was

hourglass control of element. Hourglass modes are inadmissible zero-energy modes of deformation (producing zero strain on the system) that could occur when 2D and 3D isoparametric elements and shell and thick shell elements are used. ABAQUS has various algorithms (e.g., enhanced, relax stiffness and viscous) for inhibiting the hourglass modes. The algorithm employed in this study was the enhanced method, which as stated in the manual "refines the pure stiffness method based on the enhanced assumed strain method" The algorithm essentially provides resistance to hourglassing when the model includes nonlinear materials. Moreover, ABAQUS User Manual recommends this algorithm, particularly when modeling foam materials, because it facilitates more accurate prediction of a displaced configuration returning to its original configuration through the unloading path.

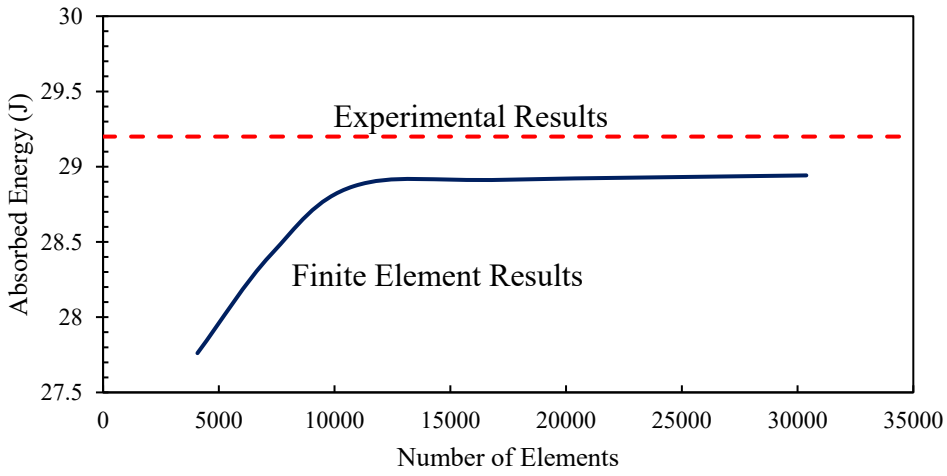

Figure 3-4. Mesh convergence analysis of numerical model

3.5 Results and Discussions

In this section, the results obtained through impact tests and post-impact assessment of the specimens are presented. Subsequently, the 3DFG's features and discussion of the results are also presented.

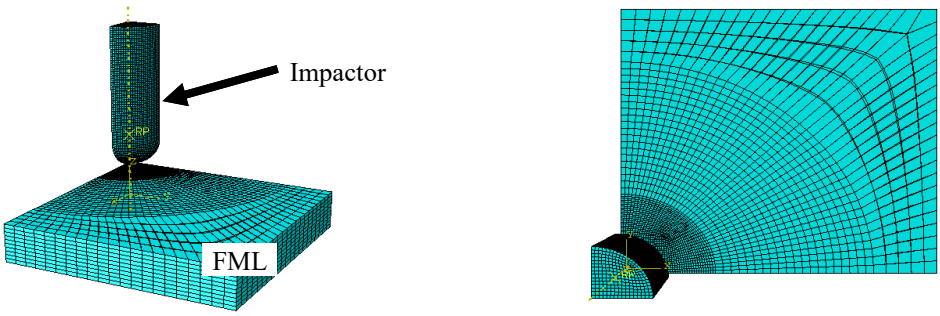

(a) (b)

Figure 3-5. (a) Isometric and (b) Plan views of the quarter-symmetry mesh used to simulate impactor and 3DFG-FML specimen.

3.5.1 Flexural Stiffness

As stated, the 3-point bending test method was employed to establish the flexural stiffness of the FML specimens. This is in concert with the work of Liu (Liu 1988), who suggested that the degradation of mechanical properties due to delamination can be assessed using the results obtained from a bending analysis. Liu's suggested methodology was on the premise that the LVI response of composite laminates would, to some extent, be due to plate bending; therefore, the variation in the flexural stiffness values can be an indicative of development of delamination in his impacted FMLS. Moreover, in order to make a more unbiased comparison of the performance of our FMLs, the overall weight of each specimen is used to report the results in the form of specific stiffness, as presented in Table 3-4.

As expected, the flexural stiffness of FMLs comprised of woven fabrics increased by the increase in the number of layers of FRP. In addition, the results revealed that the bending stiffness of the 3DFG-FML was higher than the FML hosting four biaxial woven layers, but observed to be less than the FMLS hosting seven and 16 layers of FRP. Consequently, it was expected that the perforation impact energy capacity of 3DFG-FML would be greater than the 3-layer FRP, but lower than the 7- and 16-layer of FRP. However, when the

specific flexural stiffness values of the FMLs are compared, the 3DFG-FML exhibits the largest specific stiffness among all the FMLS; this is attributed to the fact that the 3DFG-FML is the lightest and thickest among the FMLs tested. As a result, 3DFG-FML could possess the highest perforation impact energy when compared to comparable (i.e., weight-wise) FRP laminate.

Table 3-4. Flexural stiffness of the FMLs

Specimen ID	Flexural Stiffness ($N\text{-}m^2$)	Specific Flexural Stiffness ($N\text{-}m^2/g.mm^{-3}$)
3DF-FML	269.28	5729.53
4-layer FML	178.23	1916.40
7-layer FML	356.96	2189.96
16-layer FML	1287.25	3460.34

3.5.2 Failure Impact Energy

The following equation is used to predict the limit of impact energy for second mode of failure of the tested specimens. This simple equation evaluates the energy that causes fiber failure as a result of deformation of the non-impacted surface of the FMLs.

$$E = \frac{\sigma^2 wtL}{18E_f} \tag{3.1}$$

In the above equation, σ is the flexural strength, w, L and t are the width, unsupported length and thickness of specimen, respectively, and E_f is the flexural modulus. The estimated results, which formed the baseline for the establishment of the impact energies used in tests are presented in Table 3-5.

Table 3-5. Comparison of the estimated and experimentally obtained energy of the FMLs

Specimen ID	Flexural Modulus (GPa)	Flexural Strength (MPa)	Estimated Impact Energy (J)	Experimental Impact energy (J)
4-layer FML	18.51	80	39.4	30
7-layer FML	15.38	165	43.8	60
16-layer FML	14.72	250	57.8	140

The comparison of the predicted values obtained by the equation to the experimental results revealed that while the equation could predict the impact energy fairly accurately (i.e., close to the experimental results), however, the discrepancies between the results increased as the thickness of specimen increased. The error margin grew up to 59% in the case of the specimen that hosted 16 layers of FRP. This growing error margin could be primarily attributed to the shear deformation that becomes more pronounced in thicker specimens, which is not accounted for by the equation.

Figure 3-6 (a-d) shows the time histories of impactor's displacement, impact force and force-deflection for 4-, 7- and 16-Layer, and 3DFG-FML specimens, respectively. The major damage mode observed in the specimens was in the form of a permanent (residual) deformation remaining in some of the specimens. The formation of the permanent deformation has an essential role in dissipating impact energy. In other words, the higher the permanent deformation, the larger would be the impact energy dissipation. Moreover, the area below the force-displacement curve is also an indicator of the absorbed impact energy. The results shown in the figure also demonstrate that the absorbed energy by 3DFG-FML is larger than those endured by the other three FML types. On the other hand, the central deformation of 3DFG-FML is greater than those of 7- and 16-layer FMLs, but close to that of 4-layer FML.

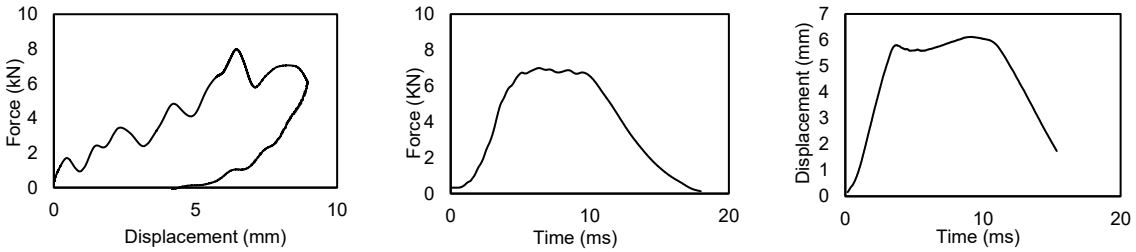

(a)

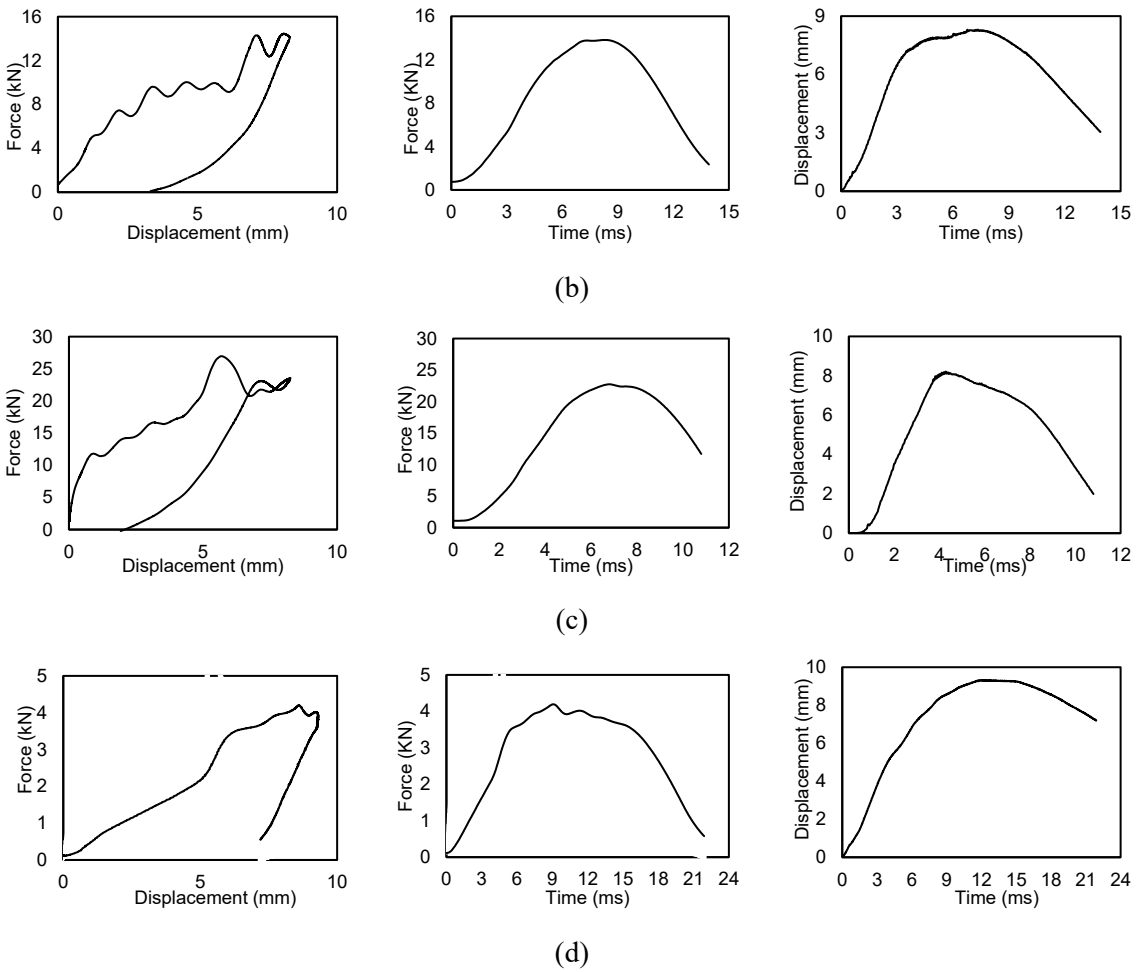

Figure 3-6. Impact responses corresponding to the second failure mode for (a)4-layer FML, (b)7-layer FML, (c)16-layer FML and (d)3DFG-FML

The maximum and minimum impact capacities were exhibited by the 16-layer and 3DFG FMLs, respectively. The slope of the initial portion of the force-displacement curves could also be used as a gauge for assessing specimens' apparent stiffness. According to the results, the apparent stiffness of 16-layer FML was the largest, and the remaining specimens' stiffness decreased in the following order: 7-layer, 4-layer and 3DFG FMLs.

Figure 3-7 depicts the impact energy values that developed various modes of damage/failure (the modes described earlier), for all the FMLs tested. As expected, 16-layer FML exhibited significantly greater impact energy capacity. Moreover, the impact

energy capacity of 7-layer FML was greater than those made with the 3DFG and 4-layer of FRP, respectively. As stated earlier, in order to gain a better perspective of performance of individual FMLs, the impact energies were also normalized with respect to the weight of the FMLs; the results are illustrated in Figure 3-8. Interestingly, the normalized results illustrate much closer values of impact capacity among the FMLs; the results indicate that 3DFG-FMLs performed at par, except for the third failure mode, where the 16-layer FML performed the best (i.e., no failure, hence, not appearing in the chart). This observation indicates that by increasing the layers of woven fiberglass, the impact resistance to weight ratio of resultant FML increases.

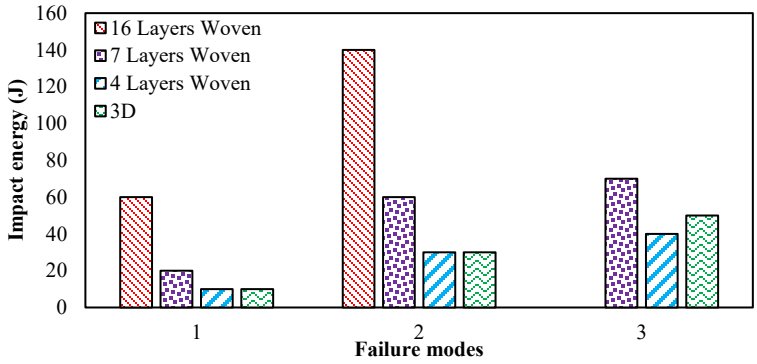

Figure 3-7. Variation of the impact energy absorption capacity of FMLs for the various failure modes

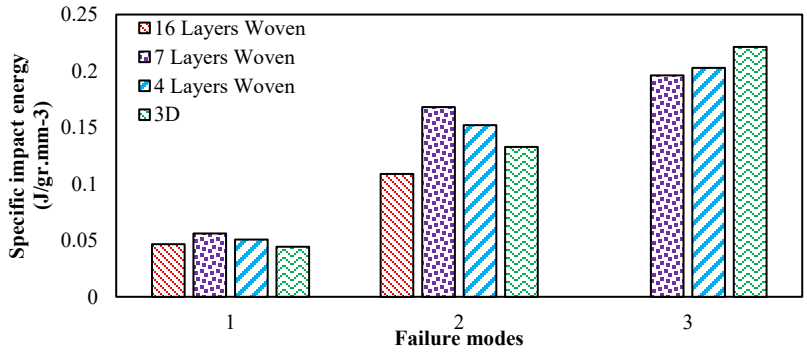

Figure 3-8. Variation of the specific impact energy absorption capacity of FMLs for the various failure modes

The energy restitution coefficient (ERC) is an indicator of a material's capacity to absorb energy. ERC is a parameter that is commonly used for the quantitative comparison of impact results of different materials. The ERC is taken as the squared ratio of the velocity, V, of the impactor before and after impact (Sadighi, Pärnänen et al. 2012)

$$ERC = V_{Rebound}^2 / V_{Impact}^2 \tag{3.2}$$

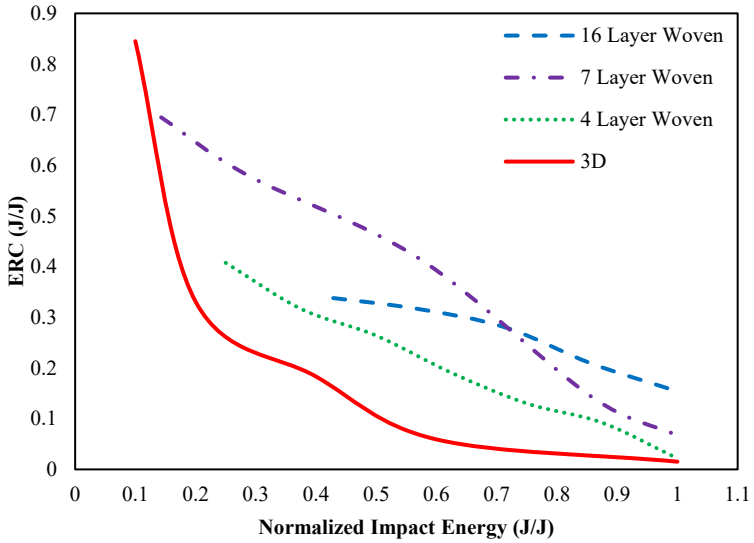

Figure 3-9. Variation in ERC as a function of normalized impact energy of the FMLs

The range of ERC is 0<ERC<1, where ERC=1 would indicate a purely elastic impact, while ERC=0 would indicate that all the energy from the impactor head has been transferred to the specimen. The above equations can also be represented in terms of absorbed and impact energies as:

$$ERC = 1 - E_{absorbed} / E_{impact} \tag{3.3}$$

where $E_{absorbed}$ corresponds to the area under the force-deformation curve. The smaller values of ERC imply that the material has a greater ability to absorb the impact energy. Figure 3-9 illustrates the variation of ERC profiles as a function of the normalized

impacting energy for all types of FMLs. It should be noted that the normalized value is obtained by normalizing the impact energy of each specimen with respect to the largest value of corresponding impact energy (i.e., magnitude of the energy that causes complete penetration of the specimen). Comparison of the ERC curves demonstrate that, in general, the energy absorption capacity decreases as a function of the normalized impact energy. Furthermore, the comparison clearly indicates that the 3DFG-FML possesses the largest specific energy absorption capacity. Moreover, the 4-layer FML's response at the highest impact energy is quite similar to that of 3DFG-FML.

3.5.3 FMLs Deformation Response

Values of the maximum deformation (depression), caused by the impactor for each failure mode are illustrated in Figure 3-10. The maximum deformation values have been normalized with respect to the thickness of the corresponding specimen in order to facilitate a more rational comparison. Since the capacity of the impact test equipment was not adequate to cause the complete penetration of the 16-layer FML, no value has been reported for this specimen in the chart.

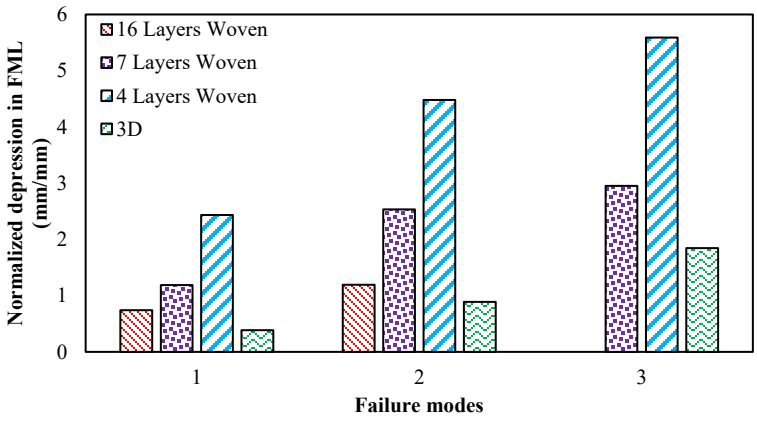

Figure 3-10. Maximum values of the normalized depression in FMLs corresponding to each failure mode

Comparison of the results for the 4-, 7- and 16-layer FMLs reveals that as one would expect, the increase in the thickness of FMLs (which represents the increase in the number of layers of FRP portion) mitigates the value of the deformation. The results also reveal that the normalized maximum deformations occurred in the 3DFG-FMLs are the lowest among the all tested FMLs; the lower magnitudes are mainly attributed to the relatively greater thickness of the 3DFG-FML specimens.

The residual deformation here corresponds to the deformation depth that remains on the surface of a specimen after the completion of an impact event. This value could be considered as a gauge for evaluating the "spring-back" characteristic of FMLs. The post-impact deformation depth, or residual deformation, is considered as an important parameter from the serviceability point of view (Sadighi, Pärnänen et al. 2012). For this reason, the residual deformations on both sides of specimens were measured and reported in Figure 3-11. As in above, these values have been normalized with respect to the thickness of the corresponding specimens. As expected, the residual deformation increases as a function of the increasing magnitude of impact energy. The residual deformations on the impact-side of the 3DFG-FMLs laminate are larger than those observed for the other types of FML; this fact is indicative of the higher energy absorption capacity of this class of FML.

The residual deformation on the surface opposite to the impact surface (i.e., non-impacted surface) of FMLs was also evaluated, and the normalized values are illustrated in Figure 3-12. The results clearly exhibit that the deformation on the reverse side of the FML is virtually non-existence in the 3DFG-FML. In other words, the unique structure of 3DFG-FML manages to essentially eliminate the second mode of failure (i.e., damage in the opposite metallic surface) compared to FMLs reinforced with the woven fiberglass fabric.

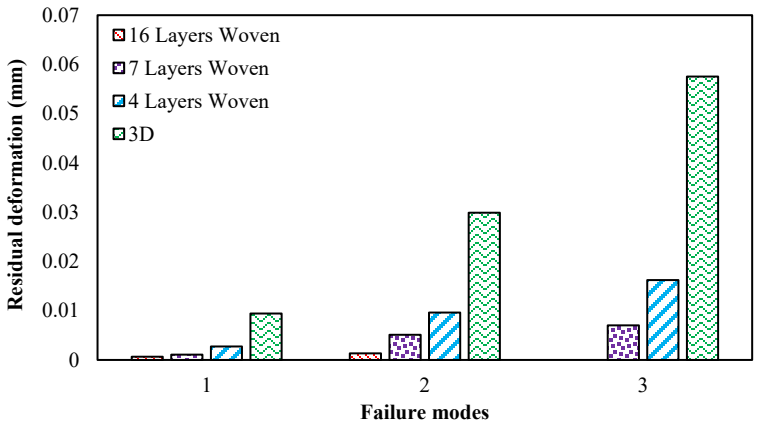

Figure 3-11. The measured residual deformation of the FMLs (on the impacted side) for each failure mode

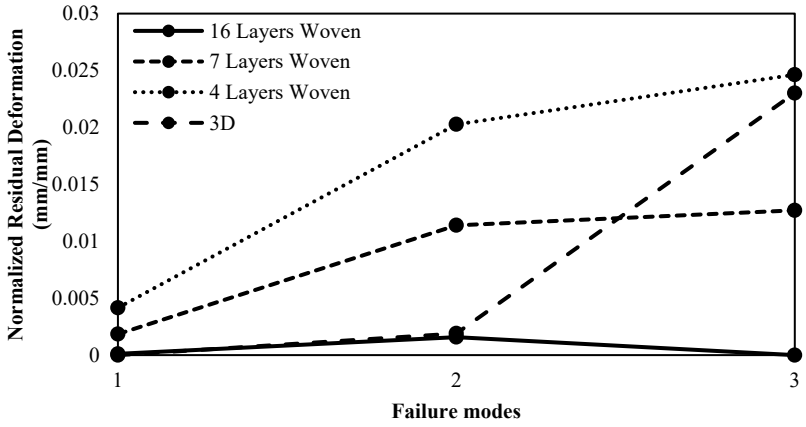

Figure 3-12. The measured residual deformation of the FMLs (on the reverse side) for each failure mode

3.5.4 Delamination Areas

One of the most common modes of damage for the conventional FML configurations subjected to low velocity impact is the delamination that could develop within their FRP layers and/or within FRP/metallic interfaces. In order to observe the explore such delaminations, the specimens were carefully cut at the location of impact, after the impact event. Figure 3-13 shows a view of a typical impact damage in one of the 16-layer FML specimens, which reveals both mode 1 and 2 failure.

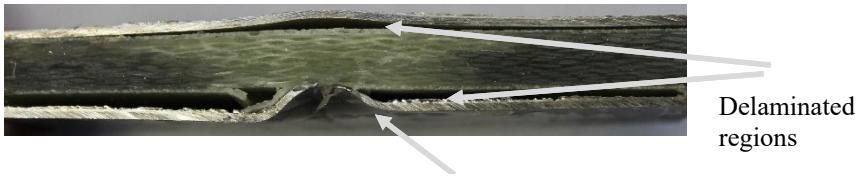

Figure 3-13. Cross-section view of the impacted region of a 16-layer FML corresponding to the second failure mode

Figure 3-14 illustrates the extent of the delamination region as a result of impact for all three modes of failure in the FMLs. As stated earlier, due to the resilient structure of the 3D fabric, no delamination was observed in the 3DFG-FMLs; therefore, the reported value for 3D fabrics is taken as the length of damaged or crushed region developed due to impact. The results reveal that despite the higher impact capacity and stiffness of 16-Layer FML, this FML group suffered the largest delamination area among all FML specimens. Moreover, in contrast, the damage region developed in the 3DFG-FML was observed to be the smallest, which is attributed to the unique configuration of the 3D fabric.

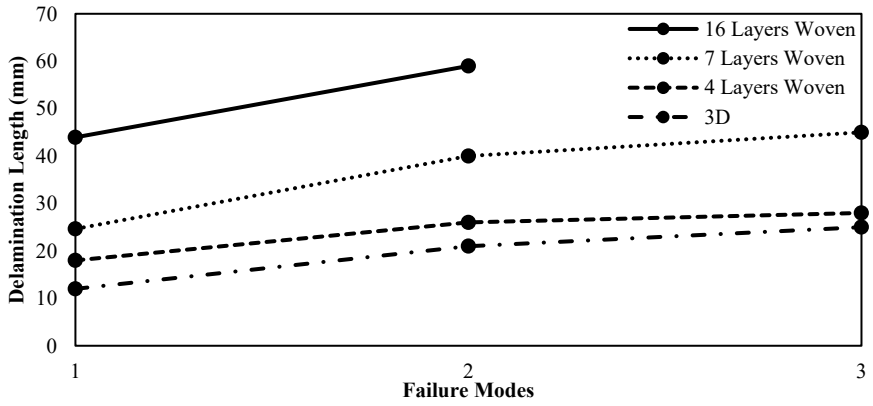

Figure 3-14. Extent of the delamination region in the FMLs for each failure mode

The variation in the areas of delamination developed in the woven FRP-FMLs depends on several factors, including the ultimate strain of fibers, the mismatch in the layers Poisson's ratio (i.e., the difference in fiber directions of adjacent layers), resin's toughness and the

overall thickness of specimens. In general, the larger is the ultimate strain of the fibers, the larger would be the area of delamination. That is because, when the ultimate strain of fiber is low, the impact energy would be mainly consumed by fiber breakage mechanism, as opposed to by advancing the delamination area. That is also the reason for the small increase in the delamination area observed when considering the second and third modes of failure. In other words, in transition of damage from the second mode of failure to the third, the impact energy would be mainly absorbed by rupturing of the fibers.

The relatively much greater delamination areas that developed in 16-layer FMLs are believed to have been caused due to two main reasons. Firstly, the impact energy absorbed by the 16-layer FMLs is considerably greater in magnitude than that absorbed by the 7-layer FMLs (for a specific mode of failure). Secondly, the thinner FRPs of the other FMLs are comparatively more flexible, thus making the specimens more susceptible to flexural stress as opposed to shear stresses. Conversely, the thicker FRP in 16-layer FMLs deforms less in comparison to other FMLs, which in turn leads to the development of larger magnitude of transverse shear stress. It is noteworthy to mention that the pine tree shape of the damage areas is also believed to be a result of the above-mentioned postulated phenomenon (Abrate 2011).

3.6 Numerical Results

As mentioned earlier, one of the objectives of this study is to evaluate the integrity and limitations of the finite element method in simulating the impact response of such complex assemblies as the 3DF-FMLs. For this, the simulation results were compared against those obtained experimentally.

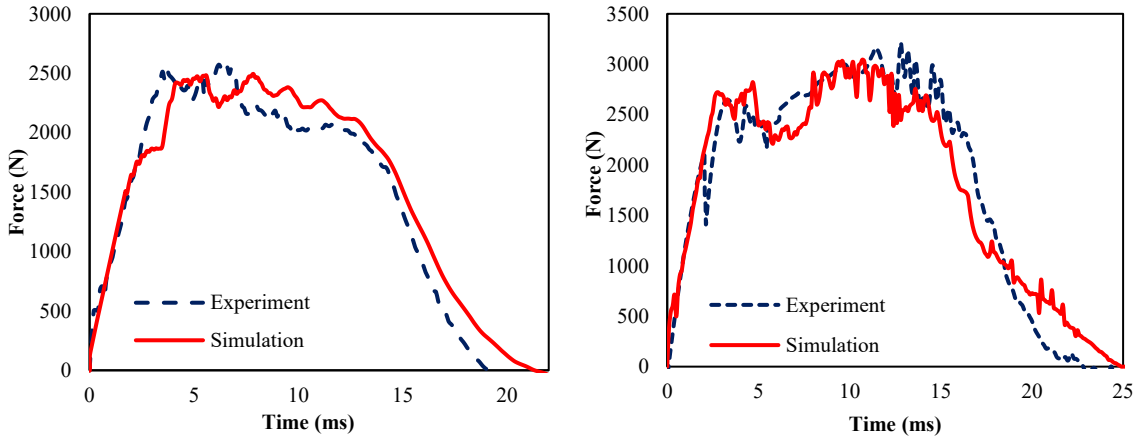

Figure 3-15. Force-time history of 3DFG-FML subject to impact energy of (a) 20 J and (b) 40 J

Figure 3-15 depicts the force-time history of 3DF-FML at two different levels of energy (i.e., 20 J and 40 J). As seen, in the initial phase of contact, where the behavior of material is in the elastic regime, the slopes of the curves obtained numerically and experimentally are quite similar results. After this stage, the discrepancy between the results becomes greater; however, the discrepancy is lower when specimen is impacted with a higher energy than that impacted with a lower energy. The maximum contact forces recorded during the experiments and those established by the FE analyses are presented in Table 3-6. The comparison of results indicates a good agreement between the experimental and numerical values. It can be, therefore, concluded that the maximum contact force can be predicted with a good accuracy by the finite element method. Moreover, for both energy levels, the contact period of FE simulations is greater than those recorded during the experiment. This could be attributed to the approximate value of the friction coefficient and contact properties adopted in the analyses. An increase in the value of friction may improve the accuracy of simulation's contact time. Consequently, the friction coefficient was increased to 0.3 and 0.4, respectively, in order to investigate its effect on prediction of the contact

period. Figure 3-16 depicts the force time history of 3DFGF-FML for three different magnitudes of friction coefficients. The results reveal that the increase in the friction coefficient decreased and improved the value of the contact period obtained through the simulations. As seen, among the three selected coefficients, the friction coefficient of $\mu=0.3$ produced the closest simulation contact period to that observed experimentally.

Figure 3-17 illustrates the force-displacement history of 3DF-FML extracted at two different energy levels (i.e., 20 J and 40 J). As can be seen, the recorded displacement values are smaller than those obtained numerically. This variation of displacement values may contribute to the inherent shortfall in the equation used to predict the absorbed energy. As reported, the measured error associated with the predicted impact energy is greater than the ones related to maximum contact force. This difference may be attributed to the shell elements used in modeling the response of composite and metallic plates. It is postulated that the use of solid elements may improve the predicted displacement values, however at a much higher computational and man-power costs.

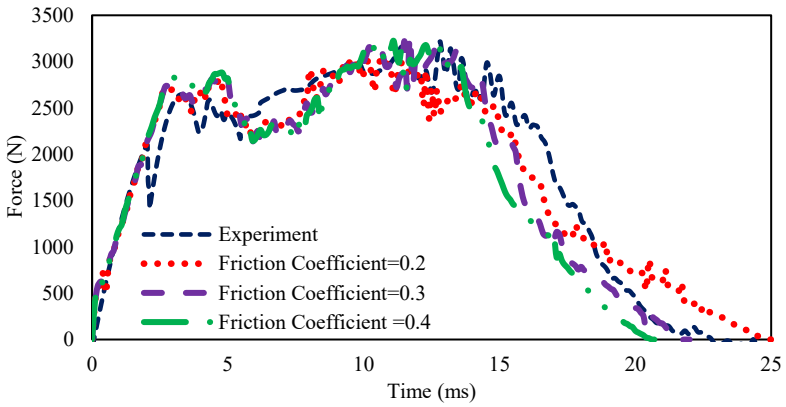

Figure 3-16. Influence of the friction coefficient value on the force-time history of 3DFG-FML, subjected to 40 J impact energy, predicted by FEA

Table 3-6. Comparison of the experimental and numerically predicted values of the maximum contact force

Impact Energy (J)	Maximum Contact Force (kN)		% Difference
	Experimental	Simulation	
20	2.583	2.494	3.44
40	3.214	3.045	5.26

Figure 3-18 depicts the damage profiles obtained experimentally and from the computational simulation for the two levels of impact energy for 3DFG-FML. The results reveal that the damaged level predicted with FE simulation resembles very closely to actual damage observed.

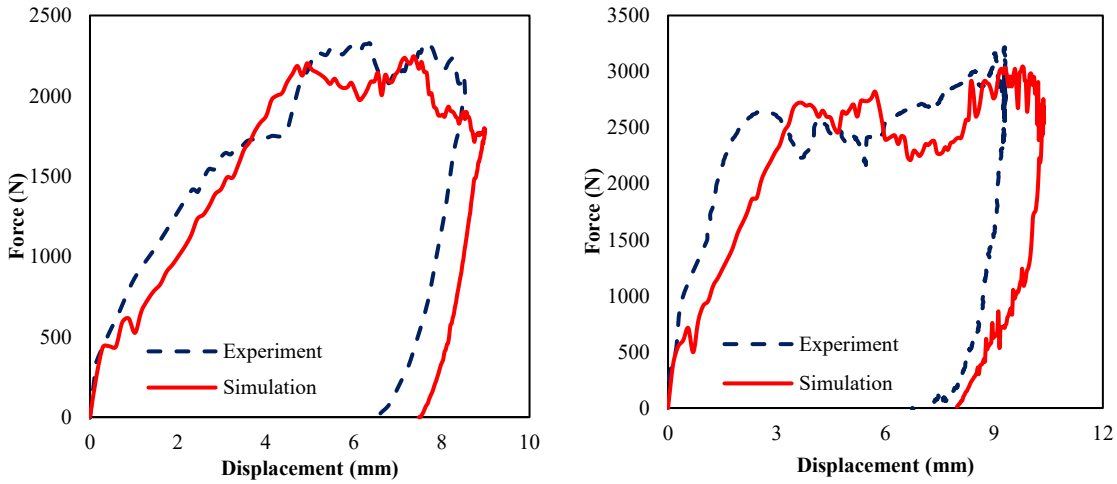

Figure 3-17. Force-displacement graph of 3DFG-FML subjected to impact energy of (a) 20 J and (b) 40 J

3.7 3DFGF's Special Features

As stated earlier, one of the main goals in the present study has been to investigate the performance of a relatively recently developed 3DFG, and to assess its viability as a candidate for developing cost-effective FMLs with resiliency against low velocity impact. To that end, the results acquired through the impact and bending tests and their comparison

against those obtained from FMLs formed in the conventional manner are summarized in this section.

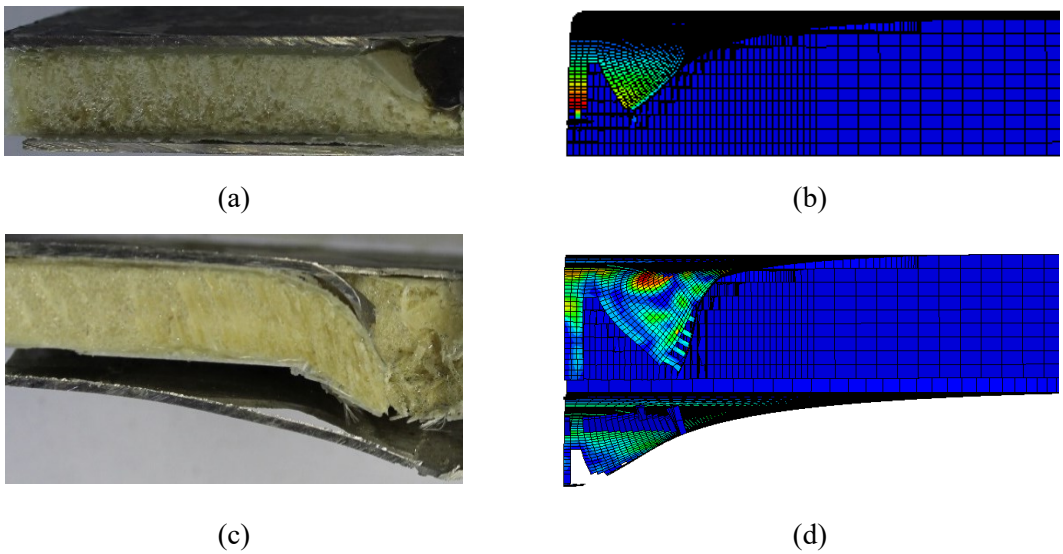

Figure 3-18. Cross-section of a typical damaged region observed experimentally (left) and simulated computationally (right) at two different impact energy levels of (a & b) 20 J, (c & d) 40 J.

As discussed in the previous section, in general, 3DFG FMLs exhibited similar impact energy capacity as did the four layers of woven fiberglass fabric. On the other hand, the failure mechanisms observed in FMLs hosting the 3DFG was significantly different from those exhibited by FMLs hosting the woven fabrics, which was attributed to the unique configuration of fibers in the 3DFG. In a woven FRP, the multiaxial fibers appear to transfer the impact load in both directions, thus a larger area of fabric contributes in resisting the impact energy. On the other hand, the load transfer along the fibers leads to larger damage zones (in this case, larger delamination areas). As mentioned in section 4.4, in the woven-fabric-FMLs the diameter of the delaminated areas was considerably larger than the impactor's diameter. Conversely, in the case of 3DFG-FMLs, there are no laterally oriented fibers within the core region, since all the fibers (whose volume fraction is

comparatively much less than those placed on the top and bottom surfaces of 3DFG), are oriented through the thickness direction. Therefore, the impact energy is absorbed mainly by crushing of the vertical fibers and the supporting foam beneath the region of impact (see Figure 3-19), which leads to lower impact resistance of the FML and a smaller damage area.

Figure 3-19. Typical failure pattern seen in 3DF-FMLs at the second-stage impact loading

The relatively large fracture strain limit and elastic modulus of FRP laminates used in the FMLs enable FRPs to exhibit a more resilient bending capacity and exhibiting a stiffer through-the-thickness response when subjected to a low-velocity impact. In other words, when such a panel is impacted, the FRP laminate bends and transfers a portion of the impact energy to the second neighboring magnesium plate. This stress transition in turn causes the development of delamination in between the FRP/FRP interfaces, FRP/magnesium interfaces, as well as in the formation of early-stage deformation and damage in the magnesium plates. Conversely, the 3DFG provides more damping effect; as a result, a majority of the local deformation created by the impactor remains permanently in the FMLs formed with the 3DFG. This leads to the development of a relatively large residual deformation at the impacted side of this class of FMLs, as discussed in section 3.5.3. This feature of the 3DFG in turn protects the non-impact side of the FML against damage; that is believed to be the reason for the absence of any indentation (damage) on the magnesium plate located on the reverse side of this class of FMLs, as can be seen in Figure 3-19.

It should be noted, however that overall, both the 3DFG and laminated FRP possess some specific positive attributes that are imparted to their respective FMLs. Therefore, depending on the given application, one could strategically harness these attributes in desired proportions and thus optimize the performance of FMLs. The next phase of our investigation will involve exploration into the impact response of FMLs formed by the simultaneous usage of both fabric types.

3.8 Conclusion

The work presented in this paper aimed at investigating the response of FMLs made with a special 3D fiberglass fabric and magnesium alloy plates subjected to low-velocity impact. The response of this novel FML is compared to the response of FMLs formed by 4-layer, 7-layer and 16-layer laminated woven fabrics and magnesium plates. The notable findings of the study are as follows:

- The bending stiffness of the 3DFG-FML was observed to be larger than those FMLs formed by four biaxial woven layers, but was less than the FMLs made with 7- and 16-layers of FRP. However, the specific flexural stiffness of 3DFG-FMLs was observed to be the largest among all the FMLs; this positive attribute is believed to be due to the relatively lighter weight and greater thickness of the 3DFG.

- The time-history response of FMLs indicated that 3DFG-FML could absorb the highest impact energy in comparison to the other three FML types. On the other hand, the deformation caused by the impactor was larger in 3DFG-FMLs than those exhibited by 7- and 16-layer FMLs; the deformation was also very similar to those observed in 4-layer FMLs. Furthermore, the largest apparent stiffness was exhibited by the 16-layer FMLs; the

apparent stiffness is ranked in a descending order as follows: 7- and 4-layer FML, and by 3DFG-FML, respectively.

- The 16-layer FMLs exhibited the largest impact energy capacity among all FMLs considered here. Moreover, the impact energy capacity of 7-layer FMLs was larger than 3DFG and 4-layer FMLS, respectively. However, when the results were normalized with respect to the mass of the specimens, the performances of 3DFG-FMLs and 4-layer FRP-FMLs became fairly similar and closer to that exhibited by the 7-layer FML. In addition, it was observed that the increase in FRP layer number increased the specific impact resistance of the FMLs.

- The results also revealed that an increase in the number of fiberglass layers in FRP portion of FMLs could mitigate the size of deformation caused by the impactor. Moreover, the normalized maximum values of residual deformation observed in the 3DFG-FMLs were lower than those corresponding to the 4- and 7-layer FMLs when the first and second modes of failure were considered, while it was not so in impact events resulting in full-penetration.

- The residual deformations on the impact-side of the 3DFG-FMLs laminate were observed to be larger than those observed for the other types of FML; this fact is indicative of the higher energy absorption capacity of this class of FML. Furthermore, the depression on the reverse side of the FML was virtually non-existence in 3DFG-FMLs. This is believed to be due to the unique configuration of the 3DFG.

- The 16-Layer FMLs suffered the largest delamination area among all FML specimens, despite the large impact capacity and stiffness of the FML, while the damage region developed in the 3DFG-FMLs was the smallest.

- Finite element simulation of the response of 3DFG-FML produced good agreement with the experimental observations. Therefore, the contact force, absorbed energy and impact response of such FMLs could be predicted by the finite element method with a reasonably high accuracy.

3.9 Acknowledgements

The research was funded by the National Science and Engineering Research Council of Canada (NSERC) and AUTO21, a Network Centre of Excellence in automotive. The authors are grateful to the granting agencies.

3.10 References

Abrate, S. (2011). Impact engineering of composite structures, Springer Science & Business Media.

Alderliesten, R., C. Rans and R. Benedictus (2008). "The applicability of magnesium based Fibre Metal Laminates in aerospace structures." Composites Science and Technology 68(14): 2983-2993.

ASTM-C364 (2006). Edgewise Compressive Strength of Sandwich Constructions. Philadelphia, American Society for Testing and Materials West Conshohocken.

ASTM-C365 (2010). Standard test method for flatwise compressive properties of sandwich cores, American Society for Testing and Materials West Conshohocken.

ASTM-C393 (2000). Standard Test Method for Flexural Properties of Sandwich Constructions, American Society for Testing and Materials West Conshohocken.

ASTM-D790 (1997). Standard test methods for flexural properties of unreinforced and reinforced plastics and electrical insulating materials, American Society for Testing and Materials West Conshohocken.

Botelho, E. C., R. A. Silva, L. C. Pardini and M. C. Rezende (2006). "A review on the development and properties of continuous fiber/epoxy/aluminum hybrid composites for aircraft structures." Materials Research 9(3): 247-256.

Cortes, P. and W. Cantwell (2004). "Fracture properties of a fiber-metal laminates based on magnesium alloy." Journal of materials science 39(3): 1081-1083.

Cortes, P. and W. Cantwell (2006). "The fracture properties of a fibre–metal laminate based on magnesium alloy." Composites Part B: Engineering 37(2): 163-170.

Dursun, T. and C. Soutis (2014). "Recent developments in advanced aircraft aluminium alloys." Materials & Design 56: 862-871.

Hashin, Z. (1983). "Analysis of composite materials." J. appl. Mech 50(2): 481-505.

Hibbitt, T. (2002). ABAQUS Theory Manual and Analysis User's Manual, Hibbitt, Karlsson and Sorensen. Inc., USA.

Laliberte, J., C. Poon, P. Straznicky and A. Fahr (2000). "Applications of fiber-metal laminates." Polymer composites 21(4): 558-567.

Lee, D., C. Morillo, S. Oller, G. Bugeda and E. Oñate (2013). "Robust design optimisation of advance hybrid (fiber–metal) composite structures." Composite Structures 99: 181-192.

Liu, D. (1988). "Impact-induced delamination—a view of bending stiffness mismatching." Journal of composite materials 22(7): 674-692.

Morinière, F., R. Alderliesten, M. Sadighi and R. Benedictus (2013). "An integrated study on the low-velocity impact response of the GLARE fibre-metal laminate." Composite Structures 100: 89-103.

Pärnänen, T., R. Alderliesten, C. Rans, T. Brander and O. Saarela (2012). "Applicability of AZ31B-H24 magnesium in fibre metal laminates–an experimental impact research." Composites Part A: Applied Science and Manufacturing 43(9): 1578-1586.

Sadighi, M., R. Alderliesten and R. Benedictus (2012). "Impact resistance of fiber-metal laminates: a review." International Journal of Impact Engineering 49: 77-90.

Sadighi, M. and S. A. Hosseini (2013). "Finite element simulation and experimental study on mechanical behavior of 3D woven glass fiber composite sandwich panels." Composites part b: engineering 55: 158-166.

Sadighi, M., T. Pärnänen, R. Alderliesten, M. Sayeaftabi and R. Benedictus (2012). "Experimental and numerical investigation of metal type and thickness effects on the impact resistance of fiber metal laminates." Applied Composite Materials 19(3-4): 545-559.

Seyed Yaghoubi, A., Y. Liu and B. Liaw (2011). "Low-velocity impact on GLARE 5 fiber-metal laminates: influences of specimen thickness and impactor mass." Journal of Aerospace Engineering 25(3): 409-420.

Starikov, R. (2013). "Assessment of impact response of fiber metal laminates." International Journal of Impact Engineering 59: 38-45.

Taheri-Behrooz, F., M. Shokrieh and I. Yahyapour (2014). "Effect of stacking sequence on failure mode of fiber metal laminates under low-velocity impact." Iranian Polymer Journal 23(2): 147-152.

Tooski, M. Y., R. Alderliesten, R. Ghajar and S. Khalili (2013). "Experimental investigation on distance effects in repeated low velocity impact on fiber–metal laminates." Composite Structures 99: 31-40.

Ulacia, I., C. P. Salisbury, I. Hurtado and M. J. Worswick (2011). "Tensile characterization and constitutive modeling of AZ31B magnesium alloy sheet over wide range of strain rates and temperatures." Journal of Materials Processing Technology 211(5): 830-839.

Zhu, S. and G. Chai (2014). "Low-velocity impact response of fiber-metal laminates–A theoretical approach." Proceedings of the Institution of Mechanical Engineers, Part L: Journal of Materials: Design and Applications 228(4): 301-311.

Zhu, S. and G. B. Chai (2012). "Low-velocity impact response of fibre–metal laminates–Experimental and finite element analysis." Composites Science and Technology 72(15): 1793-1802.

Chapter 4: Experimental and Numerical Investigation into the Influence of Stacking Sequence on the Low-Velocity Impact Response of New 3D FMLs

Zohreh Asaee and Farid Taheri

Published in Composite Structures, Volume 140, PP 136-146, 2016

4.1 Abstract

The present study investigates, both experimentally and computationally, influence of the stacking sequence on the low-velocity impact response of a new fiber metal laminated (FML) concept, formed with magnesium alloy sheets and a new class of true 3D fiberglass fabric (3DFGF). Two different thicknesses of the 3DFGF and four different configurations of FMLs are considered. In particular, the stiffness, strength, energy absorption and failure modes of these configurations of FMLs against impact are compared. To make the comparison unbiased, the impact capacities of FMLs are normalized with respect to their weight and cost, which are the two significant parameters that govern the selection of design of mechanical systems. In addition to the experiments, a finite-element model is constructed using the commercial finite-element code ABAQUS/Explicit, in conjunction with its VUMAT facility, to analyze the impact response of the FMLs. Good agreements between the experimental and computational results are obtained, demonstrating that the model can be used to predict the response of such FMLs and further optimize the configuration and response of such sophisticated systems.

4.2 Introduction

3D-fiberglass (3DFG) fabrics are a novel generation of fiberglass woven/braided fabrics that offer significant potential for use in different demanding applications such as those in automotive, aerospace, marine, and other suitable applications. Their superior bending stiffness and strength, light weight, high-energy absorption capacity when subject to impact loading, excellent thermal insulation and acoustic damping are some of the notable features of this new class of composites. In general, a true 3DFGF consists of two bi-directional woven fabrics knitted together by vertical braided glass fiber pillars (see Figure 4-1). There are also other types of woven/knitted fiber-glass fabrics that are often termed as 3D fabric, but they are not truly 3D. Therefore, owing to this unique structure, 3DFGFs mitigate the delamination issue generating by interlaminar shear stresses, which is one of the primary concerns with the traditional fabrics (Asaee, Shadlou et al. 2015). Moreover, by virtue of having core cavities, they offer additional attributes that were briefly mentioned above. As a result of the above-mentioned positive attributes, these unique fabrics are rendered as an effective alternative constituent in fabrication of effective and resilient fiber metal laminates (FMLs).

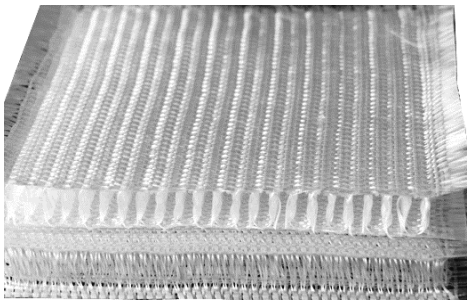

Figure 4-1. The 3D fiberglass fabric (3DFGF)

FMLs, in general, have also been proven as effective light-weight, cost-effective and resilient composite materials for use in demanding structural applications, especially when

weight is a primary design concern. A typical FML consists of a layer (or layers) of fiber laminate composite sandwiched between light-weight metal sheets (traditionally, aluminum alloys). In addition to the aforementioned attributes, FMLs also offer: high specific strength, better tolerance to fatigue crack growth, and good formability (Sadighi, Alderliesten et al. 2012). The most well-known and commonly-used FML is the GLARE, which is manufactured by thin sheets of aluminum and layers of prepreg unidirectional E-glass/epoxy. There are six different grades of GLARE, which are graded based upon the thickness of their aluminum element and different configurations of fibers.

A considerable number of researchers have studied the impact characterization of FMLs, especially the GLAREs (Abdullah and Cantwell 2006, Fan, Cantwell et al. 2011, Seyed Yaghoubi, Liu et al. 2011, Tsartsaris, Meo et al. 2011, Seyed Yaghoubi and Liaw 2012, Morinière, Alderliesten et al. 2013, Yarmohammad Tooski, Alderliesten et al. 2013). For instance, Zhu et al. (Zhu and Chai 2012) investigated the low-velocity impact response and failure modes of FMLs consisting of aluminum alloys and two different types of fiber-reinforced plastics (FRP), namely woven and unidirectional fiberglass fabrics. The corresponding maximum contact force, contact duration and corresponding failure modes of these FMLs were compared. The results revealed that the impact resistance of FMLs made with unidirectional fibers was greater than the resistance of the other FMLs due to a greater strength exhibited in the perforation state.

As stated, the most common metal used in the formation of FML is aluminum; however, magnesium alloys (MgAs) have also been recently utilized in manufacturing of FMLs. FMLs consisting of magnesium alloys are rendered as a good alternative to GLARE for automotive applications; this is mainly due to their lower density (35% lower than that of

aluminum), greater strength to weight ratio, improved electromagnetic shielding capability, excellent corrosion resistance and the lower- cost (Botelho, Silva et al. 2006, Sadighi, Alderliesten et al. 2012).

Despite the positive attributes of MgAs, surprisingly, the number of studies that have considered FMLs made of MgAs is very limited (Cortes and Cantwell 2004, Cortes and Cantwell 2006, Pärnänen, Alderliesten et al. 2012, Sadighi, Pärnänen et al. 2012). One of the notable studies is that by Alderliesten et al. (Alderliesten, Rans et al. 2008), who explored the application of magnesium alloys in FMLs used in aerospace structures by monitoring their overall behavior. They noted, while the total weight of FMLs was lower than aluminum alloy based FMLs, so were their static and fatigue properties. Therefore, selection of magnesium or aluminum alloys would be governed by the specific structural application.

As mentioned earlier, 3DFG fabrics are newly developed fabrics, which have made their way into the market fairly recently. Therefore, besides the earlier study conducted by the authors, to the best of their knowledge, no other study has investigated the performance of FMLs made of such fabrics subjected to low velocity impact loadings. Moreover, another related short come in the literature is the lack of effective and accurate numerical simulation methods for predicting the response of such complex 3DFGF FMLs.

As for investigations considering the response of 3DFG fabrics, they are also very scarce. One of the few studies conducted on simulation of response of 3D fabric is the work of Sadighi et al. (Sadighi and Hosseini 2013, Hosseini, Sadighi et al. 2015), who employed a 3D finite-element model to model the glass fabric and its surrounding epoxy matrix, in order to predict the behavior of three-dimensional woven glass-fiber sandwich composites.

The model was constructed by the CATIA software, and subsequently it was imported into the ABAQUS commercial finite-element analysis (FEA) software for analysis. They obtained a good agreement between their FEA and experimental results.

Noting the potential positive impact response of 3D-FMLs, the main objective of the present study is to carry out a systematic investigation into the low-velocity impact response of a new class of FML, formed by sandwiching light-weight foam filled 3DFG, in between thin sheets of magnesium alloy. As briefly alluded to, this new class of FML was introduced earlier by the authors (Asaee, Shadlou et al. 2015), and its performance was compared against the conventional FMLs made with various layers of biaxial woven in place of the 3DFG fabric. The results revealed that the 3D-FML offered outstanding impact absorption capacity.

In summary, the main goal of the present research is to gain more insight into performance of the 3D-FML, and optimize its configuration based on weight and cost for applications in automotive industry. To achieve the goals, in addition to the experimental investigation, a finite-element simulation frame work is established, using the ABAQUS/Explicit FEA software, in order to simulate and predict the behavior of this relatively complex 3DFGF-FML. The mechanical properties of 3DFGF required for simulation is extracted from the results of three-point bending, edgewise and flatwise compression tests. The FE results are then validated against the experimental results.

4.3 Experimental Work

4.3.1 Specimen Preparation and Configuration

The fiber-metal laminates investigated in this study are formed by 3DFG fabric and magnesium alloy sheets. The AZ31B sheets of 0.5 mm thickness, were supplied by the

MetalMart International (Commerce, CA). As stated earlier, two different thickness of the 3DFG fabric, that is, 4 mm and 10 mm, were acquired through China Beihai Fiberglass Co. Ltd. (Jiujiang City, China), to manufacture the FML specimens. The resin used in this study was Araldite LY 564 (Bisphenole-A Epoxy Resin), along with Aradur 2954 (cycloaliphatic polyamine) hardener, supplied by the Huntsman Co. (West Point, GA). In order to enhance the impact strength of 3DFG, the hollow space of fabric was filled with an 8-lbs density pour-type urethane foam supplied by the US Composites (West Palm Beach, FL 33407).

The bonding surfaces of Mg sheets were first sand-blasted with 20/40 grits sand. Afterwards, the sanded surfaces were cleaned with compressed air and then wiped clean with acetone, to promote good bonding. The FML specimens were fabricated by vacuum bagging technique in two steps. First, resin was applied gently to the 3D fabrics along the so-called "negative direction of the core dumping" (see Appendix A), so to "awaken" the fabrics and to facilitate them to "stand up" to its maximum height. The wetted fabrics were put in an oven and cured for two hours at 60°C first, and then for eight hours at 120°C. The cured 3D panels were cut into 110mm × 110 mm size specimens. Subsequently, the polyurethane foam was injected into the core cavities of the 3D fabric and let cure (for 5min). The FML panels were then assembled by sandwiching the foam-filled 3D fiberglass fabrics and magnesium sheets, using the epoxy resin. The panels were subsequently vacuum bagged to remove the excess resin and to obtain optimal bonding. Finally, the assembled FML plates were put in an oven and cured using the same regime as described earlier.

Details of the stacking sequence of the four groups of FML specimens are summarized in

Table 4-1, and also represented pictorially in Figure 4-2. The designations 3DFML-10 and 3DFML-4 refers to FML having 3DFGFs with the thickness of 10mm and 4mm, respectively. The 3DFML-4-2/3 FML consisted of three layers of magnesium alloy sheets, inter-leaved with two layers of 4 mm 3DFGF. This configuration has the same flexural stiffness as the 3DFML-10. Furthermore, 3DFML-4-2/2, having two layers of magnesium and one layer of 4 mm 3DFGF, has almost the same weight and material cost as the 3DFML-10. It should be noted that the bending stiffness values of the foam impregnated 3DFGFs were determined by conducting 3-point bending tests, as per ASTM-C393 standard (ASTM-C393 2000), using an Instron servo-hydraulic test machine (model 8500+), equipped with a 25 kN load-cell. Subsequently, the flexural stiffness of the differently configured FMLs was established using equation (4.1):

$$bD_{11} = \sum_{k=1}^{n} \int_{Z_k}^{Z_{k+1}} \bar{Q}_{11}^{k} Z^2 dZ = \frac{1}{3} \sum_{k=1}^{n} \bar{Q}_{11}^{k} (Z_{k+1}^3 - Z_k^3) \quad (4.1)$$

Table 4-1. Stacking Sequence

Lay-up	Stacking Configuration	Average Thickness (mm)	Areal Density (kg/m^2)	Flexural Stiffness (N-m^2/m)
3DFML-10	Mg/3DFGF(10mm)/Mg	11	6.05	1.43
3DFML-4	Mg/3DFGF(4mm)/Mg	5	4.25	0.33
3DFML-4-2/3	Mg/3DFGF(4mm)/Mg/3DFGF(4mm)/Mg	9.5	7.40	1.43
3DFML-4-2/2	Mg/3DFGF(4mm)/3DFGF(4mm)/Mg	9	6.10	1.27

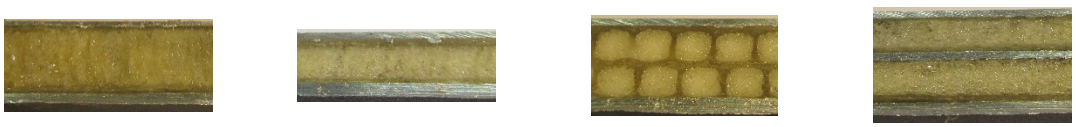

3DFML-10 3DFML-4 3DFML-4-2/3 3DFML-4-2/2

Figure 4-2. Four configurations of tested FML specimens

4.3.2 Testing

Low-velocity impact tests were carried out using a modified Charpy impact test equipment, which has been described in the previous publication of authors (Asaee, Shadlou et al. 2015). A dynamic load cell with the capacity of 225 kN and three proximity sensors were implemented to measure the load-time history and impact velocity which are presented in Figure 4-3. Moreover, a PHOTRON high-speed camera was used to record the impact events with the rate of 2000 fps in order to assess the displacement of the impact region, using the Motion Analysis software (See Figure 4-4). The data obtained from the load cell and proximity sensors were recorded using a digital data-acquisition system and analyzed by a code developed in the MATLAB environment. The desired properties such as the impact energy, absorbed energy, contact time and force time history curves were all extracted from the analysis of data.

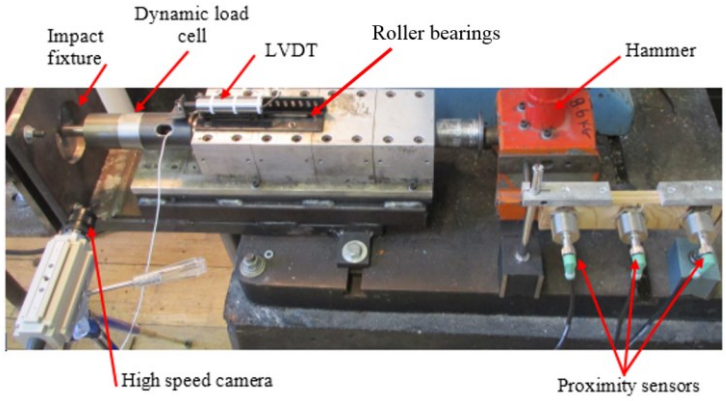

Figure 4-3. The Impact test sensors and fixture

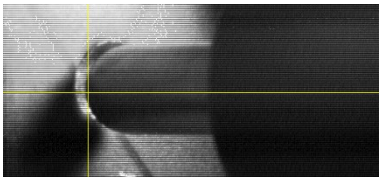

Figure 4-4. A typical image captured by the high-speed camera, which is subsequently post-proceeded by the Motion Analysis software

4.4 Finite Element Analysis

As briefly stated, there is a notable paucity of research on numerical (simulation) methods that aim at predicting the response of 3D-fiber-reinforced composite-based FMLs (Asaee, Shadlou et al. 2015). To compensate the lack of such analysis, the previous study of authors (Asaee, Shadlou et al. 2015), introduced a finite-element frame work, using the commercial finite-element code ABAQUS/Explicit. The good agreement between the experimental and computational results demonstrated that the proposed simulation model could be used to predict the response of 3DFGF-based FMLs.

In the present study, the previous modeling technique is extended to model all three constituents of the FMLs (i.e., the magnesium sheets, fiberglass plies and foam core) with the use of C3D8R element of the ABAQUS, which is the conventional 8-node solid element, but using a reduced integration scheme. Moreover, the new modeling framework includes a sophisticated 3D failure criterion, capable of predicting failure of the composite constituents of FML, through an in-house developed damage model (VUMAT).

In the new modelling framework, the magnesium alloy sheets were modeled as an elastic-plastic material with a rate-dependent behavior. The onset of damage in magnesium layers was simulated using the ductile damage criterion available in the ABAQUS.

The 3DFG fabric, which consists of two bi-directional woven fabrics, was also simulated using C3D8R element. The woven fabrics were simulated as two layers of unidirectional fabrics, oriented at 0^{o} and 90^{o}, respectively (Fan, Guan et al. 2011, Zhu and Chai 2012). As stated, user-defined 3D damage model (VUMAT) was developed and implemented into the ABAQUS for predicting the damage evolution within the woven laminate. The

implemented damage mechanism had two components: a damage initiation criterion and a damage evolution criterion.

The damage initiation criterion accounts for both fiber failure and matrix failure. Hashin's failure criterion (Hashin 1980) and Puck's action plane model (Puck and Schürmann 1998) were considered for modeling the damage mechanism in fibers and matrix constituents, respectively. The fiber failure modes include consideration of fiber breakage, through thickness cracking and shear failure, modeled by the following mathematical formulations (Shi, Swait et al. 2012):

Tensile failure of fiber:

$$F_{fLt} = \left(\frac{\sigma_1}{X^T}\right)^2 + \alpha\left(\frac{\sigma_{12}}{S_{12}}\right)^2 + \alpha\left(\frac{\sigma_{31}}{S_{31}}\right)^2 \geq 1 \tag{4.2}$$

Compressive failure of fiber:

$$F_{fLc} = \left(\frac{\sigma_1}{X^C}\right)^2 \geq 1 \tag{4.3}$$

Combined tensile and shear failure of fiber (through the thickness direction):

$$F_{fT(Z)t} = \left(\frac{\sigma_2 + \sigma_3}{Y^T}\right)^2 + \frac{\sigma_{23}^2 - \sigma_2\sigma_3}{S_{23}^2} + \left(\frac{\sigma_{12}}{S_{12}}\right)^2 + \left(\frac{\sigma_{31}}{S_{31}}\right)^2 \geq 1 \tag{4.4}$$

Combined compression and shear failure of fiber (through the thickness direction):

$$F_{fT(Z)c} = \frac{1}{Y^C}\left[\left(\frac{Y^C}{2S_{23}}\right)^2 - 1\right](\sigma_2 + \sigma_3) + \left(\frac{\sigma_2 + \sigma_3}{2S_{23}}\right)^2 + \frac{\sigma_{23}^2 - \sigma_2\sigma_3}{S_{23}^2} + \left(\frac{\sigma_{12}}{S_{12}}\right)^2 + \left(\frac{\sigma_{31}}{S_{31}}\right)^2 \geq 1 \quad (4.5)$$

where X^T, X^C, Y^T and Y^C refer to the tensile and compressive strengths in the longitudinal and transverse directions, respectively. S_{12}, S_{23} and S_{31} express the fiber shear strength measured in the 1-2, 2-3 and 3-1 directions, respectively (see Table 4-2). σ_{ij} and α represent the stress tensor and contribution factor in each mode. In this study, value of α as set to 1.

Table 4-2. Mechanical Properties of glass fiber-reinforced Composite (Nagaraj 2005)

Orthotropic properties	E_1 = 37 GPa, E_2 = 8.5 GPa, E_3 = 8.5 GPa, ν_{12} = 0.254, ν_{13} = 0.254, ν_{23} = 0.428, G_{12} = 4.7 GPa, G_{13} = 4.7 GPa, G_{23} = 3.28 GPa
Strength Properties (MPa)	X^T = 750, X^C = 780, Y^T = 44, Y^C = 44, Z^T = 40, Z^C = 40, S_{12} = 30, S_{23} = 30, S_{31} = 30

The matrix failure criterion, based on the puck's action plane model, is defined as follows:

Tensile and compressive matrix mode:

$$F_{mt,c} = \left[\left(\frac{\sigma_{11}}{2X^T}\right)^2 + \frac{\sigma_{22}^2}{|Y^T \times Y^C|} + \left(\frac{\sigma_{12}}{S_{12}}\right)^2\right] + \sigma_{22}\left(\frac{1}{Y^T} + \frac{1}{Y^C}\right) \geq 1 \quad (4.6)$$

The damage evolution model can be expressed in terms of damage index D_i as:

$$D_i = \frac{\delta_{eq}^f(\delta_{eq} - \delta_{eq}^0)}{\delta_{eq}(\delta_{eq}^f - \delta_{eq}^0)} \quad (\text{Where } i = Lt, Lc, Tt, Tc, Zt, Zc, Mt, Mc) \quad (4.7)$$

where D_i is the damage index defined for each particular damage mode. δ_{eq}^0 and δ_{eq}^f are the initial equivalent displacements of the i^{th} failure mode calculated at element's integration stations at the onset of failure initiation, and are graphically at the state of

complete damage, respectively. The states of δ_{eq}^{0} and δ_{eq}^{f}, represented in Figure 4-5 for the various modes, depend on the elastic stiffness and degrading strength parameters specified as part of the damage initiation definition.

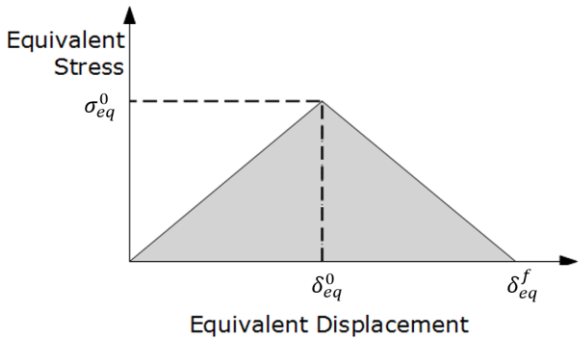

Figure 4-5. Typical damage evolution mechanism

The stiffness matrix is reduced by applying the damage index, D_i, when the value of the failure criterion (equation (4.7)) exceeds unity. The reduced stiffness matrix takes the following form:

$$C_d = \begin{bmatrix} b_L^2 C_{11} & b_L b_T C_{12} & b_L b_Z C_{13} & 0 & 0 & 0 \\ b_L b_T C_{12} & b_T^2 C_{22} & b_T b_Z C_{23} & 0 & 0 & 0 \\ b_L b_Z C_{13} & b_T b_Z C_{23} & b_Z^2 C_{33} & 0 & 0 & 0 \\ 0 & 0 & 0 & b_{LT} C_{44} & 0 & 0 \\ 0 & 0 & 0 & 0 & b_{ZL} C_{55} & 0 \\ 0 & 0 & 0 & 0 & 0 & b_{TZ} C_{66} \end{bmatrix} \tag{4.8}$$

In the above matrix, C_{ij} is the component of undamaged stiffness matrix;

where $b_L = 1 - D_L$, $b_T = 1 - D_T$, $b_Z = 1 - D_Z$ and

$b_{LT} = \left(\frac{2(1-D_L)(1-D_T)}{2-D_L-D_T}\right)^2$, $b_{TZ} = \left(\frac{2(1-D_T)(1-D_Z)}{2-D_T-D_Z}\right)^2$, $b_{ZL} = \left(\frac{2(1-D_Z)(1-D_L)}{2-D_Z-D_L}\right)^2$ and

$\Omega_{fL} = max(D_{Lt}, D_{Lc})$, $\Omega_{fT} = max(D_{Tt}, D_{Tc})$, $\Omega_{fZ} = max(D_{Zt}, D_{Zc})$ and

$\Omega_{ML} = \Omega_{MT} = \Omega_{Mz} = max(D_{Mt}, D_{Mc})$ and

$D_L = max(\Omega_{fL}, \Omega_{ML}), D_T = max(\Omega_{fT}, \Omega_{MT}), D_Z = max(\Omega_{fZ}, \Omega_{MZ})$

Furthermore, the C3D8R element was also used to model the foam part of the 3DFGF. The foam material was defined using the crushable foam material constitutive model of the ABAQUS, which accounts for volumetric hardening (Hibbitt 2002). The damage initiation and failure mechanism of the crushable foam was simulated using the ductile damage criterion in conjunction with a shear damage criterion. Evolution of the damage in the material was based on the fracture energy. It should be noted that, the three-point bending test, and flatwise and edgewise compressive tests were carried out as per appropriate ASTM standards (ASTM-C393 2000, ASTM-C364 2006, ASTM-C365 2010), in order to evaluate the foam's modulus of elasticity, plastic response, fracture energy and fracture strain (see Table 4-3).

Table 4-3. Mechanical properties of the foam evaluated based on ASTM standards

Density (Kg/m^3)	Compressive Elastic Modulus (MPa)	Compressive Strength (MPa)	Compressive fracture Strain (mm/mm)	Fracture Energy ($N\text{-}mm/mm^2$)
128	435	7.0	0.055	0.326

It should be noted that due to the symmetric geometry and boundary conditions, only a quarter symmetry portion of the geometry was modeled, as illustrated in Figure 4-6. A convergence analysis was performed by varying the mesh density within the plane and through the thickness of the model. The impactor was modeled as a rigid body, using the 3D discrete rigid shell element of the ABAQUS. At this stage, a rigid mass element was used and connected to a reference point on the rigid body, in order to impart the impact load to the specimen. Moreover, the interfaces of the magnesium layers and fiberglass part,

and that between composite core and fiberglass were considered to be fully intact (as perfectly bonded) and were tied accordingly. However, as the stresses within these bonded regions surpass a certain limit, thereby indicating the onset of debonding within a given interface (e.g., between the metallic lower plate and composite, as shown in Figure 4-18), then, the associated ties are vanished. This is because the adjacent hosting elements, simulating the failed fiberglass region of the panels are removed as governed by the selected failure and damage evolution criteria.

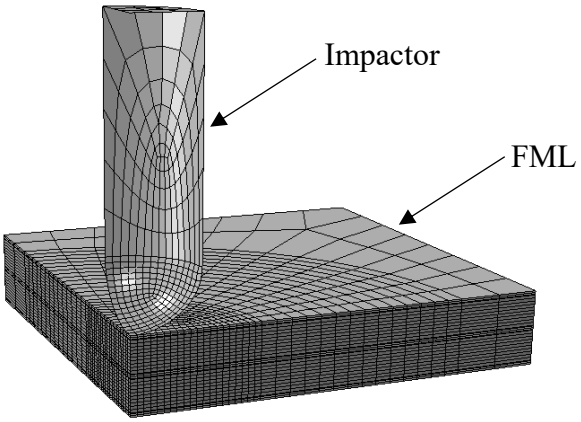

Figure 4-6. Isometric view of the quarter–symmetry model of impactor and 3DFG-FML specimen

The contact interface of the impactor and FML's top surface was simulated using the general contact algorithm of the ABAQUS/Explicit, with the normal contact and tangential component of the contact modelled using the friction coefficient $\mu = 0.3$ (Asaee, Shadlou et al. 2015).

4.5 Results and Discussions

4.5.1 Force-time history

A total of 48 FML samples were tested under low velocity impact loading conditions, subject to energy levels of 40 J, 50 J, 70 J, 100 J and 120 J. Three specimens were tested

for each energy level. However, only FML groups 3DFML-4-2/2 and 3DFML-4-2/3 were tested at the energy levels of 100 J and 120 J, since the other groups could not endure impact energies greater than 70 J. The force-time history, impact energy, absorbed energy, impact velocity and deflection values were extracted from the signals captured through the dynamic load cell, proximity sensor and high-speed camera.

The energy absorption capacity of the specimens, which is relevant to the area under the force-time history curve, was calculated by the following equation (Abrate 2011):

$$\Delta E_0 = E_a[1 - E_a/4E_0] \tag{4.9}$$

where $E_a = V_0 \int_0^\tau P\, dt$, and V_0, E_0 and P are the impactor's initial velocity, impact energy and the load at time τ, respectively.

Figure 4-7 (a) represents a set of typical force-time history curves for one specimen from each group of specimens tested at impact energy of 40 J. As seen, the contact time noted in 3DFML-4 and 3D-FML-10 are greater than the contact time observed for the other two specimens. Nevertheless, the greater peak load observed in groups 3DFML-4-2/2 and 3DFML-4-2/3 reflects the higher-energy absorption capacity of these groups of specimens in comparison to 3DFML-4 and 3DFML-10 groups of specimens. The observed symmetric force-time history corresponding to specimens 3DFML-4-2/2 and 3DFML-4-2/3 reveals the elastic response of the specimens. Since 3DFML-10 and 3DFML-4-2/3 groups have equal flexural stiffness, the initial slope of the force-time history curves represents the elastic response of FMLs, which as seen are essentially similar. The smooth trend in the curve corresponding to the specimen in group 3DFML-10, which continues up to reaching the peak load, indicates the elastic response of this group of FMLs. Moreover, the sudden

dip in the curve after the peak signifies the perforation of the impacted side. The prolonged descent in the curve after this stage is associated with the impactor crushing the core, which is subsequently encountered by the elastic displacement of the non-impacted side. It should be noted that, under 40 J impact energy, a crack was developed on the impacted face of specimens in group 3DFML-10. The first dip after the peak load on the force-time history response of 3DFML-4 group also revealed the development of a crack on the impacted side of that group of specimens. The subsequent oscillation of in the force-time history curve and the second peak signify the development of a crack on the reverse side of the specimen.

It should be noted that, as seen, the magnitude of force in the time-history curves do not reduce to zero, as one would expect. This is because after the first (primary) impact, the impactor bounces back and hits the specimen for the second time. However, since we are interested only on the primary impact event, thus the data related to second impact (which also includes noise) has been removed from the diagram. It should also be noted that the response of each specimen was captured on video through a high-speed camera. The video clearly revealed that when the impactor bounced back and hit the specimen for the second time, the impacted surface did not return to its rest position. Moreover, in some of the tests (the impact higher energy tests), the elapsed period of time between the first and second impact was so short that it could not be capture by our data acquisition, whose maximum sampling rate is 10 kHz.

Figure 4-7(b) illustrates the force-time history response of the tested specimens subjected to 50 J impact energy. The greater contact forces in 3DFML-4-2/2 and 3DFML-4-2/3 groups imply a higher-energy absorption capacity in comparison to 3DFML-4 and 3DFML-10 groups of specimens, also accompanied with higher contact times. The

presence of first peak loads on the curves associated with 3DFML-4-2/2 and 3DFML-4-2/3 groups indicates the initiation of a crack on the impacted side of the specimens. The follow-up smooth part of the curves indicate that the reverse side did not experience any damage. Moreover, the presence of two peak loads on the time history of the 3DFML-10 group infers that a crack was developed on the reverse side of the specimen. Therefore, the second failure mode in specimens of group 3DFML-10 occurred only when the applied energy reached to 50 J. Furthermore, the existence of two peak loads on the 3DFML-4 group's curve indicated the extension of crack on the non-impacted side of the specimen.

The force-time history response of specimens that were subjected to 70 J impact is depicted on Figure 4-7*(*c). The existence of two peaks of the curves for groups 3DFML-10 and 3DFML-4 implies the development of a crack at both sides of the specimens. The prolonged follow-up part of the two curves signify the perforation of the impactor through the specimens, and the differences are due to the friction between the impactor and materials. As a result, the contact times in 3DFML-10 and 3DFML-4 group of specimens are greater than those corresponding to 3DFML-4-2/2 and 3DFML-4-2/3 groups. Moreover, the energy absorption capacity of the 3DFML-10 group is higher than the capacity of the 3DFML-4 group under perforation failure mode.

The specimens in group 3DFML-10 and 3DFML-4 were perforated when impacted at the energy level of 70 J; therefore, they were not subjected to the higher impact energy levels. Figure 4-7(d) and (e) illustrate the load-time history response of specimens in groups 3DFML-4-2/2 and 3DFML-4-2/3 subject to impact energies of 100 J and 120 J. The existence of two peak loads, and the subsequent prolonged portion observed on the curve corresponding to 3DFML-4-2/2 group implies perforation of the impactor through the

specimen, and development of a crack on the reverse side of the specimens, when subjected to energy levels of 100 J and 120 J, respectively. Furthermore, the two peak loads seen on the time history curves of 3DFML-4-2/3 group subjected to the impact energy level of 120 J signify the development of a crack on the reverse side of the specimen.

4.5.2 Energy Absorption Capacity

Figure 4-8 represents variation in the energy restitution coefficient (ERC) as a function of the impact energy. The ERC is an indicator of the energy absorption capacity, defined by the following equation:

$$ERC\% = \left(1 - \frac{E_{absorbed}}{E_{impact}}\right) \times 100 \tag{4.10}$$

where the absorbed impact energy, $E_{absorbed}$, is calculated by equation (4.9). The ERC's value ranges between zero and 100. Inspection of equation (4.10) reveals that the lower the value of ERC, the higher would be the energy absorption capacity of the FML. Therefore, the higher ERC values of the 3DFML-4 group imply that this configuration offers the lowest energy absorption capacity among the configurations tested. However, 3DFML-4-2/2 group, whose overall thickness is lower than the 3DFML-10 group, offers a higher-energy absorption capacity. Under the lower impact energies, 3DFML-4-2/2 group specimens exhibited a greater ability to absorb energy in comparison to specimens of 3DFML-4-2/3 group.

In general, 3DFGF has a tendency to absorb more energy than the magnesium plate. As a result, when FMLs were subjected to impact energies below the level causing perforation, the 3DFML-4-2/2 group configuration (with two layers of 3DFGF stacked on each other),

exhibited a greater energy absorption capacity than group 3DFML4-2/3 (which had one layer of magnesium between the two 4 mm thick 3DFGFs).

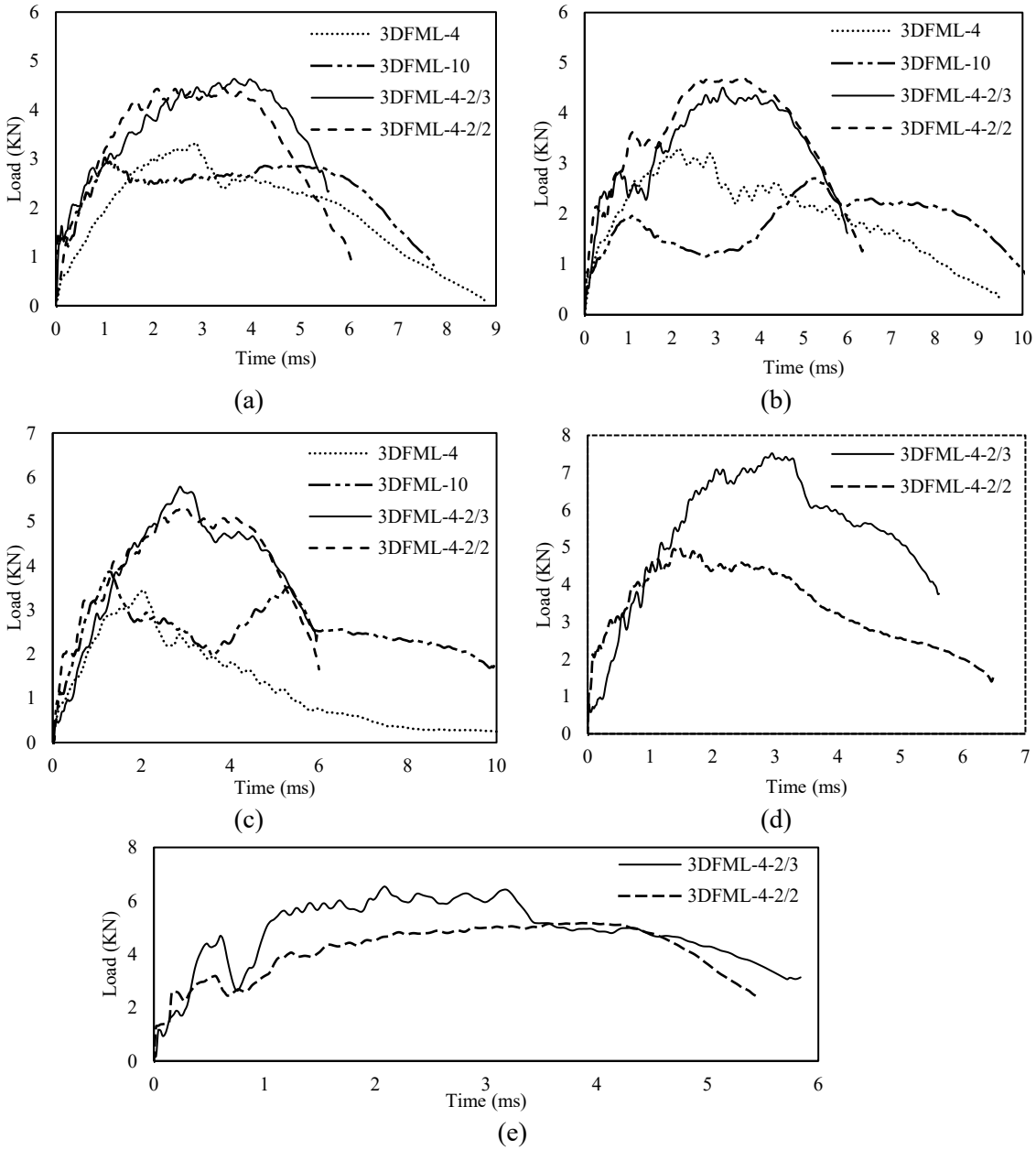

Figure 4-7. Typical Force-time history of four groups of specimens subjected to impact energies of 40 J, (b) 50 J, (c) 70 J, (d) 100 J and (e) 120 J.

In all, however, the impact capacity of 3DFML-4-2/3 group, owing to the additional layer of magnesium, was greater than that of 3DFML-4-2/2 Moreover, groups' 3DFML-10 and

3DFML-4-2/3, which had similar flexural stiffness, exhibited different ability to absorb the impact energies. In fact, group 3DFML-4-2/3 exhibited a higher absorption capacity in comparison to the 3DFML-10 regardless of the applied impact energy. Nonetheless, 3DFML-10 exhibited the highest capacity of absorption at the perforation limit. The large thickness and continuous and consistent core in group 3DFGF-10 lead to the absorption of more energy under the condition when the impactor perforated the FML.

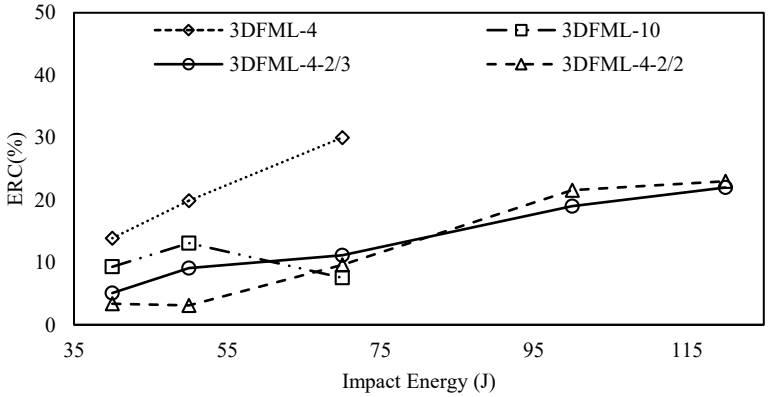

Figure 4-8. The variation of the ERC as a function of the impact energy for all tested FMLs

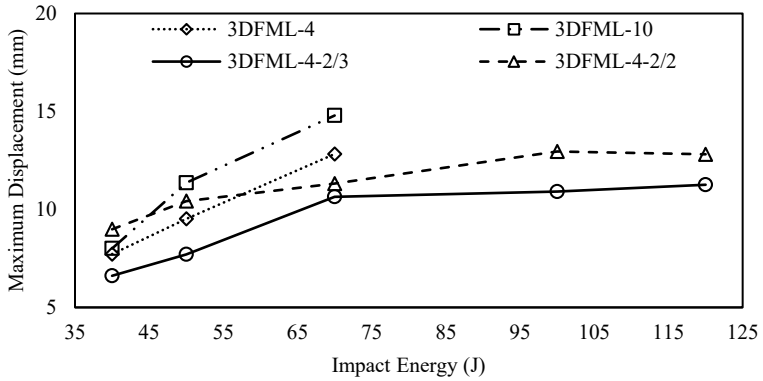

Figure 4-9. Variation of the maximum displacement as a function of the applied energy

The maximum values of the out-of-plane displacement of specimens tested at various impact energy levels are illustrated in Figure 4-9. Comparison of the results reveals that groups' 3DFML-10 and 3DFML-4-2/3 exhibited the highest and lowest maximum displacement, respectively, despite the fact that their flexural stiffness was similar. In other

words, the damage extent was the greatest in the 3DFML-10 group among the considered FMLs.

4.6 Failure Modes

Figure 4-10 depicts the impact energy levels corresponding to a specific type of damage or failure mode. The damage/failure modes have been defined as the following:

- Mode-1 signifies presence of a crack on the impacted surface
- Mode-2 signifies the development of a crack on the non-impacted side of the specimen.
- Finally, mode-3 refers to failure in the form of through-thickness perforation of the specimen.

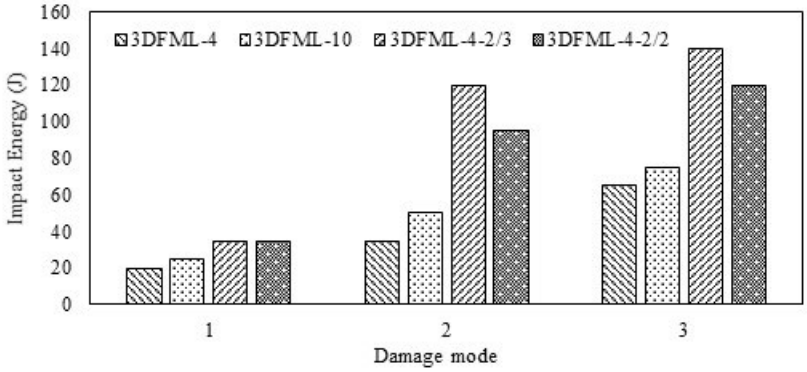

Figure 4-10. Variation in the impact strength organized in terms of the failure modes

The summary of the failure modes corresponding to the four groups of specimens is depicted in Figure 4-11 to 4-13. The results indicate that one of the most important features of 3DFML-10, 3DFML-4-2/2 and 3DFML-4-2/3 groups is their ability to prevent damage progress to the non-impacted side of the specimen on the first mode of failure. Moreover, the second layer magnesium and 3DFGF present in specimens of group 3DFML-4-2/2 and 3DFML-4-2/3 are protected from damage. This feature signifies that these groups of FML

can easily be repaired in-service, should they become damaged (i.e., by only repairing the top surface metal).

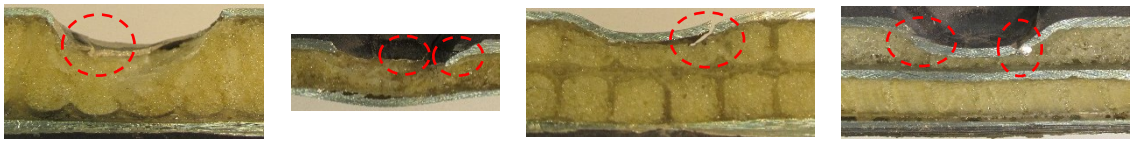

(a) (b) (c) (d)

Figure 4-11. Mode-1 type failure for the four groups of specimens 3DFML-10, (b) 3DFML-4, (c) 3DFML-4-2/2 and (d) 3DFML-4-2/3

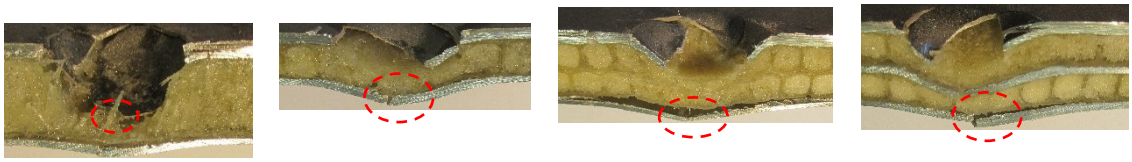

(a) (b) (c) (d)

Figure 4-12. Mode-2 type failure for the four groups of specimens 3DFML-10, (b) 3DFML-4, (c) 3DFML-4-2/2 and (d) 3DFML-4-2/3

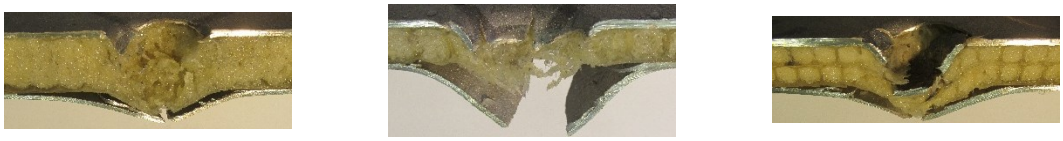

(a) (b) (c)

Figure 4-13. Mode-3 type failure for the four groups of specimens (a) 3DFML-10, (b) 3DFML-4, and (c) 3DFML-4-2/2

The results reveal that group 3DFML-4-2/3, as expected, provides the highest strength regardless of the level of impact. Interestingly, although groups 3DFML-10 and 3DFML-4-2/3 possess a similar flexural strength, nevertheless, their impact strengths are significantly different. Moreover, the impact capacity of the 3DFML-10 group is very close to the capacity of the 3DFML-4 group under the applied energies; however, they are more significantly damaged at higher-energy levels, and in fact, could not endure impact energies beyond 80 J.

4.6.1 Performance Normalization

In general, weight and cost of materials are the two primary parameters that govern the selection of a given design. Therefore, in order to compare the performance of FMLs based on the aforementioned perspectives, the impact energies corresponding to each failure mode were normalized with respect to FMLs materials' cost and weight, as presented in Figure 4-14 and 4-15.

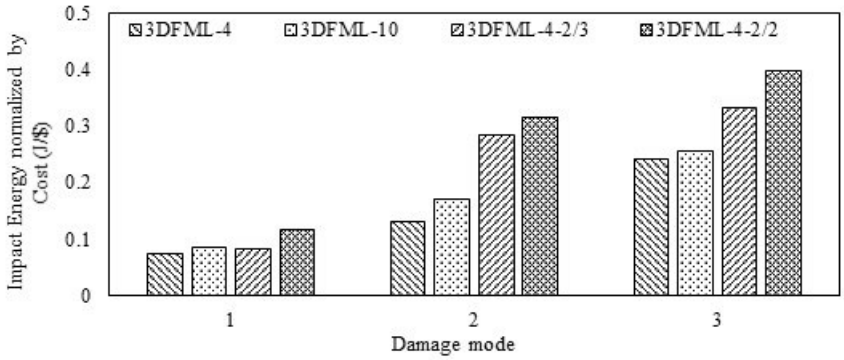

Figure 4-14. Variation of the impact strength of FMLs normalized with respect to cost as a function of the failure modes

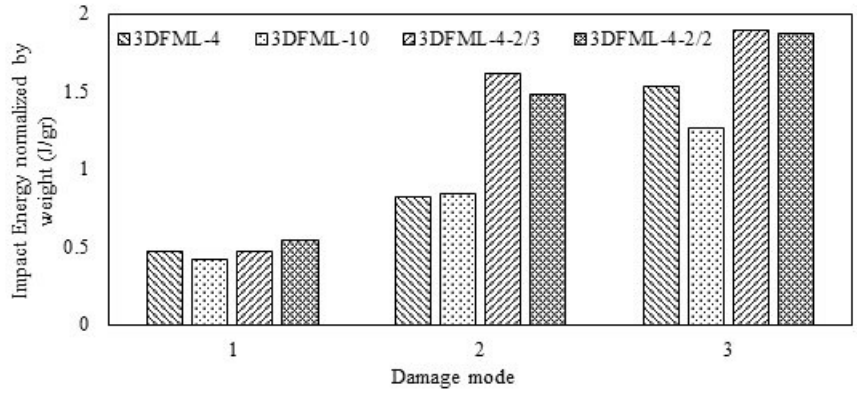

Figure 4-15. Variation of the impact strength of FMLs normalized with respect to weight as a function of the failure modes

From the cost perspective, 3DFML-4-2/2 group offers the highest normalized impact strength among the FMLs tested, especially when considering the perforation strength. Obviously, the lower cost associated with 3DFML-4-2/2 group would render this FML as

the preferred group in comparison to 3DFML-4-2/3 group. Accordingly, in applications where the cost is the governing factor, then group 3DFML-4-2/2 leads the way. Moreover, although the costs of groups 3DFML-10 and 3DFML-4-2/2 are almost equal, there is a significant difference between their normalized impact strengths, rendering 3DFML-4-2/2 group as the more preferable FML. Furthermore, the similar normalized impact strength of groups 3DFML-4 and 3DFML-10 implies that their performance is comparable, from cost perspective.

Figure 4-15 illustrates the impact capacities normalized with respect to weight, and organized in terms of the failure modes. The lightest weight associated to the 3DFML-4-2/2 group contributes in producing equal specific perforation energy as that of 3DFML-4-2/3 group. However, the specific impact energy of 3DFML-4-2/3 group is the greatest, if the second mode of failure is considered. Moreover, the specific impact energy causing penetration is greater in group 3DFML-4 in comparison to group 3DFML-10, which highlights the significance of 3DFGF-4 group's lighter weight. In all, groups 3DFML-4-2/2 and 3DFML-4-2/3 would be rendered as the more effective FMLs in mechanical applications where the weight governs the design selection.

4.7 Finite Element Simulation Results

As mentioned earlier, there is a clear lack of research work in regard to the simulation of composites made of 3D fiberglass. As a result, in an earlier study, the authors developed a FE framework using the ABAQUS/Explicit commercial software, to simulate the behavior of 3DFGF under impact loading condition (Asaee, Shadlou et al. 2015). The initial model used the conventional shell elements. To further improve the accuracy of the model, that model is modified in the present study, and the 3D solid (brick) element is used to model

every constituent of the FML. Moreover, a set of sophisticated and more accurate failure criteria are implied, so to further improve the failure prediction capability of the model. The results obtained through the revised modeling techniques are compared against the experimental results, as well as the results produced by the previous FE model.

Figure 4-16 presents comparison of the FE and experimental results for the four FML groups, 3DFML-4, 3DFML-10, 3DFML-4-2/2 and 3DFML-4-2/3, impacted at the different energy levels. As seen, the initial slope of the time history curve, which signifies the elastic behavior of the FML, is quite similar to that observed experimentally. Moreover, the model can successfully predict the contact force and post-damage response of the FMLs. The predicted number of peak loads demonstrates that the incorporated damage evolution model could effectively predict the failure mechanism of the impacted FMLs with a good accuracy. Furthermore, the maximum contact forces captured during the experiments and those calculated by the FE analyses are presented in Table 4-4. The comparison of results proves a good agreement between the experimental and FE results.

Table 4-4. Comparison of the experimental and numerically predicted values of the maximum contact force

Specimen ID	**Maximum Contact Force (kN)**		**(%) Difference**
	Experiment	Simulation	
3DFML-10	3.862	3.896	0.88
3DFML-4-2/3	5.781	5.802	0.36

Figure 4-17 depicts the force-time history of group 3DFML-10 under an impact energy of 70 J obtained through the FE simulations and experiment. The results are also compared to FE results produced in the earlier study, where the shell element was used to model the laminates. As seen, the FE model generated using the solid element could predict the behavior of FML more accurately than the model generated using the shell element. The

predicted contact forces and contact time at the peak load were proved to be also more accurately predicted by the FE model that used the solid element.

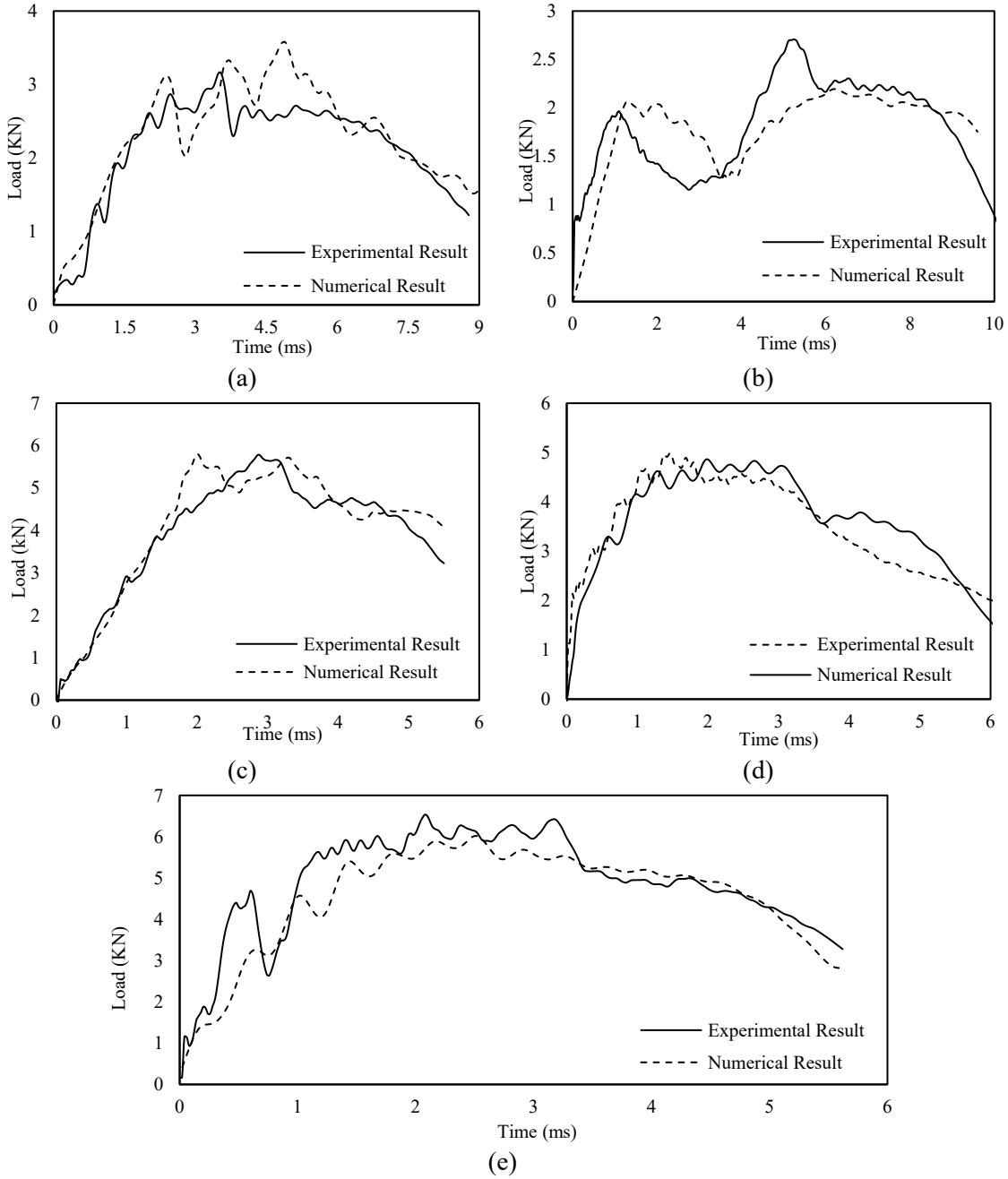

Figure 4-16. Force time history of (a) 3DFML-4 (b) 3DFML-10 (c) 3DFML-4-2/3 (d) 3DFML-4-2/2 and (e) 3DFML-4-2/3 under impact energy of 40 J, 50 J, 70 J, 100 J and 120 J

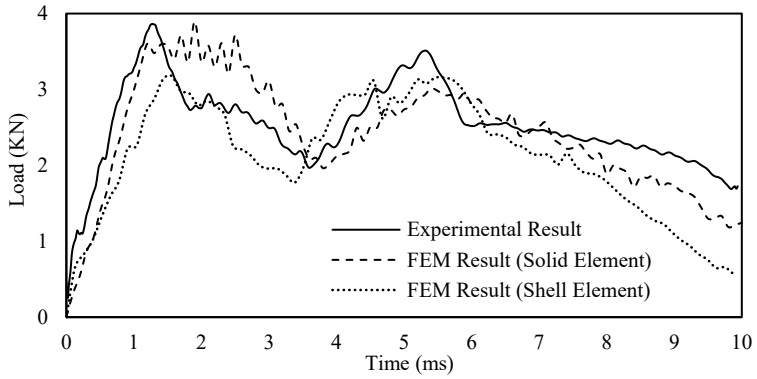

Figure 4-17. Force-time history of 3DFML-10 subjected to 70J from experiment and predicted using FE models generated by shell elements and solid elements

Figure 4-18 illustrates the failure profiles acquired experimentally and the predicted results by the FE simulation for groups 3DFM-10 and 3DFML-4-2/2 tested at energy levels of 70 J and 100 J, respectively. The comparison shows that the damaged failure patterns predicted by FE simulation are very similar to the actual damage observed experimentally.

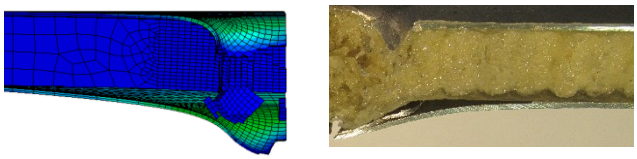

(a) 3DFML-10 specimen subject to 70J impact

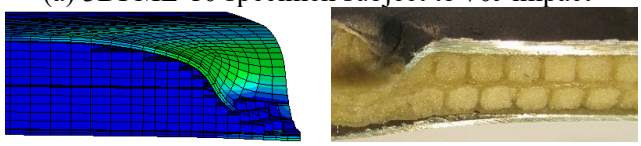

(b) 3DFML-4-2/2 specimen subject to 100J impact

Figure 4-18. Comparison of the through-thickness failure patterns obtained through FE-simulations (left) and experiments (right)

4.8 Conclusion

FMLs consisting of 3D fiberglass fabric and magnesium plates were fabricated using the hand layup and vacuum bagging processes. Two different thickness of fabric (i.e., 4mm and 10mm) were used to develop four different configurations of FMLs as reported in Table 4-1. The configurations were selected based on producing FMLs with similar

flexural stiffness, or similar weight and cost. In other words, two groups, identified as 3DFMl-10 and 3DFML-4-2/3, had equal bending stiffness, while groups 3DFML-10 and 3DFML-4-2/2 had similar weight and materials cost.

Comparison of the results demonstrated that 3DFML-10 group provided a higher contact stiffness and energy absorption capacity than the 3DFML-4 group. However, when two layers of 4 mm thick 3DFGF were combined to construct the FMLs of groups 3DFML-4-2/3 and 3DFML-4-2/2, comparatively, they proved to exhibit more superior impact capacity. The specimens in group 3DFML-4-2/3, which had similar flexural stiffness to those in group 3DFML-10, showed considerably a higher contact stiffness and energy absorption capacity values in comparison to specimens in the 3DFML-10 group. In addition, 3DFML-4-2/2 group, which had similar cost and weight as group 3DFML-10, produced a greater contact load duration and absorbed energy capacity compared to group 3DFML-10.

Since the two important governing parameters in selection of the design of a given component are weight and cost, to generate unbiased comparison, the resulting impact capacities of the four tested groups of FMLs were also normalized with respect to materials' cost and weight of the FMLs. The results indicated that 3DFML-4-2/2 configuration could provide the greatest impact strength from the cost perspective. From the weight perspective, both 3DFML-4-2/3 and 3DFML-4-2/2 configurations produced equally the greatest impact capacity. In all, generally, comparison of the results implied that 3DFML-4-2/2 and 3DFML-4-2/3 configuration would exhibit the performance from all perspectives.

The developed FE framework, whose results were validated by the experimental results, proved to offer an effective and accurate means for predicting the impact response, failure modes of the differently configured FMLs. This framework, including its user-developed failure criteria, can be used to further examine the influence of various parameters governing the performance of such relatively complex class of FML in an effective and reliable manner.

4.9 Acknowledgement

This research was funded by the National Science and Engineering Research Council of Canada (NSERC). The authors are grateful to the granting agency.

4.10 References

Abdullah, M. and W. Cantwell (2006). "The impact resistance of polypropylene-based fibre–metal laminates." Composites science and technology 66(11): 1682-1693.

Abrate, S. (2011). Impact engineering of composite structures, Springer Science & Business Media.

Alderliesten, R., C. Rans and R. Benedictus (2008). "The applicability of magnesium based Fibre Metal Laminates in aerospace structures." Composites Science and Technology 68(14): 2983-2993.

Asaee, Z., S. Shadlou and F. Taheri (2015). "Low-velocity impact response of fiberglass/magnesium FMLs with a new 3D fiberglass fabric." Composite Structures 122: 155-165.

ASTM-C364 (2006). Edgewise Compressive Strength of Sandwich Constructions. Philadelphia, American Society for Testing and Materials West Conshohocken.

ASTM-C365 (2010). Standard test method for flatwise compressive properties of sandwich cores, American Society for Testing and Materials West Conshohocken.

ASTM-C393 (2000). Standard Test Method for Flexural Properties of Sandwich Constructions, American Society for Testing and Materials West Conshohocken.

Botelho, E. C., R. A. Silva, L. C. Pardini and M. C. Rezende (2006). "A review on the development and properties of continuous fiber/epoxy/aluminum hybrid composites for aircraft structures." Materials Research 9(3): 247-256.

Cortes, P. and W. Cantwell (2004). "Fracture properties of a fiber-metal laminates based on magnesium alloy." Journal of materials science 39(3): 1081-1083.

Cortes, P. and W. Cantwell (2006). "The fracture properties of a fibre–metal laminate based on magnesium alloy." Composites Part B: Engineering 37(2): 163-170.

Fan, J., W. Cantwell and Z. Guan (2011). "The low-velocity impact response of fiber-metal laminates." Journal of Reinforced Plastics and Composites 30(1): 26-35.

Fan, J., Z. Guan and W. Cantwell (2011). "Numerical modelling of perforation failure in fibre metal laminates subjected to low velocity impact loading." Composite structures 93(9): 2430-2436.

Hashin, Z. (1980). "Failure criteria for unidirectional fiber composites." Journal of applied mechanics 47(2): 329-334.

Hibbitt, T. (2002). ABAQUS Theory Manual and Analysis User's Manual, Hibbitt, Karlsson and Sorensen. Inc., USA.

Hosseini, S. A., M. Sadighi and R. Maleki Moghadam (2015). "Low-velocity impact behavior of hollow core woven sandwich composite: Experimental and numerical study." Journal of Composite Materials 49(26): 3285-3295.

Morinière, F., R. Alderliesten, M. Sadighi and R. Benedictus (2013). "An integrated study on the low-velocity impact response of the GLARE fibre-metal laminate." Composite Structures 100: 89-103.

Nagaraj, M. (2005). "Experimental and computational investigation of FRP-reinforced glulam columns including associated software development [Master of applied science thesis]." Department of Civil and Resource Engineering, Dalhousie University.

Pärnänen, T., R. Alderliesten, C. Rans, T. Brander and O. Saarela (2012). "Applicability of AZ31B-H24 magnesium in fibre metal laminates–an experimental impact research." Composites Part A: Applied Science and Manufacturing 43(9): 1578-1586.

Puck, A. and H. Schürmann (1998). "Failure analysis of FRP laminates by means of physically based phenomenological models." Composites Science and Technology 58(7): 1045-1067.

Sadighi, M., R. Alderliesten and R. Benedictus (2012). "Impact resistance of fiber-metal laminates: a review." International Journal of Impact Engineering 49: 77-90.

Sadighi, M. and S. A. Hosseini (2013). "Finite element simulation and experimental study on mechanical behavior of 3D woven glass fiber composite sandwich panels." Composites part b: engineering 55: 158-166.

Sadighi, M., T. Pärnänen, R. Alderliesten, M. Sayeaftabi and R. Benedictus (2012). "Experimental and numerical investigation of metal type and thickness effects on the impact resistance of fiber metal laminates." Applied Composite Materials 19(3-4): 545-559.

Seyed Yaghoubi, A. and B. Liaw (2012). "Thickness influence on ballistic impact behaviors of GLARE 5 fiber-metal laminated beams: Experimental and numerical studies." Composite Structures 94(8): 2585-2598.

Seyed Yaghoubi, A., Y. Liu and B. Liaw (2011). "Low-velocity impact on GLARE 5 fiber-metal laminates: influences of specimen thickness and impactor mass." Journal of Aerospace Engineering 25(3): 409-420.

Shi, Y., T. Swait and C. Soutis (2012). "Modelling damage evolution in composite laminates subjected to low velocity impact." Composite Structures 94(9): 2902-2913.

Tsartsaris, N., M. Meo, F. Dolce, U. Polimeno, M. Guida and F. Marulo (2011). "Low-velocity impact behavior of fiber metal laminates." Journal of Composite Materials 45(7): 803-814.

Yarmohammad Tooski, M., R. C. Alderliesten, R. Ghajar and S. M. R. Khalili (2013). "Experimental investigation on distance effects in repeated low velocity impact on fiber–metal laminates." Composite Structures 99(0): 31-40.

Zhu, S. and G. B. Chai (2012). "Low-velocity impact response of fibre–metal laminates–Experimental and finite element analysis." Composites Science and Technology 72(15): 1793-1802.

Chapter 5: Enhancement of Performance of 3D Fiber Metal Laminates under Low Velocity Impact– A coupled Numerical and Experimental Investigation

Zohreh Asaee and Farid Taheri

Published in Journal of Sandwich Structures & Materials, 2017

5.1 Abstract

The main objective of the present study is to examine the level of enhancement in performance of 3D fiber metal laminates (3DFML) under low velocity impact, when reinforced by different types of reinforcing face-sheets (i.e., fiberglass or carbon). Three layup configurations of the fabrics are considered in this investigation. The impact response of each of these configurations are assessed numerically using ABAQUS/Explicit, a commercially available finite element software. Specifically, each configuration's impact capacity, deformation, contact time and energy absorption capacity are evaluated. The numerical results are validated by comparison against experimental results. Moreover, a semi-empirical equation is developed for evaluating the impact capacity of such panels, as a function of impact energy, capable of accounting the influence of any type of reinforcement. Finally, the most efficient reinforced 3DFMLs are identified based on their impact strength with respect to their overall weight and cost.

Keywords: 3D Fiber Metal Laminates, Low Velocity Impact Response, Finite Element Simulation, Impact Strength.

5.2 Introduction

During the last decades, the competition between metallic and composite materials as the material of choice for automotive applications has become increasingly fierce (Marsh 2014). There are several criteria that are considered in order for a material be deemed suitable for use in transport vehicles. The most notable considerations are given to weight, cost, safety and crashworthiness, reconcilability and life cycle of a given material (Ghassemieh 2011).

Fiber metal laminates (FML) are a group of hybrid materials developed to meet the abovementioned criteria, taking advantage of the positive attributes of both metals and composites, and transforming them into a hybrid material. The first generation of FML was created in the 80's in the Delf university of technology (Sadighi, Alderliesten et al. 2012). Since then, various types of FMLs have been developed, categorized based on the type of metal, and type and configuration of fiber/cloth used to form them (Chai and Manikandan 2014). An emerging generation of FMLs is the 3D fiber metal laminates (3DFML), which consist of a single or multi layers of 3D fiberglass fabric (3DFGF), sandwiched between two or more layers of magnesium alloys or other type of metallic alloys (see Figure 5-1) (Asaee, Shadlou et al. 2015). The 3DFGF itself is a relatively recently developed fabric, formed by two layers of orthogonal woven fabric, knitted together by series of fiberglass pillars. The fabric has, therefore, hollow core structure, which could be filled by a foam, to further improve its mechanical properties and performance (Asaee and Taheri 2015).

Traditionally, the main application of FMLs has been in aerospace structures; however, their use has also been noted in automotive and marine structures. The more prevalent use of this material in automotive necessitates full exploration of damage tolerance and

crashworthiness of this class of hybrid composites. Consequently, the investigation of impact response of composite materials and FMLs has been of interest to many investigators (Davies, Hitchings et al. 1996, Vlot 1996, Caprino, Spataro et al. 2004, Hosur, Chowdhury et al. 2007, Payeganeh, Ghasemi et al. 2010, Abrate 2011, Fan, Cantwell et al. 2011, Seyed Yaghoubi, Liu et al. 2011, Sadighi, Pärnänen et al. 2012, Seyed Yaghoubi and Liaw 2012, Yaghoubi, Liu et al. 2012, Zhu and Chai 2012, Morinière, Alderliesten et al. 2013, Rathnasabapathy, Mouritz et al. 2013, Starikov 2013, Tooski, Alderliesten et al. 2013, Yarmohammad Tooski, Alderliesten et al. 2013, Zhu and Chai 2013, Taheri-Behrooz, Shokrieh et al. 2014, Bienias, Jakubczak et al. 2016, Heydari-Meybodi, Mohammadkhani et al. 2016, De Cicco, Asaee et al. 2017).

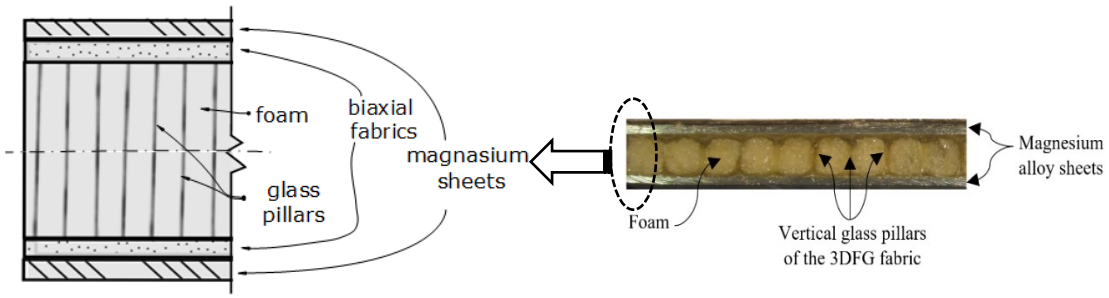

(a) (b)

Figure 5-1. FML's configuration of (a) schematic details (b) actual FML

For instance, Zhu et al. (Zhu and Chai 2012) studied the low-velocity impact of aluminum-based FMLs hosting two different types of fibers (unidirectional and woven). They concluded that when the impactor mass is much larger than the mass of the FML, the low-velocity impact response of the FML would be similar to that exhibited under quasi-static condition. Moreover, it was demonstrated that the FMLs formed by unidirectional fabrics sustained more perforation damage in comparison to those formed by woven fabrics. They also simulated the response of their FMLs with a commercial software (ABAQUS). In

another study, Subbaramaiah et al. (Subbaramaiah, Prusty et al. 2017) investigated the axial crushing response of a FML in form of a top-hat structure. The main application of top-hat structures is their use as an energy-absorbing aircraft sub-floor structure. They explained that the crushing mode of the top-hat structure made of GLARE was too complicated due to the different failure modes exhibited by its constituents. In addition, a numerical simulation was performed to predict the crushing mechanism of the top-hat structure. The developed FE model was able to accurately estimate the damage mechanism of the top-hat structure.

As explained earlier, 3DFGF is a new generation of truly 3D fabrics introduced to the market relatively recently. As a result, the number of research works exploring the mechanical performance of this fabric are currently limited (Vaidya, Hosur et al. 2000, Hosur, Abdullah et al. 2004, Vaidya, Vaidya et al. 2008, Karahan, Gül et al. 2012, Asaee and Taheri 2015, Hosseini, Sadighi et al. 2015, Asaee and Taheri 2016, Kus, Durgun et al. 2016, Zhou, Liu et al. 2016). One of the studies conducted by Zhou et al. (Zhou, Liu et al. 2016), investigated the shear response of 3DFGFs by experimental, theoretical and numerical approaches. They performed a double shear lap test and evaluated the shear modulus and load-deflection curve of the material in the weft and warp principle directions. They found that the shear modulus in the warp direction was greater than that obtained along the weft direction. They also obtained good agreement between their experimental and FE results. Furthermore, they also validated their theoretical model by comparison of its results to their experimental data. In another study, Fan et al. (Fan, Chen et al. 2014) studied the failure mechanism of 3DFGF under three-point bending test. They performed the experiments for sixteen groups of specimens based on different core structure and skin

thicknesses. The results showed that the flexural and tensile properties of the fabric were indeed stronger in the weft direction. According to their experimental observations, the failure mechanisms of their 3D fabric were observed as skin fracture, skin yielding, skin crippling, tensile failure, indentation and core shearing.

To the best of authors' knowledge, no research had investigated the mechanical response of the 3DFMLs prior to those conducted by the authors. In fact, this new class of FML was first introduced by the authors, and comparison of the mechanical performance of various configurations of the 3DFML compared to the traditionally formed 2D FMLs was documented (Asaee, Shadlou et al. 2015, Asaee and Taheri 2016, Asaee, Mohamed et al. 2017, Asaee, Mohamed et al. 2017). The results demonstrated the superior performance of the 3D fabric and FMLs formed by it in comparison to the conventional FMLs, under both static and impact loadings. Moreover, the most optimal configuration of the 3DFML was established in terms of impact strength, weight and material cost (Asaee and Taheri 2016). It should be noted that none of the previous studies conducted by the authors explored the objective set for the present study, as explained in the following paragraph.

The main objective and distinct contribution of the present study is to investigate whether the impact response of the 3DFML could be further enhanced by incorporating additional layers of glass or carbon FRP, in a cost-effective manner. For that, three different layup configurations of reinforcing layers are considered in order to examine the effects of fabric type and fiber orientation on FML's impact performance. A finite element model is also developed to simulate the impact response of the 3DFMLs. The simulation is performed for 10 groups of 3DFMLs, subjected to 26 different impact energies. The impact response of 3DFMLs reinforced by fiberglass and carbon are also compared with respect to the

overall weight and cost of materials (i.e., the two primary design parameters). Moreover, additional experimental tests are conducted on the most effective layup configurations of the two types of fabrics that were established through the numerical investigation, by subjecting the optimized panels to four different impact energies. The numerical and experimental data are compared to establish the integrity of the FE models. Furthermore, a semi-empirical equation is developed for predicting the maximum sustained impact force of such 3DFMLs.

5.3 Finite Element Simulation Procedure

The finite element model includes modelling of four different constituents of the 3DFML: the magnesium sheets, additional reinforced fabrics, top and bottom fiberglass fabric layers of the 3DFGF and its foam core. The mechanical properties of each constituent were established by conducting a series of tests. Appropriate size magnesium, fiberglass and carbon fabric reinforced epoxy coupons were prepared and subjected to tensile and low-velocity impact tests (under different impact energies). The 3DFGF has a complex structure; therefore, an extensive experimental investigation was conducted on the 3DFGF fabric to establish its basic mechanical properties. The investigation examined two possible configurations of the fabrics; that is, with their cavities filled with a foam or free (Asaee and Taheri 2015, Asaee and Taheri 2016). The tests conducted were three-point bending test, edge-wise compression and low-velocity impact tests. In the following paragraphs, the details of simulation of the performance of each of the constituent are described.

The magnesium alloy sheets were simulated as an elastic-plastic material with strain rate-dependent behavior, using C3D8R element of ABAQUS/Explicit. C3D8R is an eight-node solid element with reduced integration. The onset of damage in magnesium was simulated

using ductile damage model available in the code. Furthermore, evolution of damage in the magnesium sheets was simulated based on the energy principle, by including material's linear softening response to simulate development of a crack and the subsequent perforation of impactor into the sheets. Mechanical properties of the magnesium alloy used in the FE simulation are presented in Table 5-1.

Table 5-1. Mechanical Properties of Materials

Material	Mechanical Properties
Magnesium AZ31-B	ρ = 1780 kg/m^3, E = 36 GPa, v = 0.3, σ_y = 230 MPa
3DFGF	Fiberglass (Nagaraj 2005): ρ = 1750 kg/m^3, E_1 = 37 GPa, E_2 = 8 GPa, v_{12} = 0.31, G_{12} = G_{13} = 4.7 GPa, G_{23} = 3.2 GPa, X^T = 780 MPa, X^C = 750 MPa, Y^T = 50 MPa, Y^C = 120 MPa Foam: ρ = 128 kg/m^3, E = 50 MPa, v = 0, K = 1.1,(Whisler and Kim 2015) K_t = 0.8 (Whisler and Kim 2015)
Reinforcing fiberglass epoxy layers	ρ = 1750 kg/m^3, E_1 = 40 MPa, E_2 = 8 MPa, v_{12} = 0.25, G_{12} = G_{13} = 4 GPa, G_{23} = 2.8 GPa, X^T = 1000 MPa, X^C = 600 MPa, Y^T = 50 MPa, Y^C = 120 MPa
Reinforcing carbon epoxy layers	ρ = 1600 kg/m^3, E_1 = 120 GPa, E_2 = 6.2 GPa, v_{12} = 0.35, G_{12} = G_{13} = 5 GPa, G_{23} = 3.5 GP, X^T = 1500 MPa, X^C = 1200 MPa, Y^T = 30 MPa, Y^C = 140 MPa

The fiberglass and carbon reinforced fabrics were defined as "lamina" type with their mechanical properties reported in Table 5-1. Response of these constituents were simulated by the conventional shell element of ABAQUS, using the composite layup manager facility of the code. Damage mechanism of the fabric was established using the Hashin damage criterion, associated with the energy-based damage evolution. The mesh was created using the reduced integration shell element (S4R) of ABAQUS/Explicit.

The next constituents of 3DFMLs are the top and bottom fiberglass fabric/epoxy surfaces, connected together by glass pillars, forming cavities that are foam infilled. The fiberglass fabric layers were modeled using the conventional shell (S4R) element. Their mechanical

properties are presented in Table 5-1. The core part of the 3DFGF was simulated as a crushable foam, using the average results of hardening curves obtained through a series of compression tests conducted on a square block of foam injected 3DFGF fabrics. Note that the curves also included the contributions of the glass pillars of 3D fabric. Moreover, it should be noted that in the simulations, it was assumed that the through-thickness compressive stress would be sustained by the combined foam-core/pillar constituents, while the top and bottom fiberglass fabric layers would endure the bending stresses (Asaee, Shadlou et al. 2015). The equivalent mechanical properties of foam core are also presented in Table 5-1.

Finally, as briefly alluded earlier, the onset of damage and its growth in the foam were defined using the ductile damage criterion in conjunction with the shear damage criterion and energy-based method associated with exponential softening behavior.

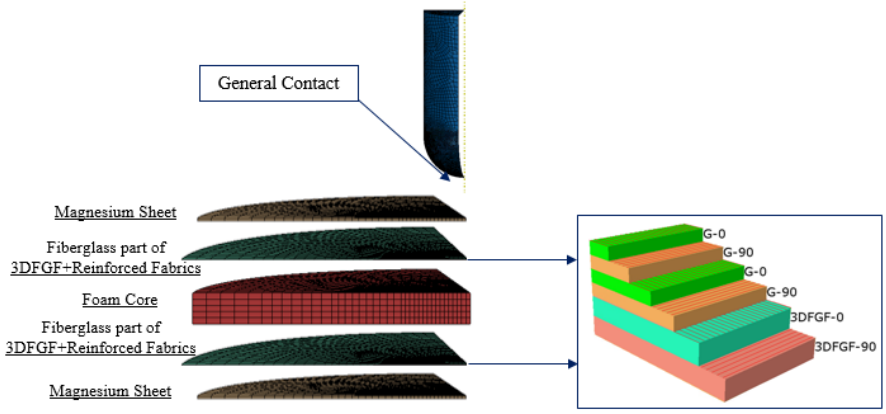

Figure 5-2. Details of FE model of the reinforced-3DFML

The impactor was simulated as a 3D discrete rigid body. All constituents of 3DFML were tied together. A general contact surface algorithm between the impactor and 3DFML was defined. The contact algorithm accounted for the normal hard contact, and the associated

tangential component was accounted for by assuming a friction coefficient of 0.3. Detail of the model is presented in Figure 5-2.

The impacted specimen has two axes of symmetry (i.e., x and y axis; see Figure 5-3) therefore, a quarter of the geometry would need to be simulated, as depicted in Figure 5-3. The symmetry boundary condition was imposed by restraining the appropriate degrees of freedom of the nodes falling within the planes (in this case, the two orthogonal edges of the model). In addition, a mesh convergence analysis was performed by changing the mesh density of the model. The mesh density has been refined within and near the impacted region, thereby facilitating extraction of data for construction of an accurate force-displacement curve.

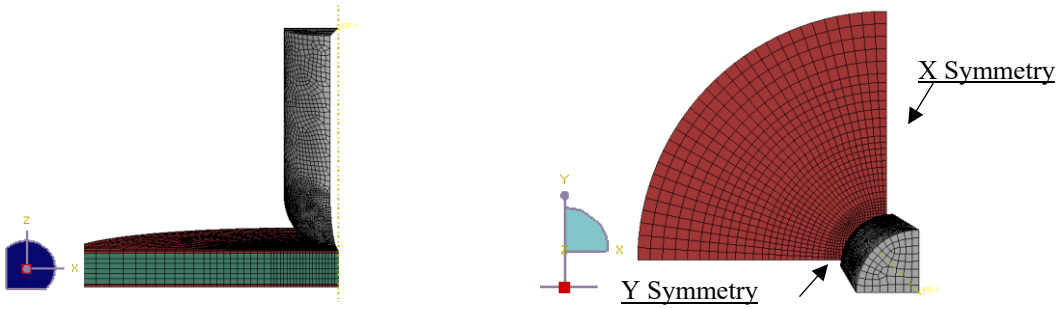

Figure 5-3. Quarter symmetry model of the 3DFML and impactor (a) Isometric view and (b) top view

5.4 Experimental Procedure

Magnesium metal sheets, 3D fiberglass fabric, epoxy resin and polyurethane foam were obtained to construct 3DFML panels. AZ31B magnesium sheets (0.5 mm thickness) were acquired through Metalmart International (Commerce, CA). Four-mm thick 3DFGF was supplied by the China Beihai Fiberglass Co. Ltd. (Jiujiang City, China). The resin used in this study was Araldite LY1564 (Bisphenole-A epoxy resin), which was combined with

Aradur 2954 (cycloaliphatic polyamine) hardener, supplied by the Huntsman Co. (West Point, CA). The foam, which was injected into the core cavities of the 3DFGF after the fabric was cured, was an 8-lb density pour-type urethane foam supplied by US Composite (West Palm Beach, FL 33407). Fabrication of the 3DFML is a multi-step process. The first step entailed fabrication of 3DFGF, by applying the resin to fabric. The wetted fabric was cured in an oven for two hours at 60 °C and eight hours at 120 °C. Subsequently, the two-part polyurethane foam was mixed and injected into the core cavities of 3D fabric and let cure for 5 min. The next step of 3DFML fabrication followed sandwiching the foam-injected 3DFGF in between the magnesium sheets. To promote optimal bonding surfaces, the magnesium sheets were sand-blasted with 20/40 grits crushed glass beads, and then cleaned with compressed-air and wiped clean with acetone. Afterwards, magnesium sheets, the reinforced glass- or carbon fabrics were wetted with an appropriate amount of epoxy resin and the foam-filled 3DFGF were assembled together and vacuum-bagged to obtain optimal bonding. Finally, the assembled FML panels were put in an oven and cured using the same regime as described earlier. Specimens with dimensions of 100 mm x 100 mm were then extracted from the panels.

The specimens were then subjected to low-velocity impact tests, carried out using a modified Charpy impact test equipment. The equipment was equipped with a dynamic load cell with 225 kN capacity, whose data was captured to generate the load-time history of each impact event. In addition, three proximity sensors and a Dynamic Linear Variable Differential Transformer (DLVDT) sensor were utilized to measure the impact velocity and displacement at impacted region, respectively. The impact event was recorded using a PHOTRON high speed camera with rate of 2000 fps in order to assess the damage

mechanism of impacted specimens. The recorded signals from the transducers were analyzed to calculate force-, displacement- and energy-time histories, absorbed energy and contact time of each impact test. Details of the impact fixture and sensors used to capture the signals is illustrated in Figure 5-4.

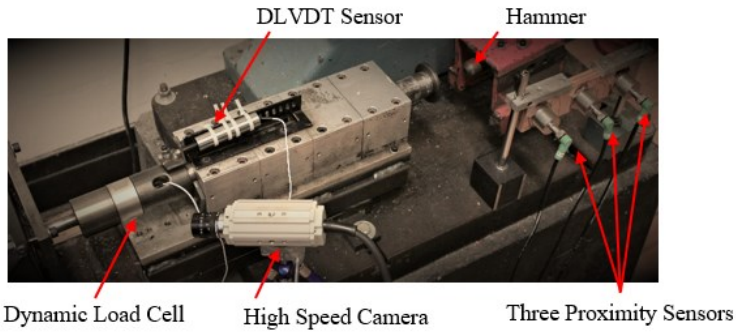

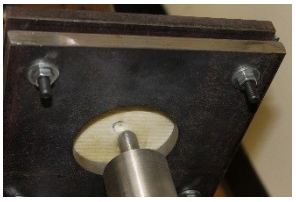

(a) (b)

Figure 5-4. (a) The Impact test set up, (b) The fixture used to hold the specimen

5.5 Results and Discussions

A total of 260 finite element analyses was performed for modelling response of 10 groups of specimens having different layup configurations. These specimens were subjected to 26 different impact energies. Table 5-2 presents the configuration details of simulated models. The first group of the simulated specimens was the original 3DFML configuration (referred to baseline specimens, hereafter), serving as the benchmark for comparison with the subsequent analyses. The second to fourth and fifth to tenth groups of simulated specimens were 3DFML specimens reinforced with glass and carbon fabrics, respectively. Three different layup configurations were considered to investigate the effects of layup orientation on the level of improvement generated on the impact response of 3DFMLs. These three different configurations are depicted in Figure 5-5. In the next section, the effects of each type of reinforced fabric on the LVI response of the 3DFMLs will be

investigated. Afterwards, the LVI response of two groups will be compared against one-another.

Table 5-2. Configurations of the reinforced-3DFML specimens

Layup ID	Reinforced Fabric Type	Layup Configuration
3DFML	-----	$[Mg/\overline{3DFGF}]_s$
3DFML-G1	Glass	$[Mg/\pm 45_2/\overline{3DFGF}]_s$
3DFML-G2	Glass	$[Mg/\pm 90/\pm 45/\overline{3DFGF}]_s$
3DFML-G3	Glass	$[Mg/\pm 90_2/\overline{3DFGF}]_s$
3DFML-C1	Carbon	$[Mg/\pm 45_2/\overline{3DFGF}]_s$
3DFML-C2	Carbon	$[Mg/\pm 90/\pm 45/\overline{3DFGF}]_s$
3DFML-C3	Carbon	$[Mg/\pm 90_2/\overline{3DFGF}]_s$
3DFML-C4	Carbon	$[Mg/\pm 45/+45/\overline{3DFGF}]_s$
3DFML-C5	Carbon	$[Mg/\pm 90/\pm 45/+45/\overline{3DFGF}]_s$
3DFML-C6	Carbon	$[Mg/\pm 90_2/90/\overline{3DFGF}]_s$

(a) (b) (c) (d)

Figure 5-5. Schematic layup configurations of non-reinforced and reinforced-3DFMLs; (a) baseline 3DFML, (b) 3DFML-G1 & -C1, (c) 3DFML-G2 & -C2, (d) 3DFML-G3 & -C3

5.5.1 Impact Response of Glass-Reinforced 3DFML

As mentioned earlier, three different configurations of additional FRP layers were considered for reinforcing the baseline 3DFML to investigate the influence of such additional layers in enhancing the response of 3DFMLs under low velocity impact. The impact response of the 3DFMLs was numerically analyzed with ABAQUS/Explicit subject to 26 different impact energies. The load- and displacement-time histories and force-displacement graphs for 12 different impact energies are presented in Figure 5-6 and 5-7, respectively. Under the lower impact energies (3 J and 11 J), the trend in variation of force-

time history curves during the loading stage is basically linear and more-or-less similar, followed by a relatively comparable slope during the subsequent unloading stage. For the impact energies that caused a crack to develop on the impacted side, the force-time history curves are linear up to their first spike, followed by the subsequent sudden drop in load, which indicate formation of a crack on the impacted surface. After this stage, the specimens resist further loading up to a certain magnitude, at which unloading gets initiated. Moreover, the variation in force-displacement curves is fairly similar to the force-time history curves, that is, exhibiting similar spikes, drop and rise in capacity, followed by the final unloading. In the specimens that experienced perforation and penetration, the remaining unloading is relatively steady, followed by a flat slope, evidencing impactor's full-penetration.

The observed failure modes are essentially characterized within three different failure modes. Mode 1 refers to a failure mode in which a crack is developed on the impacted surface of the specimen. When a crack is developed on the reverse side, it is referred to as mode 2. Finally, full perforation of specimen by the impactor is identified as mode 3 failure. Examination of the force-time histories and force-displacement graphs of the four configurations shown in Figure 5-6 and 5-7 implies that the inclusion of reinforcing glass fabrics postponed the formation of a crack in 3DFMLs, and increased their apparent load carrying capacity. The three categories of damage/failure modes of 3DFMLs reinforced with additional glass fabrics are presented in Figure 5-8.

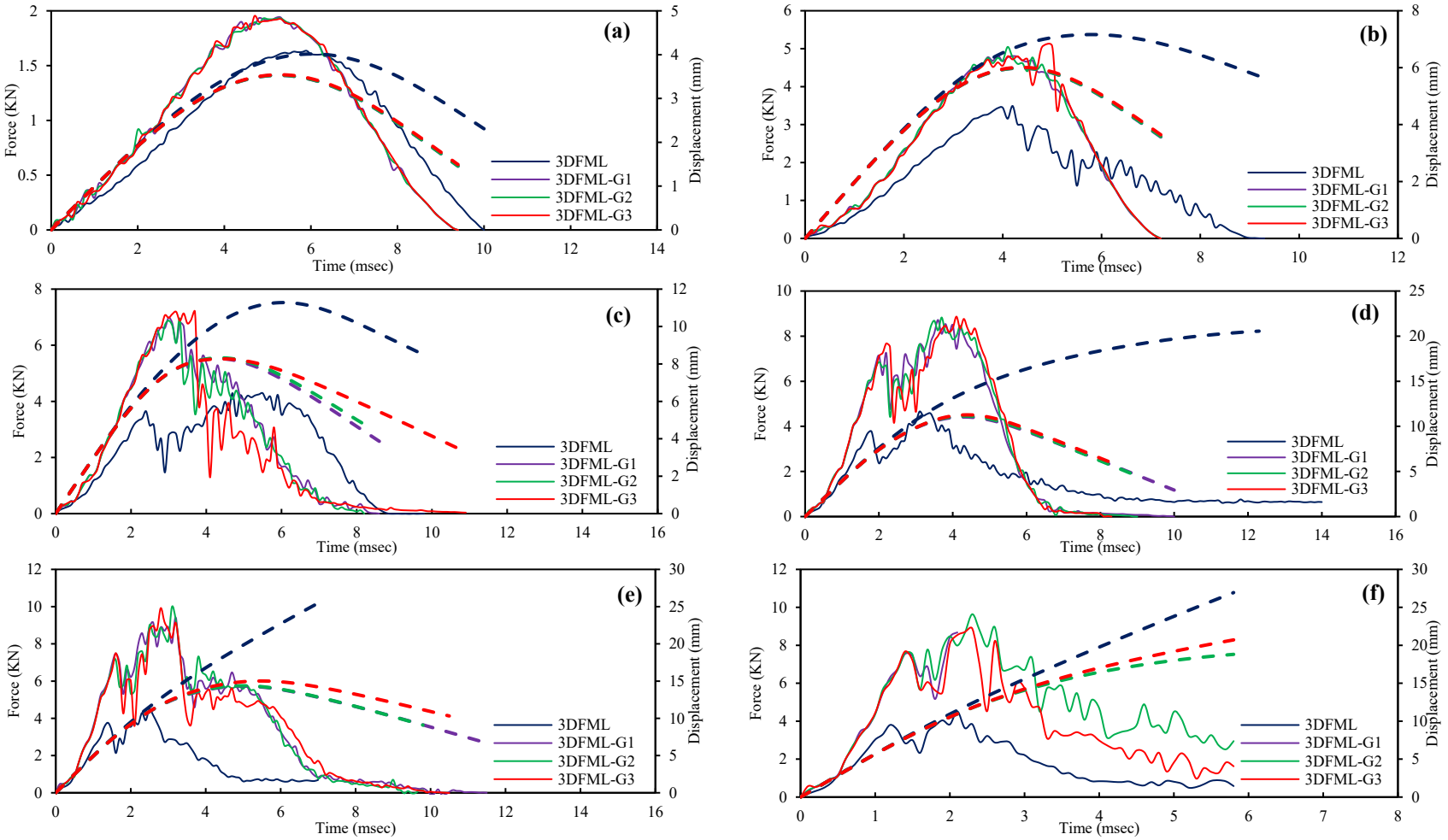

Figure 5-6. Force- and displacement-time history of fiberglass reinforced-3DFMLs at energy levels of (a) 3 J, (b) 11 J, (c) 25 J, (d) 45 J, (e) 70 J and (f) 100 J (Note: Force curves are in solid-lines, while displacement curves are dashed-lines)

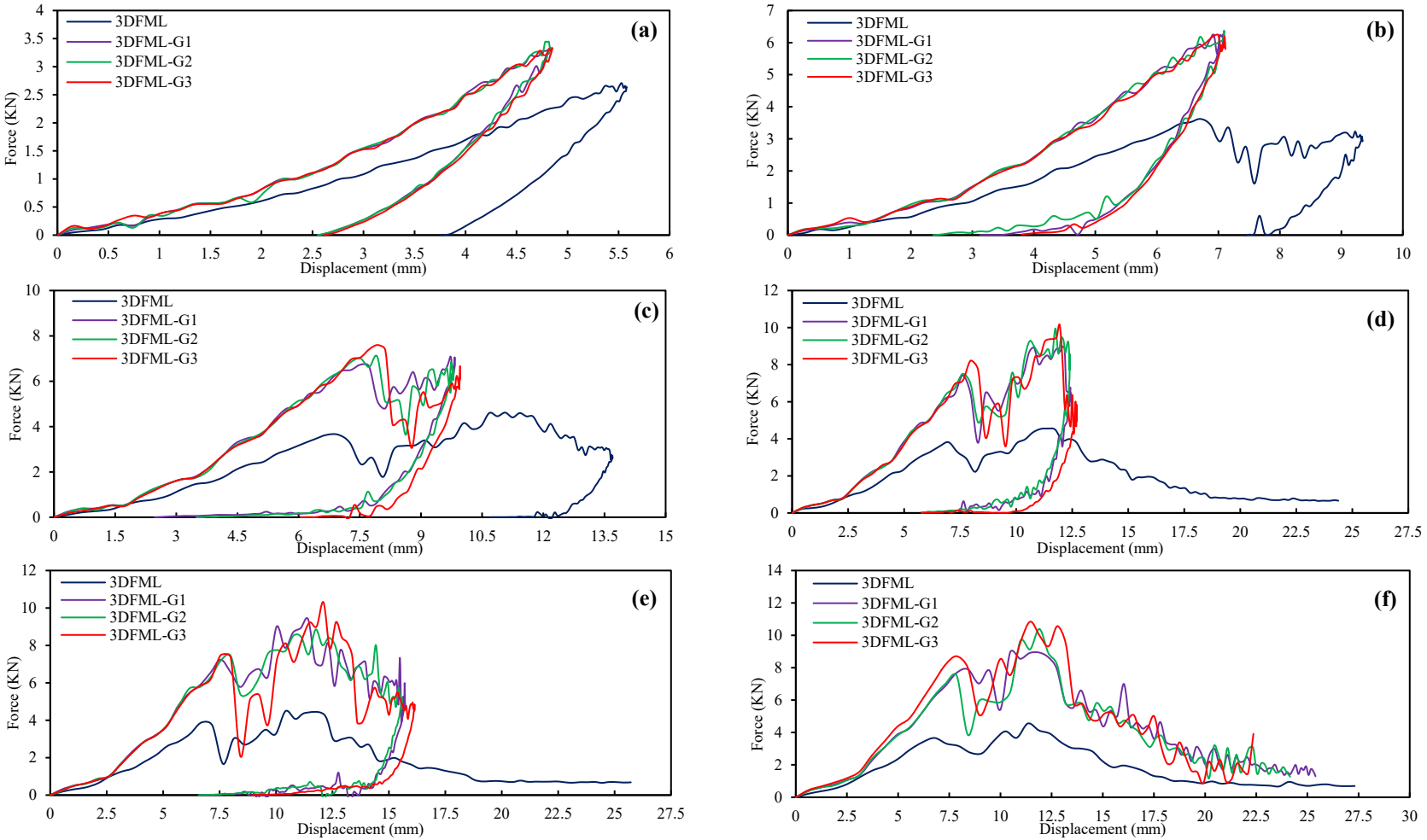

Figure 5-7. Force-displacement curves of fiberglass reinforced-3DFMLs at energy levels of (a) 6 J, (b) 18 J, (c) 35 J, (d) 57 J, (e) 85 J and (f) 110 J (Note: Force curves are in solid-lines, while displacement curves are dashed-lines)

As can be seen, in comparison to the strength of baseline 3DFML, the impact strength was improved by 56%, 71% and 144%, with respect to the aforementioned failure modes, respectively. Interestingly, however, regardless of the configuration of added glass fabrics (i.e., G1, G2 and G3), the enduring impact energies of the reinforced 3DFMLs are identical within each failure category. This would indicate that the configuration of fabric layers would not affect the energy endurance of these FMLs.

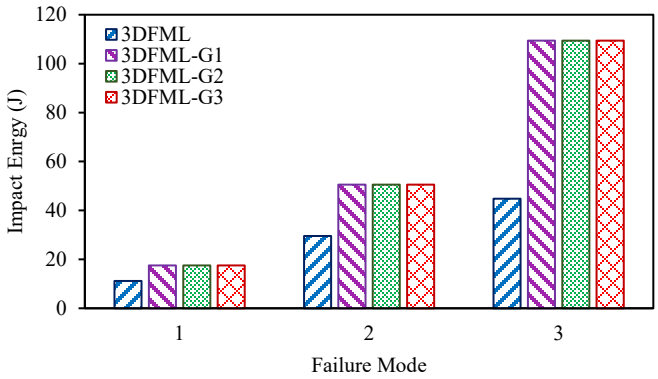

Figure 5-8. Variation in the sustained impact energy of the glass-reinforced 3DFMLs as a function of the failure modes

The variations in maximum contact force, maximum displacement and absorbed energy for the four groups of tested specimens (i.e., those reinforced with glass (3DFML-Gi), and the baseline 3DFML) subjected to 26 different impact energies, are depicted in Figure 5-9. Comparison of the maximum sustained force values indicates that significant improvement could be achieved by addition of glass reinforcement (i.e., by 89%, 103% and 115% improvement, corresponding to 3DFML-G1, -G2 and -G3 respectively, compared to baseline 3DFML). However, as seen, comparatively, the level of enhancement observed in 3DFMLs reinforced with different layup configurations is not as significant. Furthermore, graphs of the displacement and absorbed energy variations show, similarly, that addition of the reinforcing fabric could decrease the maximum deformation sustained by specimens

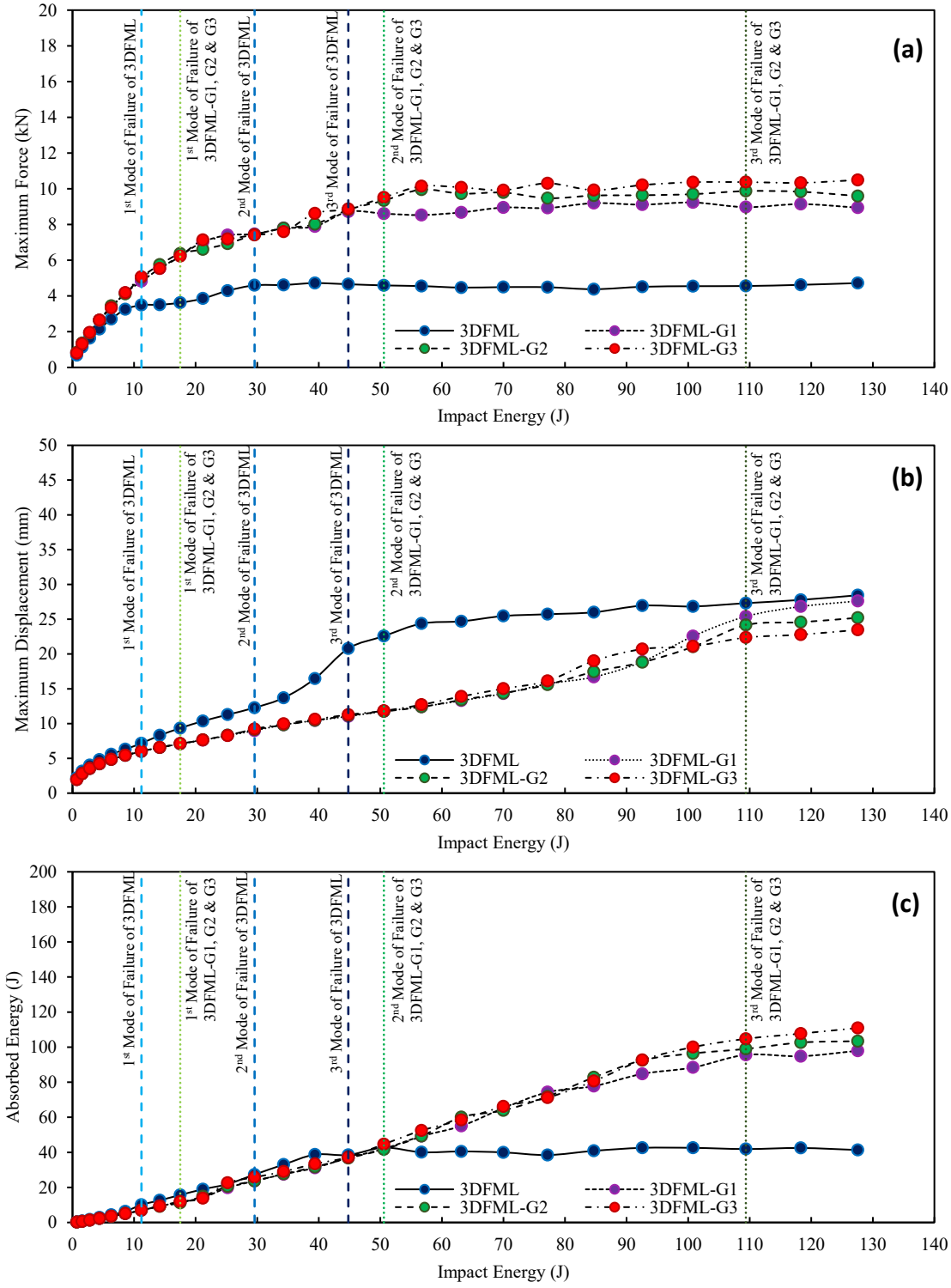

Figure 5-9. Comparison of variation of (a) the maximum sustained impact force, (b) maximum deformation, and (c) absorbed energy as a function of impact energy of the base-3DFML and those reinforced with glass fabric

that experienced the first two failure modes, but that the enhancement was not significant for those sustaining penetration modes of failure. In contrast, the energy absorption endurance was enhanced under all failure modes; in fact, the absorbed energy values exhibited by 3DFML-G1, -G2 and -G3 increased by a maximum of 136%, 150% and 180%, respectively.

The other interesting observation is the trend in variation of the maximum endured force. As seen, variation of the maximum sustained force with respect to the impact energy is somewhat linear up to the first mode of failure, after which the rate of change decreases between the first and second failure modes. However, after the second failure mode, the variation becomes insignificant, essentially remaining unchanged once penetration occurs. This trend in response is also in concert with the numerical results that depict the response of all four groups of specimens. In addition, the variations in the maximum sustained displacement and absorbed energy due to impact follows a set trend. The variations up to the onset of penetration is slightly linear for both mentioned parameters, but thereafter remain constant. Based on these observed trends, an equation can be fitted to the graph, by which one could predict the contact force. Such equations could minimize the need for conducting time-consuming and costly detailed analysis, and in turn promoting the applications of 3DFMLs in various industries. Such equations will be presented later, and the integrity and accuracy of the proposed equation would be examined.

5.5.2 Impact Response of Carbon-Reinforced 3DFML

Three different layup configurations of carbon-reinforced 3DFMLs were considered to investigate the effects of carbon fabrics on enhancing the mechanical response of 3DFMLs. Similar to the glass-reinforced 3DFMLs, mechanical response of this group of 3DFMLs

were numerically simulated under 26 different impact energies. Force- and displacement-time histories and force-displacement graphs were generated as illustrated in Figure 5-10 and 5-11, respectively. The trends in the time history curves are similar to that observed for the glass-reinforced group. Under the relatively lower impact energies, the rate of change of load is more-or-less linear before causing the first mode of failure. As the impact energy increases, a sudden peak appears in the curves, indicating development of a crack on the impacted side of the specimen. Under greater impact energies, another spike develops on the curve, which evidences the development of a second crack on the reverse side of the specimen. The variation in energy absorption of this group of specimens associated with the three defined failure modes are presented in Figure 5-12. The results presented in the figure show that as seen for the case of 3DFMLs reinforced with glass fabric, the absorbed impact energies causing each failure mode are essentially the same for the three different groups of carbon fabric-reinforced 3DFMLs. This would indicate that the different configuration of fabric layers would not enhance energy absorption capacities of the 3DFMLs. The results indicate that 16% and 42% of additional energy would be required for the specimens to experience the second and third failure modes, respectively.

Variations in the maximum sustained load, displacement and absorbed energy for the four groups of 3DFMLs are presented in Figure 5-13. The results reveal that the carbon-reinforced 3DFMLs sustained a greater contact force in comparison to the base-3DFML. While the greatest gain was exhibited by the 3DFML-C3, nonetheless, the enhancement exhibited by this reinforced FML was not significantly greater than those shown by the FMLs reinforced with different layers of carbon fabric (the enhancements were 7%, 16% and 25% for the three configurations, respectively). Moreover, the FMLs reinforced with

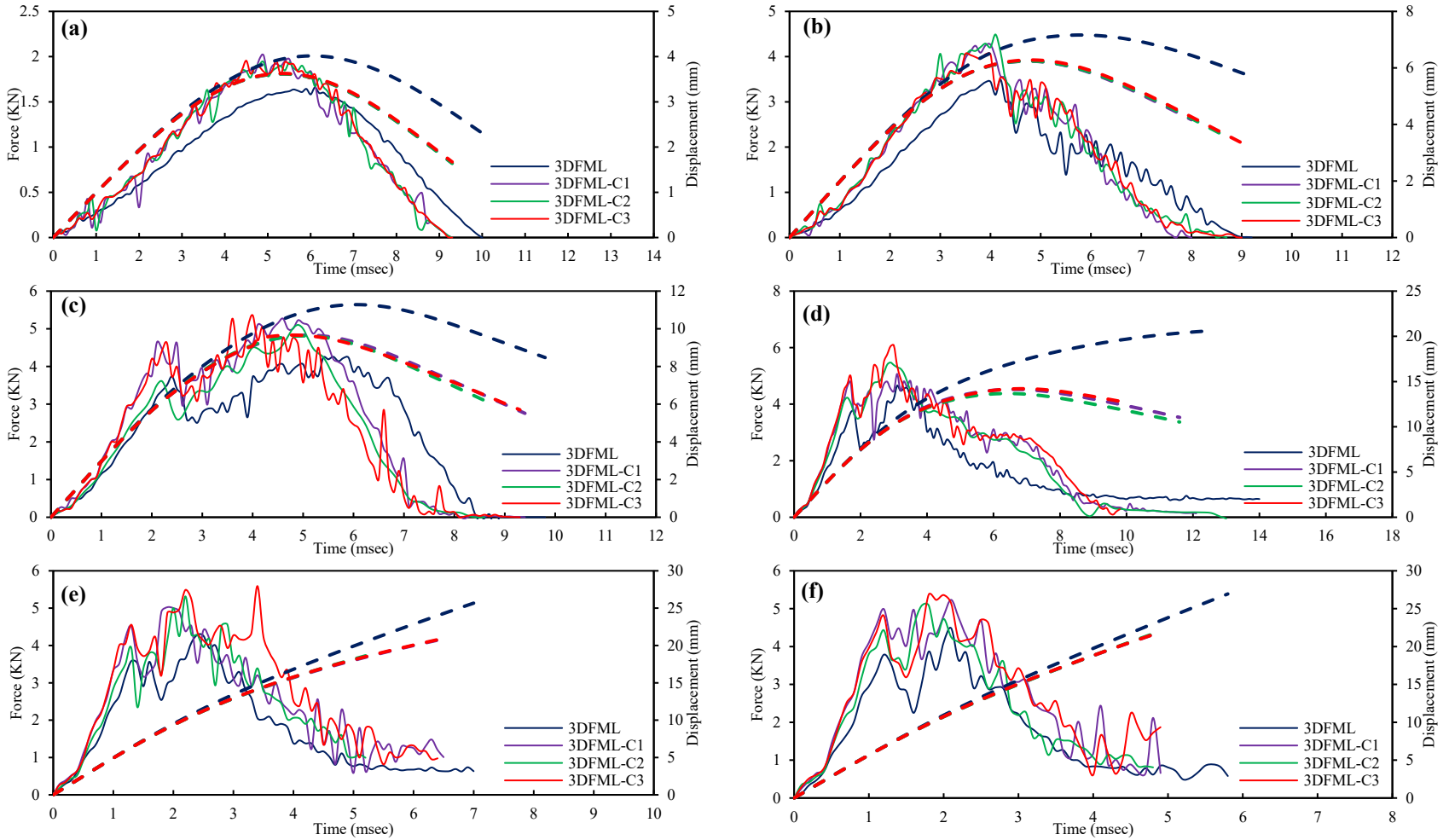

Figure 5-10. Force- and displacement-time history of carbon reinforced-3DFMLs at energy levels of (a) 3 J, (b) 11 J, (c) 25 J, (d) 45 J, (e) 70 J and (f) 100 J (Note: Force curves are in solid-lines, while displacement curves are dashed-lines)

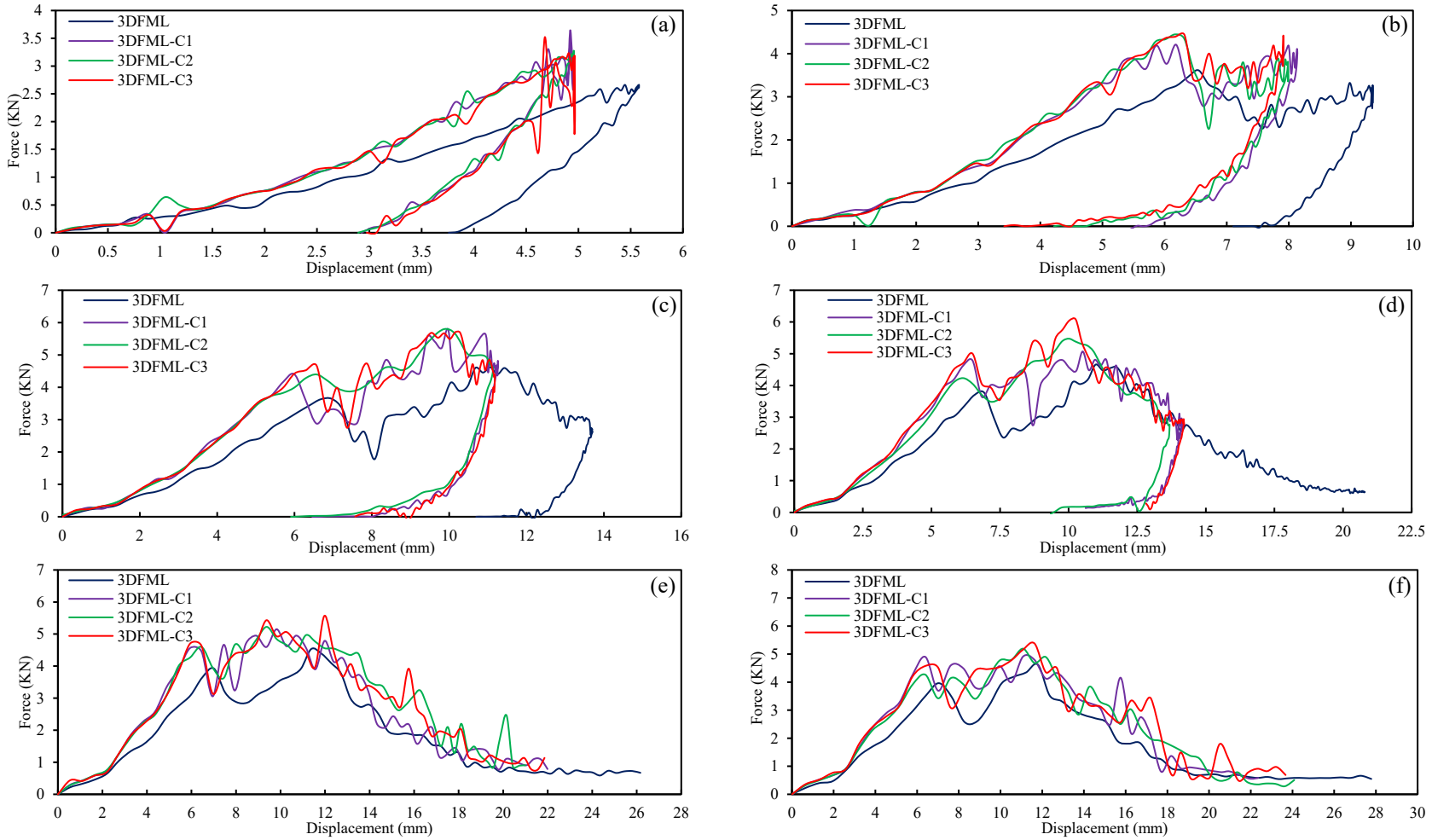

Figure 5-11. Force-displacement curves of fiberglass reinforced-3DFMLs at energy levels of (a) 6 J, (b) 18 J, (c) 35 J, (d) 57 J, (e) 85 J and (f) 110 J

carbon fabric endured less deformation in comparison to the base-3DFML. In the same vein, the energy absorption capacity of the 3DFML-C1, C2, and C3 was improved by 36%, 25% and 45%, respectively, when compared to the base-3DMLs. Finally, similar to the case of the glass-reinforced groups, logical trends in load carrying capacity and deformation are observed; these trends are used as the basis for developing practical equation for assessing the response of these FMLs, as will be presented later.

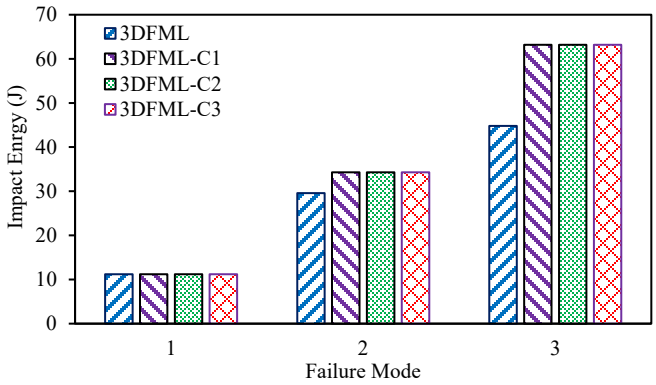

Figure 5-12. Variation in energy absorption capacity of carbon reinforced-3DFMLs for each failure modes

5.5.3 Comparison of the Performance of Glass- and Carbon-Reinforced 3DFMLs

The low-velocity impact response of the six groups of glass- and carbon-reinforced 3DFMLs were presented in previous sections. However, in order to perform a more comparable analysis, three additional groups of carbon-reinforced 3DFMLs were considered, whose bending stiffness values were equal to those of glass-reinforced 3DFMLs counterparts. In other words, the bending stiffness values of 3DFML-C4, -C5 and -C6 layout configurations, as presented in Table 5-2, are comparable to those of 3DFML-G1, -G2 and -G3, respectively. The impact response of these 3DFMLs are illustrated in Figure 5-14. Results indicate that under the lower impact energies, the impact responses of glass-reinforced and carbon-reinforced 3DFMLs are comparable. However, as the impact

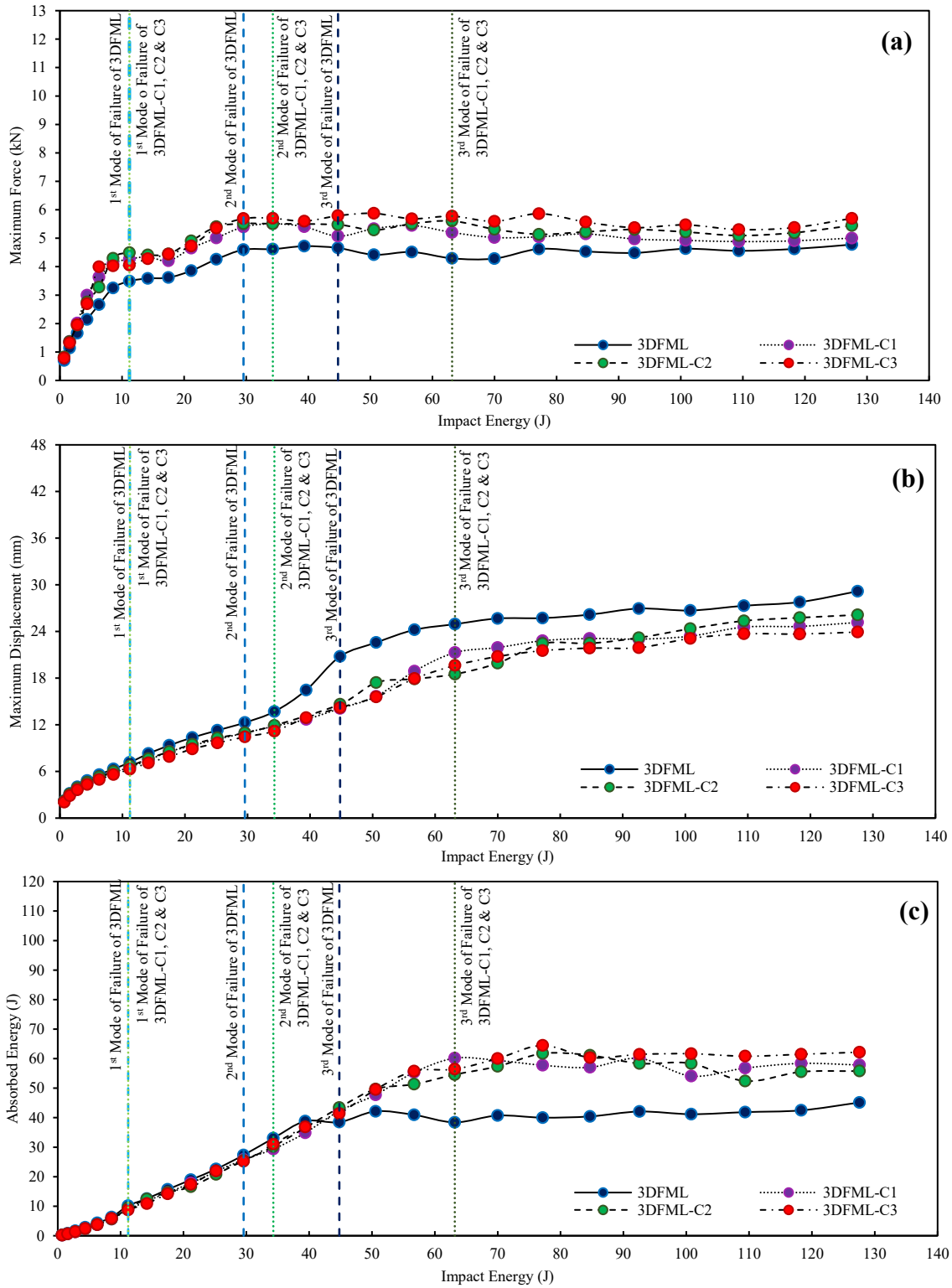

Figure 5-13. Comparison of the variation of (a) the maximum sustained impact force, (b) maximum deformation, and (c) absorbed energy as a function of impact energy of the base-3DFML and those reinforced with carbon fabric

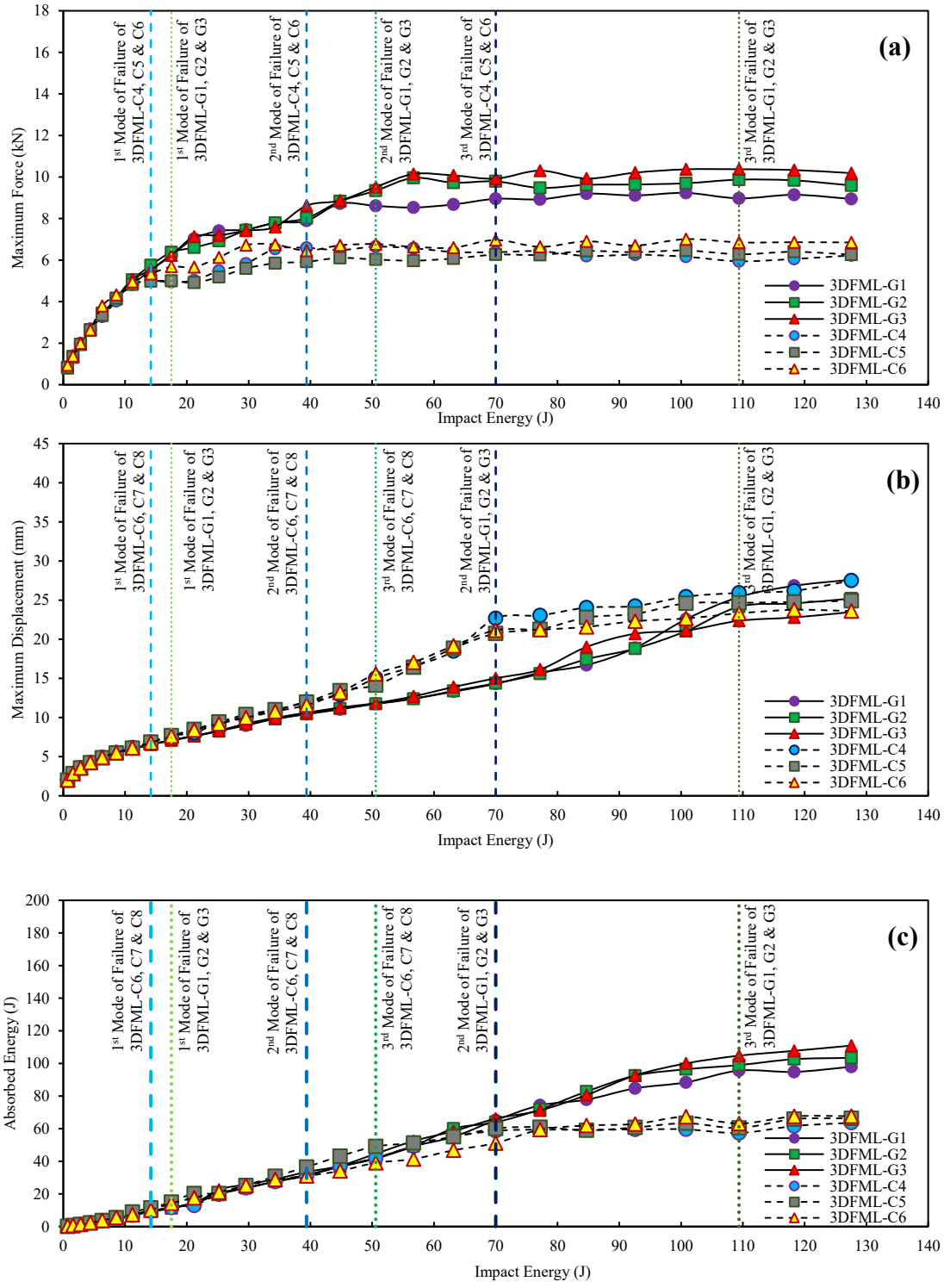

Figure 5-14. Comparison of variation of (a) the maximum sustained impact force, (b) maximum deformation, and (c) absorbed energy as a function of impact energy for glass- and carbon-reinforced 3DFML having similar bending stiffness

energy is increased, the difference between the response exhibited by the two categories increases as well. In general, glass-reinforced 3DFMLs offer greater resistance against impact than their carbon-reinforced counterparts. However, both groups exhibit a more-or-less similar maximum sustained deformation within all failure categories.

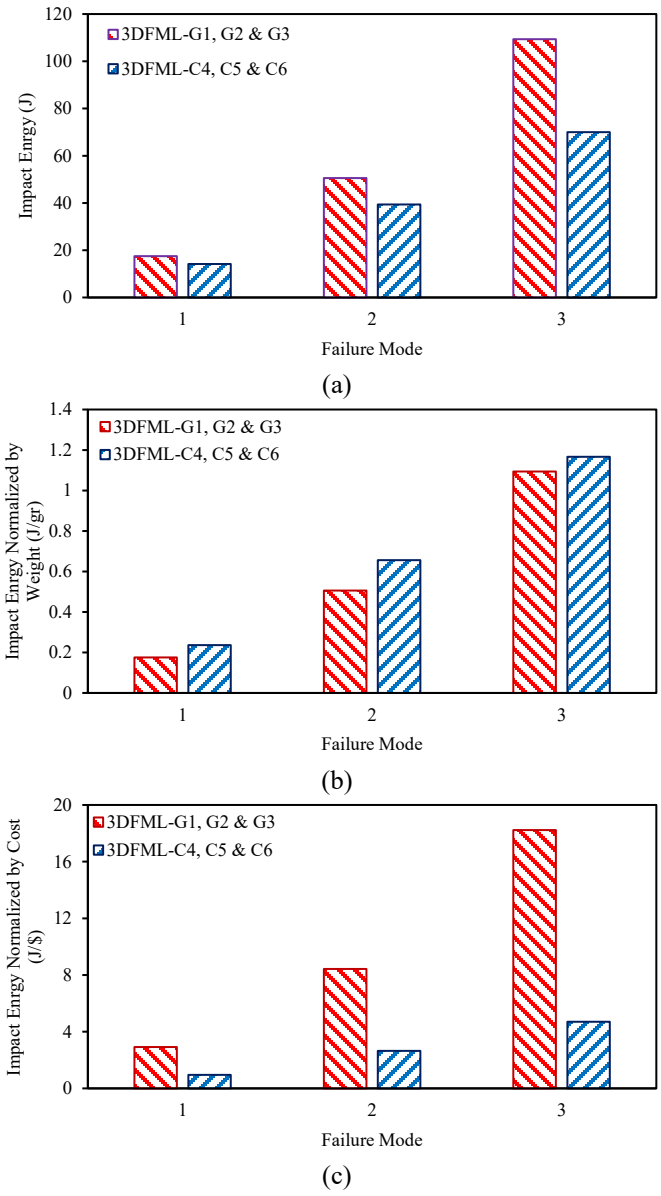

Figure 5-15. Variation of the impact strength of glass- and carbon-reinforced 3DFMLs, having similar bending stiffness, under different failure modes (a) impact strength, (b) impact strength normalized with respect to weight and (c) impact strength normalized with respect to cost

Furthermore, the impact strengths of the two groups of FMLs are presented in terms of the previously mentioned failure modes, as illustrated in Figure 5-15. As can be seen, values of the impact energy causing the first mode of failure are similar for both groups of specimens; however, the difference amongst the values increased in the second and third failure modes. Specifically, the energy absorption capacities of 3DFML-G1, -G2 and -G3 specimens were superior to those of 3DFML-C4, -C5 and -C6 by 23%, 28% and 56%.

At this juncture, the two primary parameters that govern the design selection, that is: material's weight and cost, will be compared for the two groups of specimens. For that, the impact energy causing a defined failure mode in the specimen was normalized with respect to the weight and cost of the given 3DFML. The results are presented in Figure 5-15. The results indicate that in applications where the weight would be the governing selection criterion, carbon reinforced-3DFML would offer the optimal performance. From that perspective, the impact strengths corresponding to the first, second and third failure modes of carbon reinforced-3DFMLs are greater than those exhibited by the equivalent glass reinforced FMLs by 35%, 30% and 8%, respectively. On the other hand, if the overall cost would be of concern, then the performance of glass-reinforced 3DFMLs is shown to be superior to those of carbon-reinforced FMLs.

Overall, among all the configurations considered here, from the perspectives of weight and cost, the impact performance of 3DFML-G3 and -C3 is observed to be the most optimal ones, respectively. However, when considering the overall levels of enhancement, then one could conclude that the 3DFML-G3 would offer the most optimal performance.

5.5.4 Experimental Investigation

Based on the numerical results, as demonstrated in the previous section, 3DFML-C3 and 3DFML-G3 offered the best performances among all the layup configurations considered in this study. Therefore, in order to verify the results, the response of these two configurations subject to low velocity impact were investigated experimentally. Specifically, the response of each of these two reinforced 3DFMLs and baseline 3DFML was investigated under four and three different impact energies, respectively. The force- and displacement-time history results of the impact tests and corresponding FE results of baseline 3DFML are presented in Figure 5-16.

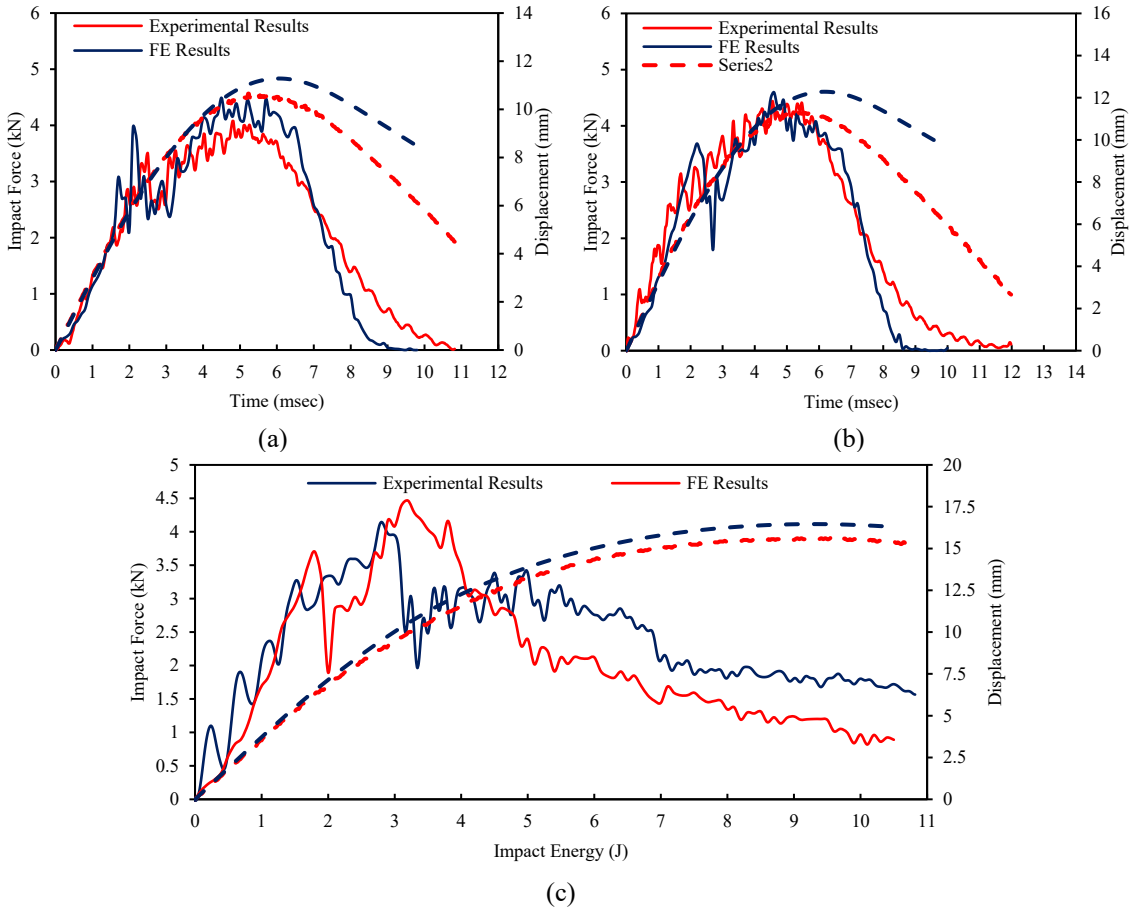

Figure 5-16. Force- and displacement-time histories of baseline 3DFML impacted at energy levels of (a) 10 J, (b) 25 J, (c) 45 J

Similar results are also presented for 3DFML-G3 and 3DFML-C3 in Figure 5-17. Figure 5-18 depicted the failure patterns of baseline- and reinforced-3DFMLs predicted by FE simulation and those obtained by experiments. It should be noted that fabric parts were simulated using shell elements, therefore the total thickness of reinforced-3DFML were graphically different from the impacted specimens. Good agreements between the computed and experimental results are observed, indicating that the developed FE framework could capture the response of such complexly structured 3DFMLs with a reasonable accuracy.

5.5.5 Proposed Analytical Equation

As explained earlier, the variation of the maximum force sustained by the 3DFML panels with respect to impact energy followed a logical trend. Consequently, the trend was used to establish a practical semi-empirical equation, by which the gain in load carrying capacity of 3DFML panels reinforced with additional glass or carbon fabrics could be predicted in reference to the strength of the baseline 3DFML. The maximum load carrying capacity, F, could be described by an exponential type equation, as follows:

$$F = F_1^{(0)} \frac{D_{11}}{D_{11}^{(0)}} \left(\frac{D_{66}}{D_{66}^{(0)}} \right)^{0.25} \left(\frac{D_{11}}{D_{66}} \right)^{0.4} \left(1 - e^{-\alpha^{(0)} I \frac{D_{66}^{(0)}}{D_{66}}} \right) \tag{5.1}$$

where $F_1^{(0)}$ and $\alpha^{(0)}$ are two parameters determined based on the numerically or experimentally produced data. $F_1^{(0)}$ is the impact force corresponding to the first damage mode of baseline 3DFML (i.e., when a crack is developed on the impacted side), whose value is *3.5* kN for the thickness of 3DFML considered in this study. The second parameter, $\alpha^{(0)}$ represents the parameter calibrated based on the results of baseline 3DFML, and is equal to *0.12* . $D_{11}^{(0)}$, $D_{66}^{(0)}$, D_{11} and D_{66} are the bending stiffness and shear stiffness of the

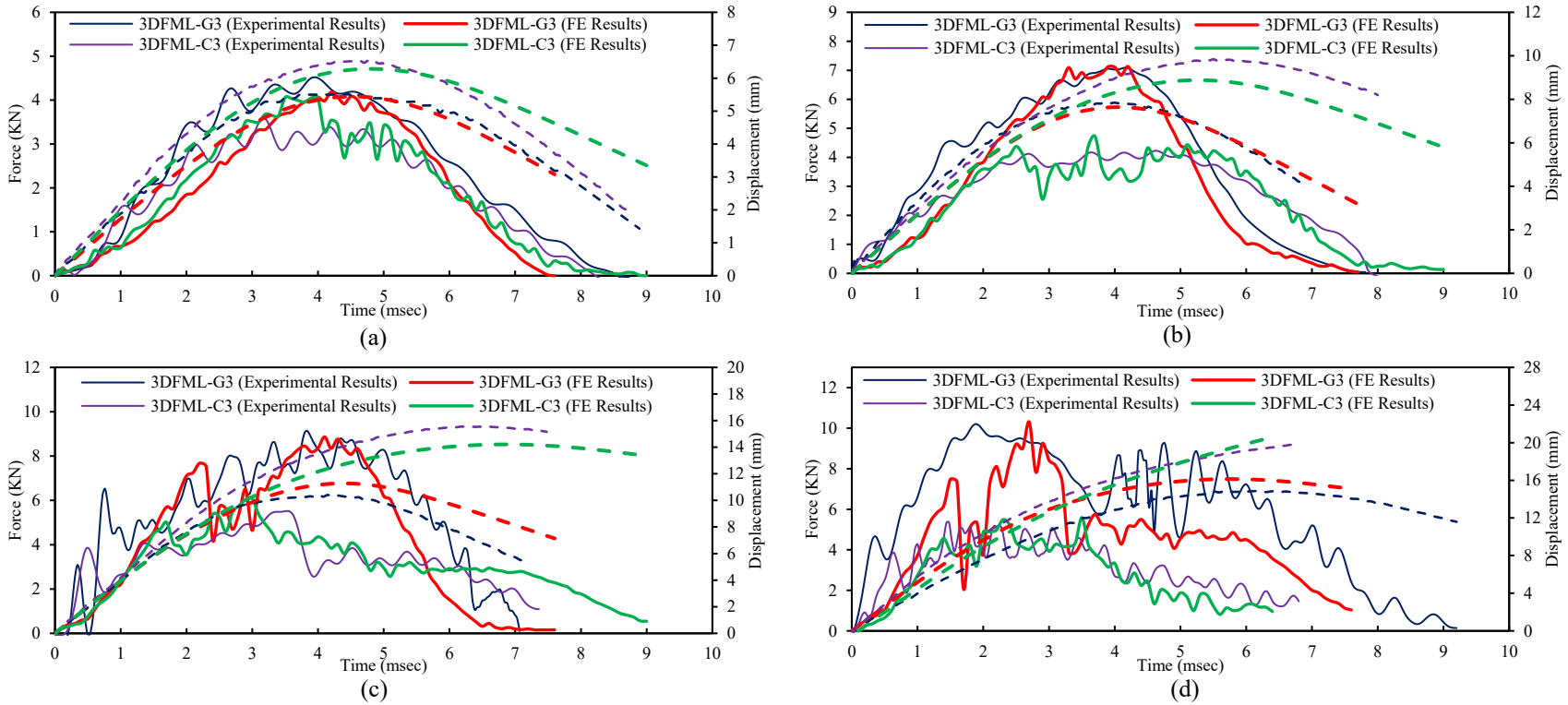

Figure 5-17. Force- and displacement-time histories of 3DFML-G3 and 3DFML-C3 impacted at energy levels of (a) 10 J, (b) 25 J, (c) 45 J, (d) 70 J

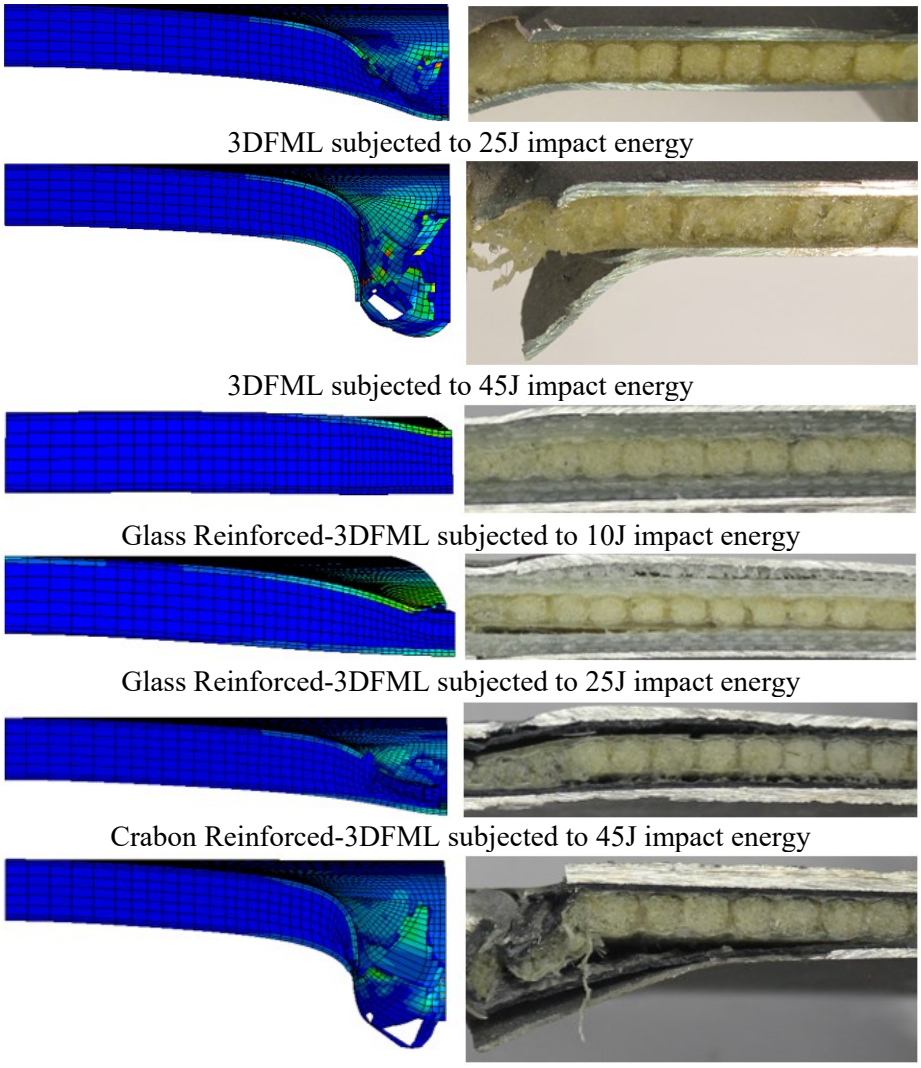

Figure 5-18. Comparison of failure type of reinforced-3DFMLs obtained through FE simulations (left) and experiments (right)

baseline- and reinforced-3DFML, respectively. The $^{(0)}$ superscript refers to the baseline 3DFML. F and I are the impact capacity and energy, respectively. The developed equation is applicable to all three 3DFMLs configurations considered here (i.e., the baseline 3DFML, and glass- and carbon-reinforced 3DFMLs).

To verify and examine the accuracy of the developed equation, the values of the maximum force computed by FE are compared against the predicted values. The comparison is done

for the five different layup configurations of reinforced 3DFML (having different numbers of reinforced layers), that were impacted with different impact energies, as illustrated in Figure 5-19 and 5-20. The results present the range of applicability of the developed equation for predicting the impact capacity of the various 3DFMLs. Further verification is done by comparing the predicted analytical values with those obtained computationally and experimentally, as presented in Figure 5-21. Furthermore, the error margins between the predicted and experimental results are reported in Table 5-3. Comparison of the calculated errors reveals that the proposed equation can reliably predict the impact capacity of 3DFMLs.

Table 5-3. Comparison of the margin of error between the values obtained by the proposed analytical equation and numerical simulations with respect to experimental results

Impact Energy (J)	Baseline 3DFML				
	Experimental Results (kN)	Numerical (FE) Results (kN)	(%) Error	Analytical Equation Results (kN)	(%) Error
10	4.08	4.88	19.59	4.57	11.96
25	4.44	4.29	3.26	4.66	5.07
45	4.15	4.66	12.36	4.88	17.67
Glass Reinforced 3DFML (3DFML-G3)					
10	4.52	4.18	7.48	4.74	4.91
25	7.09	7.19	1.48	7.95	12.11
45	9.13	8.87	2.89	9.43	3.31
70	10.20	9.92	2.76	9.69	5.03
Carbon Reinforced 3DFML (3DFML-C3)					
10	3.59	3.83	6.59	3.83	6.66
25	4.22	4.82	14.30	5.20	23.17
45	5.51	5.79	5.08	6.57	19.32
70	5.34	5.59	4.71	6.64	24.42

It should be noted that the proposed equation is developed by the curve fitting method applied to the results obtained from FE simulations. It is assumed that the impact force in reinforced-3DFML is related to the variation in the system's stiffness. Therefore, the stiffness of reinforced panels, impact force and impact energy were used as the variables,

in conjunction with nonlinear regression method, to develop the semi-empirical relationship presented above. The integrity of proposed equations has been verified by examination of the response of various configurations of reinforced-3DFML, demonstrating their expected reliability and accuracy for predicting the impact force of reinforced-3DFML with up to six additional layers of glass or carbon fabrics. However, it is believed that the equations can be used to predict response of reinforced-3DFML with additional layers, considering the fact that the safety factor used in design would compensate for the low error margins. The developed equation can therefore be used by engineers for design and analysis of various configurations of 3DFMLs in practice. The use of proposed equations would eliminate the need for conducting time-consuming tests and FE simulation.

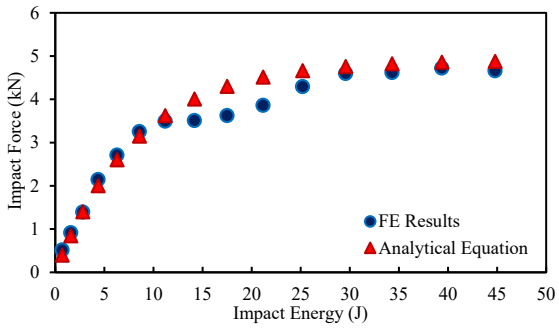

$[Mg, \overline{3DFGF}]_s$

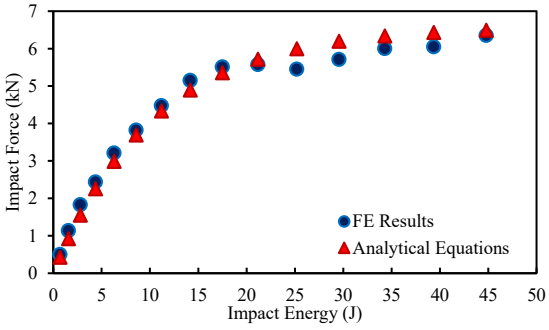

$[Mg, \pm 90, \overline{3DFGF}]_s$

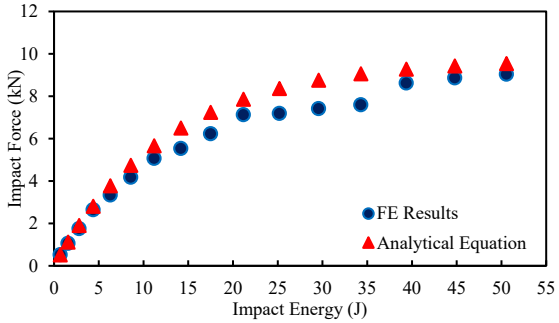

$[Mg, \pm 90_2, \overline{3DFGF}]_s$

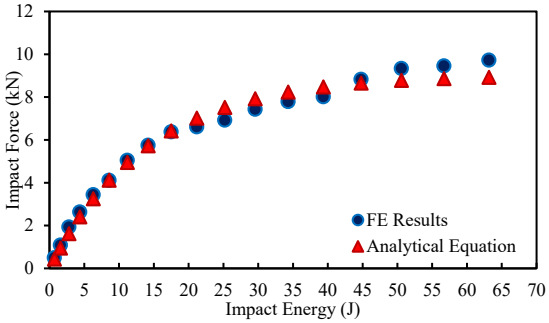

$[Mg, \pm 90, \pm 45, \overline{3DFGF}]_s$

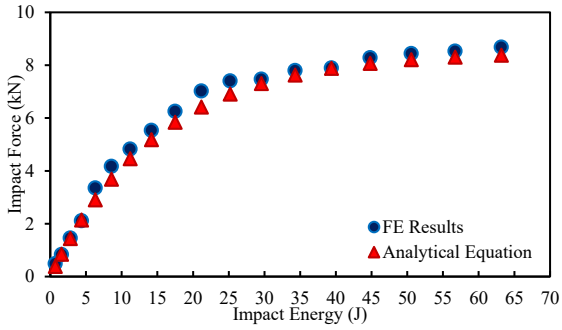

$[Mg, \pm 45_2, \overline{3DFGF}]_s$

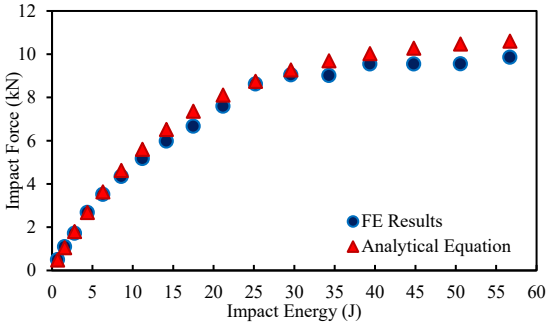

$[Mg, \pm 90_3, \overline{3DFGF}]_s$

Figure 5-19. Comparison of the impact force obtained by the analytical equation and FEA for the baseline and various configurations of glass-reinforced 3DFMLs

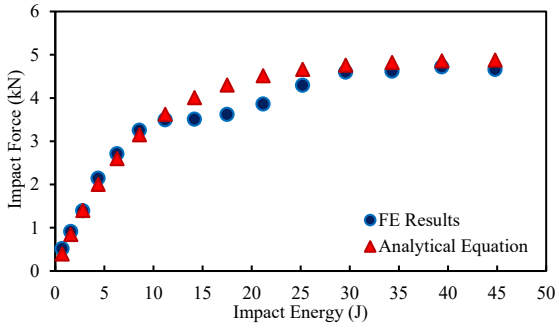

$[Mg, \overline{3DFGF}]_s$

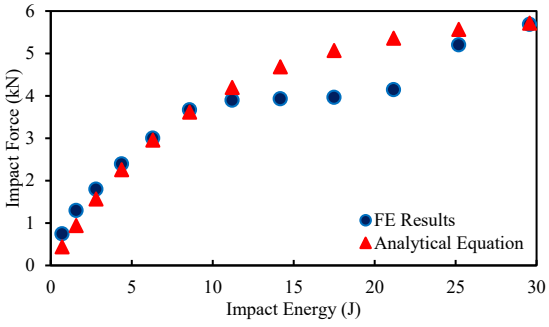

$[Mg, \pm 90, \overline{3DFGF}]_s$

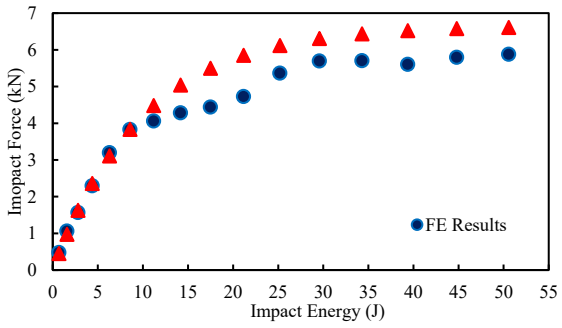

$[Mg, \pm 90_2, \overline{3DFGF}]_s$

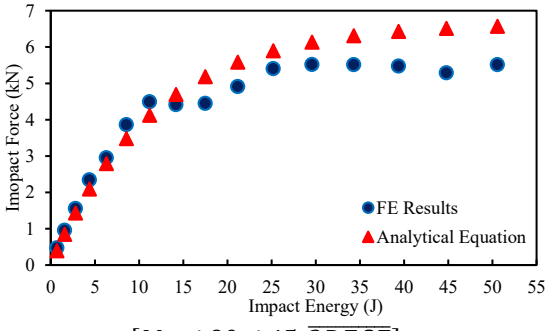

$[Mg, \pm 90, \pm 45, \overline{3DFGF}]_s$

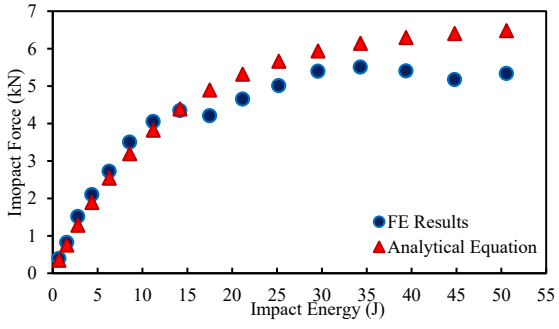

$[Mg, \pm 45_2, \overline{3DFGF}]_s$

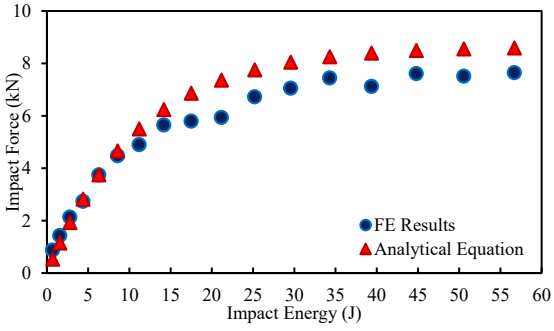

$[Mg, \pm 90_3, \overline{3DFGF}]_s$

Figure 5-20. Comparison of the impact load carrying capacity obtained by the analytical equation and FEA for the baseline and various configurations of carbon-reinforced 3DFMLs

5.6 Conclusion

The primary objective of this study was to investigate the level of gain in performance of a new class of 3D fiber metal laminates (3DFMLs), when reinforced by additional reinforcing layers, subjected to low velocity impact. Fiberglass and carbon fabrics were considered as the reinforcing fabrics. Three different layup configurations were considered for each type of reinforcement. A finite element (FE) model was developed to simulate the impact response of the reinforced 3DFMLs. In total, 10 groups of 3DFMLs were examined under 26 different impact energies. Moreover, to make an unbiased comparison, the impact response of carbon- and glass-reinforced 3DFMLs of equal bending stiffness was examined. The results revealed that the inclusion of fiberglass reinforced could render the 3DFML with optimal performance. Analysis of the results identified $(Mg/\pm 90_2/\overline{3DFGF})_S$ configuration as the most optimal FML among all the configurations considered in this study.

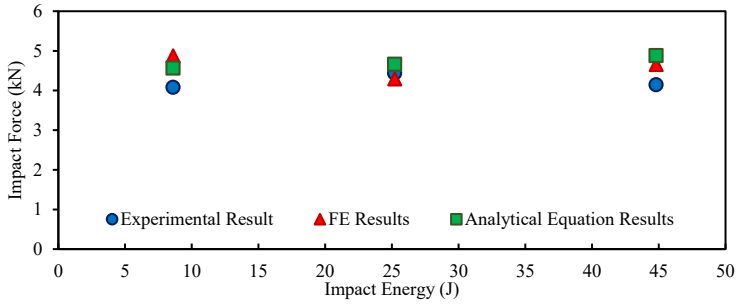

(a)

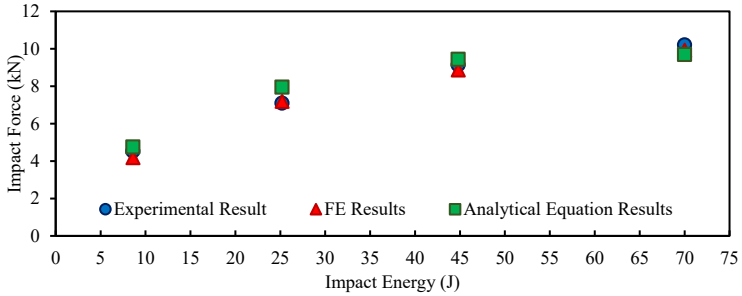

(b)

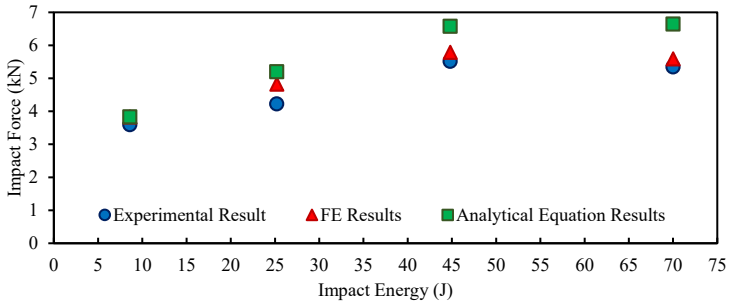

(c)

Figure 5-21. Variation of the impact load carrying capacity as a function of impact energy obtained experimentally, numerically and analytically for (a) baseline 3DFML, (b) 3DFML-G3 and (c) 3DFML-C3

Moreover, a semi-empirical equation was developed for predicting the impact response of such reinforced 3DFMLs. The integrity of the proposed equation was verified comparing its predictions against the experimental and numerical results. The proposed equation can serve as a preliminary practical tool for establishing the most optimal configuration of such reinforced 3DFMLs against impact loading.

5.7 Acknowledgement

This financial support received through the National Science and Engineering Research Council of Canada (NSERC) in support of this study is gratefully appreciated. The Killam scholarship and Amelia Earhart fellowship awarded to the first author are also gratefully acknowledged.

5.8 References

Abrate, S. (2011). Impact engineering of composite structures, Springer Science & Business Media.

Asaee, Z., M. Mohamed, D. De Cicco and F. Taheri (2017). "Low-Velocity Impact Response and Damage Mechanism of 3D Fiber-Metal Laminates Reinforced with Amino-Functionalized Graphene Nanoplatelets." International Journal of Composite Materials 7(1): 20-36.

Asaee, Z., M. Mohamed, S. Soumik and F. Taheri (2017). "Experimental and numerical characterization of delamination buckling behavior of a new class of GNP-reinforced 3D fiber-metal laminates." Thin-Walled Structures 112: 208-216.

Asaee, Z., S. Shadlou and F. Taheri (2015). "Low-velocity impact response of fiberglass/magnesium FMLs with a new 3D fiberglass fabric." Composite Structures 122: 155-165.

Asaee, Z. and F. Taheri (2015). Characterization of the Mechanical and Impact Response of a New-Generation 3D Fiberglass Fabric. American Society of Composites-30th Technical Conference.

Asaee, Z. and F. Taheri (2016). "Experimental and numerical investigation into the influence of stacking sequence on the low-velocity impact response of new 3D FMLs." Composite Structures 140: 136-146.

Asaee, Z. and F. Taheri (2016). Experimental Studies on the Impact Response of 3D Fiberglass Fabric Subject to Different Size Impactors. Proceedings of the American Society for Composites: Thirty-First Technical Conference.

Bienias, J., P. Jakubczak and K. Dadej (2016). "Low-velocity impact resistance of aluminium glass laminates–Experimental and numerical investigation." Composite Structures 152: 339-348.

Caprino, G., G. Spataro and S. Del Luongo (2004). "Low-velocity impact behaviour of fibreglass–aluminium laminates." Composites Part A: Applied Science and Manufacturing 35(5): 605-616.

Chai, G. B. and P. Manikandan (2014). "Low velocity impact response of fibre-metal laminates–A review." Composite Structures 107: 363-381.

Davies, G., D. Hitchings and G. Zhou (1996). "Impact damage and residual strengths of woven fabric glass/polyester laminates." Composites Part A: Applied Science and Manufacturing 27(12): 1147-1156.

De Cicco, D., Z. Asaee and F. Taheri (2017). "Low-velocity impact damage response of fiberglass/magnesium fiber-metal laminates under different size and shape impactors." Mechanics of Advanced Materials and Structures 24(7): 545-555.

Fan, H., H. Chen, L. Zhao, J. Zhou, F. Jin, J. Zheng and N. Kuang (2014). "Flexural failure mechanisms of three-dimensional woven textile sandwich panels: Experiments." Journal of Composite Materials 48(5): 609-620.

Fan, J., W. Cantwell and Z. Guan (2011). "The low-velocity impact response of fiber-metal laminates." Journal of Reinforced Plastics and Composites 30(1): 26-35.

Ghassemieh, E. (2011). Materials in automotive application, state of the art and prospects, INTECH Open Access Publisher.

Heydari-Meybodi, M., H. Mohammadkhani and M. Bagheri (2016). "Oblique Low-Velocity Impact on Fiber-Metal Laminates." Applied Composite Materials 24(3): 611-623.

Hosseini, S. A., M. Sadighi and R. Maleki Moghadam (2015). "Low-velocity impact behavior of hollow core woven sandwich composite: Experimental and numerical study." Journal of Composite Materials 49(26): 3285-3295.

Hosur, M., M. Abdullah and S. Jeelani (2004). "Manufacturing and low-velocity impact characterization of hollow integrated core sandwich composites with hybrid face sheets." Composite Structures 65(1): 103-115.

Hosur, M. V., F. Chowdhury and S. Jeelani (2007). "Low-velocity impact response and ultrasonic NDE of woven carbon/epoxy—Nanoclay nanocomposites." Journal of Composite Materials 41(18): 2195-2212.

Karahan, M., H. Gül, J. Ivens and N. Karahan (2012). "Low velocity impact characteristic of 3D integrated core sandwich composites." Textile Research Journal 82(9): 945-962.

Kus, A., I. Durgun and R. Ertan (2016). "Experimental study on the flexural properties of 3D integrated woven spacer composites at room and subzero temperatures." Journal of Sandwich Structures and Materials.

Marsh, G. (2014). "Composites and metals–a marriage of convenience?" Reinforced Plastics 58(2): 38-42.

Morinière, F., R. Alderliesten, M. Sadighi and R. Benedictus (2013). "An integrated study on the low-velocity impact response of the GLARE fibre-metal laminate." Composite Structures 100: 89-103.

Nagaraj, M. (2005). "Experimental and computational investigation of FRP-reinforced glulam columns including associated software development [Master of applied science thesis]." Department of Civil and Resource Engineering, Dalhousie University.

Payeganeh, G., F. A. Ghasemi and K. Malekzadeh (2010). "Dynamic response of fiber–metal laminates (FMLs) subjected to low-velocity impact." Thin-Walled Structures 48(1): 62-70.

Rathnasabapathy, M., A. Mouritz and A. Orifici (2013). Experimental and numerical investigation of low velocity impacts of fibre-metal laminates. AIAC15: 15th Australian International Aerospace Congress, Australian International Aerospace Congress.

Sadighi, M., R. Alderliesten and R. Benedictus (2012). "Impact resistance of fiber-metal laminates: a review." International Journal of Impact Engineering 49: 77-90.

Sadighi, M., T. Pärnänen, R. Alderliesten, M. Sayeaftabi and R. Benedictus (2012). "Experimental and numerical investigation of metal type and thickness effects on the impact resistance of fiber metal laminates." Applied Composite Materials 19(3-4): 545-559.

Seyed Yaghoubi, A. and B. Liaw (2012). "Thickness influence on ballistic impact behaviors of GLARE 5 fiber-metal laminated beams: Experimental and numerical studies." Composite Structures 94(8): 2585-2598.

Seyed Yaghoubi, A., Y. Liu and B. Liaw (2011). "Low-velocity impact on GLARE 5 fiber-metal laminates: influences of specimen thickness and impactor mass." Journal of Aerospace Engineering 25(3): 409-420.

Starikov, R. (2013). "Assessment of impact response of fiber metal laminates." International Journal of Impact Engineering 59: 38-45.

Subbaramaiah, R., B. Prusty, G. Pearce, S. Lim and R. Thomson (2017). "Crashworthy response of fibre metal laminate top hat structures." Composite Structures 160: 773-781.

Taheri-Behrooz, F., M. Shokrieh and I. Yahyapour (2014). "Effect of stacking sequence on failure mode of fiber metal laminates under low-velocity impact." Iranian Polymer Journal 23(2): 147-152.

Tooski, M. Y., R. Alderliesten, R. Ghajar and S. Khalili (2013). "Experimental investigation on distance effects in repeated low velocity impact on fiber–metal laminates." Composite Structures 99: 31-40.

Vaidya, A., U. Vaidya and N. Uddin (2008). "Impact response of three-dimensional multifunctional sandwich composite." Materials Science and Engineering: A 472(1): 52-58.

Vaidya, U., M. Hosur, D. Earl and S. Jeelani (2000). "Impact response of integrated hollow core sandwich composite panels." Composites Part A: Applied Science and Manufacturing 31(8): 761-772.

Vlot, A. (1996). "Impact loading on fibre metal laminates." International Journal of Impact Engineering 18(3): 291-307.

Whisler, D. and H. Kim (2015). "Experimental and simulated high strain dynamic loading of polyurethane foam." Polymer Testing 41: 219-230.

Yaghoubi, A. S., Y. Liu and B. Liaw (2012). "Stacking sequence and geometrical effects on low-velocity impact behaviors of GLARE 5 (3/2) fiber–metal laminates." Journal of thermoplastic composite materials 25(2): 223-247.

Yarmohammad Tooski, M., R. C. Alderliesten, R. Ghajar and S. M. R. Khalili (2013). "Experimental investigation on distance effects in repeated low velocity impact on fiber–metal laminates." Composite Structures 99(0): 31-40.

Zhou, G., C. Liu, W. Li and X. Wang (2016). "Shear behavior of 3D woven hollow integrated sandwich composites: Experimental, theoretical and numerical study." Applied Composite Materials 24(4): 787-801.

Zhu, S. and G. B. Chai (2012). "Low-velocity impact response of fibre–metal laminates–Experimental and finite element analysis." Composites Science and Technology 72(15): 1793-1802.

Zhu, S. and G. B. Chai (2013). Impact of aluminum, CFRP laminates, fibre-metal laminates and sandwich panels. Composite Materials and Joining Technologies for Composites, Volume 7, Springer: 199-205.

Chapter 6: Experimental and Numerical Characterization of Delamination Buckling Behavior of GNP-Reinforced New Class of 3D Fiber-Metal Laminates

Zohreh Asaee, Mbarka Mohamed, Sadman Soumik and Farid Taheri

Published in Thin-Walled Structures, Volume 112, PP 208-216, 2017

Zohreh Asaee is the principal researcher and author of this article. She conducted the research as a part of her PhD program. She mentored the second and third authors during the process of specimen preparation and experimental investigation. Moreover, she analyzed the experimental results, and conducted the numerical simulations. She prepared the draft of the article, which was subsequently revised and enhanced by her supervisor. She also applied the necessary revisions prior to publication of the articles. All works were done under supervision and guidance of her supervisor, Prof. Farid Taheri.

6.1 Abstract

The delamination buckling behavior of graphene nano platelets (GNP) reinforced 3D fiber-metal laminates (3DFMLs) is investigated experimentally and numerically. In this study, the resin used to bond the metallic layers to the 3D fiberglass fabric (3DFGF) is reinforced with GNP, with the aim of improving the delamination resistance at the interface, thus enhancing the overall stability response of the 3DFMLs. For that, four different weight-percentages of GNP are used to establish the effect of GNP content on the stability (buckling) response of the 3DFMLs. In total, four groups of specimens with four different delamination lengths are used to investigate the effects of GNP on the buckling capacity of the 3DFMLs. In addition to the experimental investigation, a nonlinear finite element model is developed, using the commercial finite element code ABAQUS, to simulate the delamination buckling response of the 3DFMLs. The numerically obtained critical

buckling capacities and failure modes are compared to the experimental results. Good agreements between the finite element (FE) and experimental results are obtained.

6.2 Introduction

A new class of hybrid materials, referred to as fiber metal laminates (FMLs), have emerged in the market in the recent decades. This class of hybrid materials is formed by combining thin layers of metallic alloys with sheets of fiber-reinforced plastic (FRP). The most significant feature of a FML is the improved mechanical properties in comparison to those of its constituents (i.e., FRP and metal), offering improved specific strength and stiffness, excellent fatigue performance and impact strength (Sinmazçelik, Avcu et al. 2011, Sadighi, Alderliesten et al. 2012). Consequently, due to the enhanced and unique mechanical properties of FMLs, they have been increasingly utilized in the aerospace industry.

As mentioned earlier, FMLs have been introduced to the market relatively recently; therefore, the research database in regard to their response under different loading conditions is quite limited. FML structural components used in auto bodies, aircraft fuselages and wings are susceptible to axial loads; consequently, their buckling response should be fully characterized and understood. In an effort to understand the stability response of traditionally used FMLs, Remmers *et al.* (Remmers and de Borst 2001) investigated the buckling behavior of GLARE (acronym for GLAss REinforced aluminum laminate), that hosted a delamination. They concluded that the presence of a delamination resulted in a decreased residual strength and promoted earlier collapse of their FML. A FE model was developed in a meso-mechanical level with a solid-like shell element, used to model each individual layer. The layers were connected to one-another by interface elements, which accommodated modelling of the delamination. Moreover, Scanning

Electron Microscope (SEM) images were used to examine the failure mechanism of their FML in comparison to those produced by their FE results. Their results revealed that the delamination would have a strong influence on the post-buckling stiffness of GLARE.

In another study, Frizzell *et al.* (Frizzell, McCarthy et al. 2011) examined the integrity of a three-dimensional FE model constructed for simulation of jointed FMLs. The damage mechanism of the aluminum layers and composite plies of their FMLs were defined by using a plasticity model and a 3D damage mechanism model, respectively. In that study, the authors investigated the effects of mesh sensitivity in relation to the strain-softening model used in their simulation. Good agreement was obtained between their experimental and numerical results. The numerical model could predict the damage initiation and damage growth of jointed FML with a reasonable accuracy. However, some discrepancies (such as overestimated initial stiffness, and unclear ultimate load limit), were observed between their FE and experimental results. Al-Azzawi *et al.* (Al-Azzawi, McCrory et al.) developed a bi-linear cohesive zone modeling (CZM) to examine the behavior of a manufacturing defect in GLARE-FML when used as splices or doublers. They also investigated the effects of delamination on the buckling response of GLARE. They used the digital image correlation technique to monitor the response of their FML, trace the delamination growth, and evaluate the strain energy release rates. The collected data was used to validate their FEM results.

As stated earlier, the number of studies on the buckling behavior of delaminated FMLs is quite limited, while a significant number of studies have been conducted for establishing the stability response of FRP (Chai, Babcock et al. 1981, Chen 1991, Larsson 1991, Chattopadhyay and Gu 1994, Kim and Hong 1997, Kachanov 2012, Wang, Harvey et al.

2015, Yap, Chai et al. 2015, Gong, Chen et al. 2016). For example, Gu *et al.* (Gu and Chattopadhyay 1999) examined the mechanics and mechanisms of delamination buckling and post-buckling of a graphite/epoxy laminated composite. The critical load and post-buckling load-carrying capacity of epoxy composites were investigated by compression tests. Moreover, the effects of stacking sequence, and the location and length of delamination on the buckling response of the composite were studied. It was shown that the buckling mode of the composites was affected by the location and length of the delamination. Furthermore, the experimental results were compared against the numerical results obtained through a model that used a new higher-order theory. Esfahani *et al.* (Esfahani, Ghasemnejad et al. 2010) investigated, experimentally and numerically, the effects of delamination location on the buckling response of hybrid composite beams. The laminated composites with various layups and different defect locations were tested to determine the buckling load. It was shown that the delamination position and laminate layup sequence affected the buckling modes and the critical loads. The FEM simulation of their test specimens was carried out by ANSYS finite element software. The numerical results were verified by the experimental data.

Hwang *et al.* (Hwang and Liu 2002) studied the buckling and post-buckling behavior of composite laminates hosting multiple delaminations under uniaxial compression. The through-the-width delamination had a triangular shape to simulate the damage due to an impact. The critical delamination growth loads obtained for a single delamination, and multiple delaminations were compared. The comparison showed that the critical load for the single delamination was much higher than those corresponding to the specimens with

multiple-delaminations. Moreover, the triangular shape of delaminations in those specimens having multiple-delaminations affected the critical delamination growth loads.

6.3 Motivation and Objectives

The problems of buckling and post-buckling of composites have been well studied, and computational simulation of such phenomena have been carried out by several investigators. However, there exist a clear lack of such investigations when FMLs are considered, in particular, in relation to the complex structure of the 3DFML introduced in this paper. Moreover, there is a paucity of works in regard to the delamination response of GNP reinforced bonded interfaces, especially when the interface is subjected to compressive loading. The work presented herein attempts to address some of the mentioned shortfalls. It should be noted that the 3DFML introduced in this investigation is not a simple hybrid system as the conventional FMLS, whose response can be predicted by the well-established layer-wise theories. In contrast, the FML under the study is a complex 3D structural system, whose response could only be captured by an appropriate finite element analysis (FEA) framework. For this purpose, a commercial FE software, namely ABAQUS/CAE, has been used in this study.

The main objective of the current study is therefore, to investigate delamination buckling response of a new class of FML, namely a FML formed by a truly 3D glass foam-filled fabric (See Figure 6-1), which was introduced in the previous works of the authors (Asaee, Shadlou et al. 2015, Asaee and Taheri 2015, Asaee and Taheri 2016). As mentioned in our previous publications, the main application of the developed 3DFML is for fabrication of body panels for automobiles and trucks. Our systematic evaluation of the impact response of 3DFML observed a different form of damage mechanism in comparison to that

witnessed in testing of conventional FMLs. Specifically, no delamination occurrence was observed in the fabric, while delamination occurred only at the metal/3DFG fabric interface. This is believed to be due to the unique structure of the 3DFGF. Therefore, this complex structure yields a markedly different delamination buckling response in comparison to the conventional FML. In fact, the static behavior of 3DFML is also significantly different from the conventional FML.

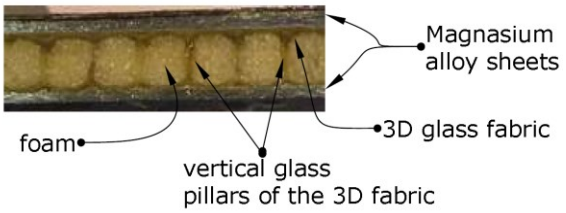

Figure 6-1. The 3D fiber metal laminate (3DFML)

In this study, the buckling response of the new 3DFML is studied for two distinct categories of 3DFML. The first category specimens were fabricated by adhering the metallic sheets to 3D glass structure by a neat epoxy resin, while in the second category specimens, the resin was reinforced with graphene nanoplatelets. GNPs were selected, as an effective reinforcing agent, due to their excellent mechanical properties and their significantly lower cost when compared to other forms of nanocarbons, such as carbon-nanotubes, multi-walled carbon-nanotubes, and nanocarbon fibers.

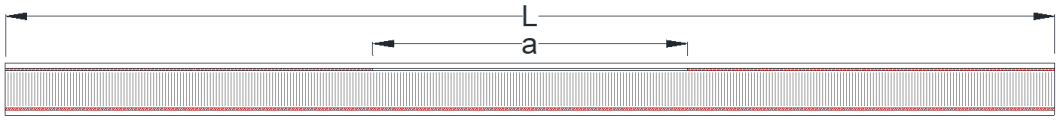

Figure 6-2. Schematic of the delaminated specimen

In order to investigate the effects of GNPs on the buckling response of 3DFMLs, four different weight percentages (wt%) of GNPs are considered (i.e., 0, 0.5, 1 and 2 wt%).

Moreover, the effects of delamination length on the buckling capacity of 3DFML are also investigated through 3DFMLs hosting a delamination length (a), with four different length (L) ratios (i.e., a/L = 0, 0.3, 0.5 and 0.7; See Figure 6-2 and Table 6-1).

Table 6-1. Specimen Details

Specimen ID	GNP wt%	Delamination Length Ratio (a/L)
3DFML-4-0	0	0, 0.3, 0.5, 0.7
3DFML-4-0.5	0.5	0, 0.3, 0.5, 0.7
3DFML-4-1	1	0, 0.3, 0.5, 0.7
3DFML-4-2	2	0, 0.3, 0.5, 0.7

In addition, a finite element (FE) model is developed, using the commercial FE software ABAQUS/CAE, to predict the buckling response of all aforementioned GNP-based 3DFML specimens.

6.4 Experimental Investigation

6.4.1 Materials

As stated, the FML specimens used in this investigation were formed by a 3D E-glass fabric (3DFGF) and magnesium alloy sheets. AZ31B magnesium sheets of 0.5 mm thickness were acquired through the MetalMart International (Commerce, CA). Moreover, the 4 mm thick 3D E-glass fabric was supplied by China Beihai Fiberglass Co. Ltd. (Jiujiang City, China). In order to enhance the overall mechanical properties of the 3DFGF, the hollow cores of fabric were filled with an 8-lb density urethane foam supplied by the US Composites (West Palm Beach, FL 3340). Furthermore, the resin used for this research was Araldite LY 654 (Bisphenol-A epoxy resin), along with Aradur 2954 (cycloaliphatic polyamine) hardener, supplied by the Hunstman Co. (West point, GA). The GNP nanoparticles were obtained from XG Science (Lansing, MI), with average thickness, t, of 7 nm and average particle diameter, D, of 25 μm, Figure 6-3 (a) and (b) depict the SEM

image of a few GNP nanoparticles, and schematic of an idealized GNP particle, respectively.

(a) (b)

Figure 6-3. GNP nanoparticle (a) SEM image; (b) schematic of the idealized GNP (Ahmadi-Moghadam and Taheri 2014)

6.4.2 Specimen Preparation

Prior the fabrication of GNP-3DFML, the GNP particles were thoroughly mixed with the resin using a mechanical stirrer operated at 1000 rpm for 15 minutes. Through this study, three different GNP weight percentages were considered (i.e. 0.5%, 1% and 2%). Afterwards, the GNP-resin slurry was passed through a three-roll mill (Torrey Hill Technology, San Diego, CA) to disperse the GNP particles. Subsequently, the GNP-resin was mixed with the Aradur 2954 hardener and degassed in a vacuum chamber for 30 minutes.

The specimens in this research were consisted of one layer of the 3DFGF, sandwiched within two layers of magnesium sheets. In order to create a biased delamination region within each specimen, a piece of 0.05 mm thick Teflon was put at the interface of magnesium sheet and 3DFGF, running along the entire width of each specimen. The fabrication of GNP-3DFML is a two-step process. The first step entails fabrication of 3DFGF and filling the hollow core of fabric with the foam. The detailed fabrication process of the 3DFGF can be found in (Asaee, Shadlou et al. 2015). Subsequently, the GNP-3DFML panels were assembled by sandwiching the foam filled 3DFGF in between the two

magnesium alloy sheets, adhered by the GNP-reinforced resin. Note that the bonding surfaces of magnesium sheets were first sandblasted, cleaned with compressed air, and then wiped with acetone and let air-dry. The panels were vacuum bagged to remove the excess air and resin, and to achieve an optimal interface bond. They were then cured in an oven for two hours at 60°C, and then for eight hours at 120°C.

6.4.3 Test Procedure

The buckling tests were conducted using an Instron servo-hydraulic test machine (model 8500+) equipped with a 25 kN load-cell. Variations in the applied load and actuator's displacement data was collected using a data-acquisition system and stored in a PC. An adjustable fixture, as shown in Figure 6-4, was designed to hold variable thicknesses specimens. Each specimen was clamped at both ends in the fixture. Furthermore, two extensometers (a laser extensometer on one side and a mechanical strain extensometer on the other side) were placed on each specimen to ensure that the specimen did not undergo bending during the test. A total of 48 specimens were tested as per ASTM-C364, with the displacement rate of approximately 0.5 mm/min.

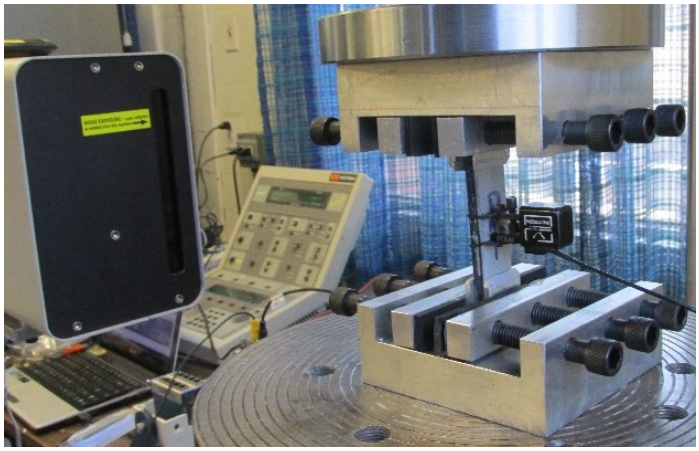

Figure 6-4. Specimen holding fixture used in the buckling tests

6.4.4 Results and Discussion

As mentioned earlier, in order to investigate the effects of the two main selected parameters (i.e., GNP wt% content and delamination length) on the buckling response of 3DFML specimens, a total of 48 specimens were subjected to a compressive loading condition. Load and displacement data versus time, obtained through the loading machine and transducers were recorded for each specimen. The critical load, buckling load, maximum displacement and delamination growth work were then extracted from the data and compared.

6.4.4.1 Influence of Delamination Length and wt% Inclusion of GNP

The load-displacement curves of the four groups of specimens (i.e., with delaminated length ratios of a/L = 0, 0.3, 0.5 and 0.7) are illustrated in Figure 6-5. The variations in load-displacement response of the 3DFML specimens are almost similar (i.e., having a linear trend, followed by the onset of instability). As briefly mentioned earlier, due to the unique fiber arrangement of the 3DFGF, no delamination was observed to occur within the fabric. However, delamination could occur at the interface of metal to 3DFGF. This leads to a local buckling mode, because of near-surface proximity of the delamination and the thick composite core. In all cases, delamination initiated and grew prior to the onset of buckling. The sudden drop in the load-displacement paths, which has been identified a black circle in the following graphs, corresponds to the initiation of a delamination. Therefore, the load corresponding to that point is referred to as the critical load. The variation of the critical load as a function of wt% of GNP are illustrated in Figure 6-6 (a).

The results indicate that the increase in initial delamination length affects the critical load. The critical load of 3DFMLs with an initial delamination ratio of 0.3 is half of that recorded

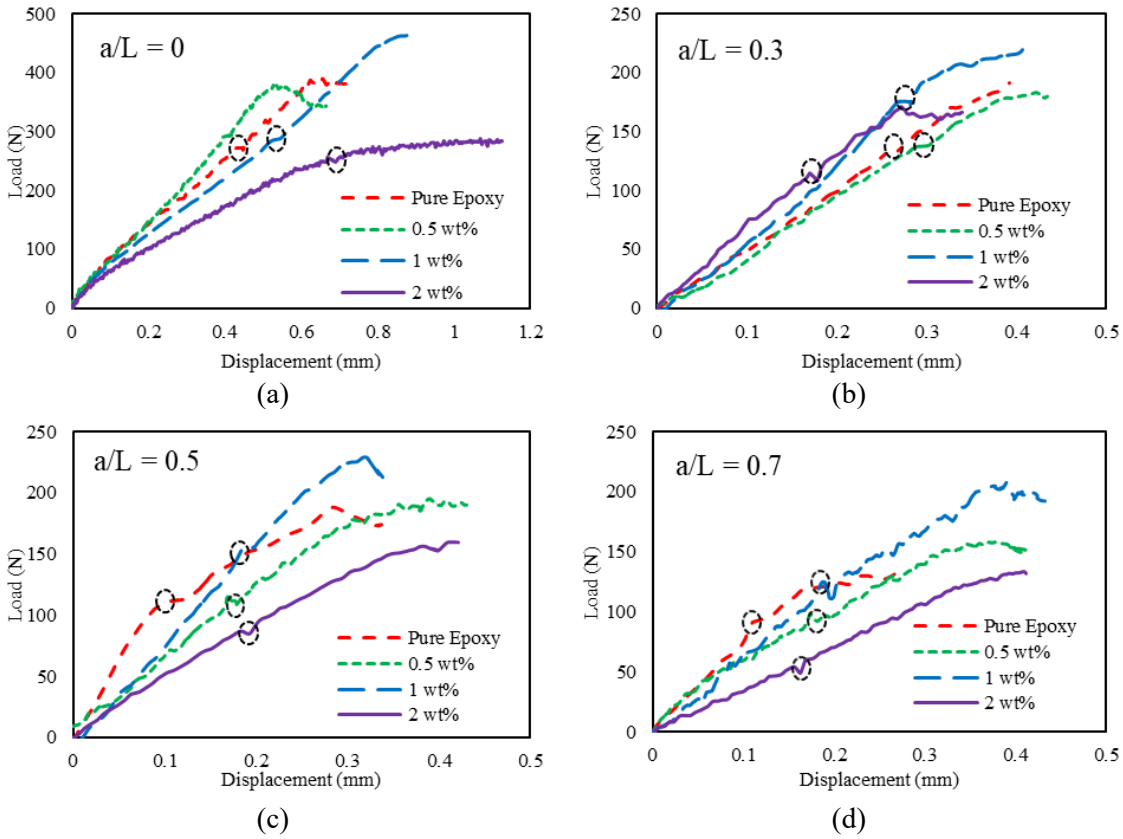

Figure 6-5. Influence of delamination length as a function of GNP wt% content on the buckling responses of 3DFML; (a) a/L=0, (b) a/L=0.3, (c) a/L=0.5 and (d) a/L=0.7

for the intact specimens. However, when the delamination ratio increased from 0.3 to 0.7, the reduction in buckling capacity was 20%. It should be noted that the addition of 0.5 wt% of GNP to the neat epoxy did not change the critical capacity of 3DFMLs by a considerable margin. In comparison, the addition of 1 wt% of GNP to the resin increased the critical capacity by 20%, especially in the delaminated cases. In contrast, when the GNP content was increased to 2 wt%, it adversely impacted the critical load of 3DFMLs by reducing it significantly. This is believed to have been caused due to the agglomeration of GNP particles. It should be noted that the trend noted here (that is, the improvement gained in mechanical properties as a result of addition of nanoparticles) up to a certain content (or loading, a terminology often used), and the potential degradation of properties, (as a result

of addition of higher nanoparticle loadings) has been observed by several investigators (for instance, see references (Gojny, Wichmann et al. 2005, Shokrieh, Ghoreishi et al. 2014, Sun, Fan et al. 2015). Moreover, similar trend has also been observed in the case of inclusion of microparticles in various resins (see for instance references (Lv, Sun et al. 2011) and (Taheri 1997)).

The results indicate that the addition of 0.5 wt% of GNP to the epoxy adhesive could not enhance the buckling load capacity of 3DFML in the case of a/L = 0 and 0.3. However, in the two other cases (i.e., a/L = 0.5 and 0.7), the buckling capacity increased by 15% and 25%, respectively. From the perspective of ductility, it can be seen that virtually in all cases, the inclusion of GNP improved specimens' ductility, regardless of the delamination length. Moreover, the maximum gain was obtained at 1 wt% GNP inclusion.

In the same vein, specimens with 1 wt% GNP exhibited the greatest buckling capacity among all specimens with delamination lengths of a/L = 0, 0.5 and 0.7. In the case of specimens with a/L = 0.3, the buckling capacities of all groups of specimens were virtually identical. In summary, it is concluded that the optimal amount of GNP that would yield the maximum buckling capacity of the 3DFML would be at 1 wt%. This is because in most cases, 2 wt% GNP contents actually decreased the buckling capacity of 3DFML. This is postulated to have been caused, most probably, due to the agglomeration of GNP particles at that wt% content.

Figure 6-6 (b) depicts the variation in the buckling capacity as a function of wt% content of GNP of specimens with various delamination lengths. As discussed earlier, the optimal effect of 1 wt% GNP content on the buckling capacity is quite apparent. Moreover, the buckling capacity of 3DFML specimens with short delamination length are almost

identical, regardless of the GNP content. However, the buckling capacity of the specimens hosting larger delamination length increased slightly as the GNP content increased.

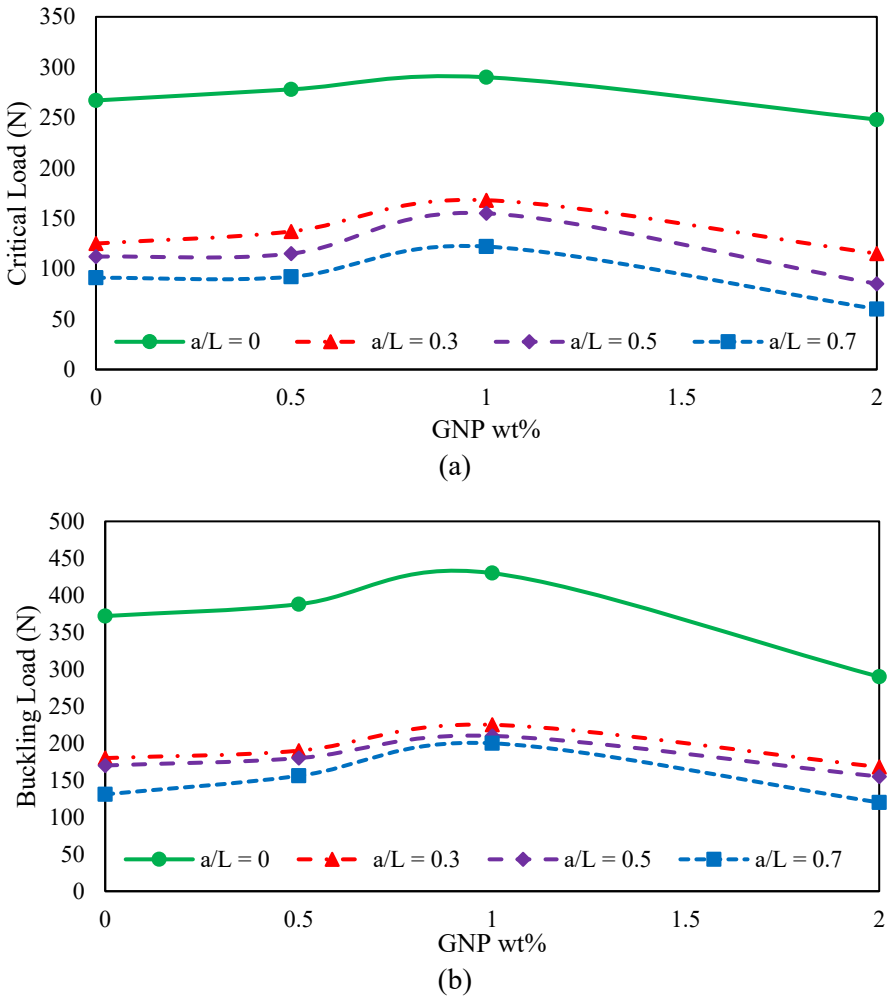

Figure 6-6. Variation in the (a) delamination growth load and (b) buckling capacity as a function of GNP wt% content of 3DFML specimens hosting a delamination with various lengths

6.4.4.2 Influence of Delamination Length

Figure 6-7 presents the variations in buckling capacity as a function of the delamination length in specimens fabricated with different weight percentages of GNP particles. The results indicate that as expected, the mere presence of a delamination within specimens would decrease the buckling capacity of 3DFMLs by as much as 50%. However, an

increase in the delamination length would not affect the outcome by any significant margin. The results also indicate that 3DFML specimens with 1 wt% GNP produced the largest buckling capacity among all specimens.

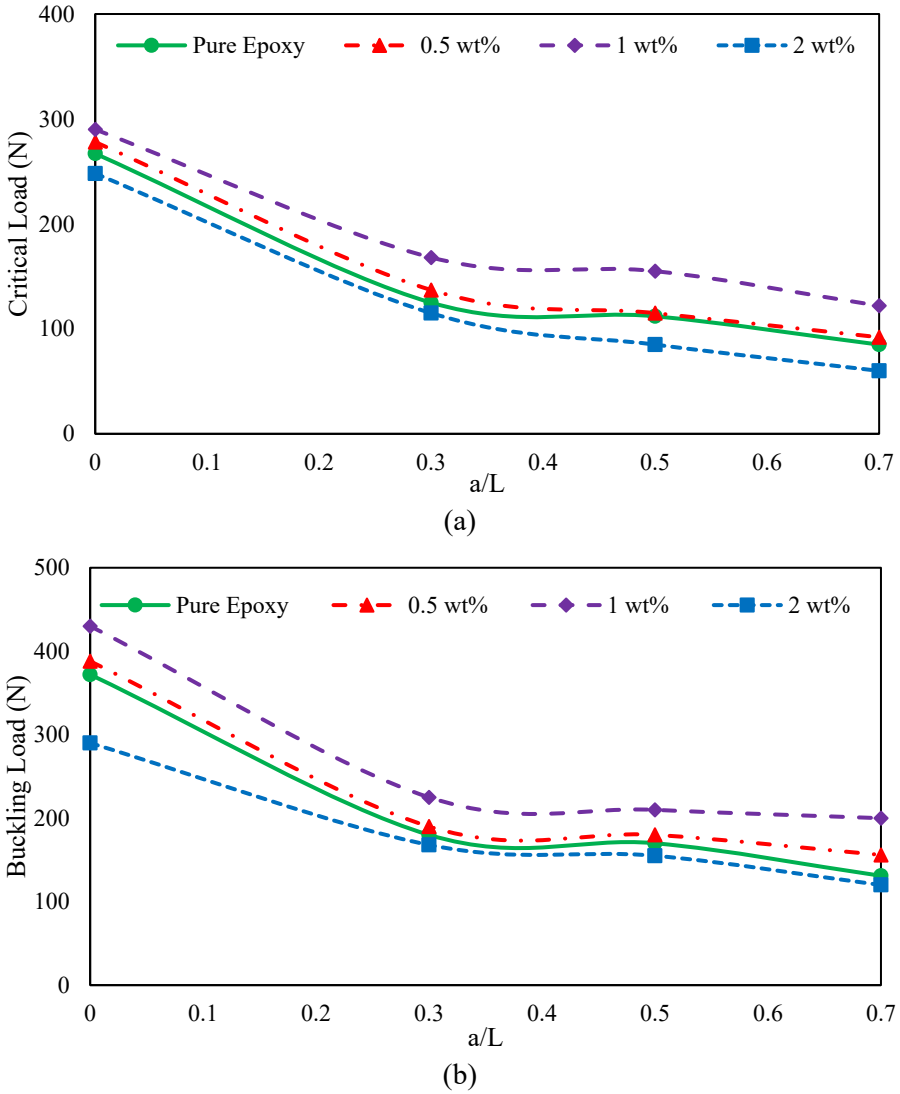

Figure 6-7. Variation in the (a) critical load and (b) buckling load as a function of delamination length for the specimens with various wt% contents of GNP

Figure 6-8 illustrates the variation in the fracture work for all four groups of 3DFMLs as a function of the delamination length. The fracture work is obtained by evaluating the area under the load-displacement curves up to the load at which debonding of metallic sheet

from the 3D fiberglass core of the 3DFMLs was initiated. As can be seen, the work of the intact 3DFML specimens formed by 1 wt% GNP is almost twice the work values exhibited by the other specimens. Moreover, as expected, the presence of delamination decreased the fracture work in all groups of specimens tested by a significant margin, regardless of the wt% inclusion of GNP. However, it appears that the presence of higher wt% of GNP could make a positive contribution at larger delamination lengths.

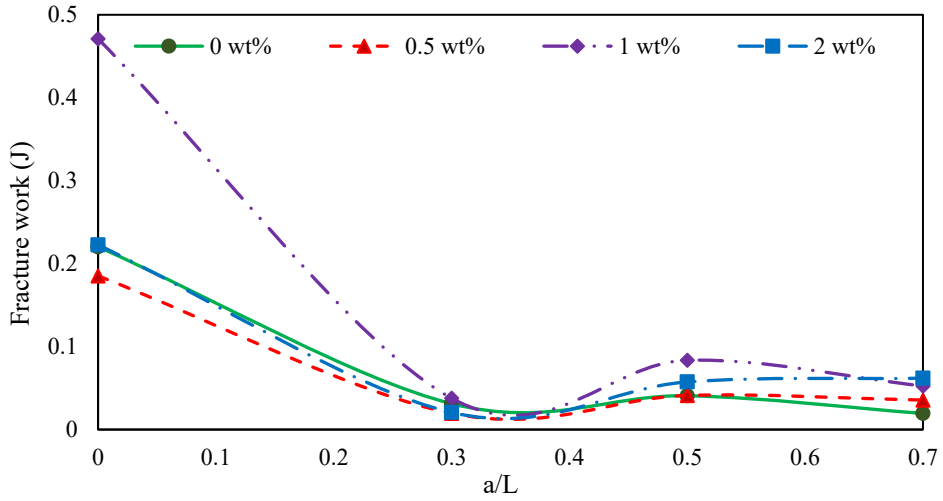

Figure 6-8. Variation of the fracture work as a function of delamination length for specimens with various wt% contents of GNP

It can, therefore, be concluded that inclusion of 0.5 and 1 wt% GNP particles within the resin could enhance the performance of delaminated 3DFMLs by suppressing the growth of delamination. This enhancement is apparently increased as the delamination growth is increased.

6.5 Finite Element Simulation

6.5.1 General Modeling Consideration

ABAQUS/CAE commercial FE software was used for simulating the buckling response of the aforementioned 3DFML specimens. Several studies have been conducted on the

numerical analysis of buckling of delaminated FRPs (Lee, Gurdal et al. 1993, Tay, Shen et al. 1999, Kouchakzadeh and Sekine 2000, Gaudenzi, Perugini et al. 2001, Camanho, Davila et al. 2003, Cappello and Tumino 2006, Liu, Hou et al. 2011, Ovesy, Mooneghi et al. 2015). However, as noted in the previous works of the authors, there is a notable lack of research in assessing the capability of numerical methods for simulating the response of 3D fiber-reinforced composite-based FMLs. As a result, the authors examined the viability of the finite-element framework for predicting the response of the 3DFMLs, subject to impact loading, using the commercial finite-element code ABAQUS (Asaee, Shadlou et al. 2015, Asaee and Taheri 2016). Good agreement between the experimental and computation results was obtained in their investigations.

In the present study, the previous modelling framework is extended to simulate the buckling and post-buckling responses of 3DFML. This study aims at evaluating the extent of capability of finite element method in predicting the response of such complex hybrid structural materials under compressive loading condition. Due to symmetry in the geometry, only one-half of the specimens was modeled. The analysis was conducted by applying displacement to the appropriate nodes, as was the case in the actual experiments. Note that the ply orientations in the 3D fabric are bi-axial, thus symmetric about the mid-span of the geometry. It should be noted that although there exists a through-thickness symmetry plane, nevertheless, since the buckling response may be asymmetric, one cannot take advantage of that symmetry plane. The simulation was done by discretizing the 3D system as its equivalent 2D plane strain system. All four constituents of the system (i.e., the magnesium alloy sheets, 3DFG fabric consisting of fiberglass plies and its foam core,

and adhesive layers), were all modeled individually. The model details are shown in Figure 6-9.

Table 6-2. Mechanical Properties of E-glass fiber-reinforced composite and foam evaluated based on ASTM standards (Nagaraj 2005)

Orthotropic properties of glass fiber-reinforced Composite	E_1 = 37 GPa, E_2 = 8.5 GPa, ν_{12} = 0.254, G_{12} = 4.7 GPa,
Mechanical properties of foam	E (Compressive Elastic Modulus) = 435 MPa, S (Compressive Strength) = 7.0 MPpa

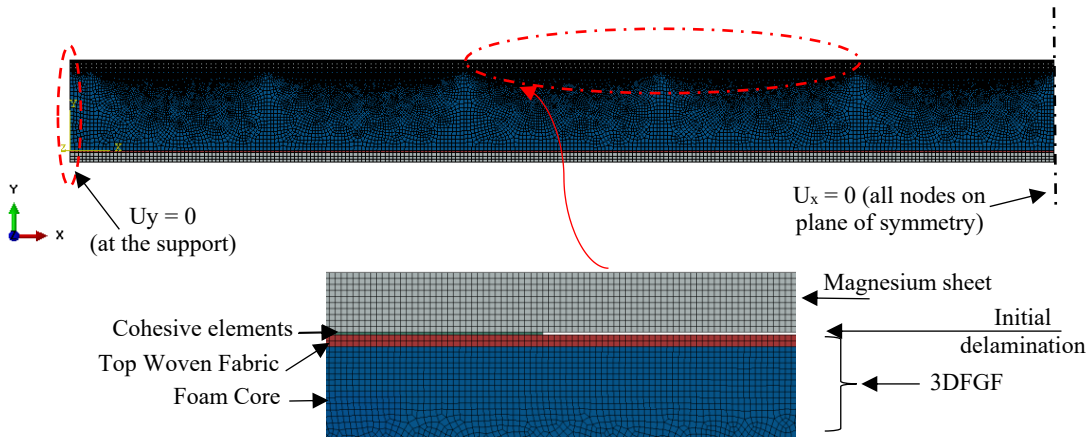

Figure 6-9. Details of the FE model, including the boundary conditions

The magnesium alloy sheets were modeled as an elastic-plastic material, using the piecewise plasticity model in ABAQUS. The 3DFGF fabric was simulated in three segments, the top woven fabrics, the foam core and the bottom woven fabric. The woven fabrics were modeled as an orthotropic elastic material. The core part filled with the foam was simulated as a crushable foam. The properties of the crushable foam was obtained by conducting a set of compression tests on square blocks of foam injected 3DFGF, performed as per ASTM standard (ASTM-C365 2010). In other words, the combined foam and glass fiber pillars were considered to act in an aggregate and homogenous manner, thus could be effectively simulated as a crushable foam with the equivalent properties evaluated

experimentally. For the sake of space and brevity, the reader is directed to our previous study (Asaee, Shadlou et al. 2015) for further details of the approach used to simulate the response of the 3DFGF fabric. The magnesium layers and two parts of 3DFGFs were meshed using CPE4R element of ABAQUS, which is a 4-node bilinear plane strain quadrilateral element with reduced integration. A surface-to-surface contact was defined to eliminate the inter-penetration of various segments of the model.

6.5.2 CZM Modeling Consideration

The cohesive zone modelling technique (CZM) was used to simulate the behavior of the adhesive layer (i.e., the epoxy resin containing GNPs). It should be noted that ABAQUS uses a traction-separation law in conjunction with its cohesive element; specifically, a combined linear-exponential traction-separation law is used. In other words, the damage and its propagation are simulated based on the material properties provided for the cohesive elements, as well as the interaction properties used in modelling the cohesive surfaces. It should be noted that the geometrically nonlinear behavior of composites affects the delamination crack propagation and nonlinear fracture process. Liu et al. (Liu, Gu et al. 2015) conducted a study to explore the influence of cohesive zone modelling parameters (including the cohesive mode's shapes, cohesive strength and cohesive element's thickness), on the post-buckling and delamination response of composites under compression loading. It was shown that the shape of the curves used in depicting the cohesion of materials did not have a considerable effect on the response. They, however, demonstrated the faster rate of numerical convergence that could be attained when the exponential CZM was used in modelling the cohesive-zone, in contrast to the bilinear CZM.

As mentioned earlier, a combined linear-exponential traction-separation law was used in the cohesive element. This model assumes a linear elastic behavior at the interface, up to the onset of a damage (i.e., at the onset of separation of the cohesive surfaces), followed by an exponentially decaying damage evolution regime. The linear elastic behavior is defined by an elastic constitutive matrix, represented by equation (6.1), which relates the nominal stresses to the nominal strains along the interface.

$$t = \begin{Bmatrix} t_n \\ t_s \\ t_t \end{Bmatrix} = \begin{bmatrix} k_{nn} & k_{ns} & k_{nt} \\ k_{ns} & k_{ss} & k_{st} \\ k_{nt} & k_{st} & k_{tt} \end{bmatrix} \begin{Bmatrix} \varepsilon_n \\ \varepsilon_s \\ \varepsilon_t \end{Bmatrix} = K\varepsilon, \quad K = \frac{E}{t_0} \tag{6.1}$$

$$\varepsilon_n = \frac{\delta_n}{t_0}, \varepsilon_s = \frac{\delta_s}{t_0}, \varepsilon_t = \frac{\delta_t}{t_0}$$

In the above equation, t_n, t_s and t_t are the traction stresses in the normal and the first and second shear directions, respectively; δ_n, δ_s, δ_t, t_0, E and K are the corresponding separation counterparts, initial thickness of cohesive element (i.e., bond or interface layer thickness), and the elastic modulus and stiffness matrix of the interface material, respectively.

When the stresses and/or strains reach to their maximum (or limiting) values (that is, after the linear traction-separation region of the curve has been completed), the damage is presumed to initiate at that stage. Several damage initiation criteria exist; the one implemented in this study is the maximum nominal stress criterion. The criterion postulates that the process of material degradation would be initiated when the maximum stresses meet the following mathematical equality (6.2).

$$\max\left\{\frac{\langle t_n \rangle}{t_n^{max}}, \frac{t_s}{t_s^{max}}, \frac{t_t}{t_t^{max}}\right\} = 1 \tag{6.2}$$

where $\langle t_n \rangle = 0.5(t_n + |t_n|)$

Upon the onset of a damage, the material properties will be degraded according to the selected damage evolution law. According to the damage evolution law selected in this study, the stiffness of material is degraded in an exponential fashion. It should be noted that in general, three essential parameters (namely, the stiffness, strength and the fracture energy) would affect and control the damage initiation and evolution of the cohesive element. In this study, the damage evolution law is defined based on the variation of the fracture energy. In other words, the fracture is assumed to be dissipated exponentially as the damage progresses. The fracture energy, which is equivalent to the area under the traction-separation curve (obtained experimentally), is inputted as a material property. It should be noted that the stiffness degradation is applied by means of a damage index with softening behavior, as shown in Figure 6-10 and mathematically described by equation (6.4).

$$t_n = \begin{cases} (1-D)\bar{t}_n, & \text{when } \bar{t}_n \geq 0 \\ \bar{t}_n & \text{otherwise} \end{cases} \tag{6.3}$$

$$t_s = (1-D)\bar{t}_s$$

$$t_t = (1-D)\bar{t}_t$$

in which, $\bar{t}_n, \bar{t}_s$ and $\bar{t}_t$ are the predicted traction stresses without considering the damage effects.

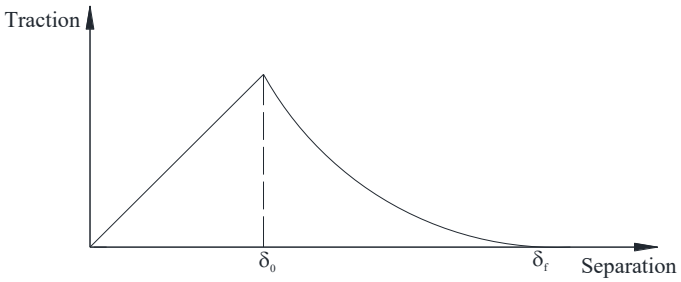

Figure 6-10. Schematic representation of the CZM traction-separation model used in this study

The value of damage index varies within the range of zero to one. The index value represents the damage evolution in the material. When the value reaches one, the element would be deleted. The damage index affects the traction stresses according to the following equations.

$$D = \int_{\delta_m^0}^{\delta_m^f} \frac{T_{eff}\, d\delta}{G^c - G_0} \tag{6.4}$$

where T_{eff} is the effective traction, δ is the displacement, and G_o and G^C are the initial and critical strain energy release rates (or fracture toughness), respectively.

Moreover, evolution of damage due to the combined effect of the normal and shear stresses across the interface follows the model suggested by Benzeggagh-Kenane (BK) (Benzeggagh and Kenane 1996), mathematically represented by equation (6.5).

$$G_n^C + (G_s^C - G_n^C)\left\{\frac{G_s + G_t}{G_s + G_n}\right\}^{\eta} = G_n + G_s + G_t \tag{6.5}$$

where *n*, *s* and *t* subscripts refer to values of the strain energy release rate corresponding to normal, tangential and shear directions, while superscript *C* signifies the critical value, and η is a parameter obtained experimentally.

Aboura (Aboura 1993) conducted a study on the woven composites to verify the generality of Benzeggagh-Kenane criterion. It was shown that the value of parameter η would depend on the resin type, but would be independent of the rate of loading. They suggested values of $\eta = 2$ for brittle resins, or $\eta = 3$ for ductile resins. In this study, the value of $\eta = 2$ was used due to the brittle nature of the epoxy resin. Moreover, the BK mixed mode model is

known to be suitable for the cases that the fracture energies along the first and second directions are similar.

Table 6-3. Mechanical properties of adhesive for various wt% content of GNPs (Chatterjee, Nafezarefi et al. 2012, Ahmadi-Moghadam 2015)

Mechanical Properties	Neat Epoxy	0.5 wt%	1 wt%	2 wt%
E (Gpa)	2.66	2.80	2.88	2.86
K_{IC} (Pa.$\sqrt{m}$)	0.77	0.96	1.06	1.30
K_{IIC} (Pa.$\sqrt{m}$)	1.71	1.68	1.61	1.50

To model the adhesive layer (or the cohesive zone), COH2D4 element of ABAQUS was used. COH2D4 is a two-dimensional 4-node cohesive element. The properties of GNP-reinforced epoxy, including its elastic modulus, strength and fracture toughness values were obtained experimentally, as reported in Table 6-3 based on our previous works (Ahmadi-Moghadam 2015, Ahmadi-Moghadam, Sharafimasooleh et al. 2015, Ahmadi-Moghadam and Taheri 2015). Moreover, the element deletion option of ABAQUS was used to investigate the growth of delamination located within the interface of magnesium sheet and 3DFGF. A mesh convergence study was carried out in order to establish the optimal mesh by varying the mesh density. As for establishing the thickness of the CZM, Liu et al. (Liu, Gu et al. 2015) did a comparative study on simulating the load-strain and load-deflection curves of laminates by using the exponential CZM, using bond (cohesive element) thicknesses of 0 , 0.1 and 0.5 mm. It was shown that the finite-thicknesses and zero-thickness cohesive elements lead to basically consistent results. Therefore, in this study, the actual physical thickness value of 0.1 mm was used as the thickness of CZM.

6.5.3 Stability Analysis Scheme

A nonlinear stability analysis was performed to simulate the response of the 3DFML specimens, including their buckling response. It should be noted that usually a sinusoidal imperfection, usually matching to the first fundamental mode of the structure is used to initiate the instability in such numerical analysis (see, for instance (Remmers and De Borst 2001)). However, our extensive work in the area of stability modelling and analysis has shown that this commonly used scheme is not the best means for conducting such analysis, because the bias in the prescribed shape (i.e., in a sin or a cosine forms) will promote buckling modes favoring the prescribed biased shapes, which would not be similar to the real situation. In real situations, the imperfections are seldom in the form of a sine curve, and are usually in a random and unbiased form. Therefore, in this study we modeled the imperfection by imposing a series of sinusoidal (hence, relatively unbiased) imperfections to the system, with amplitudes equal to 1% of the specimen's thickness. The imposed imperfection is schematically shown in Figure 6-11. This scheme minimizes the influence of imperfection in promoting a biased buckling mode. The following mathematical expression describe the imposed imperfection.

$$\delta_0 = \begin{cases} 0.01t\left(\sin\dfrac{\pi x_i}{L}\right) & i = 2,4,6 \\ -0.01t\left(\sin\dfrac{\pi x_i}{L}\right) & i = 1,3,5 \end{cases} \tag{6.6}$$

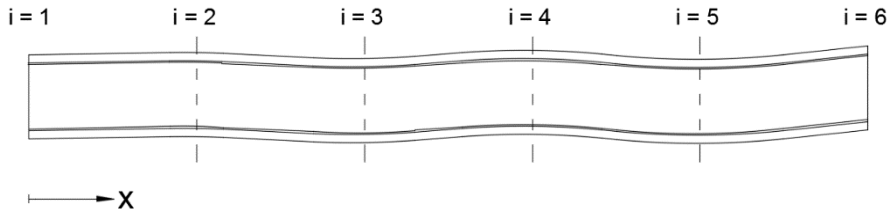

Figure 6-11. The initial imperfection applied to various segments of the FE model ***(the scale is exaggerated for better visual)***

6.5.4 Results and Discussion

The FE prediction of the variation of displacement as a function of the applied load of the groups of specimens with various wt% GNP contents are shown in Figure 6-12. Subsequently, the predicted buckling capacities are compared to the experimental values in Figure 6-13. As seen, good agreements are obtained between the predicted results and experimental values. However, the margin of error for groups of specimens with of 1 and 2 wt% GNP contents are greater than those associated to the other two groups.

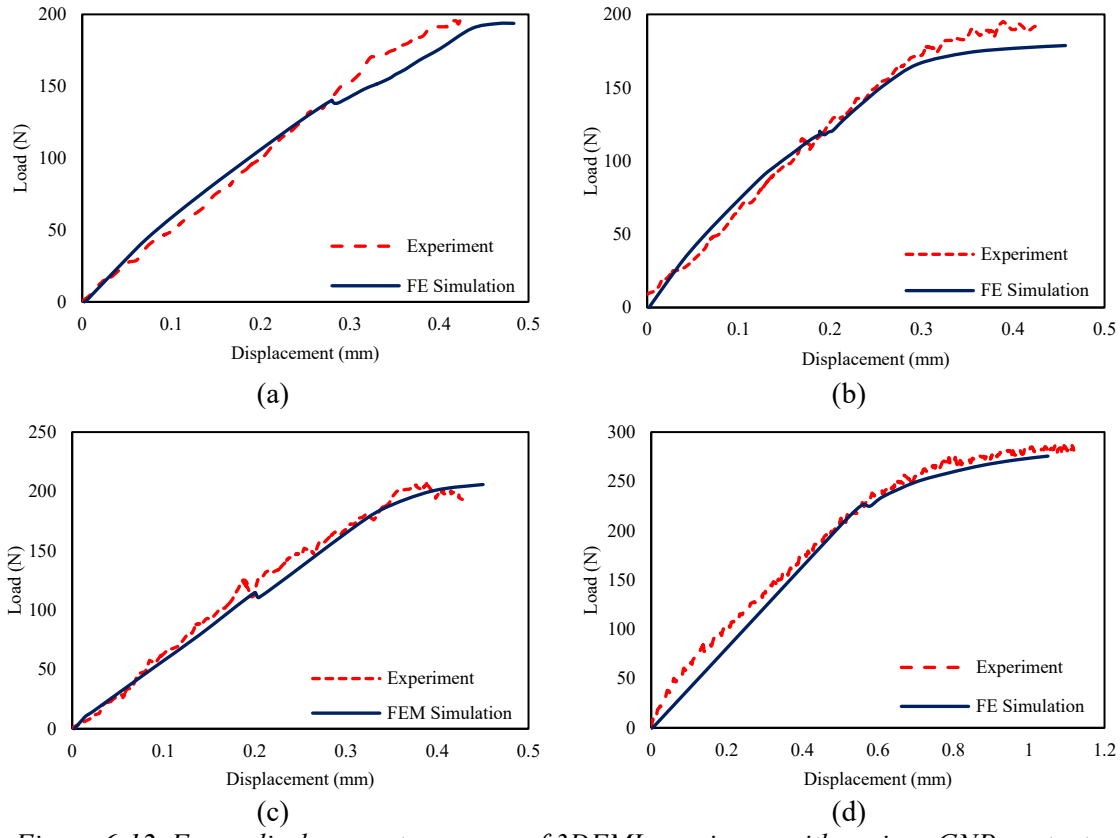

Figure 6-12. Force-displacement response of 3DFML specimens with various GNP contents, hosting a delamination with various lengths: (a) with 0 wt% GNP and a/L = 0.3, (b) with 0.5 wt% GNP and a/L = 0.5, (c) with 1 wt% GNP and a/L = 0.7 and (d) with 2 wt% GNP and a/L = 0

Furthermore, Figure 6-14 represents a typical damage profile predicted by the FE analysis in comparison to the experimentally observed one. From the results, it is concluded that

the proposed modelling framework can accurately predict the buckling response of GNP-reinforced 3DFMLs. In addition, Figure 6-15 illustrates the delamination growth and the ensuing buckling mode of 3DFMLs as predicted by the FEM analysis.

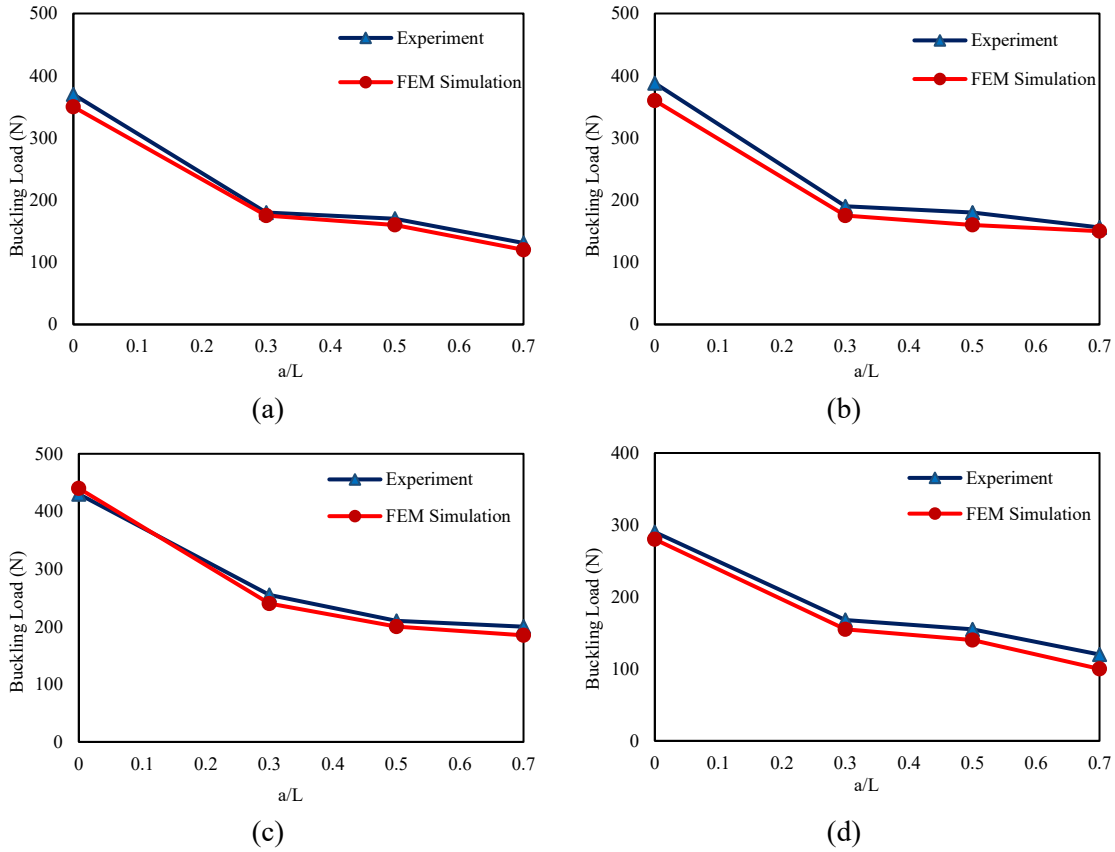

Figure 6-13. FE predictions of buckling capacity as a function of delamination length with the experimental results for 3DFML specimens containing various wt% GNPs (a) 0 wt%, (b) 0.5 wt%, (c) 1 wt% and (d) 2 wt%

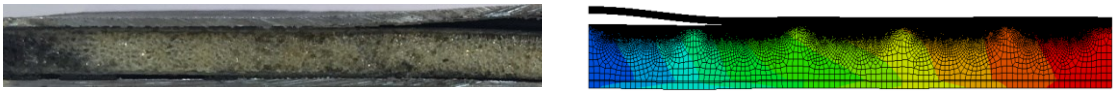

Figure 6-14. Comparison of the buckling failure profile obtained through the FE-simulation (left) and the experimentally observed(right)

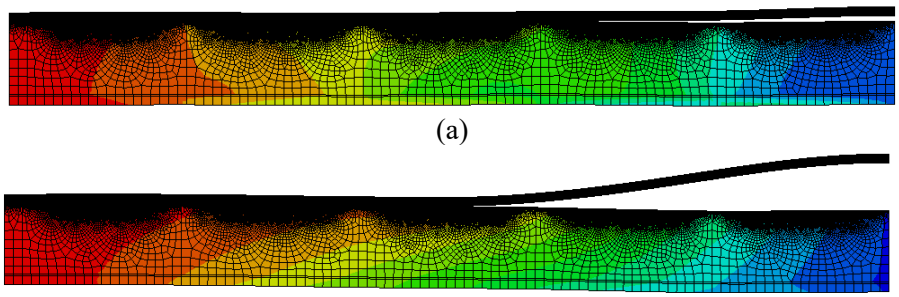

(a)

(b)

Figure 6-15. FEM prediction of (a) delamination growth and (b) buckling response of 3DFMLs due to compressive load.

6.6 Conclusion

The delamination buckling response of GNP-reinforced 3DFML has been investigated experimentally and numerically. As mentioned earlier, the main purpose behind the inclusion of graphene nanoplatelets within the adhesive/resin was to investigate whether the growth of a delamination developed on the metallic/FRP interface could be mitigated, and thus improving the stability of such 3DFMLs under compressive loading conditions. Therefore, four different weight percent contents of GNPs within the resin used to bond the metallic sheets to 3D glass fabric (i.e. 0, 0.5, 1 and 2 wt%) were considered. Comparison of the results revealed that there exists an optimal GNP wt% content by which the buckling capacity of the 3DFMLs could be significantly improved. In other words, the optimal GNP content of 1 wt% increased the buckling capacity of the 3DFML by approximately 50%. In comparison, when 2 wt% GNP content was considered, the buckling capacity of the 3DFML became actually less than that of the 3DFML formed by the neat resin. This degradation is attributed to the agglomeration of GNP particles within the resin.

Furthermore, the influence of length of a delamination that could develop within the metal/FRP interfaces in such 3DFMLs was also found to significantly affect their stability.

To examine the extent of the effect, four different delamination lengths (or more specifically, different delamination length ratios, that is: a/L = 0, 0.3, 0.5 and 0.7) were considered. The results indicated that, as expected, the presence of a delamination could significantly affect the buckling capacity of such 3DFMLs. While the reduction in the buckling capacity of the specimens formed by either the neat resin or those with various GNP contents was not very significant at relatively larger delamination length (i.e., a/L>0.3). In other words, the buckling capacity was significantly reduced (by as much as 50%) in the presence of a delamination, regardless of the wt% GNP content. Nonetheless, some moderate increases in the buckling capacity were noted in the 3DFML specimens that were formed with the resin that contained GNP particles.

In summary, it is concluded that the inclusion of a proper amount of the relatively inexpensive GNP particles within the resin used to adhere 3DFML's constituents could result in a significant improvement in the stability response of such FMLs when hosting a delamination.

Another significant contribution of the present study is the demonstration of the integrity of a finite element framework that was developed to simulate the performance of such 3DFMLs. ABAQUS/CAE was used in the framework, along with the use of cohesive zone modelling technique (CZM) for tracing the growth of the delamination present at the interface of metal and FRP of the 3DFGF. It was demonstrated that the adopted FE framework could accurately predict the buckling load and failure modes of 3DFMLs. The framework can therefore be utilized to effectively optimize the performance of such 3DFML under various loading conditions.

6.7 Acknowledgement

This financial support received through the National Science and Engineering Research Council of Canada (NSERC) in support of this study is gratefully appreciated. The Killam scholarship awarded to the first author is also gratefully appreciated.

6.8 References

Aboura, Z. (1993). Etude du processus de délaminage mode I, mode II et mode mixte(I+ II) de matériaux composites à renforts tissés à différentes vitesses de sollicitation.

Ahmadi-Moghadam, B. (2015). Development of A Highly Resilient Graphene Nanoplatelet Resin/Adhesive, Dalhousie University.

Ahmadi-Moghadam, B., M. Sharafimasooleh, S. Shadlou and F. Taheri (2015). "Effect of functionalization of graphene nanoplatelets on the mechanical response of graphene/epoxy composites." Materials & Design 66, Part A: 142-149.

Ahmadi-Moghadam, B. and F. Taheri (2014). "Effect of processing parameters on the structure and multi-functional performance of epoxy/GNP-nanocomposites." Journal of Materials Science 49(18): 6180-6190.

Ahmadi-Moghadam, B. and F. Taheri (2015). "Influence of graphene nanoplatelets on modes I, II and III interlaminar fracture toughness of fiber-reinforced polymer composites." Engineering Fracture Mechanics 143: 97-107.

Al-Azzawi, A., J. McCrory, L. Kawashita, C. Featherston, R. Pullin and K. Holford Delamination Characteristics of Splices and Doublers in GLARE Laminates during Buckling. 11th World Congress on Computational Mechanics

Asaee, Z., S. Shadlou and F. Taheri (2015). "Low-velocity impact response of fiberglass/magnesium FMLs with a new 3D fiberglass fabric." Composite Structures 122: 155-165.

Asaee, Z. and F. Taheri (2015). Characterization of the Mechanical and Impact Response of a New-Generation 3D Fiberglass Fabric. American Society of Composites-30th Technical Conference.

Asaee, Z. and F. Taheri (2016). "Experimental and numerical investigation into the influence of stacking sequence on the low-velocity impact response of new 3D FMLs." Composite Structures 140: 136-146.

ASTM-C365 (2010). Standard test method for flatwise compressive properties of sandwich cores, American Society for Testing and Materials West Conshohocken.

Benzeggagh, M. and M. Kenane (1996). "Measurement of mixed-mode delamination fracture toughness of unidirectional glass/epoxy composites with mixed-mode bending apparatus." Composites science and technology 56(4): 439-449.

Camanho, P. P., C. Davila and M. De Moura (2003). "Numerical simulation of mixed-mode progressive delamination in composite materials." Journal of composite materials 37(16): 1415-1438.

Cappello, F. and D. Tumino (2006). "Numerical analysis of composite plates with multiple delaminations subjected to uniaxial buckling load." Composites science and technology 66(2): 264-272.

Chai, H., C. D. Babcock and W. G. Knauss (1981). "One dimensional modelling of failure in laminated plates by delamination buckling." International Journal of Solids and Structures 17(11): 1069-1083.

Chatterjee, S., F. Nafezarefi, N. H. Tai, L. Schlagenhauf, F. A. Nüesch and B. T. T. Chu (2012). "Size and synergy effects of nanofiller hybrids including graphene nanoplatelets and carbon nanotubes in mechanical properties of epoxy composites." Carbon 50(15): 5380-5386.

Chattopadhyay, A. and H. Gu (1994). "New higher order plate theory in modeling delamination buckling of composite laminates." AIAA journal 32(8): 1709-1716.

Chen, H.-P. (1991). "Shear deformation theory for compressive delamination buckling and growth." AIAA journal 29(5): 813-819.

Esfahani, M., H. Ghasemnejad and P. Barrington (2010). Experimental and numerical buckling analysis of delaminated hybrid composite beam structures. Applied Mechanics and Materials, Trans Tech Publ.

Frizzell, R. M., C. T. McCarthy and M. A. McCarthy (2011). "Simulating damage and delamination in fibre metal laminate joints using a three-dimensional damage model with cohesive elements and damage regularisation." Composites Science and Technology 71(9): 1225-1235.

Gaudenzi, P., P. Perugini and A. Riccio (2001). "Post-buckling behavior of composite panels in the presence of unstable delaminations." Composite Structures 51(3): 301-309.

Gojny, F. H., M. H. Wichmann, B. Fiedler and K. Schulte (2005). "Influence of different carbon nanotubes on the mechanical properties of epoxy matrix composites–a comparative study." Composites Science and Technology 65(15): 2300-2313.

Gong, W., J. Chen and E. A. Patterson (2016). "Buckling and delamination growth behaviour of delaminated composite panels subject to four-point bending." Composite Structures 138: 122-133.

Gu, H. and A. Chattopadhyay (1999). "An experimental investigation of delamination buckling and postbuckling of composite laminates." Composites science and technology 59(6): 903-910.

Hwang, S.-F. and G.-H. Liu (2002). "Experimental study for buckling and postbuckling behaviors of composite laminates with multiple delaminations." Journal of reinforced plastics and composites 21(4): 333-349.

Kachanov, L. (2012). Delamination buckling of composite materials, Springer Science & Business Media.

Kim, H.-J. and C.-S. Hong (1997). "Buckling and postbuckling behavior of composite laminates with a delamination." Composites science and technology 57(5): 557-564.

Kouchakzadeh, M. A. and H. Sekine (2000). "Compressive buckling analysis of rectangular composite laminates containing multiple delaminations." Composite Structures 50(3): 249-255.

Larsson, P.-L. (1991). "On multiple delamination buckling and growth in composite plates." International Journal of Solids and Structures 27(13): 1623-1637.

Lee, J., Z. Gurdal and J. GRIFFIN, OH (1993). "Layer-wise approach for the bifurcation problem in laminated composites with delaminations." AIAA journal 31(2): 331-338.

Liu, P., S. Hou, J. Chu, X. Hu, C. Zhou, Y. Liu, J. Zheng, A. Zhao and L. Yan (2011). "Finite element analysis of postbuckling and delamination of composite laminates using virtual crack closure technique." Composite Structures 93(6): 1549-1560.

Liu, P. F., Z. P. Gu, X. Q. Peng and J. Y. Zheng (2015). "Finite element analysis of the influence of cohesive law parameters on the multiple delamination behaviors of composites under compression." Composite Structures 131: 975-986.

Lv, X. Y., Y. Sun, Z. C. Jiang, Y. H. Zhang and M. W. Di (2011). Mechanical property of nano-particles reinforced epoxy resin composite materials. Advanced Materials Research, Trans Tech Publ.

Nagaraj, M. (2005). "Experimental and computational investigation of FRP-reinforced glulam columns including associated software development [Master of applied science thesis]." Department of Civil and Resource Engineering, Dalhousie University.

Ovesy, H., M. A. Mooneghi and M. Kharazi (2015). "Post-buckling analysis of delaminated composite laminates with multiple through-the-width delaminations using a novel layerwise theory." Thin-Walled Structures 94: 98-106.

Remmers, J. and R. De Borst (2001). "Delamination buckling of fibre–metal laminates." Composites Science and Technology 61(15): 2207-2213.

Remmers, J. J. C. and R. de Borst (2001). "Delamination buckling of fibre–metal laminates." Composites Science and Technology 61(15): 2207-2213.

Sadighi, M., R. Alderliesten and R. Benedictus (2012). "Impact resistance of fiber-metal laminates: a review." International Journal of Impact Engineering 49: 77-90.

Shokrieh, M., S. Ghoreishi, M. Esmkhani and Z. Zhao (2014). "Effects of graphene nanoplatelets and graphene nanosheets on fracture toughness of epoxy nanocomposites." Fatigue & Fracture of Engineering Materials & Structures 37(10): 1116-1123.

Sinmazçelik, T., E. Avcu, M. Ö. Bora and O. Çoban (2011). "A review: Fibre metal laminates, background, bonding types and applied test methods." Materials & Design 32(7): 3671-3685.

Sun, T., H. Fan, Z. Wang, X. Liu and Z. Wu (2015). "Modified nano Fe 2 O 3-epoxy composite with enhanced mechanical properties." Materials & Design 87: 10-16.

Taheri, F. (1997). "Improvement of strength and ductility of adhesively bonded joints by inclusion of SiC whiskers." Journal of Composites, Technology and Research 19(2): 86-92.

Tay, T., F. Shen, K. Lee, A. Scaglione and M. Di Sciuva (1999). "Mesh design in finite element analysis of post-buckled delamination in composite laminates." Composite Structures 47(1): 603-611.

Wang, S., C. M. Harvey, B. Wang and A. Watson (2015). "Post-local buckling-driven delamination in bilayer composite beams." Composite Structures 133: 1058-1066.

Yap, C. W., G. B. Chai, J. Song and S. C. Joshi (2015). "Upper and lower bound buckling load of perfect and delaminated fiber-reinforced composite columns." Composite Structures 122: 376-389.

Chapter 7: A Mechanistic Model Proposed for Assessing the Strength of a Novel 3D Fiberglass Fabric Subjected to Out-of-Plane Compressive Loading

Zohreh Asaee, Meisam Asgari and Farid Taheri

Submitted to Journal of Mechanics of Materials and Structures

Zohreh Asaee is the principal researcher and author of this article. She conducted the research as part of her PhD program. She also collaborated with the second author during the development of the analytical model described within the article. The second author was a postdoctoral fellow within the group. Moreover, she carried out the analysis of results, conducted all numerical simulations, and wrote the draft article, which was subsequently revised and enhanced by her supervisor. All works were done under supervision and guidance of her supervisor, Prof. Farid Taheri.

7.1 Abstract

An analytical model is developed for estimating the strength of 3D fiberglass fabrics (3DFGFs) subjected to an out-of-plane compressive loading. The developed model accounts for the strength of all constituents of the fabric (i.e., the woven fabric layers, fiberglass pillars and foam). The contribution of each constituent on the compressive strength of fabric is investigated. The derivation entails evaluation of an integro-differential equation that models the deformation of the fiberglass pillar within a unit-cell, which cannot be solved analytically, thus, it is solved with the Rayleigh method. In addition, the response of four different configurations of the 3DFGF, subjected to a flatwise compression loading, is investigated experimentally. Finally, a finite element (FE) model is constructed to analyze the compressive response of the panels. The results obtained by the developed model agree well with the FE and experimental results.

Keywords: 3D fiberglass fabrics, numerical analysis, critical load, stability, Rayleigh's method, finite element simulation, compressive loading.

7.2 Introduction

A novel generation of truly three-dimensional fiberglass woven fabric, herein referred to 3D fiberglass fabric (3DFGF), has been recently introduced into the market. The 3DFGF is comprised of two layers of woven bi-directional fiberglass fabrics, knitted together by a series of fiberglass fibers (hereafter referred to pillars or columns). As observed in Figure 7-1, the unique structure of 3DFGF fabric provides a series of hollow cores in between the two woven fabrics. This unique and complex structure of the fabric significantly enhances the resulting mechanical properties in comparison to its conventional 2D counterparts. In other words, the composite made from this 3D fabric offers comparatively more superior bending stiffness and strength, lighter weight, excellent thermal insulation and acoustic damping, as well as a remarkable energy absorption capacity under impact loading (Sadighi and Hosseini 2013). Since 3DFGF is new to the market, a very limited number of studies are available that have investigated the mechanical behavior of 3DFGFs under different loading conditions (Bannister, Braemar et al. 1999, Van Vuure, Pflug et al. 2000, Shyr and Pan 2004, Hosur, Abdullah et al. 2007, Wang, Li et al. 2009, Fan, Zhou et al. 2010, Nji and Li 2010, Fan, Zhao et al. 2013, Karahan, Gul et al. 2013, Yu, Cao et al. 2014, Zhao, Li et al. 2014, Chen, Zheng et al. 2015, Asaee and Taheri 2016). Some examples are the work of Li *et al.* (Li, Zhao et al. 2015), who investigated the effect of thickness of the face sheets on the bending response and failure mechanism of 3DFGF. For this purpose, 3D integrated woven spacer composites with thick face sheets were fabricated using 3D integrated woven technology and VARIM process. The results demonstrated the important influence of face sheets' thickness on the mechanical properties of the composite, by significantly improving

the load-bearing capacity of the 3D composite. Moreover, the damage mechanism observed for the fabric varied in the composite that had a thicker face sheet.

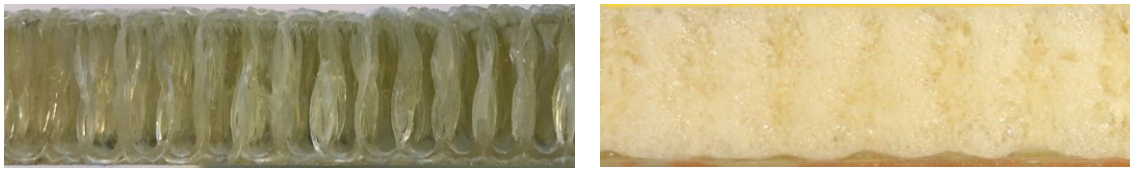

(a) (b)

Figure 7-1. The 3D fiberglass fabric (3DFGF) (a) without foam, (b) with foam.

Sadighi *et al.* (Sadighi and Hosseini 2013) investigated the mechanical properties of three-dimensional woven glass-fiber sandwich composite experimentally and numerically. The three-point and four-point bending, flatwise and edgewise compression and shear tests were conducted on three different core thicknesses in two principal directions. In addition, a 3D finite element (FE) model was developed using ABAQUS FE code. The simulation considered, in detail, both the fabric and the surrounding resin. The detailed model was constructed using CATIA computer-aided design software, and then exported to ABAQUS. The FE results were compared and validated against the experimental results. Good agreement between the FE results and experimental data was obtained.

In another study conducted by Li *et al.* (Kashani, Sadighi et al. 2014), the bending response of 3D integrated woven spacer composites with two different thicknesses were characterized. The tests were conducted at room and cryogenic temperatures. Scanning Electron Microscopy (SEM) micrographs and macro-fracture morphology were employed to study the deformation and failure mechanisms of the composite. Their results revealed that the bending properties at a cryogenic temperature were significantly improved in comparison to the specimens tested at room temperature. Moreover, it was shown that the damage and failure mechanisms were affected by the core thickness and temperature. Three

different failure mechanisms were observed for composites with different core thicknesses when tested at room temperature. At the cryogenic temperature, the failure mechanism was more brittle; however, the interfacial adhesion capacity was improved.

Asaee *et al.* (Asaee and Taheri 2015) investigated the mechanical properties of 3DFGFs, shown in Figure 7-1, for two different thicknesses of the fabric, through the three-point bending and flatwise compressive tests conducted along the two orthogonal directions of the fabric. In order to improve the mechanical response of the fabric, the hollow cores within the fabric were filled with a foam. Their results demonstrated that the 3DFGF with the smaller thickness exhibited higher bending and compressive strengths. Moreover, the mechanical properties of 3DFGFs in bending and compression were increased by approximately twofold when the core cavities were filled with a foam.

To reiterate, one of the significant properties of 3DFGF is their superior energy absorption capacity under an impact loading, which justifies the attention given to this unique and complexly structured fabric (Vaidya, Hosur et al. 2000, Hosur, Abdullah et al. 2004, Shyr and Pan 2004, Vaidya, Vaidya et al. 2008, Karahan, Gül et al. 2012, Asaee, Mohamed et al. 2017). Another notable study is the experimental and numerical investigations conducted by Hosseini *et al.* (Hosseini, Sadighi et al. 2015), on the low-velocity impact performance of a 3D woven hollow core sandwich composites. The impact tests were conducted on the specimens with different thicknesses, at three different energy levels. The impact data and properties of the tested specimens, such as the damage modes, perforation loads, load-time and energy-time curves, contact time, force-displacement and deflection-energy curves were presented. The results indicated that the panel with greater thickness exhibited a higher energy absorption capacity. Moreover, a FE model was developed using

FE package ABAQUS/Explicit, to predict the impact behavior of their tested specimens. The FE results were validated through comparison with the experimental data.

Asaee *et al.* (Asaee, Shadlou et al. 2015, Asaee and Taheri 2016, Asaee, Mohamed et al. 2017) developed a new class of fiber metal laminates (FML), referred to as 3DFML, comprised of the same 3D glass fabric (as shown in Figure 7-1), and magnesium alloy sheets. The low-velocity impact response of the 3DFML was investigated experimentally and also simulated computationally. In order to obtain a more comprehensive understanding of the performance of their FML, the performance of their 3DFML was compared against the conventional FMLs, which are fabricated with layers of woven fabrics instead of the 3D fabric. Moreover, the effect of stacking configuration of the materials was examined on the response of 3DFML. As a result, the responses of four different configurations of FMLs formed by two different thicknesses of 3DFGF and various layers and configurations of metallic sheets were considered. The results were classified and presented as a function of the impact strength, overall weight, and cost. In addition to the experimental investigation, they developed a FE model, using the commercial FE software ABAQUS/Explicit, in order to analyze the impact response of 3DFML. The VUMAT facility of ABAQUS was used to implement an effective three-dimensional failure criterion. The comparison of the FE results with the experimental measurements indicated that the developed FE model could predict the response of their proposed 3DFMLs accurately and reliably.

The main goal of the present study is to gain a deeper understanding of the compressive strength of the 3DFGF, and to assess the contribution of the individual constituents of the fabric in sustaining compressive loads. To do so, in addition to conducting a set of

compression tests on the 3DFGF, an analytical model is developed to analyze the strength of the 3DFG fabric, and to examine the contribution of its constituents.

The experiments are conducted on two different thicknesses of 3DFGF (i.e., 4 mm and 10 mm), and with two different configurations; that is, (i) fabrics with their hollow cores filled with foam, and (ii) fabrics without foam-infill. Moreover, a FE model is developed, using the commercial FE software ABAQUS, to analyze the response of the 3DFGFs subjected to a compressive loading. There are several reasons for developing the modelling approach. Firstly, we wanted to establish whether the approach could be used as a practical and cost-effective means for predicting the response of such complex 3D foam-filled fabrics, especially when more complex geometries are encountered in practical designs. Secondly, it could be used to optimize the performance of the 3D system, when used with metal sheets, to render cost-effective and resilient FMLs. Finally, it enabled us to have a comparative means in validated the contribution of the system's constituents in bearing an applied compressive load. The developed FE model is purposely simplified in order to simulate the complicated structure of 3DFGF in a practical manner and reduce the CPU run time, thus to make it cost-effective. For that, the fiberglass columns and their contribution are considered in a smeared way in conjunction with the elements used to idealize the foam core. This was followed by the development of an analytical model that accounts for the three constituents of the 3DFGF (i.e., the woven fabric, fiberglass pillars, and foam). The contribution of each constituent is also calculated by the model, and discussed. Subsequently, the integrity of the developed model is established by comparing its results with the experimental and FE results.

7.3 Experimental Investigation

3DFGFs with the thickness of 4 mm and 10 mm used in this study were supplied by the China Beihai Fiberglass, Co. Ltd. (Jiujiang City, China). Moreover, the foam used to fill the hollow cores of the 3DFGFs was an 8-lb density polyurethane foam supplied by the US Composites (West Palm Beach, FL 33407). The resin used in this study was Araldite LY 564 (Bisphenole-A Epoxy Resin), along with Aradur 2954 (cycloaliphatic polyamine) hardener, supplied by the Huntsman Co. (West Point, GA).

The specimens tested in this study were fabricated using the hand layup method. Prior to fabrication, Araldite LY 564 resin was mixed with the Aradur 2954 hardener using an electric paddle mixer and degassed in the vacuum chamber at room temperature for an hour. Afterwards, the resin applied onto the 3DFG fabrics along the negative direction of the core dumping, in order to facilitate the maximum height of the core (see manufacturer's website for additional explanations (www.fiberglassfiber.com)). The curing process of the wetted fabric based on the manufacture instructions was two hours at 60 °C, followed by eight hours at 120 °C. Subsequently, the foam was injected into the hollow core of the 3DFGF panels.

As briefly noted earlier, the tested specimens were categorized into four main categories, as listed in Table 7-1. For each category, five specimens with the noted dimensions were tested. The flatwise compression test was performed according to ASTM-C365 (ASTM-C365 2010). An Instron servo-hydraulic test machine (model 8500+) was employed to conduct the compression test. The deformation of the specimens due to a compressive loading was measured using a non-contact laser extensometer.

Table 7-1. Mechanical properties of tested specimens (Asaee and Taheri 2015).

Configuration	Flexural Stiffness ($N\text{-}m^2$)	Flexural Strength (MPa)
3DFGF-4	1.55	32.23
3DFGF-4 with Foam	1.64	49.25
3DFGF-10	4.44	13.63
3DFGF-10 with Foam	6.66	22.28

7.4 Finite Element Simulation

The commercial finite element software ABAQUS 6.14-2 was used to simulate the response of the 3DFGFs under a compressive loading. As discussed earlier, the 3DFG fabric consists of two bidirectional woven layers, attached to one another with a series of fiberglass fibers. After the application of the resin and its cure, these fibers act as pillars or columns in transferring the applied load from one layer of bidirectional fabric to the other.

As discussed earlier, previously the authors developed a new class of FMLs (3DFML) consisting of a 3DFGF and magnesium sheets, targeting applications in automotive industry (Asaee, Shadlou et al. 2015, Asaee and Taheri 2016). The integrity of the 3DFML was examined under impact loading. Moreover, in order to predict the behavior of 3DFML (especially those with various configurations), without the requirement for costly experiments, a FEM modeling approach was developed to simulate the structural response of the novel FML. It should be noted that 3DFGF has a complicated structure, and appropriate simplifications must be implemented in order to make the simulation approach practical and cost-effective. As a result, the foam-filled 3DFG fabric has been simulated by three constituents, namely: its upper and lower bi-directional fabric layers, and its core, which includes the vertical E-glass pillars that join the fabric layers.

The woven fabrics at the top and bottom layers were modeled as two layers of unidirectional fabric with orthotropic elastic materials. A majority of the bending stresses in these 3D composites gets carried out by these woven layers. However, an applied compressive load is carried by both the pillars and the foam occupying the core cavities (when foam present). Foam's properties used in the simulation are the average results of hardening curves obtained through the edgewise compression tests conducted on the foam. The mechanical properties of the fiberglass fabric and polyurethane foam used in the FE simulation are presented in Table 7-2.

Table 7-2. Mechanical Properties of E-glass fiber-reinforced composite and foam evaluated based on ASTM standards (ASTM-C365 2010).

Orthotropic properties of E-glass fiber-reinforced epoxy Composite	E_1 = 37 GPa, E_2 = 8.5 GPa, ν_{12} = 0.254, G_{12} = 4.7 GPa, G_{13} = 4.7 GPa, G_{23} = 3.28 GPa, X^T = 780 MPa, Y^T = 44 MPa, X^C = 750 MPa, Y^C = 44 MPa, Z^T = 30 MPa, Z^C = 30 MPa
Mechanical properties of foam	Compressive Elastic Modulus (MPa) = 435 MPa, Compressive Strength (MPa) = 7.0 MPa

The conventional 4-node shell element (S4R) of ABAQUS was used to simulate the woven layers, in conjunction with Hashin's failure criteria to predict the failure mechanism of the fabric. Moreover, the foam was modeled using 8-node solid elements (C3D8R) of ABAQUS. The damage mechanism of the crushable foam was defined using the ductile damage criterion in conjunction with the shear damage criterion. A more detailed explanation of the FE model could be found in (Asaee, Shadlou et al. 2015, Asaee and Taheri 2015, Asaee and Taheri 2016). Figure 7-2 illustrates the FE model. The normal direction and rotational degrees of freedom of the bottom shell section of the model were restrained. Moreover, a uniform pressure was applied on the top shell part to simulate the

actual compression load that was applied to the 3DFGF during the experiment. Furthermore, a mesh convergence study was carried out in order to establish the optimal mesh that produces results with a reasonable accuracy and efficiently, by varying the mesh density through the thickness and surfaces.

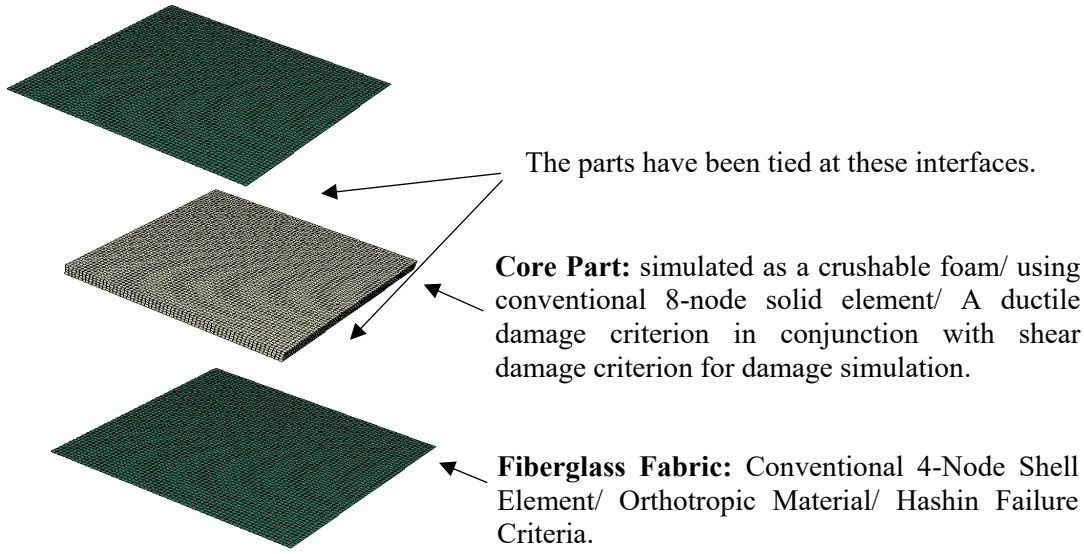

Figure 7-2. The detail of the 3DFGF's FE model.

As briefly stated earlier, the FE model does not include the fiberglass pillars, as they would increase the number of elements of the model and increasing the solution time, thus diminishing the practicality of the modeling approach, without improving the accuracy of the result by an appreciable margin. Instead, their contribution is considered in a smeared fashion, within the elements that were used to model the crushable foam constituent of the FML. The numerical results will be compared against the experimental results to validate the integrity of the developed approach. The approach will also enable us to achieve the main objective of this study, which is to establish the contribution of each constituent of this FML (from the perspective of load carrying capacity.)

7.5 Development of the Analytical Model

The present section briefly provides the details of the analytical model developed to predict the compressive strength of 3DFGF composites. In this model, the biaxial woven fabrics are modeled individually. In addition, the fiberglass pillars and their interactions with the foam core and the two woven layers are also individually considered.

7.5.1 Modeling Assumptions

The following simplifying assumptions have been made in developing the model:

- The applied compressive load is assumed to have been uniformly distributed on the surface of one of the 3DFG panels.
- Only a selected representative segment (unit volume) of the 3DFG fabric is considered. The segment includes a total of four cells, which in turn includes a total of four pillar cross-sections, as illustrated in Figure 7-3.
- The pillars are assumed to be completely straight (while, in actuality, they are somewhat curved).
- The distance between adjacent pillars is assumed to be a constant value, denoted by symbol *a*. The value of this distance is taken as the average value of the distances measured amongst the pillars in the tested specimens.
- A circular cross-section, with radius of *r,* is assumed for each pillar.
- The connections between the two woven glass layers and pillars are assumed to be non-rigid (i.e., flexible). Therefore, two identical torsional springs are used (one at each ends of the pillar), to account for the connection flexibility. These springs are assumed to deform linearly.

– Failure of the panel is assumed to occur once the fiberglass pillars become unstable, and the compressive stress within the foam core reaches its crushing value.

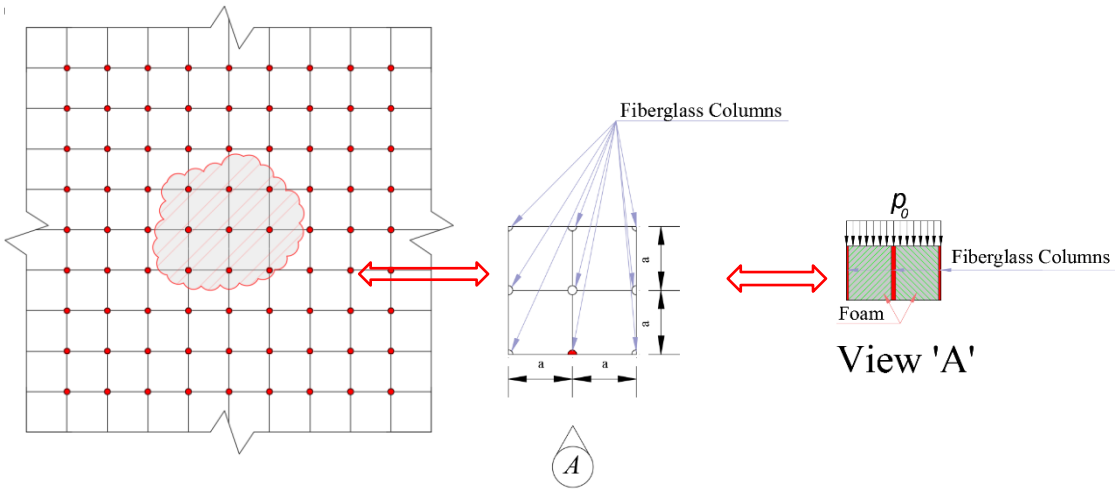

Figure 7-3. Details of the 3D fiberglass fabric considered in both the numerical analysis and analytical model. From left to right: top view of the 3DFGF; top schematic view of a representative unit volume comprised of four cells and pillars; side view of the representative unit volume and the uniformly applied load, P_0.

In view of the above assumptions and figure, one of the fiberglass pillars of the unit volume, as modeled, is shown schematically in Figure 7-4. As briefly stated, since the woven layer in contact with the applied compressive load would undergo bending, the resistance of the woven layer to this out-of-plane bending, at the point of connection to the pillar, is modeled by a linear spring of stiffness K_{eq}. The two identical torsional springs that represent the connection flexibility of the pillar to two woven fabrics, have each stiffness k_t.

The unit volume is assumed to be subjected to a uniformly distributed on its upper layer, as shown in Figure 7-3. This load is resisted by the foam and the pillars existing within the unit volume. The total force and the reaction forces are assumed to be in equilibrium, represented by the following equation:

$$4P_0a^2 = F_{foam} + n \times F_{pillar} \tag{7.1}$$

in which n denotes the number of pillars (in this case, a total of four), and F_{foam} and F_{pillar} represent the force in the foam core and pillars, respectively. The geometric parameter, a, is illustrated in Figure 7-3.

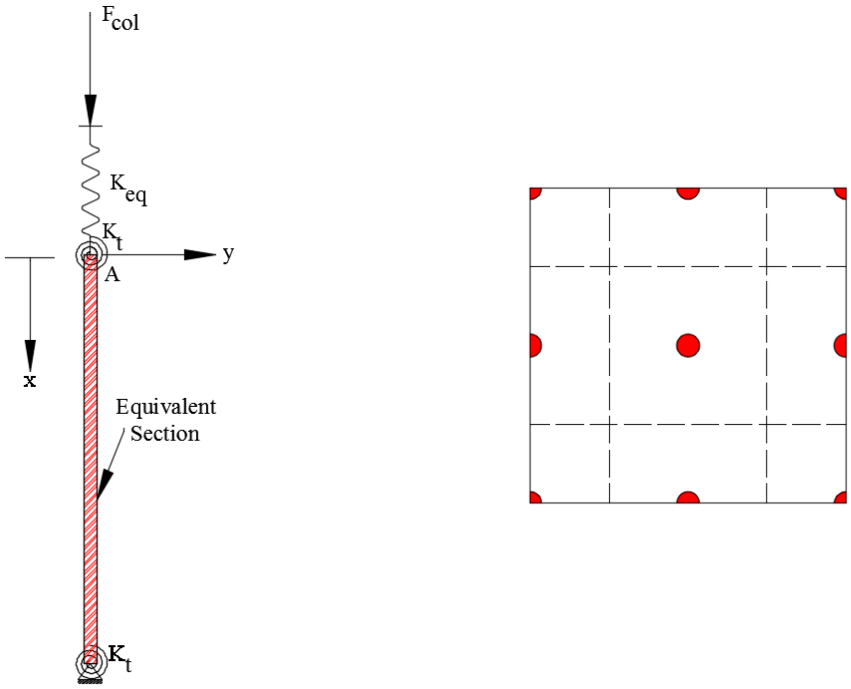

Figure 7-4. (Left) model of a single glass pillar with its equivalent boundary conditions, (right) top view of the unit cell and the tributary areas associated with the pillars.

The compressive stress, due to the applied uniform pressure, within the foam is obtained by

$$\sigma_{foam} = \frac{F_{foam}}{A_{Foam}} = \frac{F_{foam}}{4a^2 - nA_{pillar}} \tag{7.2}$$

In the above equation, σ_{foam} represents the compressive stress in the foam, and A_{foam} denotes the net cross-sectional areas of the foam, while nA_{pillar} denotes the total cross-sectional area of the pillars existing within the representative volume, where in this case, n equals 4. It

should be noted that the value of term nA_{pillar} is significantly smaller than that of $4a^2$ term (the ratio is approximately 0.008); thus, it could be neglected. Furthermore, the critical value of the applied load is assumed to cause failure of the 3DFGF by crushing of the foam. Thus, for the 3DFGF to be in an undamaged state, the compressive stress in the foam must be lower than the crushing strength of the foam; that is:

$$\sigma_{foam} \leq \sigma_{C,foam} \tag{7.3}$$

where $\sigma_{C,foam}$ represents the crushing strength of foam core. Consequently, the force in the foam core, in the limiting case, is represented by

$$F_{foam} = 4\, a^2\, \sigma_{C,foam}. \tag{7.4}$$

The next step is to evaluate the second term on the right-hand side of equation (7.1), which would be equivalent to the total buckling capacity of the fiberglass pillars existing within the selected volume. However, it is noted that two parameters govern the magnitude of the transferred forces within the pillars. These parameters are the stiffness of the woven layers, and that of the foam surrounding the pillars.

Consider a single glass pillar within the representative volume, as shown in Figure 7-4. In order to model the response of this pillar to the applied load, one must consider the flexural resistance of the upper layer of the 3DFGF. To approximate the flexural stiffness of the layer, in view of the geometry of the 3DFGF model shown in Figure 7-3, it is assumed that the woven layers are clamped at locations that fall between each two adjacent pillars. Thus, one can use the following partial differential equation to represent the lateral deflection of the clamped thin plate subjected to the uniformly applied pressure is (Timoshenko and Woinowsky-Krieger 1959)

$$\nabla^4 w = \frac{p_0}{D} \text{ with } D = \frac{Et^3}{12(1-\vartheta^2)} \tag{7.5}$$

in which *t, D, w, E* and *v* denote the thickness, flexural stiffness, through-thickness deflection, Young's modulus, and Poisson's ratio of the woven fiberglass layer, respectively. According to the Grashof's formulae (Grashof 1878), the maximum out of plane deflection of a clamped square plate under a uniform load is obtained as

$$w_{max} = 0.0057 \frac{Pa^2}{D} = \frac{P}{K_{eq}} \tag{7.6}$$

which is the consequence of the solution of the partial differential equation (7.5) for the assumed geometry and boundary conditions. Thus, the equivalent stiffness of the plate at its center is obtained by

$$K_{eq} = \frac{174.72\, D}{a^2} \tag{7.7}$$

The parameters K_{eq} and K_t shown in the equivalent model of the single pillar (Figure 7-4) represent the equivalent stiffness value of the woven layer that is subjected to the out-of-plane displacement, and the resisting stiffness of the connection locations of the woven plates to the pillar, respectively.

The use of the virtual work theorem is considered as an effective technique for establishing a closed-form solution for evaluating the buckling capacity of the complex system. The theorem states that if a body is in equilibrium under the action of prescribed surface and body forces, then the work done by these forces causes an additional small (or virtual) displacement, measured from the equilibrium state. One can then equate the change in the strain energy of the system, neglecting the second-order terms in the increments of strain (Sokolnikoff and Specht 1956). In other words:

$$\delta W_{ext} = \delta W_{int} \tag{7.8}$$

where δW_{ext} denotes the external work done by the surface and body forces, while δW_{int} represents the strain energy of the system. The external work of the system shown in Figure 7-4 is represented by:

$$\delta W_{ext} = F_{pillar}\delta_A. \tag{7.9}$$

where δ_A is the axial displacement of the pillar, as schematically shown in Figure 7-5. Note that contrary to the common assumption used in representing a beam's deformation, in which the axial displacement is neglected, in the proposed analytical model, as shown in Figure 7-5, the axial displacement is not neglected.

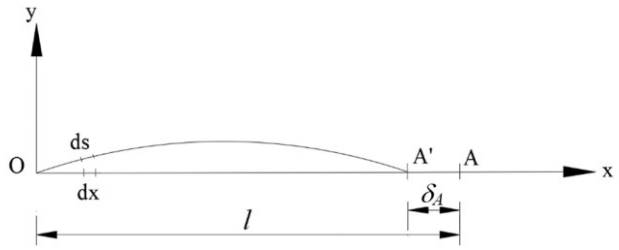

Figure 7-5. Schematic of a glass pillar's response under the applied load.

Furthermore, the equilibrium equations are constructed in the deformed state of the pillar. According to the figure, the displacement δ_A can be represented by:

$$\delta_A = \overline{OA} - \overline{OA}' = l - \int dx \tag{7.10}$$

where $l = \int ds$, and

$$ds = \sqrt{(dx)^2 + (dy)^2} = \sqrt{1 + y'^2}dx. \tag{7.11}$$

Owing to the fact that the value of y' is significantly less than 1, equation (7.11) can be approximated as:

$$\sqrt{1+y'^2}dx \approx \left(1+\frac{1}{2}y'^2\right)dx. \tag{7.12}$$

By substituting equation (7.12) into equation (7.10), one would obtain:

$$\delta_A = \int ds - \int dx = \frac{1}{2}\int_0^l y'^2 dx. \tag{7.13}$$

Thus, equation (7.9) would take the following form:

$$\delta W_{ext} = F_{pillar}\left(\frac{1}{2}\int_0^l y'^2\, dx\right). \tag{7.14}$$

Moreover, δW_{int} represents the change in the strain energy as a result of an incremental displacement, which in this case, includes two contributors:

$$\delta W_{int} = \delta W_{pillar} + \delta W_{spring}. \tag{7.15}$$

where δW_{pillar} represents the bending strain energy stored in the pillar, and is given by

$$\delta W_{pillar} = \int_0^l \frac{M^2 dx}{2EI} = \frac{1}{2}\int_0^l EIy''^2 dx \tag{7.16}$$

which, in view of $M = EIy''$, the above can be rewritten as

$$\delta W_{pillar} = \frac{1}{2}\int_0^l EIy''^2 dx. \tag{7.17}$$

Note that in the above equation, the second moment of area, *I*, is the equivalent moment of area (that is the cross-section used in the calculation of *I* is that of the glass pillar and the equivalent cross-section of the tributary area of the foam shown in Figure 7-4). The second contributor is the strain energy stored in the springs, expressed as

$$\delta W_{spring} = \sum_{i=1}^{3} \phi_i \tag{7.18}$$

in which ϕ_1 and ϕ_2 refer to the energy stored in the two identical torsional springs at the two ends of the pillar, with stiffness of k_t, and ϕ_3 represents the energy stored in the linear

spring of stiffness K_{eq} (see Figure 7-4). Note that the linear spring with stiffness K_{eq} represents the equivalent stiffness of the upper woven fabric of the 3DFGF, as described earlier. The terms ϕ_1- ϕ_3 are represented mathematically as follows:

$$\varphi_1 = \varphi_2 = \frac{1}{2} k_t \theta^2 \ , \tag{7.19}$$

where $\theta = |y'|_{x=0} = |y'|_{x=l}$, and

$$\varphi_3 = \frac{1}{2} k_{eq} \delta_A^2 = \frac{1}{2} k_{eq} \left(\frac{1}{2} \int_0^l y'^2 \, dx \right)^2. \tag{7.20}$$

Hence,

$$\delta W_{int} = \frac{1}{2} \int_0^l EI y''^2 dx + \sum_{i=1}^{3} \varphi_i \tag{7.21}$$

Equating equations (7.9) and (7.21) yields

$$F_{pillar} \left(\frac{1}{2} \int_0^l y'^2 dx \right) = \frac{1}{2} \int_0^l EI y''^2 dx + \sum_{i=1}^{3} \varphi_i \tag{7.22}$$

Equation (7.22) is a nonlinear *Integro-Differential* equation, in terms of the nonlinear deformation function, *y,* of the pillar, and does not have a closed-form solution. Thus, an approximate method is sought to solve this equation. For that, the Rayleigh method (Den Hartog 2014) is used, by which a deformation function, *y*, is assumed, which represents the deformed shape of the pillar. Such a deformation function must also satisfy the boundary conditions, which are represented as:

$$y|_{x=0} = y|_{x=l} = 0. \tag{7.23}$$

The selected deformation function has the following form:

$$y = \xi x(x - l), \tag{7.24}$$

which satisfies the aforementioned boundary conditions. Substituting equation (7.24) into (7.22) results in:

$$F_{col}\left(\frac{1}{2}\int_0^l \xi^2(4x^2+l^2-4xl)\,dx\right) = \frac{1}{2}\int_0^l EI(2\xi)^2 dx + \frac{1}{2}k_t(2\xi^2 l^2) + \frac{1}{2}\left(\frac{174.72D}{a^2}\right)\left(\frac{1}{2}\int_0^l \xi^2(4x^2+l^2-4xl)\,dx\right)^2 \tag{7.25}$$

Solving equation (7.25) yields

$$F_{pillar} = \frac{12EI}{l^2} + \frac{6k_t}{l} + \frac{1.21\,E\xi^2 t^3 l^3}{a^2(1-\nu^2)} \tag{7.26}$$

Notice that Rayleigh's method yields an upper-bound of the critical load causing the instability of the system; thus, the actual critical load of the system would be slightly less than the obtained value. Note that the first term on the right-hand side of equation (7.26) is quite similar to the equation that yields the Euler critical buckling capacity of a column (i.e., $F_{cr} = \pi^2 EI/l^2$).

Subsequently, the critical pressure P_0 that causes the onset of failure of 3DFGF due to the compressive loading is obtained by substituting equation (7.26) in (7.1), which gives:

$$P_0 = \frac{n}{4a^2}\left(\frac{12EI}{l^2} + \frac{6k_t}{l} + \frac{1.21E\zeta^2 t^3 l^3}{a^2(1-\nu^2)}\right) + \sigma_{C,foam} \tag{7.27}$$

7.6 Results and Discussions

As stated previously, the main objective of the present study is to develop an analytical model by which one could calculate the compressive strength of the 3DFGFs. In addition, estimation of the contribution of each constituent of the 3DFGFs is also desired, so that fabric's configuration could be optimized in the future. The results obtained from the proposed model have been validated against the experimental data. Here, we present and discuss the comparison of results produced by the model with the experimental and FE results, respectively.

The load-displacement curves obtained experimentally for the four groups of tested specimens are illustrated in Figure 7-6. Each curve represents a typical response seen within five tests. The results reveal that the response of 3DFGFs under compression, especially in the foam infilled case, is analogous to the response of a ductile material. As can be seen, the responses of 3DFGF specimens are almost linear, up to the load at which the infill-foam is postulated to start crushing and the pillars instability is initiated. Shortly after this stage, the load reaches a plateau, at which failure of the specimen is declared.

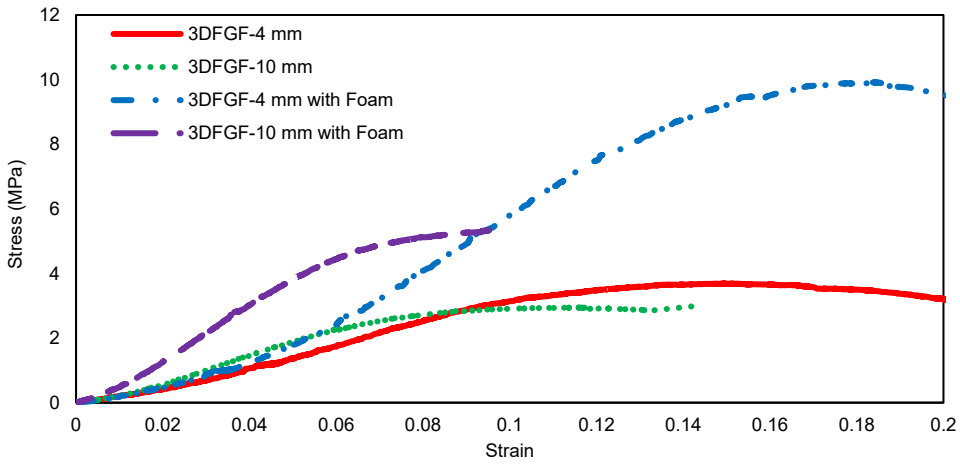

Figure 7-6. Stress-strain response of 3DFGF specimens obtained under compression.

Furthermore, comparison of the results obtained for 3DFGF-4 and 3DFGF-10 panels demonstrates that the thinner 3DFGF panels provide a relatively greater compressive strength, especially for the foam infilled panels. This is postulated to be due to the more stable performance of the comparatively shorter length glass pillars in the thinner fabric. In addition, examination of the results of the panels that had foam infill reveals the significant contribution of the foam, which acts as an effective constituent in providing lateral stability to the glass pillars, thus significantly enhancing the compressive strength of the 3DFGFs. In fact, the addition of foam increased the compressive strength of 3DFGF-4 and 3DFGF-10 by approximately 300% and 500%, respectively.

The analytical solution derived in the previous section is comprised of four main contributing terms as per equation (7.4). The first three terms on the right-hand side of equation (7.27) represent the compressive capacity of 3DFG panels, including the glass pillars' buckling capacity. Moreover, the effects of the woven layer and its connection to the pillars were considered. The second term on the right-hand side of equation (7.27) represents the elastic connection between the fiberglass pillars, and the top and bottom woven fabrics. The third term on the right-hand side of equation (7.27) denotes the load transferred to the top woven fabric. Finally, the last term of the equation represents the compressive resistance of the foam core.

The compressive strengths of 4 mm and 10 mm 3DFGFs are calculated using equation (7.27). Note that the equation includes a fitting parameter, ζ, that is used in conjunction with the Rayleigh's method. Essentially, the physical significance of this parameter is that it mimics the deformed geometry of the pillars by the parabolic function used to describe

the deformed shape. Physically, in this solution, the ζ parameter captures the maximum deformation that develops at the mid-height of the pillars as a result of the loading.

One should also appreciate the generality of the proposed solution. That is, for a given situation, one can select any appreciate function in conjunction with the Rayleigh's method, so long as the function satisfies the boundary conditions corresponding to the deformed state of the constituent being modeled. In other words, the closer is the ability of the function to mimic the deformation of the pillars (in this case), the more precise would be the estimated value of load P_0. Therefore, incorporation of other type polynomials or trigonometric functions would also work very effectively within the proposed solution framework, since these functions are smooth and continuous. Note that the selected function must also be able to conform to the boundary that exists at either ends of the pillars.

The value of parameter ζ was established by comparing the results produced by equation (7.27) with the experimental data. In other words, the compressive strength of 3DFGF was calculated at different values of ζ parameter. Figure 7-7 depicts the variation of the compressive strengths of the tested 3DFGFs as a function of ζ. By matching the predicted and experimentally evaluated compressive strengths of the two 3DFG panels, one would obtain values of 0.225 and 0.071 for ζ for the 4 mm and 10 mm thick panels, respectively. Substitution of these values into equation (7.24) produces the maximum in-plane displacement values of 1.9 mm and 3.1 mm, for 3DFGF-4 and 3DFGF-10, respectively. These values indicate that the longer is the pillars' length, the greater would be the resulting displacement. In other words, essentially, the thicker specimen tolerates a larger in-plane displacement before complete failure of the panel.

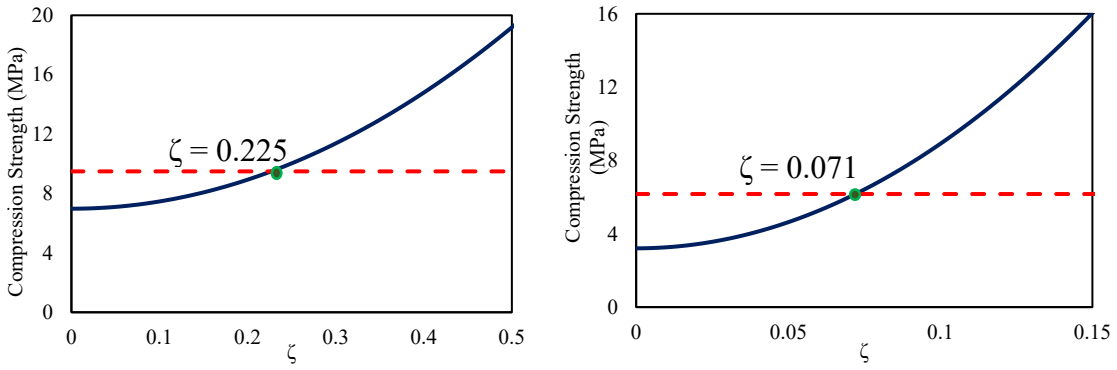

Figure 7-7. Variation of the compressive strength as a function of parameter ζ for (a) 3DFGF-4 panel with foam and (b) 3DFGF-10 panel with foam

Next, the contribution of each term of equation (7.27) on the compressive strength of each 3DFGF panel is investigated. Figure 7-8(a) presents the percent contribution of each of the four terms for the case of 3DFGF-4. The results indicate that the third term, which represents the load transferred by the woven layers, has the greatest contribution to the compressive capacity of the panel. Since the glass pillars in 3DFGF-4 panels are relatively short, they could exhibit a greater buckling capacity when compared to those longer pillars in 3DFGF-10 panels. Hence, the contribution of the pillars in the compressive capacity of the fabric is comparatively more significant than the other terms. Figure 7-8(a) also reveals the influence of the foam core as a supplementary constituent. According to the results, the foam carries approximately 20% of the overall capacity.

Similar comparison of the terms' contribution for 3DFGF-10 panel is illustrated in Figure 7-8(b). As seen, the total contributions of the woven fabric and foam core are approximately 80% of the total. As stated earlier, the buckling capacity of the pillars in the thicker panel is lower than those in the thinner panel. As a result, the contribution of the first term in 3DFGF-4 panel is significantly greater than that of 3DFGF-10 panel (by approximately 70%). Moreover, due to the smaller contribution of the glass pillars in

3DFGF-10 panel, the influence of the foam core in this panel is more significant than that in 3DFGF-4 panel. The percent contribution of the foam core reaches to approximately 30% of the total. Therefore, the injected foam plays a more effective role in the thicker panel. This finding is consistent with the experimental results. Furthermore, the results revealed that the strengths of foam infilled 3DFGF-4 and 3DFGF-10 panels would be higher than the hollow core (no foam) counterpart panels by approximately 300% and 500%, respectively.

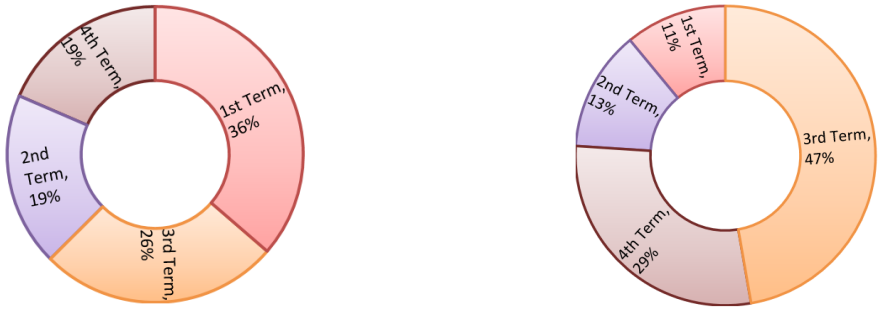

(a) (b)

Figure 7-8. Relative contribution of the four terms of equation (7.27) on the compressive load-bearing capacity of (a) 3DFGF-4 panel and (b) 3DFGF-10 panel

As mentioned earlier, FE simulation of 3DFG panels subjected to a compressive loading was also carried out using the commercial FE software ABAQUS. The evaluated compressive strengths of 3DFGF-4 and 3DFGF-10 panels obtained through the experiments, FE simulations, and the analytical method are presented in Table 7-3. Note that the presented % error values are calculated with reference to the experimental results. As can be seen, the margin of errors corresponding to the results obtained by the proposed analytical model is lower than those corresponding to the FE analysis. This is believed to be due to the fact that the individual glass pillars were not modeled in the FE model; as described earlier, in the FE model, the pillars' equivalent stiffness was added to that of

surrounding foam. However, the relatively small error margins imply that the developed FE approach can provide accurate and reliable means for predicting the strength of such 3DFGF.

Table 7-3. Comparison of the compressive strengths obtained experimentally by FE analysis and the proposed analytical model.

Specimen	Experimental Result	FE Result	Error (%)	Numerical Result	Error (%)
3DFML-4 with Foam	9.49	10.54	11.06	9.44	0.42
3DFML-10 with Foam	6.17	7.09	14.91	6.08	1.43

7.7 Summary and Conclusions

The compressive response of a novel 3D fiberglass fabric (3DFGF) was evaluated experimentally and numerically. In this unique fabric, the upper and lower biaxial woven glass fabrics are connected by a series of glass pillars, thus creating cavities. These cavities could be in-turn filled by a foam, which enhances the load carrying capacity and stiffness of the panel made of the 3DFGF.

The flatwise compression tests were performed on four groups of specimens to establish the compressive capacity of the panels. The four groups comprised of two fabric thicknesses (i.e., 4 mm and 10 mm), with and without foam infill. In addition, the panels' response was also simulated by the finite element method, using ABAQUS FE software. The reason for developing the finite element strategy was outlined earlier. It should be noted that the developed FE approach did not model the individual pillars, as the model would have been impractically large and very solution-time intensive. In turn, the influence of the pillars was accounted for by smearing their stiffness in combination to that of the foam infill.

An analytical model was also developed by considering the response of the individual constituents of the fabric (i.e., the woven layers, fiberglass pillars/columns and the foam core). The developed equations were solved by the Raleigh method. Appropriate geometrical assumptions were made to simplify the actual complex structure of 3DFGF. The compressive strength of the fabric was obtained as a function of a fitting parameter (ζ); this parameter is an indicator of a deformed shape of the fiberglass pillars. In addition, the contributions of the individual constituents of the fabrics on the resulting compressive strength were assessed by the proposed analytical model, thereby providing an insight into the individual constituent's role. The proposed solution can be effectively used in the future to optimize various constituents of the fabric, so that the load-bearing capacity of each constituent could be optimized accordingly.

The results indicated that the contributions of the woven layers and fiberglass pillars in 3DFGF-4 fabric were greater than that of the foam. However, in the case of 3DFGF-10 fabric, the woven layer and foam exhibited greater contributions. Since the height of the glass pillars in 3DFGF-10 fabric is greater than that in 3DFGF-4 fabric, the panels made by 3DFGF-10 fabric offer a lower load bearing capacity. The results obtained through the proposed analytical method corroborated very closely to the FE results. However, when the analytical results were compared to the experimental data, a better agreement was obtained. This is attributed to the fact that the glass panels' contribution to load bearing was considered discretely in the analytical model, while that was not the case in the FE analysis.

7.8 Acknowledgement

Financial support from National Science and Engineering Research Council of Canada (NSERC) is gratefully appreciated. The authors also appreciate the Killam doctoral scholarship awarded to the first author.

7.9 References

Asaee, Z., M. Mohamed, D. De Cicco and F. Taheri (2017). "Low-Velocity Impact Response and Damage Mechanism of 3D Fiber-Metal Laminates Reinforced with Amino-Functionalized Graphene Nanoplatelets." International Journal of Composite Materials 7(1): 20-36.

Asaee, Z., M. Mohamed, S. Soumik and F. Taheri (2017). "Experimental and numerical characterization of delamination buckling behavior of a new class of GNP-reinforced 3D fiber-metal laminates." Thin-Walled Structures 112: 208-216.

Asaee, Z., S. Shadlou and F. Taheri (2015). "Low-velocity impact response of fiberglass/magnesium FMLs with a new 3D fiberglass fabric." Composite Structures 122: 155-165.

Asaee, Z. and F. Taheri (2015). Characterization of the Mechanical and Impact Response of a New-Generation 3D Fiberglass Fabric. American Society of Composites-30th Technical Conference.

Asaee, Z. and F. Taheri (2016). "Experimental and numerical investigation into the influence of stacking sequence on the low-velocity impact response of new 3D FMLs." Composite Structures 140: 136-146.

Asaee, Z. and F. Taheri (2016). Experimental Studies on the Impact Response of 3D Fiberglass Fabric Subject to Different Size Impactors. Proceedings of the American Society for Composites: Thirty-First Technical Conference.

ASTM-C365 (2010). Standard test method for flatwise compressive properties of sandwich cores, American Society for Testing and Materials West Conshohocken.

Bannister, M., R. Braemar and P. Crothers (1999). "The mechanical performance of 3D woven sandwich composites." Composite Structures 47(1): 687-690.

Chen, H., Q. Zheng, P. Wang, H. Fan, J. Zheng, L. Zhao and F. Jin (2015). "Dynamic anti-crushing behaviors of woven textile sandwich composites: Multilayer and gradient effects." Journal of Composite Materials 49(25): 3169-3179.

Den Hartog, J. P. (2014). Advanced strength of materials, Courier Corporation.

Fan, H., L. Zhao, H. Chen, J. Zheng, Y. Jiang, S. Huang, N. Kuang and C. Ye (2013). "Dynamic compression failure mechanisms and dynamic effects of integrated woven sandwich composites." Journal of Composite Materials 48(4): 427-437.

Fan, H., Q. Zhou, W. Yang and Z. Jingjing (2010). "An experiment study on the failure mechanisms of woven textile sandwich panels under quasi-static loading." Composites Part B: Engineering 41(8): 686-692.

Grashof, F. (1878). Theorie der Elasticität und Festigkeit: mit Bezug auf ihre Anwendungen in der Technik, R. Gaertner.

Hosseini, S. A., M. Sadighi and R. Maleki Moghadam (2015). "Low-velocity impact behavior of hollow core woven sandwich composite: Experimental and numerical study." Journal of Composite Materials 49(26): 3285-3295.

Hosur, M., M. Abdullah and S. Jeelani (2004). "Manufacturing and low-velocity impact characterization of hollow integrated core sandwich composites with hybrid face sheets." Composite Structures 65(1): 103-115.

Hosur, M., M. Abdullah and S. Jeelani (2007). "Dynamic compression behavior of integrated core sandwich composites." Materials Science and Engineering: A 445: 54-64.

Karahan, M., H. Gül, J. Ivens and N. Karahan (2012). "Low velocity impact characteristic of 3D integrated core sandwich composites." Textile Research Journal 82(9): 945-962.

Karahan, M., H. Gul, N. Karahan and J. Ivens (2013). "Static behavior of three-dimensional ıntegrated core sandwich composites subjected to three-point bending." Journal of Reinforced Plastics and Composites 32(9): 664-678.

Kashani, M. H., M. Sadighi, A. Lalehpour and R. Alderliesten (2014). "The effect of impact energy division over repeated low-velocity impact on fiber metal laminates." Journal of Composite Materials 49(6): 793-806.

Li, D.-s., C.-q. Zhao, N. Jiang and L. Jiang (2015). "Fabrication, properties and failure of 3D integrated woven spacer composites with thickened face sheets." Materials Letters 148: 103-105.

Nji, J. and G. Li (2010). "A self-healing 3D woven fabric reinforced shape memory polymer composite for impact mitigation." Smart Materials and Structures 19(3): 035007.

Sadighi, M. and S. A. Hosseini (2013). "Finite element simulation and experimental study on mechanical behavior of 3D woven glass fiber composite sandwich panels." Composites part b: engineering 55: 158-166.

Shyr, T.-W. and Y.-H. Pan (2004). "Low velocity impact responses of hollow core sandwich laminate and interply hybrid laminate." Composite Structures 64(2): 189-198.

Sokolnikoff, I. S. and R. D. Specht (1956). Mathematical theory of elasticity, McGraw-Hill New York.

Timoshenko, S. P. and S. Woinowsky-Krieger (1959). Theory of plates and shells, McGraw-hill.

Vaidya, A., U. Vaidya and N. Uddin (2008). "Impact response of three-dimensional multifunctional sandwich composite." Materials Science and Engineering: A 472(1): 52-58.

Vaidya, U., M. Hosur, D. Earl and S. Jeelani (2000). "Impact response of integrated hollow core sandwich composite panels." Composites Part A: Applied Science and Manufacturing 31(8): 761-772.

Van Vuure, A., J. Pflug, J. Ivens and I. Verpoest (2000). "Modelling the core properties of composite panels based on woven sandwich-fabric preforms." Composites science and technology 60(8): 1263-1276.

Wang, S., M. Li, Z. Zhang and B. Wu (2009). "Properties of facesheet-reinforced 3-D spacer fabric composites and the integral multi-facesheet structures." Journal of Reinforced Plastics and Composites 29(6): 793-806.

Yu, K., H. Cao, K. Qian and H. Li (2014). "Manufacturing and Flat-wise Compression Performance of Modified 3D Integrated Sandwich Fabric Composites." Fibres & Textiles in Eastern Europe 105(3): 98-102.

Zhao, C.-Q., D.-S. Li, T.-Q. Ge, L. Jiang and N. Jiang (2014). "Experimental study on the compression properties and failure mechanism of 3D integrated woven spacer composites." Materials & Design 56: 50-59.

Chapter 8: A Practical Analytical Model for Predicting the Low-velocity Impact Response of 3D-Fiber Metal Laminates

Zohreh Asaee and Farid Taheri

Submitted to International Journal of Impact Engineering

8.1 Abstract

The main objective of present study is to develop a practical analytical model for predicting the static (indentation) and low-velocity impact responses of 3D fiber metal laminates (3DFML). An energy balance approach is used, by which the impact induced energy into various configurations of 3DFML is assumed to dissipate through shear, bending and indentation contact mechanisms. The indentation contact is formulated using the Hertz law. The contact parameters are calculated for various configurations of 3DFML. The variation in the contact parameters as a function of 3DFML configuration and the indentation area is investigated. The developed analytical model is generalized and modified based on the configurations of 3DFMLs and impactor's geometry. The integrity of the proposed analytical model is verified by comparison of its results against results obtained through experiments and numerical simulations. The numerical simulations are performed using commercial finite element software ABAQUS/Explicit. Comparison of the results indicates that the proposed model can reliably predict the maximum impact force and deformation of the 3DFMLs, up to the stage at which a crack develops on the 3DFML.

Keywords: 3D Fiber Metal Laminates, Low-velocity Impact, Analytical Solution, Finite Element Solution, Contact Law, Energy Balance Model.

8.2 Introduction

Fiber metal laminates (FMLs) are increasingly sought for applications in automotive industry because of their desirable characteristics. Compared to their fiber-reinforced polymer composites (FRP) counterparts, FMLs could offer lower weight and cost, better passenger safety (i.e., crashworthiness), and better life cycle (Ghassemieh 2011). Essentially, FMLs take advantage of the positive attributes of both metals and composites, by transforming them into a hybrid material (Marsh 2014). The first generation of FMLs was GLARE, an acronym for GLAss REinforced FML, which was developed in the Mid 80s at the Delf University of Technology (Sadighi, Alderliesten et al. 2012). Since then, various types of FMLs have emerged, which are categorized based on the types of metal and/or types of reinforced fabric used to configure them (Vlot 1993, Vogelesang and Vlot 2000, Cortes and Cantwell 2004, Botelho, Silva et al. 2006, Cortes and Cantwell 2006, Alderliesten, Rans et al. 2008, Carrillo and Cantwell 2009, Morinière, Alderliesten et al. 2013, Chai and Manikandan 2014).

One of the most recent types of FMLs is the 3D fiber metal laminates (3DFMLs), formed by using a truly 3D Fiberglass Fabric (3DFGF) (Asaee, Shadlou et al. 2015, Asaee and Taheri 2016, Asaee, Taheri et al. 2016). A typical 3DFGF and its 3DFML configuration are illustrated in Figure 8-1. The 3DFGF is a new generation of fiberglass fabric, offering advantageous characteristics, such as a great skin-core deboning resistance, impact resistance, and greater specific stiffness and strength compared to the conventional 2D woven or stitched fabrics. These attributes make the 3D fabric an excellent candidate in formation of FMLs (Sadighi and Hosseini 2013, Asaee and Taheri 2015, Hosseini, Sadighi et al. 2015, Asaee and Taheri 2016). The characteristics of the fabric's response and its

performance under both static and impact loads compared to the conventional FMLs were investigated previously by the authors (Asaee, Shadlou et al. 2015). Subsequently, the responses of various configurations of 3DFML were also examined by the authors. The selected configurations were rated based on their performance from the perspectives of weight, cost and strength (Asaee and Taheri 2016). Moreover, the enhancement in performance of 3DFMLs that could be gained by insertion of additional layers of fiberglass and carbon fabrics, and enhancement of the metallic/3DFGF interface strength by inclusions of graphene nanoplatelet particles were systematically tested and documented (Asaee, Mohamed et al. 2017, Asaee, Mohamed et al. 2017).

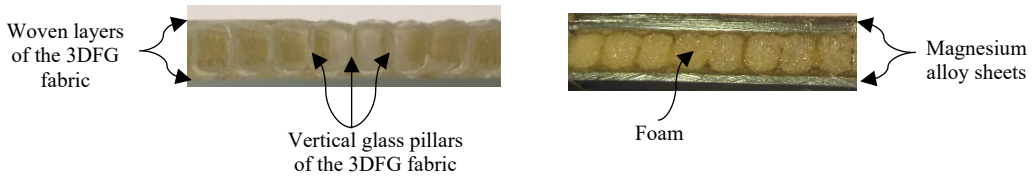

Figure 8-1. (a) 3D fiberglass fabric and (b) Details of a configuration of 3D fiber metal laminate

In recent years, significant efforts have also been expended toward developing robust analytical models for predicting the response of various configurations of FRPs, sandwich structures and FMLs (Vlot 1993, Vlot 1993, Vlot 1996, Reid and Wen 2000, Hoo Fatt, Lin et al. 2003, Caprino, Spataro et al. 2004, Abdullah and Cantwell 2006, Lin and Fatt 2006, Caprino, Lopresto et al. 2007, Payeganeh, Ghasemi et al. 2010). For example, Zhou et al. (Zhou and Stronge 2006) investigated the low-velocity impact response of HSSA lightweight sandwich panels. In general, the overall deformation of their sandwich panels was characterized by two types of deformations: (i) the local indentation developed adjacent to the location of impact, and (ii) that due to elastic deformation of the surrounding

panel. An indentation law was used to characterize the effects of localized indentation. Afterwards, the developed load-indentation relationship was used in conjunction with Reissner-Mindlin plate theory to develop an analytical model for predicting the impact response of their panels. In another study, Kiratisaevee et al. (Kiratisaevee and Cantwell 2005) investigated the low-velocity impact response of a novel sandwich structure formed by a thermoplastic-matrix, FML skins and an aluminum foam core. An analytical solution based on the generalized indentation law and energy balance model was developed to predict the maximum impact force developed during an impact event. It was found that the analytical solution was valid up to energy levels of 30J. At higher energies, the development of horizontal shear cracks on the actual metal core resulted in a sharp decrease in the maximum force, causing deviation of the predicted values from the actual values.

The main objective of the present study is to develop an analytical model for predicting the response of 3DFMLs under low-velocity impact loadings. The main thrust of the work is to develop a practical tool by which practicing engineers could predict the response of such robust 3DFMLs in a cost-effective and reliable manner. The alternative of conducting an experimental or a numerical investigation is believed to limit the applications of such effective structural panels in various industries. These alternatives are in general time-consuming and expensive, requiring specialists with advanced skills. The proposed analytical model is developed based on the energy balance model, accounting for energy dissipation through bending, shear and contact and indentation responses. The contact-indentation effect is formulated based on the Hertz contact law. The developed equations were modified and generalized to account for various configurations of 3DFMLs. Moreover, the effect of impactor geometry is considered. In addition, a finite element

model (FEM) is developed using a commercial FE software (ABAQUS/Explicit), by which effect of various parameters are also studied. The results produced by the proposed model, that is: the maximum impact force and deformation values at the panels' centre are verified by comparison against experimental and numerical results. Furthermore, to gain a better understanding of the behavior of 3DFMLs under impact loading, the contributions of shear, bending and contact in absorbing the energy are also investigated.

8.3 Development of the Analytical Model

An energy balance model is developed to analyze the impact response of 3DFML. Due to the quasi-static behavior of the light-weight 3DFML plate impacted by a heavy impactor, the initial kinetic energy of the impactor is transferred to the target through generation of a localized indentation in the contact area. This indentation is associated with the membrane, bending and shear reactions (See Figure 8-2). Therefore, the energy balance model can be presented in the following mathematical form:

$$\frac{1}{2}m_1 v_0^2 = E_c + E_b + E_s + E_m \tag{8.1}$$

where m_1 and v_0 are the mass and initial velocity of the impactor, respectively. E_b, E_s and E_m refer to the absorbed energy due to bending and shear deformation of the target, and membrane stretching of the skin. Subsequently, E_c is the amount of absorbed energy due to the indentation in the local contact region of impactor and plate.

The effect of local indentation can be calculated using the generalized Hertz contact law (Johnson 1982):

$$P = C\alpha^n \tag{8.2}$$

where C and n, are parameters related to contact, and P and α are the contact force and indentation depth, respectively. In the case of a purely elastic contact of two bodies, n is taken as 1.5 (Hertz 1881) ; however, in the case of sandwich materials, the value of n is reduced due to the lower elastic modulus of core. Therefore, the two contact parameters should be calibrated for 3DFML panel. Subsequently, the absorbed energy due to contact can be calculated by

$$E_c = \int_0^{\alpha_{max}} P d\alpha \tag{8.3}$$

Substitution of (8.2) into (8.3) and its integration yields

$$E_c = \frac{\left[\frac{P_{max}}{C}^{n+1}\right]^{1/n}}{(n+1)} \tag{8.4}$$

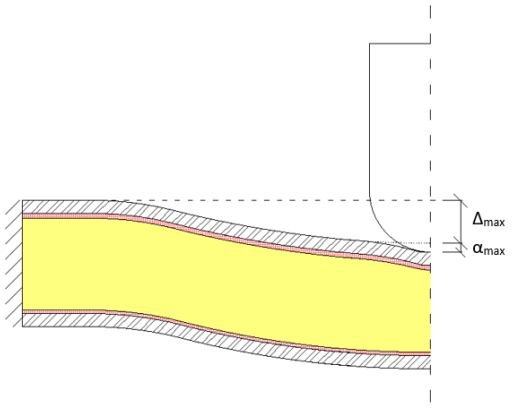

Figure 8-2. Schematic of deformed shape of the target under impactor including deformations due to indentation (α_{max}), and bending-shear (Δ_{max})

The panel reacts to the contact force, P, by bending and shear. It should be noted that stretching of the membrane is also involved; however, its contribution, in a relative sense, is negligible. As a result, the relation between force P and deflection, Δ, at the plate's centre can be represented by

$$P = K_{bs}\Delta \tag{8.5}$$

Note that Δ is the overall deflection of plate, without consideration of indentation, and K_{bs} is the effective stiffness due to the combined shear and bending effects, which can be written as

$$\frac{1}{K_{bs}} = \frac{1}{K_b} + \frac{1}{K_s} \tag{8.6}$$

Based on the classical plate theory, the effective bending stiffness of circular plate subject to a central force can be calculated by (Zenkert 1997)

$$K_b = \frac{16\pi D}{(1-\nu)(3+\nu)R^2} \tag{8.7}$$

where D and ν are the flexural rigidity of the sandwich panel and Poisson ratio of face-sheets, respectively, and R is the radius of the circular panel.

The effective shear stiffness of the target is calculated with the assumption that the load is applied in form of a uniform pressure applied over the centre portion of the plate within the contact area; so, it is related to the contact radius and impactor size by the following equation (Kiratisaevee and Cantwell 2005)

$$K_s = \frac{4\pi G\left(t_f + t_c\right)}{t_c\left(1 + 2\ln\frac{r}{a_c}\right)} \tag{8.8}$$

where G, t_f and t_c are the shear modulus of core, and face-sheet and core thicknesses, respectively. r and a_c are the radii of the impactor and contact region, respectively (See Figure 8-3). Consequently, the absorbed energy due to shear and bending deformations can be calculated by

$$E_{bs} = \frac{P_{max}^2}{2K_{bs}} \tag{8.9}$$

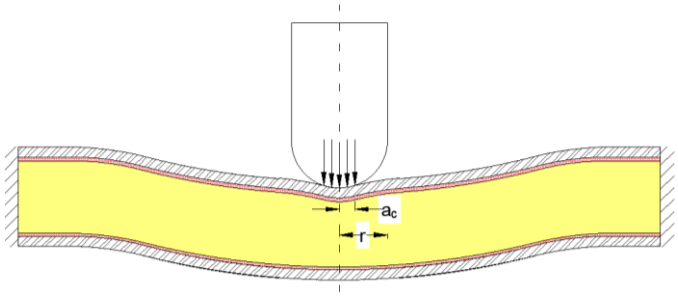

Figure 8-3. Schematic of contact radii

As a result, the energy balance represented in (8.1) can be rewritten as

$$\frac{1}{2}mv^2 = \frac{\left[{P_{max}}^{n+1}/C\right]^{1/n}}{(n+1)} + \frac{16P_{max}^2\pi DG\left(t_f + t_c\right)}{4Dt_c\left(1 + 2\ln\frac{r}{a_c}\right) + G\left(t_f + t_c\right)(1-\nu)(3+\nu)R^2} \tag{8.10}$$

Therefore, knowing the contact parameters, and geometric and mechanical properties of the panel, one can evaluate the value of P_{max} for a given impact energy.

Equation (8.10) can be rewritten as a function of the overall maximum centre location deflection at the mid-surface of the plate, Δ_{max}, and the maximum indentation depth, α_{max}, as follows

$$\frac{1}{2}mv_0^2 = \frac{1}{2}K_{bs}\Delta_{max}^2 + \frac{1}{n+1}C\alpha_{max}^{n+1} \tag{8.11}$$

The relationship between Δ_{max} and α_{max} can be expressed by

$$K_{bs}\Delta_{max} = C\alpha_{max}^{n} \tag{8.12}$$

The total displacement of the impactor is therefore the sum of the local indentation depth and global deflection.

$$w_{max} = \alpha_{max} + \Delta_{max} \tag{8.13}$$

In order to calculate the rate of change of indentation depth, mass and velocity of the impactor and target are considered (i.e., m_1, v_1, m_2 and v_2, respectively). When the impactor and target come in contact, the rates of change of the velocities during the impact can be represented by

$$m_1 \frac{dv_1}{dt} = -P \qquad \text{and} \qquad m_2 \frac{dv_2}{dt} = -P \tag{8.14}$$

Also

$$\dot{\alpha} = v_1 + v_2 \tag{8.15}$$

Differentiation of (8.15) and substitution of (8.14), with consideration of (8.2) into the resulting equation yields

$$\ddot{\alpha} = -CM\alpha^n \tag{8.16}$$

$$M = \frac{1}{m_1} + \frac{1}{m_2} \tag{8.17}$$

Multiplying both sides of (8.16) by $\dot{\alpha}$ and integrating gives

$$(\dot{\alpha}^2 - v_0^2) = -\frac{2CM}{n+1}\alpha^{n+1} \tag{8.18}$$

It should be noted that α reaches its maximum value when $\dot{\alpha} = 0$, therefore

$$\alpha_{max} = \left[\frac{(n+1)v_0^2}{2CM}\right]^{1/n+1} \tag{8.19}$$

8.4 Validation of the Analytical Model

As explained earlier, the developed analytical model, which is based on the Hertz contact law, requires values of the two contact parameters of Hertz. Therefore, the first step would be to calibrate the contact parameters for the 3DFML. For that, a finite element model was developed to simulate the contact-indentation response of the 3DFML. The FE results are

compared against the experimental results to ensure the integrity of the contact parameters. Once the parameters are established, they are plugged into the proposed analytical formula to calculate the maximum impact force and displacement. The integrity of the obtained results is verified by comparing them with those obtained experimentally and numerically.

8.4.1 Experiments

A 3DFML panel is consisted of three different constituents: magnesium alloy sheets, 3DFGF-reinforced epoxy and a polyurethane foam. AZ-31B magnesium sheets with thickness of 0.5 mm were supplied by Metalmart International (Commerce, CA). The 3DFGF fabric with thickness of 4 mm was acquired through China Beihai Fiberglass, Co. Ltd. (Jiujiang City, China). The resin used to impregnate the fabric was Araldite LY 564 (Bisphenole-A), a low viscosity and warm curing epoxy resin, along with Aradur 2954 (cycloaliphatic polyamine) hardener, both supplied by the Huntsman Co. (West Point, GA). To further enhance the mechanical properties and energy absorption of the fabric, a two-part polyurethane foam was injected into the core cavities of the cured 3DFGF-epoxy. The foam was acquired through US Composite (West Palm Beach, FL 33407). The mechanical properties of all constituents are presented in Table 8-1.

Table 8-1. Mechanical Properties of Materials

Material	Mechanical Properties
Magnesium AZ31-B	ρ = 1780 kg/m^3, E = 36 GPa, v = 0.3, σ_y = 230 MPa
3DFGF	Fiberglass: ρ = 1750 kg/m^3, E_1 = 37 GPa, E_2 = 8 GPa, v_{12} = 0.31, G_{12} = G_{13} = 4.7 GPa, G_{23} = 3.2 GPa, X^T = 780 MPa, X^C = 750 MPa, Y^T = 50 MPa, Y^C = 120 MPa Foam: ρ = 128 kg/m^3, E = 50 MPa, v = 0, K = 1.1, K_t = 0.8

Impact tests were carried out using a modified Charpy-based impact test equipment presented in Figure 8-4. It consists of a pendulum, which can be released from different angles, hitting the impactor, thus transferring various levels of impact energy to the specimen. The specimen is clamped and held by two square thick steel plates with a large circular perforation, as lustrated in Figure 8-4. A dynamic load cell and a dynamic linear-variable differential transformer (DLVDT) are used in the set-up to capture and record the impact load and specimen's centre-region deformation, respectively. Furthermore, three proximeter sensors are mounted to measure the impact velocity, as well as triggering the data-acquisition to record the data. A high-speed camera is also used to record the impact event. The captured images are used to evaluate the damage and failure modes.

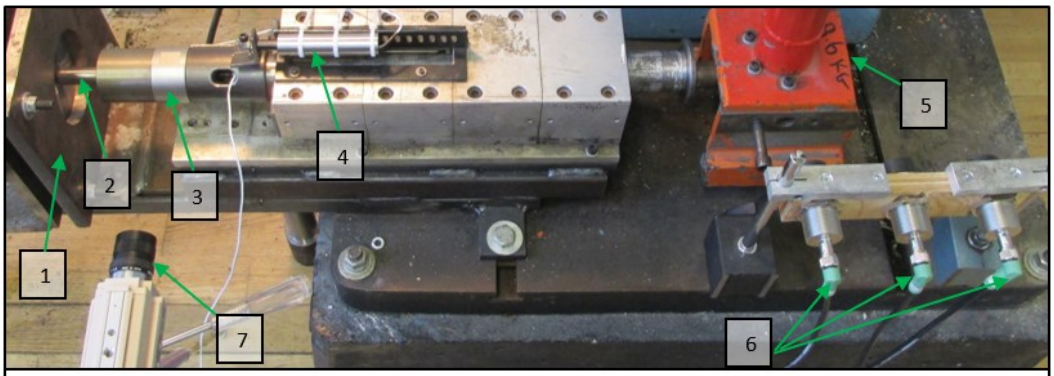

1. Fixture used to hold the specimen, 2. Impactor, 3. Dynamic load cell, 4. Dynamic LVDT, 5. Hammer, 6. Proximity sensors, 7. High speed camera

Figure 8-4. The Impact test set up

8.4.2 Finite Element Simulations

The FE simulation were performed using the commercial FE software ABAQUS/Explicit. All three constituents of 3DFML and impactor were simulated (See Figure 8-5). The impactor was assumed to be rigid and simulated as a rigid solid with the same mass and radius of the impactor. Magnesium sheets was simulated using eight-node solid element

(C3D8R) of ABAQUS/Explicit. The magnesium was defined using as an elastic-plastic material with strain-dependent behavior in conjunction with a ductile damage model to simulate evolution of the damage. Moreover, the fiberglass fabric parts of 3DFGF were defined as “lamina” type and meshed using the reduced integration shell element (S4R) available in ABAQUS/Explicit. The damage mechanism of fabric was established using the Hashin failure criterion, in conjunction with an energy-based damage evolution. Furthermore, the crushable foam model of ABAQUS/Explicit was utilized to simulate the response of foam core constituent. Isotropic hardening parameter for the core was established by conducting the standard uniaxial compression test. All three constituents of 3DFMLs were tied together.

The general surface-to-surface contact algorithm was used to trace contact of impactor and 3DFMLs. The contact algorithm accounts for the normal hard contact, as well as the tangential component of contact, by incorporating a friction coefficient of *0.3*. Due to two axes of symmetry (i.e., x and y axis), the model consisted of a quarter symmetry portion of the geometry. Convergence analysis was performed to establish an adequately fine mesh so that the response of the system could be simulated with acceptable accuracy with an optimal CPU time.

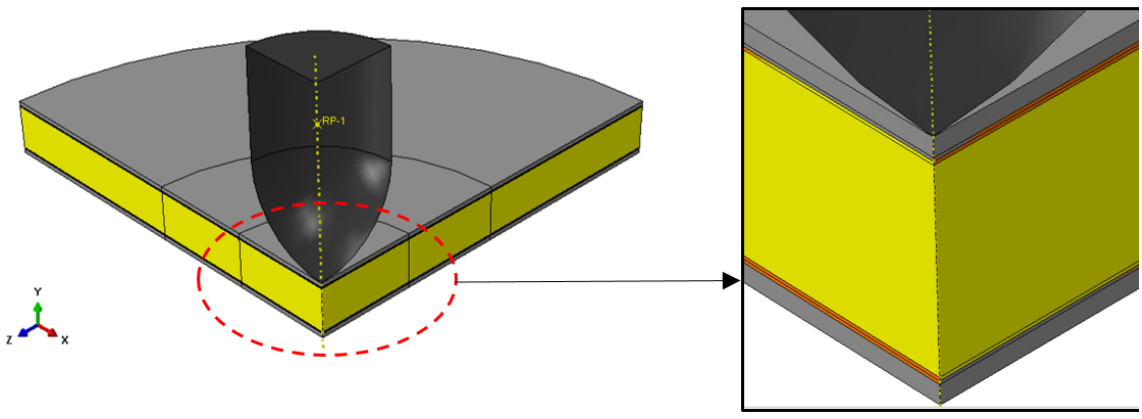

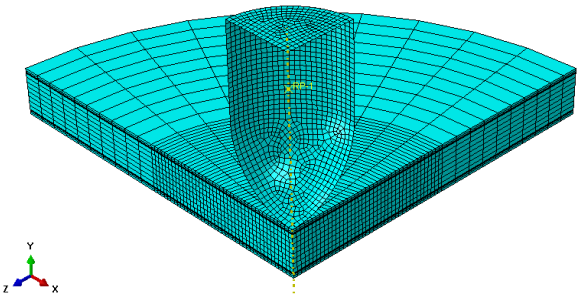

Figure 8-5. Details of FE model and mesh of the reinforced-3DFML

8.5 Results and Discussion

8.5.1 Calibration of Contact parameters

Indentation tests were conducted in order to establish and calibrate the contact parameters. Three configurations of 3DFMLs were considered, as illustrated in Figure 8-6. FE models of the configurations were constructed, and various values of the parameters were tried to match the FE results to those obtained experimentally. Variation of the contact force versus indentation depth for the three configurations obtained experimentally and from FE simulations are plotted in Figure 8-7.

3DFML 3DFML-2/2 3DFML-2/3

Figure 8-6. Three configurations of FML specimens considered

The load-indentation curves have two distinct segments: loading and unloading. The contact law presented in equation (8.2) describes the loading phase; therefore, the values of contact parameters, C and n, are established using the data related to the first segment of the curves.

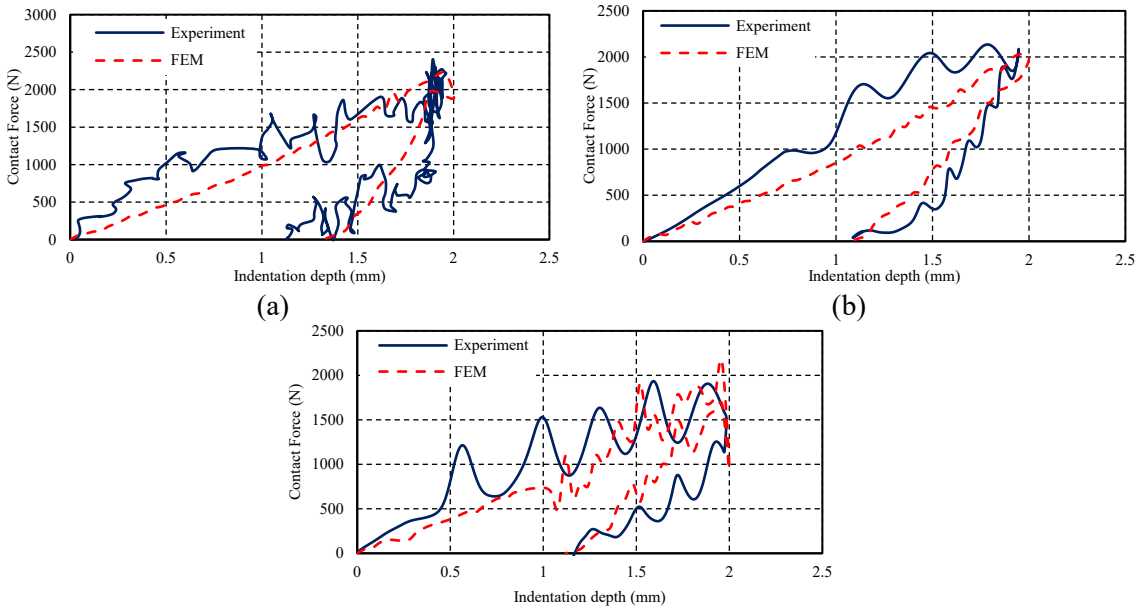

Figure 8-7. Contact force versus indentation depth for (a) 3DFML, (b) 3DFML-2/2 and (c) 3DFML-2/3.

Comparison of the experimental and FE results indicates that the FE framework could predict the response of 3DFML subject to the indentation type loading with a reasonable accuracy. The contact parameters for the three different configurations are established using the nonlinear regression method, with the results summarized in Table 8-2. The results indicate that the contact parameters obtained for all configurations are very similar. It appears that the local indentation created on the loaded face-sheets does not influence the stress state of the other face(s). In other words, only the stiffness of the top core affects its value. The effective stiffness of three configurations are depicted in Figure 8-8 by spring symbols. Therefore, it can be concluded that the contact parameters are only a function of the mechanical properties of the face-sheets and core part of the loaded side.

Table 8-2. Calculated contact parameters of three different configurations of 3DFML

	Baseline-3DFML	*3DFML-2/2*	*3DFML-2/3*
C (N/mm^n)	938.21	880.3	831.4
n	1.18	1.20	1.23

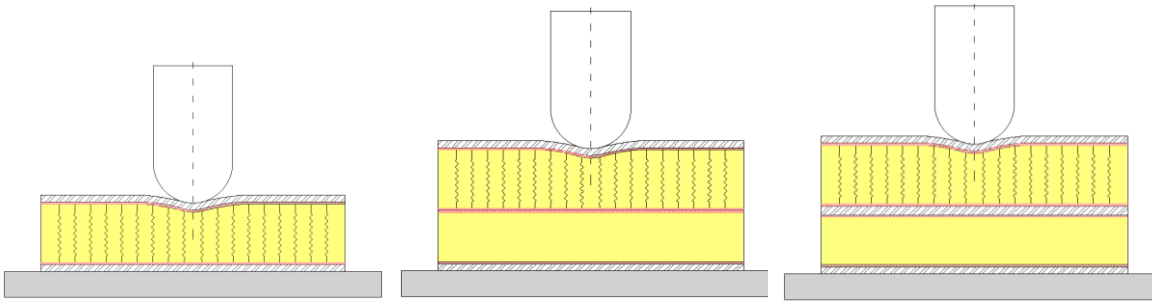

(a) (b) (c)

Figure 8-8. Constituents involved in providing the effective stiffness for the three configurations of 3DFMLs

8.5.2 Effects of Configuration on Contact Parameters

As mentioned earlier, it was postulated that the mechanical properties of the face-sheets and core govern the values of contact parameters in 3DFMLs. To further examine the validity of this hypothesis, the response of other configurations of 3DFMLs are considered here. In an earlier work, the authors conducted a study with the aim of further improving the impact responses of 3DFMLs by inserting additional reinforcement layers of fiberglass fabric on the top and bottom laminae of the 3DFGF. In total, seven different configurations of reinforced 3DFMLs were considered, as summarized in Table 8-3 and pictorially shown in Figure 8-9.

Table 8-3. Configurations of the reinforced-3DFML specimens

Layup ID	Layup Configuration
3DFML	$[Mg/\overline{3DFGF}]_s$
3DFML-G1	$[Mg/\pm 90_2/\overline{3DFGF}]_s$
3DFML-G2	$[Mg/\pm 90/\pm 45/\overline{3DFGF}]_s$
3DFML-G3	$[Mg/\pm 45_2/\overline{3DFGF}]_s$
3DFML-G4	$[Mg/\pm 90/\overline{3DFGF}]_s$
3DFML-G5	$[Mg/0/\overline{3DFGF}]_s$
3DFML-G6	$[Mg/\pm 45/\overline{3DFGF}]_s$
3DFML-G7	$[Mg/\pm 90_3/\overline{3DFGF}]_s$

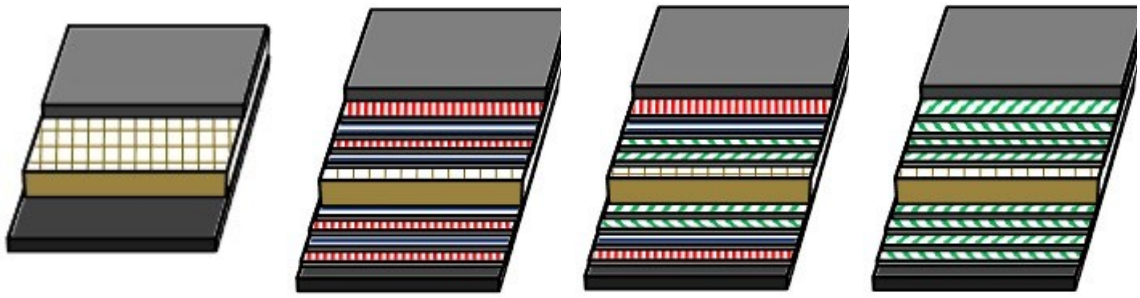

(a) (b) (c) (d)

Figure 8-9. Schematics showing the considered layup configurations of non-reinforced and reinforced-3DFMLs; (a) baseline 3DFML, (b) 3DFML-G1, (c) 3DFML-G2, (d) 3DFML-G3

Figure 8-10. Section of 3DFML reinforced with additional glass fabrics

The response of such sandwich panels subject to indentation load caused by a spherical indenter can be analytically modeled by assuming the top face-sheets acting as a plate resting on an elastic foundation, subjected to a concentrated load. The force-deflection relationship of a plate on elastic foundation under a concentrated load *P* can be computed by the following equation (Timoshenko and Woinowsky-Krieger 1959):

$$\mathrm{w}_{max} = \frac{P}{8\sqrt{Dk}} \tag{8.20}$$

where *D* and *k* are the bending rigidity of plate and stiffness of foundation, respectively. In the case of reinforced-3DFMLs considered here, the core's elastic modulus is constant for all cases. As a result, the force-indentation relation of the reinforced-3DFMLs would be dependent on the bending rigidity of the face-sheets. Assuming that parameter *n* in Equation (8.2) is constant for all types the 3DFMLs, then it may be concluded that parameter *C* would be a function of the bending rigidity of face-sheets. Therefore:

$$C^{(*)} = \sqrt{\frac{D^{(*)}}{D^{(0)}}} C^{(0)} \tag{8.21}$$

Subscripts *(0)* and *(*)* refer to the baseline- and reinforced-3DFML, respectively, and D is the bending rigidity of the face-sheets. Using the mentioned assumption, equation (8.2) can be rewritten as follows:

$$P = \sqrt{\frac{D^{(*)}}{D^{(0)}}} C^{(0)} \alpha^n \tag{8.22}$$

To validate equation (8.22), indentation behavior of the seven 3DFML configurations is simulated numerically with the established FE framework demonstrated earlier. In addition, equation (8.22) is also used to calculate the force-indentation response, and the values are compared against those obtained numerically.

The FE results, as well as those obtained using equation (8.2) are illustrated in the form of variations of the contact force as a function of indentation depth for all configurations in Figure 8-11. It can be seen that the maximum deviation between the results obtained based on the analytical solution, and numerical simulation is less than 12%.

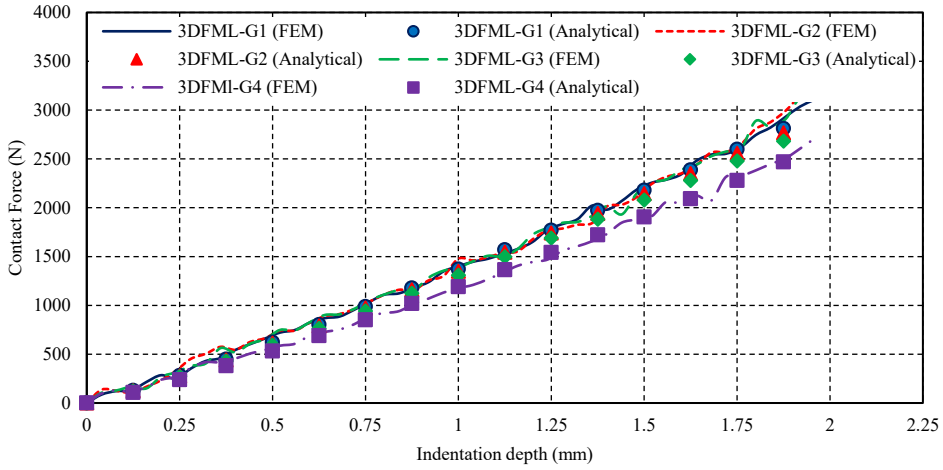

(a)

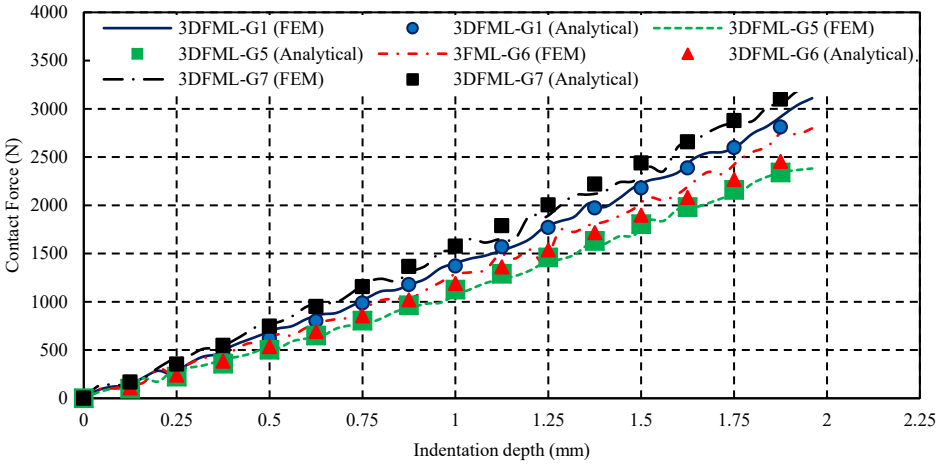

(b)

Figure 8-11. Numerical and analytical contact force-indentation for baseline and reinforced 3DFMLs

8.5.3 Influence of Indenter Geometry

Another parameter that affects the contact (more specifically, affecting the contact stiffness, *C*), is the indenter geometry. According to Hertz's contact law, the contact stiffness for contact between two homogenous isotropic solids can be evaluated by following equation (Zukas, Nicholas et al. 1992):

$$C = \frac{4}{3} E\sqrt{r} \tag{8.23}$$

where *E* is the function of elastic modulus of the two solids, *r* is the radius of curvature of the indenter. Therefore, it can be assumed that the contact stiffness, *C*, for 3DFMLs would be a function of the radius of impactor according to following relationship:

$$C^{(*)} = \sqrt{\frac{r^{(*)}}{r^{(0)}}} C^{(0)} \tag{8.24}$$

Subscripts *(0)* and *(*)* represent the state (size) of the indenter at its initial stage (i.e., $r = 8$ mm) and new state (size). Consequently, equation (8.2), which represents the force-indentation relation, can be rewritten as

$$P = \sqrt{\frac{r^{(*)}}{r^{(0)}}} C^{(0)} \alpha^n \tag{8.25}$$

The results produced by Equation (8.25) is verified by comparison with numerical results, as illustrated in Figure 8-12. The figure presents the variation of the contact force as a function of indentation depth for the 3DFML subjected to four different sizes of indenters. As can be seen, good agreement is observed between the numerical and analytical results, verifying the integrity of the analytical model.

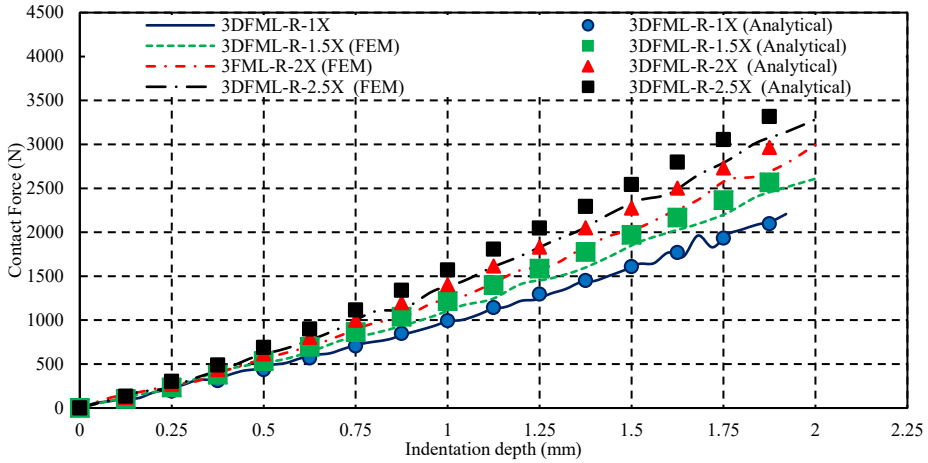

Figure 8-12. Variation of contact force as a function of indentation depth caused by different size indenters on the base 3DFML

Furthermore, to predict the contact force-indentation response of 3DFMLs with any configuration, subjected to any size indenter, one can use a more general form of the above equation, as follows:

$$P = \sqrt{\frac{r^{(*)}D^{(*)}}{r^{(0)}D^{(0)}}} C^{(0)} \alpha^n \tag{8.26}$$

The predicted responses of the 3DFML subjected to various size indenters obtained using equation (8.26) are compared with the results produced by FE, illustrated in Figure 8-13.

A maximum discrepancy of 14% is observed between the predicted analytical and FE values, which reflects the reasonable accuracy of the proposed analytical solution. As a result, equation (8.10) can be rewritten in the following more general form for calculating the contact force.

$$\frac{1}{2}mv^2 = \frac{\left[\frac{{P_{max}}^{n+1}}{C^{(0)}}\sqrt{\frac{r^{(0)}D^{(0)}}{r^{(*)}D^{(*)}}}\right]^{1/n}}{(n+1)} + \frac{16P_{max}^2\pi DG\left(t_f+t_c\right)}{4Dt_c\left(1+2\ln\frac{r^{(*)}}{a_c}\right)+G\left(t_f+t_c\right)(1-\nu)(3+\nu)R^2} \tag{8.27}$$

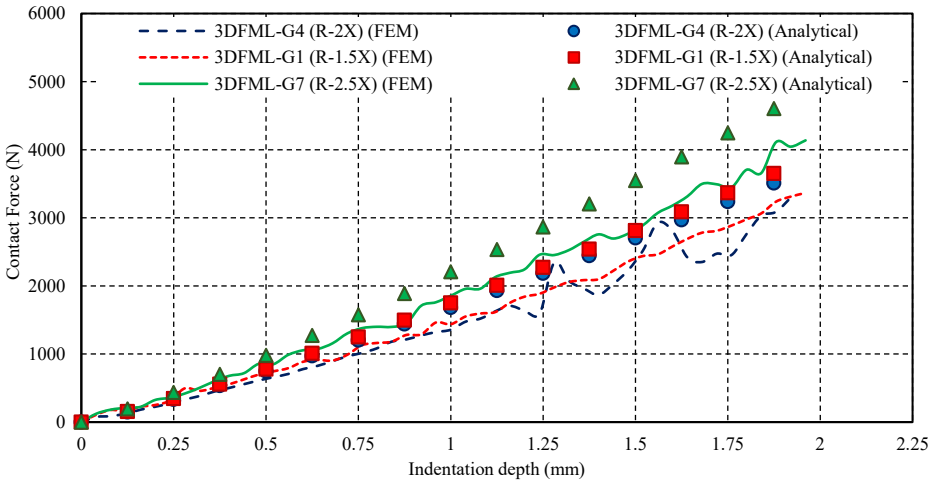

Figure 8-13. Variation of the contact force as a function of indentation developed by different size indenters on the 3DFMLs

8.6 Analysis of the Low-velocity Impact

8.6.1 Impact Load and Deformation

The developed methodology can be extended to predict the impact force generated on 3DFMLs resulting from a low-velocity impact. Here, equations (8.27) and (8.19) are used to predict the response (i.e., the impact force and deformation) of the baseline-3DFMLs at

its centre, subjected to three different impact energies. The values of contact parameters of C and n calculated earlier were used to predict the impact response. Similarly, finite element simulation of the event was also carried out. The results obtained from the analytical solution and FE simulation are plotted in the form of variation of the impact force and deformation as a function time, as illustrated in Figure 8-14. As seen, there is good agreement between the results.

Additional analyses were carried out to understand the variation in response of the panel to various impact energies, since the response would be highly nonlinear. Results obtained by the analytical model and FE simulations are presented in Figure 8-15. As can be seen, the maximum impact force increases more or less linearly as a function of the impact energy up to an energy level which causes crack initiation on the target, after which the plate gradually loses its load-carrying capacity. In a usual manner, the results obtained numerically is stiffer than those obtained analytical, with the maximum difference of 25%.

As for the deformation at the centre of the 3DFML, it also increases in proportion to the impact energy. The prediction of the analytical method correlates quite closely to those obtained from FE simulation. However, once a crack is developed in the target, the deviation between the predicted analytical results and numerical values increases since the developed analytical model does not account for any damage initiation. Notwithstanding, the maximum difference between the FE and analytical results within energy levels below that causing a crack is only 21%.

It should be noted that in real practice, where safety factors of two or higher are often used, one can effectively use the analytical model to predict the response of such complexly

configured panels in a relatively reliable manner, even when the panel has succumbed to damage.

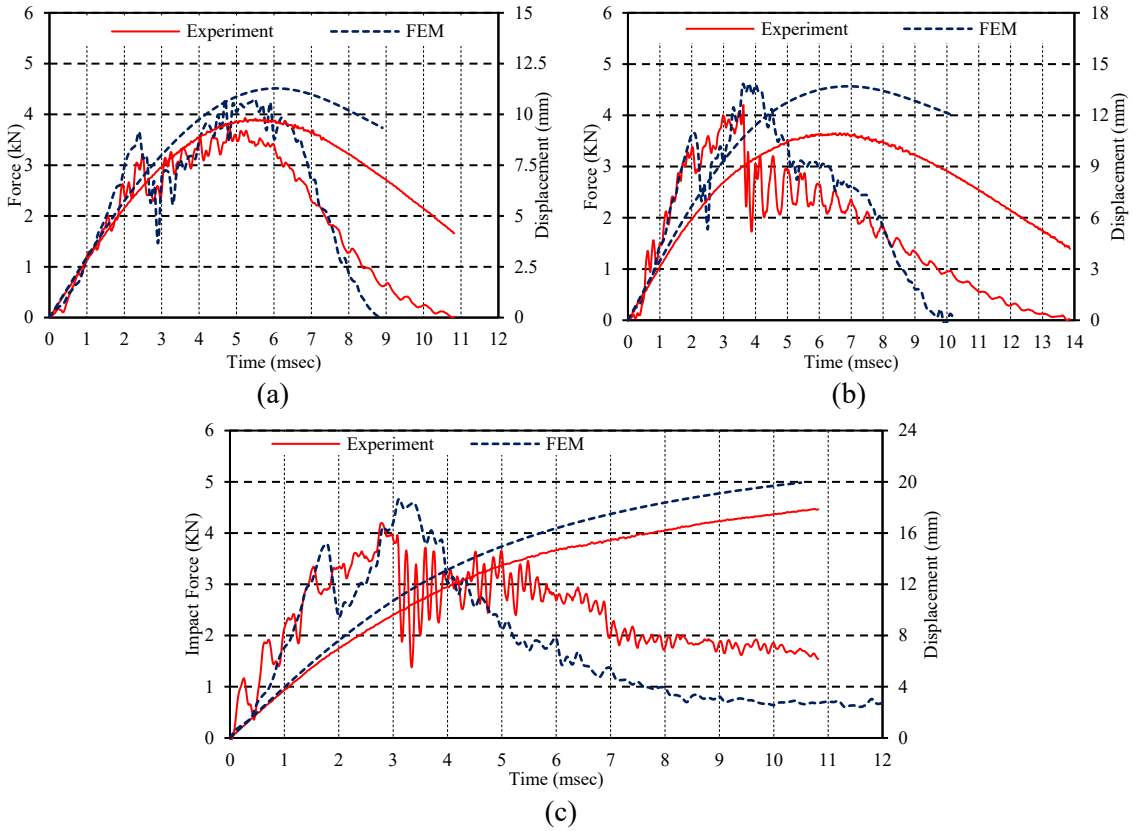

Figure 8-14. Comparison of the force- and displacement-time histories of the 3DFML subjected to impact energies of (a) 25J, (b) 34J and (c) 44J

To further examine the integrity of both the analytical and numerical models, their predicted results were compared against experimental ones. The impact experiments were performed under three different impact energies. The maximum sustained load and centre panel displacement obtained from the analytical and numerical models are compared against the experimental values as shown Figure 8-16. The error margins (% error) between the numerical and analytical results against the experimental results are summarized in Table 8-4. It can be seen that both the analytical and FE models could predict the panels'

response fairly accurately, up to the onset of a crack on the target, after which the margin of error is increased, though in a much lower rate when compared to the FE results.

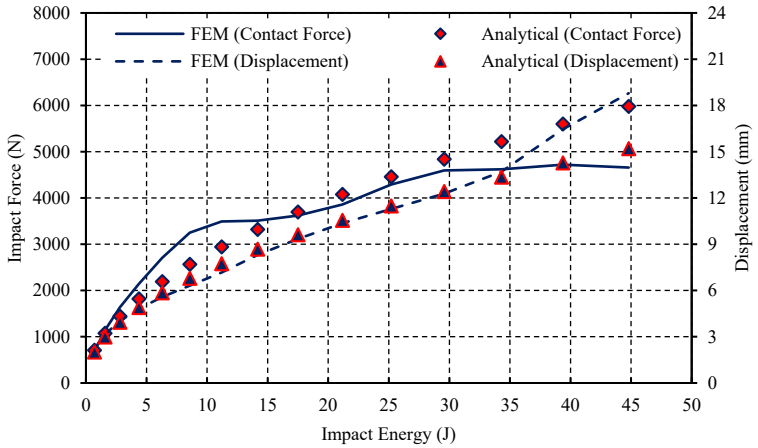

Figure 8-15. Comparison of the maximum contact force and centre panel deflection of baseline-3DFML impacted by various energy levels, obtained analytically and numerically

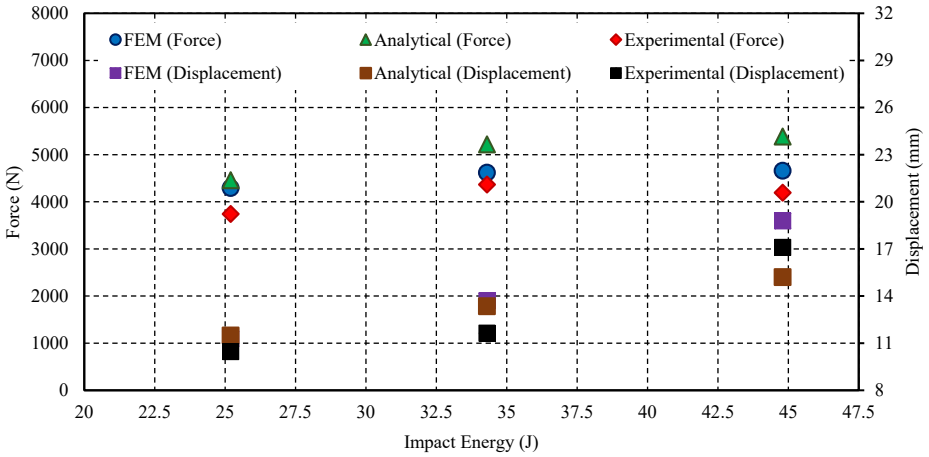

Figure 8-16. Comparison of the maximum sustained impact force and deformation as a function of the applied impact energy of the 3DFML, predicted by the analytical and FE models against the experimental values

Table 8-4. Error margin between the results produced by the analytical and FE models with respect to the experimental results

Impact Energy (J)	FE Results		Analytical Results	
	Impact Load	Deformation	Impact Load	Deformation
25	14.7%	7.8%	19.1%	9.8%
34	5.7%	17.7%	19.5%	14.7%
44	11.0%	9.9%	25.3%	11.1%

8.6.2 Influence of Configuration

As mentioned earlier, the energy balance model was generalized and modified to be applicable to different configurations of 3DFMLs. Two different configuration categories were considered. The first one was altering configurations, by using different stacking and numbers of metallic sheets and 3DFGFs. The second category was reinforced-3DFMLs, obtained by insertion of additional layers of unidirectional glass on the top and bottom surfaces of the 3DFGF. Recall that the contact parameters for these two categories were calculated in the previous section; thus, the calibrated contact values were used in conjunction with equation (8.27) to calculate the impact response of reinforced 3DFMLs.

To verify accuracy of the analytical model, three configurations of 3DFML (identified as 3DFML-2/2, 3DFML-2/3 and 3DFML-G1) were also examined experimentally. Figure 8-17 presents the damage pattern of 3DFML-2/2 and 3DFML-2/3 obtained experimentally and numerically. Good agreement between the experimental and numerical results is observed.

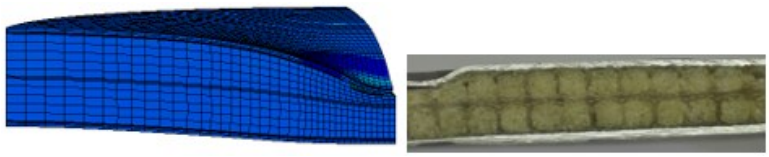

(a) 3DFML-2/2 subjected to 20J impact energy

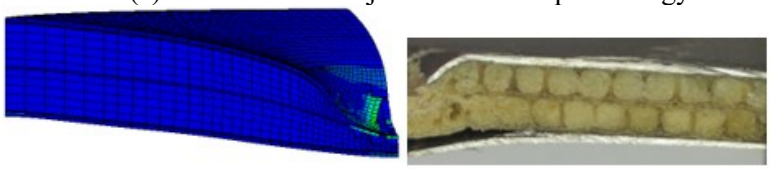

(b) 3DFML-2/2 subjected to 45J impact energy

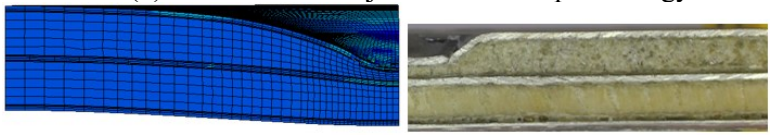

(c) 3DFML-2/3 subjected to 20J impact energy

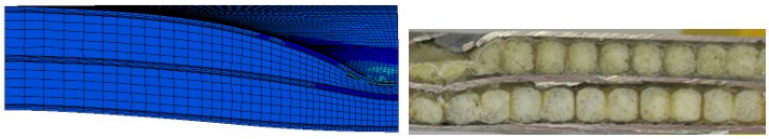

(d) 3DFML-2/3 subjected to 45J impact energy

Figure 8-17. Comparison of damage patterns of 3DFML-2/2 and 3DFML-2/3 obtained through FE simulation (left) and experiments (right)

Moreover, Figure 8-18 presents the predicted analytical, numerical and experimental values of the maximum impact force and deformation values at the centre of 3DFML-G1. Comparison of the results for all three cases implies that the analytical model can reliably predict the impact response of different configurations of 3DFMLs. As seen earlier, in general, the accuracy of the predicted results is greater at lower impact energies. At certain impact energy, a crack develops on the target, which causes some deviation between the analytical results and the experimental and numerical values; however, the error margin reaches a maximum of 25%. As also seen previously, in the usual expected way, the FE predicted results are stiffer than the actual results.

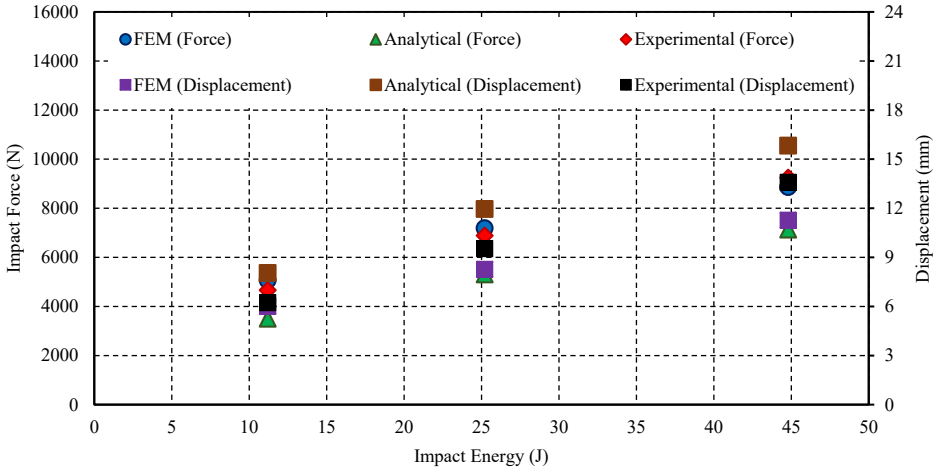

Figure 8-18. Comparison of the predicted results obtained by the analytical and FE models and experimental values for 3DFML-G1

Furthermore, comparisons of the predicted analytical and numerical results of 3DFML-G4 and 3DFML-G7 panels are presented in Figure 8-19. Similarly, a good agreement is seen

between the results predicted by the model and those produced by the FE simulation prior to development of damage on the target.

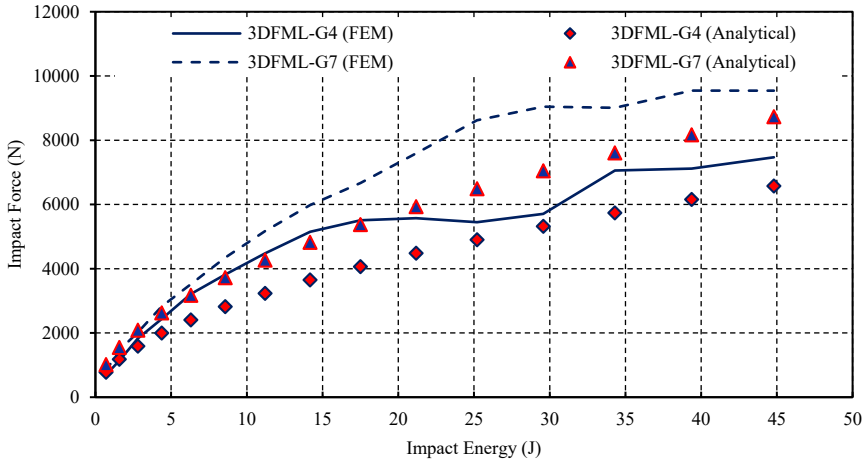

Figure 8-19. Comparison of the maximum contact force of 3DFML-G4 and 3DFML-G7 impacted by various energy levels, obtained analytically and numerically

8.6.3 Influence of Impactor Size

When the influence of indentation was being examined earlier, it was observed that indenter's size had a considerable influence on the response of 3DFMLs. Here the influence of impactor size on the performance 3DFML are numerically and analytically investigated. Two different diameters of impactors (i.e., one and half and two times the initial impactor's diameter), are considered. The results for both cases are very similar in trend; therefore, for the space sake, only the first case's (the one and half-time diameter) results are summarized in Table 8-5.

Table 8-5. Comparison of the maximum contact force and central deformation of baseline-3DFML impacted by 1.5X large impactor

Impact Energy (J)	FE Results		Analytical Results	
	Impact Load	Deformation	Impact Load	Deformation
5	2259.1	4.5	2062.5	4.6
10	3937.8	6.5	3335.6	7.3
15	4513.3	7.1	3762.4	8.2
20	5688	8.3	4618.6	10.1
25	6293.4	8.8	5047.8	10.9

30	6886.2	9.4	5477.8	11.8
35	7564.8	9.9	5908.3	12.7

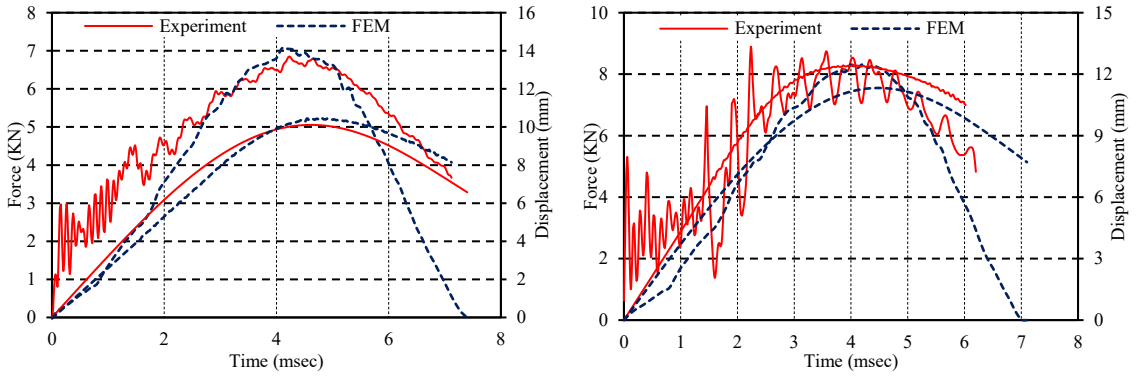

Figure 8-20. Force- and displacement-time histories of 3DFML-2/2 hit by large impactor at impact energy level (a) 30J and (b) 45J

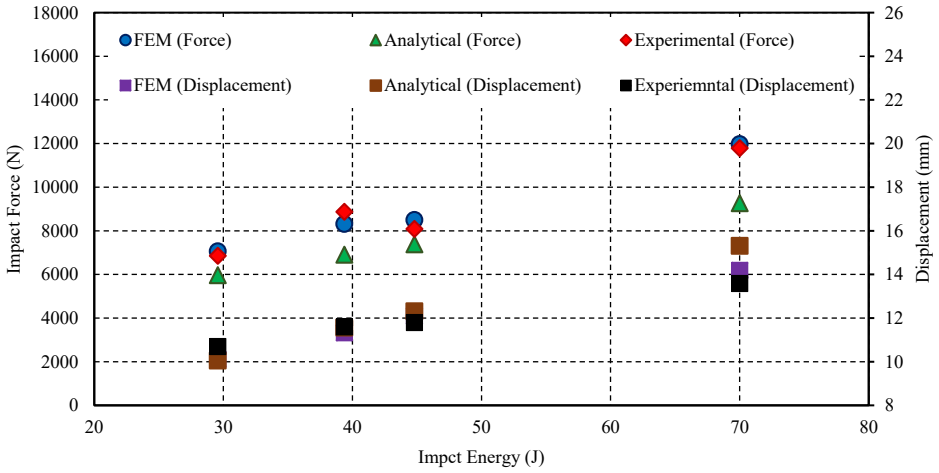

Figure 8-21. Comparison of the results predicted by the analytical with the FE and experimental values for 3DFML-2/2 hit by large impactor (variation of the sustained impact force and deformation as a function of applied impact energy)

Accuracy of the analytical model was further investigated by experimentally examining the effects of both material configurations and geometry of impactors in a unit model. Therefore, 3DFML-2/2 samples were fixed in a larger fixture (150 diameter) and hit by an impactor with a 50mm diameter. Figure 8-20 presents the impact response of 3DFML-2/2 hit by large impactors obtained experimentally and numerically. The predicted analytical

values for maximum impact force and centre-plate deformation of four different impact energies were compared against the experimental and numerical results and illustrated in Figure 8-21. It can be seen that at lower impact energies, the differences between analytical solution and FEM and experimental results are less than 12% and 5%, respectively. As expected, however, the error margin increases at energies that cause crack development in the plates.

8.6.4 Major Contributing Mechanisms in Absorbing Energy

The energy balance approach used in developing the analytical model assumes that the impact energy is absorbed by the bending and shear deformations of the target and the resulting contact friction between the impactor and panel. Therefore, to gain a better perspective of the response of 3DFML panels under impact loading, the contribution of each of the resisting parameters contact, bending and shear in the absorption of impact energy were investigated. Figure 8-22 illustrates the variation in the fraction of absorbed energies of the baseline-3DFML by the abovementioned mechanisms. As can be seen, approximately 60% of the total energy is absorbed by bending mechanism, while less than 10% of the entire energy is absorbed by shear deformation. The remaining fraction of the energy is absorbed by contact friction.

Influences of the material configuration and impactor geometry on the three energy absorbing mechanisms were also examined. The fractions of absorbed energy for the six different configurations of 3DFMLs are presented in Figure 8-23. It should be noted that in order to calculate the contributions of the three mechanisms, the energy balance represented by equation (8.11), which was rewritten it the following form was used:

$$\frac{1}{2}mv_0^2 = \frac{1}{2}\frac{P_{max}^2}{K_{bs}} + \frac{P_{max}\alpha_{max}}{n+1} \tag{8.28}$$

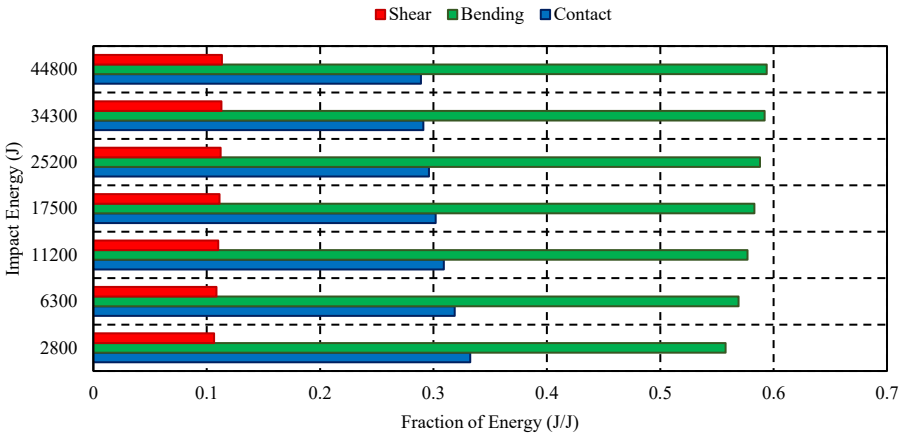

Figure 8-22. Fractions of the absorbed energy by shear, bending and contact for the baseline-3DFML subjected to various impact energies

The first and second terms on the right side of equation (8.28) represent the energies endured by shear/bending and contact mechanisms, respectively. The results reveal that insertion of the reinforced layers to the interface of metal and 3DFGF did not change the contribution of each of these two terms and their associated mechanisms in a major way. However, the proportions changed somewhat significantly for 3DFML-2/2 and 3DFML-2/3 configurations. In other words, when considering the contact energy in equation (8.28), under the same impact energy, the values of both P_{max} and α_{max} in the reinforced 3DFMLs increase in comparison to those in baseline 3DFML. This would indicate an increase in contribution of the contact mechanism in absorbing the energy. However, when examining the first term, while the K_{max} values increase significantly in the case of two reinforced 3DFMLs, the increase in P_{max} remains relatively insignificant. Nevertheless, still the bending mechanism's contribution surpasses that due to contact friction; moreover, the shear deformation's contribution remains comparatively negligible (only resisting 10% of the total energy).

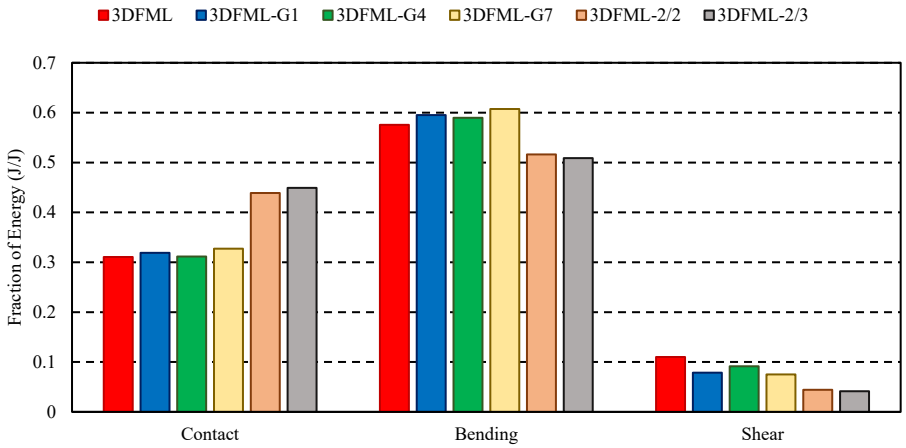

Figure 8-23. Fractions of absorbed energy by (a) contact, (b) bending and (c) shear deformations of differently configured 3DFMLs

To examine the influence of impactor's geometry, the absorption mechanism of a plate impacted by two different diameters of an impactor is investigated. The results are presented in Figure 8-24. The results reveal that the increase in diameter of the impactor would increase the shear and bending mechanism's contribution in absorbing energy. It can also be observed that the rate of increase of absorption by shear deformation is greater than that by bending. Moreover, the increase in impactor diameter resulted in a decrease in the contribution of the contact friction in absorbing the energy.

Figure 8-24. Fraction of absorbed energy by contact, bending and shear deformations of the baseline-3DFMLs impacted by two different sizes of impactors

8.7 Summary and Conclusion

A practical analytical model is developed for predicting the impact response of 3DFML panels, which incorporates the effect of contact, and bending and shear deformations. The model is based on the energy balance approach, examining the response of various configurations of 3DFML subject to both static (indentation) and low-velocity impact loadings. The contact between the impactor and panel is modeled using the Hertz contact law. Moreover, the effects of 3DFML configurations and loading tup size on the resulting contact are examined. Finally, a general formulation for predicting the response of differently configured panels to loadings is developed; the formulation provides results for both impact force and centre-plate deformation.

Responses of various configurations of the 3DFML, categorized based on the number of 3DFGFs, metallic layers and additional reinforcing layers, were examined by the proposed analytical model. To validate and verify accuracy of the analytical model, both indentation and impact tests were performed on the different configurations of 3DFML. Moreover, a FE model was developed to numerically predict the indentation and impact responses of 3DFMLs. The comparison of analytical results with numerical and experimental results indicated good agreements, verifying the integrity of the proposed analytical model. Comparison of the results revealed that results produced by the analytical model would be accurate up to the stage when a crack develops on the target. Moreover, it was observed the predicted maximum impact force has higher accuracy in comparison to the predicted centre-plate deformation values. It should be noted that in practice, the maximum values would be of main interest, thus the proposed equations would serve useful. Moreover, considering the fact that usually a minimum factor of safety of two is often used in practice;

therefore, even the post-maxima values predicted by the proposed model could also be used with a reasonable degree of confidence.

In addition, to gain a better understanding of the behavior of 3DFMLs under impact loading, contributions of the mechanisms that participate in absorbing the energy (i.e., the bending and shear deformations, and contact friction) were investigated. The results revealed that the insertion of additional reinforcing layers did not influence the participating fractions of absorbed energy by the mechanisms. In all cases studied, the contribution of shear deformation to absorb the energy was below 10% compared to the other two mechanisms; therefore, it could be concluded that one may neglect calculation of energy associated to shear deformation in the analytical model thus increasing the efficiency of the model. Moreover, the effect of impactor area on the energy absorption of 3DFMLs was also investigated. The results revealed that an increase in impactor's area may increase the contributions of bending and shear deformation in absorbing impact energy. It should be noted that contribution of shear deformation in absorbing energy could not be ignored in cases where large-size impactors are used.

8.8 Acknowledgement

This financial support received through the National Science and Engineering Research Council of Canada (NSERC) in support of this study is gratefully appreciated. The Killam scholarship, Amelia Earhart fellowship and Nova Scotia Research and Innovation Graduate scholarship awarded to the first author are also gratefully acknowledged.

8.9 References

Abdullah, M. and W. Cantwell (2006). "The impact resistance of polypropylene-based fibre–metal laminates." Composites science and technology 66(11): 1682-1693.

Alderliesten, R., C. Rans and R. Benedictus (2008). "The applicability of magnesium based Fibre Metal Laminates in aerospace structures." Composites Science and Technology 68(14): 2983-2993.

Asaee, Z., M. Mohamed, D. De Cicco and F. Taheri (2017). "Low-Velocity Impact Response and Damage Mechanism of 3D Fiber-Metal Laminates Reinforced with Amino-Functionalized Graphene Nanoplatelets." International Journal of Composite Materials 7(1): 20-36.

Asaee, Z., M. Mohamed, S. Soumik and F. Taheri (2017). "Experimental and numerical characterization of delamination buckling behavior of a new class of GNP-reinforced 3D fiber-metal laminates." Thin-Walled Structures 112: 208-216.

Asaee, Z., S. Shadlou and F. Taheri (2015). "Low-velocity impact response of fiberglass/magnesium FMLs with a new 3D fiberglass fabric." Composite Structures 122: 155-165.

Asaee, Z. and F. Taheri (2015). Characterization of the Mechanical and Impact Response of a New-Generation 3D Fiberglass Fabric. American Society of Composites-30th Technical Conference.

Asaee, Z. and F. Taheri (2016). "Experimental and numerical investigation into the influence of stacking sequence on the low-velocity impact response of new 3D FMLs." Composite Structures 140: 136-146.

Asaee, Z. and F. Taheri (2016). Experimental Studies on the Impact Response of 3D Fiberglass Fabric Subject to Different Size Impactors. Proceedings of the American Society for Composites: Thirty-First Technical Conference.

Asaee, Z., F. Taheri and T. Lay (2016). Innovative 3D Glass Fiber Metal Laminate. Advanced Materials - TechConnect Briefs 2016.

Botelho, E. C., R. A. Silva, L. C. Pardini and M. C. Rezende (2006). "A review on the development and properties of continuous fiber/epoxy/aluminum hybrid composites for aircraft structures." Materials Research 9(3): 247-256.

Caprino, G., V. Lopresto and P. Iaccarino (2007). "A simple mechanistic model to predict the macroscopic response of fibreglass–aluminium laminates under low-velocity impact." Composites Part A: Applied Science and Manufacturing 38(2): 290-300.

Caprino, G., G. Spataro and S. Del Luongo (2004). "Low-velocity impact behaviour of fibreglass–aluminium laminates." Composites Part A: Applied Science and Manufacturing 35(5): 605-616.

Carrillo, J. and W. Cantwell (2009). "Mechanical properties of a novel fiber–metal laminate based on a polypropylene composite." Mechanics of Materials 41(7): 828-838.

Chai, G. B. and P. Manikandan (2014). "Low velocity impact response of fibre-metal laminates–A review." Composite Structures 107: 363-381.

Cortes, P. and W. Cantwell (2004). "The tensile and fatigue properties of carbon fiber-reinforced PEEK-titanium fiber-metal laminates." Journal of reinforced plastics and composites 23(15): 1615-1623.

Cortes, P. and W. Cantwell (2006). "The prediction of tensile failure in titanium-based thermoplastic fibre–metal laminates." Composites Science and Technology 66(13): 2306-2316.

Ghassemieh, E. (2011). Materials in automotive application, state of the art and prospects, INTECH Open Access Publisher.

Hertz, H. (1881). "On the contact of elastic solids." J. Reine Angew Math. 92: 156-171.

Hoo Fatt, M. S., C. Lin, D. M. Revilock and D. A. Hopkins (2003). "Ballistic impact of GLARE™ fiber–metal laminates." Composite Structures 61(1): 73-88.

Hosseini, S. A., M. Sadighi and R. Maleki Moghadam (2015). "Low-velocity impact behavior of hollow core woven sandwich composite: Experimental and numerical study." Journal of Composite Materials 49(26): 3285-3295.

Johnson, K. (1982). "One hundred years of Hertz contact." proceedings of the Institution of Mechanical Engineers 196(1): 363-378.

Kiratisaevee, H. and W. Cantwell (2005). "Low-velocity impact response of high-performance aluminum foam sandwich structures." Journal of Reinforced Plastics and Composites 24(10): 1057-1072.

Lin, C. and M. S. H. Fatt (2006). "Perforation of Composite Plates and Sandwich Panels under Quasi-static and Projectile Loading." Journal of Composite Materials 40(20): 1801-1840.

Marsh, G. (2014). "Composites and metals–a marriage of convenience?" Reinforced Plastics 58(2): 38-42.

Morinière, F., R. Alderliesten, M. Sadighi and R. Benedictus (2013). "An integrated study on the low-velocity impact response of the GLARE fibre-metal laminate." Composite Structures 100: 89-103.

Payeganeh, G., F. A. Ghasemi and K. Malekzadeh (2010). "Dynamic response of fiber–metal laminates (FMLs) subjected to low-velocity impact." Thin-Walled Structures 48(1): 62-70.

Reid, S. R. and H. M. Wen (2000). 8 - Perforation of FRP laminates and sandwich panels subjected to missile impact. Impact Behaviour of Fibre-Reinforced Composite Materials and Structures, Woodhead Publishing: 239-279.

Sadighi, M., R. Alderliesten and R. Benedictus (2012). "Impact resistance of fiber-metal laminates: a review." International Journal of Impact Engineering 49: 77-90.

Sadighi, M. and S. A. Hosseini (2013). "Finite element simulation and experimental study on mechanical behavior of 3D woven glass fiber composite sandwich panels." Composites part b: engineering 55: 158-166.

Timoshenko, S. P. and S. Woinowsky-Krieger (1959). Theory of plates and shells, McGraw-hill.

Vlot, A. (1993). "Impact properties of Fibre Metal Laminates." Composites Engineering 3(10): 911-927.

Vlot, A. (1993). Low-velocity impact loading: on fibre reinforced aluminium laminates (ARALL and GLARE) and other aircraft sheet materials.

Vlot, A. (1996). "Impact loading on fibre metal laminates." International Journal of Impact Engineering 18(3): 291-307.

Vogelesang, L. B. and A. Vlot (2000). "Development of fibre metal laminates for advanced aerospace structures." Journal of Materials Processing Technology 103(1): 1-5.

Zenkert, D. (1997). An Introduction to Sandwich Construction, EMAS.

Zhou, D. and W. Stronge (2006). "Low velocity impact denting of HSSA lightweight sandwich panel." International Journal of Mechanical Sciences 48(10): 1031-1045.

Zukas, J., T. Nicholas, H. Swift, L. Greszczuk and D. Curran (1992). Impact Dynamics. Malabar, Florida, Krieger Publishing Company.

Chapter 9: Conclusion

9.1 Conclusions

The research work presented in this dissertation focused on the development of a novel class of three-dimensional fiber metal laminate (3DFML), consisting of a recently developed 3D fiberglass fabric. The work particularly concentrated on the examination of the low-velocity impact response of various configurations of the 3DFMLs. This section provides a summary of the various studies conducted within the framework of the research, and discusses the resulting achievements. The conclusions made through the studies carried out within the present dissertation will also be outlined in this chapter.

The first phase of this research investigated the performance of 3D E-glass fabrics and assessed their viability as a suitable constituent in forming FMLs that would be particularly resilient against low-velocity impact loading (LVI). For that, LVI responses of a series of 3DFMLs were investigated and compared against the conventionally produced 2D FMLs. The results of this phase of the research revealed that significant differences exist in the damage mechanism of 3D and 2D FMLs. In the case of 2DFMLs, the impact load is resisted by the multiaxial fibers; therefore, a large area of the fabric contributes in resisting the impact energy. As a result, the resulting damaged (delaminated) area would be significantly larger than the cross-sectional area of the impactor. However, in case of the 3DFMLs, the impact energy is absorbed mainly by crushing the vertical fibers and the supporting foam beneath the impact region, which ultimately curbs the extend of the damage. This response is facilitated by the significant damping effect offered by the 3D fabric and its foam infill, which localizes a great portion of the resulting impact induced deformation. In all,

3DFMLs exhibited greater energy absorption capacities in comparison to their conventional 2DFML counterparts.

The next phases of the research (chapters two and three), concentrated on the enhancement of the low-velocity impact performance of 3DFMLs through two different strategies. In the first attempt, the performance of different configurations of 3DFML was investigated. In total, two different thicknesses and four different configurations were examined. The stiffness, strength, energy absorption and failure modes of the 3DFMLs under impact loading were compared. The FMLs were ranked based on comparing the performance of the configurations that had similar flexural stiffness, or having similar weight and cost. The results demonstrated that the thicker 3DFML provided a higher contact stiffness and energy absorption capacity. However, replacement of the thicker 3D fabric with two layers of thinner fabric (which produced the same final thickness as that of the thicker fabric) produced a greater impact capacity. It should be noted that when designing a structural component, the weight and material cost of the component become the two most important parameters governing the design's selection. Therefore, in order to establish the most resilient configuration of the 3DFMLs, an unbiased comparison had to be carried out. For that, the impact strength of the aforementioned configurations was normalized with respect to material's weight and cost. As a result, the most optimized configuration was proved to be the 3DFML consisting of two layers of 4mm-thick fabric, sandwiched in between two sheets of 0.5 mm-thick magnesium alloy.

Furthermore, a finite element framework was developed, whose results were validated by the experimental results. The model is capable of predicting the impact response and failure modes of 3DFMLs with any configuration. The FE model was developed within the

commercial FE software ABAQUS/Explicit, in conjunction with its VUMAT. It could simulate the damage mechanisms in all its constituents. The comparison of FE and experimental results proved that this framework can be used to examine the influence of various parameters affecting the performance of 3DFMLs, in an effective and reliable manner.

The next strategy used for further improving the performance of 3DFMLs under impact loading was reinforcing the FMLs by additional layers of carbon or glass fabrics with various ply sequences. The developed FE model was employed to predict the impact response of the reinforced-3DFMLs under 16 different impact energies. The results revealed that the variation of the maximum force sustained by the 3DFML panels with respect to the impact energy followed a logical trend. Therefore, a semi-empirical equation was developed to predict the gain in load carrying capacity of 3DFMLs panels reinforced with additional layers of the fabrics in reference to the baseline 3DFML. The accuracy of the proposed equation was verified by comparison against the experimental and FE results. The results revealed that fiberglass reinforced-3DFMLs would offer greater impact strength when the material cost is of the concern. However, when material's weight is of concern, then carbon reinforced-3DFMLs would offer comparatively slightly better performance. The other parameter investigated was the layup sequence. The results indicated that $(Mg/\pm 90_2/\overline{3DFGF})_S$ configuration was the most optimal configuration in resisting impact loading conditions.

To further examine the mechanical response of 3DFMLs, their buckling response was investigated, as outlined in chapter 4. Since delamination at the interface of magnesium/3DFGF is one of the most likelihood locations to fail when these 3DFML are

subjected to an in-plane compressive loading, hence, the delaminated buckling response of the 3DFMLs was also investigated. Accordingly, an attempt was made to enhance the interface strength by inclusion of relatively inexpensive GNP particles within the resin at the interface. The effects of GNP content and delamination length were investigated by consideration of four different weight percentages and four delamination lengths. Comparison of the results for different GNP contents revealed that the GNP content of 1wt% produced the most optimal effect and increased the buckling capacity by 50%. In contrast, 2wt% GNP content decreased the buckling capacity due to the agglomeration of GNP particles within the resin. Furthermore, as expected, 3DFMLs specimens hosting an initial delamination showed lower buckling capacities in comparison to the baseline-3DFML specimens. The results revealed that the inclusion of GNP particles did not have an effective role in improving the buckling capacity of the 3DFMLs that hosted relatively large delamination lengths (i.e., delamination to span ratios > 0.3). However, the inclusion of an appropriate GNP content within the resin resulted in a significant improvement in the stability response of 3DFML specimens that hosted shorter delamination lengths. In addition to the experimental investigation, a finite element framework was developed using ABAQUS/CAE software to simulate the buckling behavior of 3DFMLs. The cohesive zone modelling technique was employed to simulate the response of GNP-reinforced interface within the specimens and trace the growth of the delamination present at the metal/3DFGF interface. Comparison of the numerical and experimental results confirmed that the adopted FE framework could accurately predict the buckling capacity of the specimens, as well as their failure modes.

The next phase of research entailed the development of an analytical model by which one could examine the complex load carrying mechanism of each constituent of the 3D fabrics (i.e., the woven fabric layers, fiberglass pillars and foam), when subjected to out-of-plane compressive loading. Appropriate equations were derived through evaluation of integro-differential equations that were constructed to model the deformation of the fiberglass pillars within a unit-cell. Such equations are not solvable analytically, thus, the Rayleigh method was used to solve them. To examine the integrity of the model, it was used to predict the compressive capacity of two different thicknesses of the fabric. The results were compared against the experimental and numerical results. The results revealed that for the thinner fabric, the contributions of the woven layers and fiberglass pillars were greater than that of the foam. In contrast, the woven layer and foam exhibited greater contributions in the thicker fabric. Moreover, the thicker fabric exhibited slightly lower strength than the thinner fabric, which is believed to be due to the fact that the length of the glass pillars in thicker fabric is greater than those of the thinner fabric.

The last phase of research, presented in chapter 8, entailed the development of a practical analytical model for predicting the static (indentation) and low-velocity impact responses of 3DFMLs. The model was developed based on the energy balance approach, by which the impact energy was assumed to dissipate through shear, bending and indentation contact mechanisms. The contact between the impactor and panel was modelled using the Hertz contact law. the Hertz' parameters were calibrated using the experimental and numerical results. The effects of 3DFMLs' configurations (which were investigated in chapters 4 and 5), and the indenter size on those parameters were also examined. The integrity of the model was verified by predicting the response of various configurations of 3DFMLs

impacted by various sizes of impactors. The predicted results were compared against the experimental and numerical results, leading to good agreements. It was noted that the analytical results were accurate up to the stage when a crack would develop on the target. This was as expected, since the model did not include provisions for development of any damage within the system. Moreover, to gain a better understanding of the mechanisms contributing in absorbing the impact energy, the contributions of contact, bending and shear on energy absorption capacity were calculated and compared. The results revealed that more than 50% of the impact energy in these FMLs would be absorbed in the form of bending mechanism. The contribution of shear was observed to be less than 10%; therefore, it could be concluded that one may neglect calculation of the energy associated to shear deformation in the analytical model, thus increasing the efficiency of the model.

Finally, to provide an overall and summarized perspective of the performance of the various configurations of 3DFML presented in this study, the following comparison is presented. Figure 9-1 presents an overall comparison of the performance of various configurations of 3DFML and those of high-strength steel (i.e., one of the most common material used in the automotive industry) and the widely-used GLARE FML. The results exhibit that the Glass reinforced-3DFML (this the 3DFML configuration which was reinforced with additional layers of glass fabrics) and 3DFML-4-2/2 offer greater impact strength in comparison to the steel and GLARE. Moreover, when these configurations were normalized with respect to their weight, the mentioned two configurations of 3DFMLs were 2.5 times more effective in comparison to steel. When the results were normalized with respect to material cost, once again, the two-mentioned configuration outperformed both steel and GLARE by a significant margin.

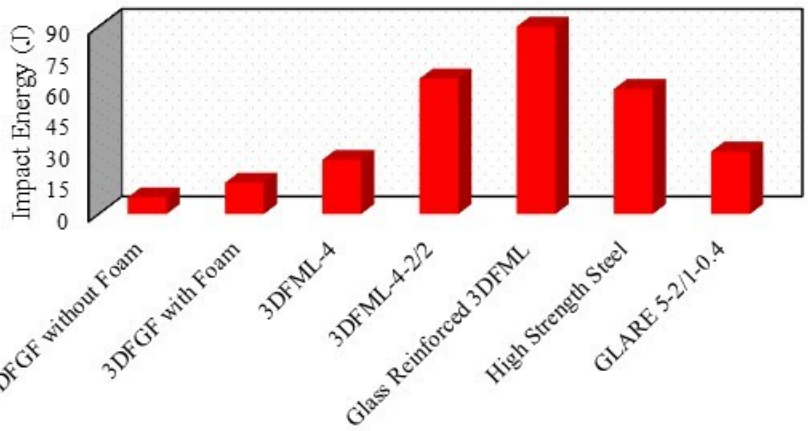

(a)

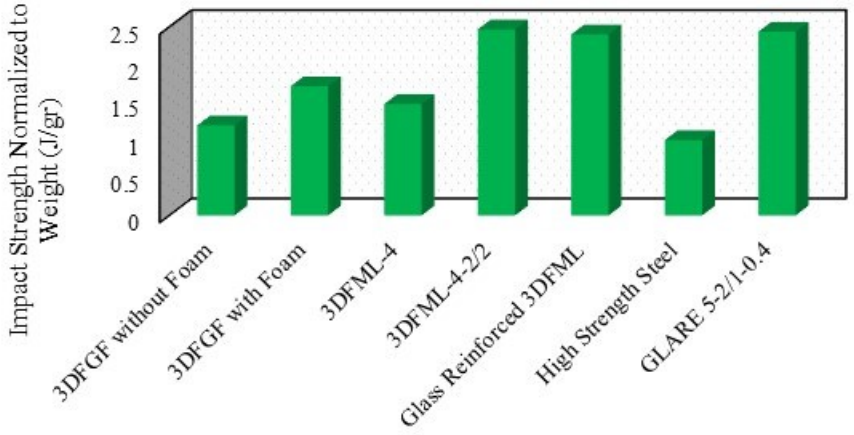

(b)

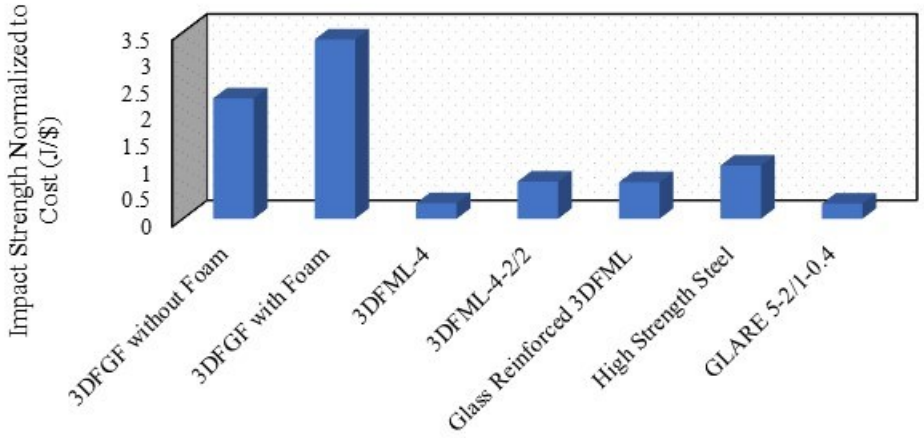

(c)

Figure 9-1. Comparison of performance of various configurations of 3DFML by high strength steel and GLARE

9.2 Recommendations

As explained, 3D fiber metal laminates are a novel class of fiber metal laminates, and therefore, the available literature is essentially limited to those presented in this dissertation. Therefore, the following recommendations are offered for continuation of the work presented herein. The recommendations are offered based on the focus of the future applications of this class of FMLs, essentially targeting the automotive industry.

- The 3DFML developed and introduced in this work is believed to be an effective alternative material for fabricating vehicles' body components. The immediate targets being vehicles' doors and bumpers. Both the out-of-plane and in-plane impacts are deemed to be the more likely loading scenarios in these components. Therefore, it is essential to examine the performance of these 3DFMLs under the in-plane impact. Moreover, these components would also be prone to multi-impact events. Therefore, the response of these 3DFMLs under multi-impacts would have to be characterized.
- One of the beneficial characteristics of 3DFMLs is the damage nature, which is usually in the form of a localized damage. This type of damage can be effectively repaired. Therefore, development of a cost-effective repair method is highly recommended. An effective repair methodology would further boost the applications of these FMLs, and improve their life-cycle cost.
- All the tests conducted on the 3DFMLs in this study were on the coupon level. Experimental investigation conducted on properly scaled components, especially those with curvatures, would be of paramount importance.

- One of the foreseen challenges associated with the mass production of 3DFMLs could be their joining method. This would be due to the specific and inherently complex structure of 3DFMLs. This issue would need significant attention, so that an effective, reliable and cost-effective joining methodology could be developed.
- Since E-glass fibers are known to be rate sensitive, it worth investigating the response of 3DFML under various rates of loading both numerically and experimentally. The results of such investigation(s) would enable one to extend the formulations presented in this study to include the constituent's rate effect.
- Since the immediate target of the application of 3DFML introduced here is in the automotive industry, the influence of environmental effects (e.g., thermal and moisture effects) on the performance of 3DFML should be investigated. In the same vein, the fatigue performance of this hybrid composite must also be established.
- Moreover, appropriate fire-returning agents should be identified to mitigate the combustibility issue of the foam used in reinforcing this hybrid composite.

References

Abdullah, M. and W. Cantwell (2006). "The impact resistance of polypropylene-based fibre–metal laminates." Composites science and technology **66**(11): 1682-1693.

Aboura, Z. (1993). Etude du processus de délaminage mode I, mode II et mode mixte(I+ II) de matériaux composites à renforts tissés à différentes vitesses de sollicitation.

Abrate, S. (2011). Impact engineering of composite structures, Springer Science & Business Media.

Agrawal, A. (2014). Planning to profit from opportunity: preparing for future demand Global steel 2014, Ernst & Young

Ahmadi-Moghadam, B. (2015). Development of A Highly Resilient Graphene Nanoplatelet Resin/Adhesive, Dalhousie University.

Ahmadi-Moghadam, B., M. Sharafimasooleh, S. Shadlou and F. Taheri (2015). "Effect of functionalization of graphene nanoplatelets on the mechanical response of graphene/epoxy composites." Materials & Design **66, Part A**: 142-149.

Ahmadi-Moghadam, B. and F. Taheri (2014). "Effect of processing parameters on the structure and multi-functional performance of epoxy/GNP-nanocomposites." Journal of Materials Science **49**(18): 6180-6190.

Ahmadi-Moghadam, B. and F. Taheri (2015). "Influence of graphene nanoplatelets on modes I, II and III interlaminar fracture toughness of fiber-reinforced polymer composites." Engineering Fracture Mechanics **143**: 97-107.

Al-Azzawi, A., J. McCrory, L. Kawashita, C. Featherston, R. Pullin and K. Holford Delamination Characteristics of Splices and Doublers in GLARE Laminates during Buckling. 11th World Congress on Computational Mechanics

Alderliesten, R., C. Rans and R. Benedictus (2008). "The applicability of magnesium based Fibre Metal Laminates in aerospace structures." Composites Science and Technology **68**(14): 2983-2993.

Asaee, Z., M. Mohamed, D. De Cicco and F. Taheri (2017). "Low-Velocity Impact Response and Damage Mechanism of 3D Fiber-Metal Laminates Reinforced with Amino-Functionalized Graphene Nanoplatelets." International Journal of Composite Materials **7**(1): 20-36.

Asaee, Z., M. Mohamed, S. Soumik and F. Taheri (2017). "Experimental and numerical characterization of delamination buckling behavior of a new class of GNP-reinforced 3D fiber-metal laminates." Thin-Walled Structures **112**: 208-216.

Asaee, Z., S. Shadlou and F. Taheri (2015). "Low-velocity impact response of fiberglass/magnesium FMLs with a new 3D fiberglass fabric." Composite Structures **122**: 155-165.

Asaee, Z. and F. Taheri (2015). Characterization of the Mechanical and Impact Response of a New-Generation 3D Fiberglass Fabric. American Society of Composites-30th Technical Conference.

Asaee, Z. and F. Taheri (2016). "Experimental and numerical investigation into the influence of stacking sequence on the low-velocity impact response of new 3D FMLs." Composite Structures **140**: 136-146.

Asaee, Z. and F. Taheri (2016). Experimental Studies on the Impact Response of 3D Fiberglass Fabric Subject to Different Size Impactors. Proceedings of the American Society for Composites: Thirty-First Technical Conference.

Asaee, Z., F. Taheri and T. Lay (2016). Innovative 3D Glass Fiber Metal Laminate. Advanced Materials - TechConnect Briefs 2016.

ASTM-C364 (2006). Edgewise Compressive Strength of Sandwich Constructions. Philadelphia, American Society for Testing and Materials West Conshohocken.

ASTM-C365 (2010). Standard test method for flatwise compressive properties of sandwich cores, American Society for Testing and Materials West Conshohocken.

ASTM-C393 (2000). Standard Test Method for Flexural Properties of Sandwich Constructions, American Society for Testing and Materials West Conshohocken.

ASTM-D790 (1997). Standard test methods for flexural properties of unreinforced and reinforced plastics and electrical insulating materials, American Society for Testing and Materials West Conshohocken.

Bannister, M., R. Braemar and P. Crothers (1999). "The mechanical performance of 3D woven sandwich composites." Composite Structures **47**(1): 687-690.

Barnes, G., I. Coles, R. Roberts, D. O. Adams and D. M. Garner (2010). Crash safety assurance strategies for future plastic and composite intensive vehicles (PCIVs), US Department of Transportation, Research and Innovative Technology Administration, National Transportation Systems Center.

Benzeggagh, M. and M. Kenane (1996). "Measurement of mixed-mode delamination fracture toughness of unidirectional glass/epoxy composites with mixed-mode bending apparatus." Composites science and technology **56**(4): 439-449.

Bienias, J., P. Jakubczak and K. Dadej (2016). "Low-velocity impact resistance of aluminium glass laminates–Experimental and numerical investigation." Composite Structures **152**: 339-348.

Botelho, E. C., R. A. Silva, L. C. Pardini and M. C. Rezende (2006). "A review on the development and properties of continuous fiber/epoxy/aluminum hybrid composites for aircraft structures." Materials Research **9**(3): 247-256.

Camanho, P. P., C. Davila and M. De Moura (2003). "Numerical simulation of mixed-mode progressive delamination in composite materials." Journal of composite materials **37**(16): 1415-1438.

Cappello, F. and D. Tumino (2006). "Numerical analysis of composite plates with multiple delaminations subjected to uniaxial buckling load." Composites science and technology **66**(2): 264-272.

Caprino, G., V. Lopresto and P. Iaccarino (2007). "A simple mechanistic model to predict the macroscopic response of fibreglass–aluminium laminates under low-velocity impact." Composites Part A: Applied Science and Manufacturing **38**(2): 290-300.

Caprino, G., G. Spataro and S. Del Luongo (2004). "Low-velocity impact behaviour of fibreglass–aluminium laminates." Composites Part A: Applied Science and Manufacturing **35**(5): 605-616.

Carrillo, J. and W. Cantwell (2009). "Mechanical properties of a novel fiber–metal laminate based on a polypropylene composite." Mechanics of Materials **41**(7): 828-838.

Carrillo, J. and W. J. Cantwell (2008). "Scaling effects in the low velocity impact response of fiber-metal laminates." Journal of Reinforced Plastics and Composites **27**(9): 893-907.

Chai, G. B. and P. Manikandan (2014). "Low velocity impact response of fibre-metal laminates–A review." Composite Structures **107**: 363-381.

Chai, H., C. D. Babcock and W. G. Knauss (1981). "One dimensional modelling of failure in laminated plates by delamination buckling." International Journal of Solids and Structures **17**(11): 1069-1083.

Chatterjee, S., F. Nafezarefi, N. H. Tai, L. Schlagenhauf, F. A. Nüesch and B. T. T. Chu (2012). "Size and synergy effects of nanofiller hybrids including graphene nanoplatelets

and carbon nanotubes in mechanical properties of epoxy composites." Carbon **50**(15): 5380-5386.

Chattopadhyay, A. and H. Gu (1994). "New higher order plate theory in modeling delamination buckling of composite laminates." AIAA journal **32**(8): 1709-1716.

Chen, H.-P. (1991). "Shear deformation theory for compressive delamination buckling and growth." AIAA journal **29**(5): 813-819.

Chen, H., Q. Zheng, P. Wang, H. Fan, J. Zheng, L. Zhao and F. Jin (2015). "Dynamic anti-crushing behaviors of woven textile sandwich composites: Multilayer and gradient effects." Journal of Composite Materials **49**(25): 3169-3179.

Cortes, P. and W. Cantwell (2004). "Fracture properties of a fiber-metal laminates based on magnesium alloy." Journal of materials science **39**(3): 1081-1083.

Cortes, P. and W. Cantwell (2004). "The tensile and fatigue properties of carbon fiber-reinforced PEEK-titanium fiber-metal laminates." Journal of reinforced plastics and composites **23**(15): 1615-1623.

Cortes, P. and W. Cantwell (2006). "The fracture properties of a fibre–metal laminate based on magnesium alloy." Composites Part B: Engineering **37**(2): 163-170.

Cortes, P. and W. Cantwell (2006). "The prediction of tensile failure in titanium-based thermoplastic fibre–metal laminates." Composites Science and Technology **66**(13): 2306-2316.

Davies, G., D. Hitchings and G. Zhou (1996). "Impact damage and residual strengths of woven fabric glass/polyester laminates." Composites Part A: Applied Science and Manufacturing **27**(12): 1147-1156.

De Cicco, D., Z. Asaee and F. Taheri (2017). "Low-velocity impact damage response of fiberglass/magnesium fiber-metal laminates under different size and shape impactors." Mechanics of Advanced Materials and Structures **24**(7): 545-555.

Den Hartog, J. P. (2014). Advanced strength of materials, Courier Corporation.

Dursun, T. and C. Soutis (2014). "Recent developments in advanced aircraft aluminium alloys." Materials & Design **56**: 862-871.

Esfahani, M., H. Ghasemnejad and P. Barrington (2010). Experimental and numerical buckling analysis of delaminated hybrid composite beam structures. Applied Mechanics and Materials, Trans Tech Publ.

Fan, H., H. Chen, L. Zhao, J. Zhou, F. Jin, J. Zheng and N. Kuang (2014). "Flexural failure mechanisms of three-dimensional woven textile sandwich panels: Experiments." Journal of Composite Materials **48**(5): 609-620.

Fan, H., L. Zhao, H. Chen, J. Zheng, Y. Jiang, S. Huang, N. Kuang and C. Ye (2013). "Dynamic compression failure mechanisms and dynamic effects of integrated woven sandwich composites." Journal of Composite Materials **48**(4): 427-437.

Fan, H., Q. Zhou, W. Yang and Z. Jingjing (2010). "An experiment study on the failure mechanisms of woven textile sandwich panels under quasi-static loading." Composites Part B: Engineering **41**(8): 686-692.

Fan, J., W. Cantwell and Z. Guan (2011). "The low-velocity impact response of fiber-metal laminates." Journal of Reinforced Plastics and Composites **30**(1): 26-35.

Fan, J., Z. Guan and W. Cantwell (2011). "Numerical modelling of perforation failure in fibre metal laminates subjected to low velocity impact loading." Composite structures **93**(9): 2430-2436.

Fan, J., Z. Guan and W. Cantwell (2011). "Structural behaviour of fibre metal laminates subjected to a low velocity impact." Science China Physics, Mechanics and Astronomy **54**(6): 1168-1177.

Frizzell, R. M., C. T. McCarthy and M. A. McCarthy (2011). "Simulating damage and delamination in fibre metal laminate joints using a three-dimensional damage model with cohesive elements and damage regularisation." Composites Science and Technology **71**(9): 1225-1235.

Gaudenzi, P., P. Perugini and A. Riccio (2001). "Post-buckling behavior of composite panels in the presence of unstable delaminations." Composite Structures **51**(3): 301-309.

Ghassemieh, E. (2011). Materials in automotive application, state of the art and prospects, INTECH Open Access Publisher.

Gojny, F. H., M. H. Wichmann, B. Fiedler and K. Schulte (2005). "Influence of different carbon nanotubes on the mechanical properties of epoxy matrix composites–a comparative study." Composites Science and Technology **65**(15): 2300-2313.

Gong, W., J. Chen and E. A. Patterson (2016). "Buckling and delamination growth behaviour of delaminated composite panels subject to four-point bending." Composite Structures **138**: 122-133.

Grashof, F. (1878). Theorie der Elasticität und Festigkeit: mit Bezug auf ihre Anwendungen in der Technik, R. Gaertner.

Gu, H. and A. Chattopadhyay (1999). "An experimental investigation of delamination buckling and postbuckling of composite laminates." Composites science and technology **59**(6): 903-910.

Guan, Z., W. Cantwell and R. Abdullah (2009). "Numerical modeling of the impact response of fiber–metal laminates." Polymer Composites **30**(5): 603-611.

Hashin, Z. (1980). "Failure criteria for unidirectional fiber composites." Journal of applied mechanics **47**(2): 329-334.

Hashin, Z. (1983). "Analysis of composite materials." J. appl. Mech **50**(2): 481-505.

Hertz, H. (1881). "On the contact of elastic solids." J. Reine Angew Math. **92**: 156-171.

Heydari-Meybodi, M., H. Mohammadkhani and M. Bagheri (2016). "Oblique Low-Velocity Impact on Fiber-Metal Laminates." Applied Composite Materials **24**(3): 611-623.

Hibbitt, T. (2002). ABAQUS Theory Manual and Analysis User's Manual, Hibbitt, Karlsson and Sorensen. Inc., USA.

Hoo Fatt, M. S., C. Lin, D. M. Revilock and D. A. Hopkins (2003). "Ballistic impact of GLARE™ fiber–metal laminates." Composite Structures **61**(1): 73-88.

Hosseini, S. A., M. Sadighi and R. Maleki Moghadam (2015). "Low-velocity impact behavior of hollow core woven sandwich composite: Experimental and numerical study." Journal of Composite Materials **49**(26): 3285-3295.

Hosur, M., M. Abdullah and S. Jeelani (2004). "Manufacturing and low-velocity impact characterization of hollow integrated core sandwich composites with hybrid face sheets." Composite Structures **65**(1): 103-115.

Hosur, M., M. Abdullah and S. Jeelani (2007). "Dynamic compression behavior of integrated core sandwich composites." Materials Science and Engineering: A **445**: 54-64.

Hosur, M. V., F. Chowdhury and S. Jeelani (2007). "Low-velocity impact response and ultrasonic NDE of woven carbon/epoxy—Nanoclay nanocomposites." Journal of Composite Materials **41**(18): 2195-2212.

Hwang, S.-F. and G.-H. Liu (2002). "Experimental study for buckling and postbuckling behaviors of composite laminates with multiple delaminations." Journal of reinforced plastics and composites **21**(4): 333-349.

Johnson, K. (1982). "One hundred years of Hertz contact." proceedings of the Institution of Mechanical Engineers **196**(1): 363-378.

Kachanov, L. (2012). Delamination buckling of composite materials, Springer Science & Business Media.

Karahan, M., H. Gül, J. Ivens and N. Karahan (2012). "Low velocity impact characteristic of 3D integrated core sandwich composites." Textile Research Journal **82**(9): 945-962.

Karahan, M., H. Gul, N. Karahan and J. Ivens (2013). "Static behavior of three-dimensional ıntegrated core sandwich composites subjected to three-point bending." Journal of Reinforced Plastics and Composites **32**(9): 664-678.

Kashani, M. H., M. Sadighi, A. Lalehpour and R. Alderliesten (2014). "The effect of impact energy division over repeated low-velocity impact on fiber metal laminates." Journal of Composite Materials **49**(6): 793-806.

Khan, S., R. Alderliesten and R. Benedictus (2009). "Post-stretching induced stress redistribution in fibre metal laminates for increased fatigue crack growth resistance." Composites Science and Technology **69**(3): 396-405.

Kim, H.-J. and C.-S. Hong (1997). "Buckling and postbuckling behavior of composite laminates with a delamination." Composites science and technology **57**(5): 557-564.

Kiratisaevee, H. and W. Cantwell (2005). "Low-velocity impact response of high-performance aluminum foam sandwich structures." Journal of Reinforced Plastics and Composites **24**(10): 1057-1072.

Kouchakzadeh, M. A. and H. Sekine (2000). "Compressive buckling analysis of rectangular composite laminates containing multiple delaminations." Composite Structures **50**(3): 249-255.

Kus, A., I. Durgun and R. Ertan (2016). "Experimental study on the flexural properties of 3D integrated woven spacer composites at room and subzero temperatures." Journal of Sandwich Structures and Materials.

Laliberte, J., C. Poon, P. Straznicky and A. Fahr (2000). "Applications of fiber-metal laminates." Polymer composites **21**(4): 558-567.

Larsson, P.-L. (1991). "On multiple delamination buckling and growth in composite plates." International Journal of Solids and Structures **27**(13): 1623-1637.

Lee, D., C. Morillo, S. Oller, G. Bugeda and E. Oñate (2013). "Robust design optimisation of advance hybrid (fiber–metal) composite structures." Composite Structures **99**: 181-192.

Lee, J., Z. Gurdal and J. GRIFFIN, OH (1993). "Layer-wise approach for the bifurcation problem in laminated composites with delaminations." AIAA journal **31**(2): 331-338.

Li, D.-s., C.-q. Zhao, N. Jiang and L. Jiang (2015). "Fabrication, properties and failure of 3D integrated woven spacer composites with thickened face sheets." Materials Letters **148**: 103-105.

Lin, C. and M. S. H. Fatt (2006). "Perforation of Composite Plates and Sandwich Panels under Quasi-static and Projectile Loading." Journal of Composite Materials **40**(20): 1801-1840.

Linde, P., J. Pleitner, H. de Boer and C. Carmone (2004). Modelling and simulation of fibre metal laminates. ABAQUS Users' conference.

Liu, D. (1988). "Impact-induced delamination—a view of bending stiffness mismatching." Journal of composite materials **22**(7): 674-692.

Liu, P., S. Hou, J. Chu, X. Hu, C. Zhou, Y. Liu, J. Zheng, A. Zhao and L. Yan (2011). "Finite element analysis of postbuckling and delamination of composite laminates using virtual crack closure technique." Composite Structures **93**(6): 1549-1560.

Liu, P. F., Z. P. Gu, X. Q. Peng and J. Y. Zheng (2015). "Finite element analysis of the influence of cohesive law parameters on the multiple delamination behaviors of composites under compression." Composite Structures **131**: 975-986.

Liu, Y. and B. Liaw (2010). "Effects of constituents and lay-up configuration on drop-weight tests of fiber-metal laminates." Applied Composite Materials **17**(1): 43-62.

Lv, X. Y., Y. Sun, Z. C. Jiang, Y. H. Zhang and M. W. Di (2011). Mechanical property of nano-particles reinforced epoxy resin composite materials. Advanced Materials Research, Trans Tech Publ.

Marsh, G. (2014). "Composites and metals–a marriage of convenience?" Reinforced Plastics **58**(2): 38-42.

Moriniere, F., R. Alderliesten and R. Benedictus (2012). "Development of fibre-metal laminates for improved impact performance." The European Physical Journal-Special Topics **206**(1): 79-88.

Morinière, F., R. Alderliesten, M. Sadighi and R. Benedictus (2013). "An integrated study on the low-velocity impact response of the GLARE fibre-metal laminate." Composite Structures **100**: 89-103.

Múgica, J., L. Aretxabaleta, I. Ulacia and J. Aurrekoetxea (2014). "Impact characterization of thermoformable fibre metal laminates of 2024-T3 aluminium and AZ31B-H24 magnesium based on self-reinforced polypropylene." Composites Part A: Applied Science and Manufacturing **61**: 67-75.

Nagaraj, M. (2005). "Experimental and computational investigation of FRP-reinforced glulam columns including associated software development [Master of applied science thesis]." Department of Civil and Resource Engineering, Dalhousie University.

Nji, J. and G. Li (2010). "A self-healing 3D woven fabric reinforced shape memory polymer composite for impact mitigation." Smart Materials and Structures **19**(3): 035007.

Ovesy, H., M. A. Mooneghi and M. Kharazi (2015). "Post-buckling analysis of delaminated composite laminates with multiple through-the-width delaminations using a novel layerwise theory." Thin-Walled Structures **94**: 98-106.

Pärnänen, T., R. Alderliesten, C. Rans, T. Brander and O. Saarela (2012). "Applicability of AZ31B-H24 magnesium in fibre metal laminates–an experimental impact research." Composites Part A: Applied Science and Manufacturing **43**(9): 1578-1586.

Payeganeh, G., F. A. Ghasemi and K. Malekzadeh (2010). "Dynamic response of fiber–metal laminates (FMLs) subjected to low-velocity impact." Thin-Walled Structures **48**(1): 62-70.

Periasamy, M., B. Manickam and K. Hariharasubramanian (2012). "Impact properties of aluminium-glass fiber reinforced plastics sandwich panels." Materials Research **15**(3): 347-354.

Powers, W. F. (2000). "Automotive materials in the 21st century." Advanced materials and processes **157**(5): 38-42.

Puck, A. and H. Schürmann (1998). "Failure analysis of FRP laminates by means of physically based phenomenological models." Composites Science and Technology **58**(7): 1045-1067.

Rathnasabapathy, M., A. Mouritz and A. Orifici (2013). Experimental and numerical investigation of low velocity impacts of fibre-metal laminates. AIAC15: 15th Australian International Aerospace Congress, Australian International Aerospace Congress.

Reid, S. R. and H. M. Wen (2000). 8 - Perforation of FRP laminates and sandwich panels subjected to missile impact. Impact Behaviour of Fibre-Reinforced Composite Materials and Structures, Woodhead Publishing**:** 239-279.

Remmers, J. and R. De Borst (2001). "Delamination buckling of fibre–metal laminates." Composites Science and Technology **61**(15): 2207-2213.

Remmers, J. J. C. and R. de Borst (2001). "Delamination buckling of fibre–metal laminates." Composites Science and Technology **61**(15): 2207-2213.

Sadighi, M., R. Alderliesten and R. Benedictus (2012). "Impact resistance of fiber-metal laminates: a review." International Journal of Impact Engineering **49**: 77-90.

Sadighi, M. and S. A. Hosseini (2013). "Finite element simulation and experimental study on mechanical behavior of 3D woven glass fiber composite sandwich panels." Composites part b: engineering **55**: 158-166.

Sadighi, M., T. Pärnänen, R. Alderliesten, M. Sayeaftabi and R. Benedictus (2012). "Experimental and numerical investigation of metal type and thickness effects on the impact resistance of fiber metal laminates." Applied Composite Materials **19**(3-4): 545-559.

Seyed Yaghoubi, A. and B. Liaw (2012). "Thickness influence on ballistic impact behaviors of GLARE 5 fiber-metal laminated beams: Experimental and numerical studies." Composite Structures **94**(8): 2585-2598.

Seyed Yaghoubi, A., Y. Liu and B. Liaw (2011). "Low-velocity impact on GLARE 5 fiber-metal laminates: influences of specimen thickness and impactor mass." Journal of Aerospace Engineering **25**(3): 409-420.

Shi, Y., T. Swait and C. Soutis (2012). "Modelling damage evolution in composite laminates subjected to low velocity impact." Composite Structures **94**(9): 2902-2913.

Shokrieh, M., S. Ghoreishi, M. Esmkhani and Z. Zhao (2014). "Effects of graphene nanoplatelets and graphene nanosheets on fracture toughness of epoxy nanocomposites." Fatigue & Fracture of Engineering Materials & Structures **37**(10): 1116-1123.

Shyr, T.-W. and Y.-H. Pan (2004). "Low velocity impact responses of hollow core sandwich laminate and interply hybrid laminate." Composite Structures **64**(2): 189-198.

Sinmazçelik, T., E. Avcu, M. Ö. Bora and O. Çoban (2011). "A review: Fibre metal laminates, background, bonding types and applied test methods." Materials & Design **32**(7): 3671-3685.

Sokolnikoff, I. S. and R. D. Specht (1956). Mathematical theory of elasticity, McGraw-Hill New York.

Starikov, R. (2013). "Assessment of impact response of fiber metal laminates." International Journal of Impact Engineering **59**: 38-45.

Subbaramaiah, R., B. Prusty, G. Pearce, S. Lim and R. Thomson (2017). "Crashworthy response of fibre metal laminate top hat structures." Composite Structures **160**: 773-781.

Sun, C., A. Dicken and H. Wu (1993). "Characterization of impact damage in ARALL laminates." Composites Science and Technology **49**(2): 139-144.

Sun, T., H. Fan, Z. Wang, X. Liu and Z. Wu (2015). "Modified nano Fe 2 O 3-epoxy composite with enhanced mechanical properties." Materials & Design **87**: 10-16.

Taheri-Behrooz, F., M. Shokrieh and I. Yahyapour (2014). "Effect of stacking sequence on failure mode of fiber metal laminates under low-velocity impact." Iranian Polymer Journal **23**(2): 147-152.

Taheri, F. (1997). "Improvement of strength and ductility of adhesively bonded joints by inclusion of SiC whiskers." Journal of Composites, Technology and Research **19**(2): 86-92.

Tan, C. and H. M. Akil (2012). "Impact response of fiber metal laminate sandwich composite structure with polypropylene honeycomb core." Composites Part B: Engineering **43**(3): 1433-1438.

Tay, T., F. Shen, K. Lee, A. Scaglione and M. Di Sciuva (1999). "Mesh design in finite element analysis of post-buckled delamination in composite laminates." Composite Structures **47**(1): 603-611.

Timoshenko, S. P. and S. Woinowsky-Krieger (1959). Theory of plates and shells, McGraw-hill.

Tooski, M. Y., R. Alderliesten, R. Ghajar and S. Khalili (2013). "Experimental investigation on distance effects in repeated low velocity impact on fiber–metal laminates." Composite Structures **99**: 31-40.

Tsartsaris, N., M. Meo, F. Dolce, U. Polimeno, M. Guida and F. Marulo (2011). "Low-velocity impact behavior of fiber metal laminates." Journal of Composite Materials **45**(7): 803-814.

U.S.D.O.E (2017). U.S. Energy and Employment Report | Department of Energy.

Ulacia, I., C. P. Salisbury, I. Hurtado and M. J. Worswick (2011). "Tensile characterization and constitutive modeling of AZ31B magnesium alloy sheet over wide range of strain rates and temperatures." Journal of Materials Processing Technology **211**(5): 830-839.

Vaidya, A., U. Vaidya and N. Uddin (2008). "Impact response of three-dimensional multifunctional sandwich composite." Materials Science and Engineering: A **472**(1): 52-58.

Vaidya, U., M. Hosur, D. Earl and S. Jeelani (2000). "Impact response of integrated hollow core sandwich composite panels." Composites Part A: Applied Science and Manufacturing **31**(8): 761-772.

Van Vuure, A., J. Pflug, J. Ivens and I. Verpoest (2000). "Modelling the core properties of composite panels based on woven sandwich-fabric preforms." Composites science and technology **60**(8): 1263-1276.

Vlot, A. (1993). "Impact properties of Fibre Metal Laminates." Composites Engineering **3**(10): 911-927.

Vlot, A. (1993). Low-velocity impact loading: on fibre reinforced aluminium laminates (ARALL and GLARE) and other aircraft sheet materials.

Vlot, A. (1996). "Impact loading on fibre metal laminates." International Journal of Impact Engineering **18**(3): 291-307.

Vlot, A., L. Vogelesang and T. De Vries (1999). "Towards application of fibre metal laminates in large aircraft." Aircraft Engineering and Aerospace Technology **71**(6): 558-570.

Vo, T. P., Z. Guan, W. Cantwell and G. Schleyer (2013). "Modelling of the low-impulse blast behaviour of fibre–metal laminates based on different aluminium alloys." Composites Part B: Engineering **44**(1): 141-151.

Vogelesang, L. B. and A. Vlot (2000). "Development of fibre metal laminates for advanced aerospace structures." Journal of Materials Processing Technology **103**(1): 1-5.

Wang, S., C. M. Harvey, B. Wang and A. Watson (2015). "Post-local buckling-driven delamination in bilayer composite beams." Composite Structures **133**: 1058-1066.

Wang, S., M. Li, Z. Zhang and B. Wu (2009). "Properties of facesheet-reinforced 3-D spacer fabric composites and the integral multi-facesheet structures." Journal of Reinforced Plastics and Composites **29**(6): 793-806.

Whisler, D. and H. Kim (2015). "Experimental and simulated high strain dynamic loading of polyurethane foam." Polymer Testing **41**: 219-230.

Wu, G. and J.-M. Yang (2005). "The mechanical behavior of GLARE laminates for aircraft structures." Jom **57**(1): 72-79.

Wu, G., J.-M. Yang and H. T. Hahn (2007). "The impact properties and damage tolerance and of bi-directionally reinforced fiber metal laminates." Journal of materials science **42**(3): 948-957.

Yaghoubi, A. S., Y. Liu and B. Liaw (2012). "Stacking sequence and geometrical effects on low-velocity impact behaviors of GLARE 5 (3/2) fiber–metal laminates." Journal of thermoplastic composite materials **25**(2): 223-247.

Yap, C. W., G. B. Chai, J. Song and S. C. Joshi (2015). "Upper and lower bound buckling load of perfect and delaminated fiber-reinforced composite columns." Composite Structures **122**: 376-389.

Yarmohammad Tooski, M., R. C. Alderliesten, R. Ghajar and S. M. R. Khalili (2013). "Experimental investigation on distance effects in repeated low velocity impact on fiber–metal laminates." Composite Structures **99**(0): 31-40.

Yu, K., H. Cao, K. Qian and H. Li (2014). "Manufacturing and Flat-wise Compression Performance of Modified 3D Integrated Sandwich Fabric Composites." Fibres & Textiles in Eastern Europe **105**(3): 98-102.

Zenkert, D. (1997). An Introduction to Sandwich Construction, EMAS.

Zhang, H., S. Gn, J. An, Y. Xiang and J. Yang (2014). "Impact behaviour of GLAREs with MWCNT modified epoxy resins." Experimental Mechanics **54**(1): 83-93.

Zhao, C.-Q., D.-S. Li, T.-Q. Ge, L. Jiang and N. Jiang (2014). "Experimental study on the compression properties and failure mechanism of 3D integrated woven spacer composites." Materials & Design **56**: 50-59.

Zhou, D. and W. Stronge (2006). "Low velocity impact denting of HSSA lightweight sandwich panel." International Journal of Mechanical Sciences **48**(10): 1031-1045.

Zhou, G., C. Liu, W. Li and X. Wang (2016). "Shear behavior of 3D woven hollow integrated sandwich composites: Experimental, theoretical and numerical study." Applied Composite Materials **24**(4): 787-801.

Zhu, S. and G. Chai (2014). "Low-velocity impact response of fiber-metal laminates–A theoretical approach." Proceedings of the Institution of Mechanical Engineers, Part L: Journal of Materials: Design and Applications **228**(4): 301-311.

Zhu, S. and G. B. Chai (2012). "Low-velocity impact response of fibre–metal laminates–Experimental and finite element analysis." Composites Science and Technology **72**(15): 1793-1802.

Zhu, S. and G. B. Chai (2013). Impact of aluminum, CFRP laminates, fibre-metal laminates and sandwich panels. Composite Materials and Joining Technologies for Composites, Volume 7, Springer**:** 199-205.

Zukas, J., T. Nicholas, H. Swift, L. Greszczuk and D. Curran (1992). Impact Dynamics. Malabar, Florida, Krieger Publishing Company.

Appendix A: Operation Manual of 3DFGF Compound by Resin

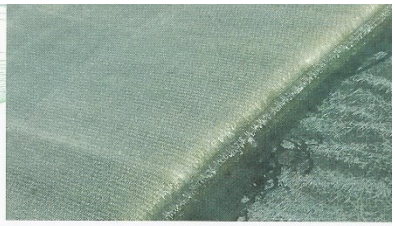

CHINA BEIHAI
FIBERGLASS
www.fiberglassfiber.com

Operation Manual of 3D Fabric compound by resin

3D fiberglass woven fabric applicate in core reinforcement of organic composite materials, after fabric and resin compound, the core appears 8-shaped in the warp direction and 1-shaped in the weft direction. It's better if you adopt hand lay up. When compound resin matrix you could based on your specific utility and require, choose epoxy, unsaturated polyester, phenolic resin or other resin. Depend on the viscosity and wettability of the resin, the resin content can be controlled at 50%-60% usually (weight percentage).

The process of 3D fiberglass woven fabric compound by unsaturated polyester as follow:

1. According to environment temperature situation, adjust the proportion of accelerant and hardening agent, keep the gelation time around 20 minute after fabric infiltrated by resin. When take the same proportion of resin, because of the spacer structure of 3D spacer fabric make the gelation time and curing time longer than other common glass fiber fabric, so we suggest you could take a small piece to have the gelation and curing test first, then confirm the system of resin and the proportion.

2. Apply 40% of the resin even brushed on the surface of the mould, after preparation the resin.

3. Foreshadowing 3D spacer on the resin and roll the rest 60% resin evenly on the top of the fabric along the direction of core dumping until the color on the whole face basically same, it means fabric has fully infiltrated by resin, and you could apply scraper by assist.

4. Rolling the fabric along the negative direction of the core dumping, the face of the fabric will uped by roll, after several rolling, it could make the fabric to be the max height.

4

Operation Manual of 3D Fabric compound with resin

Operating steps

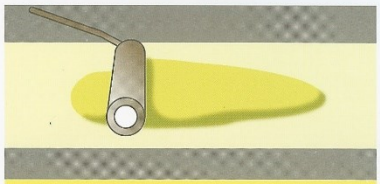

1.Apply 40% of the resin quantity on the surface of the mold and distribute it evenly.

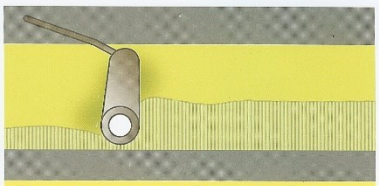

2.Apply 3D perform into the resin layer and roll it firmly but gentle.

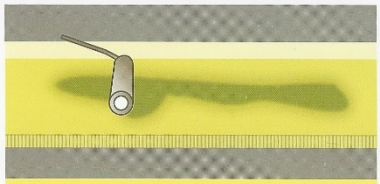

3.Apply the remaining 60% of the recom-mended resin quantity on top of the 3D perform and distribute it evenly by rolling

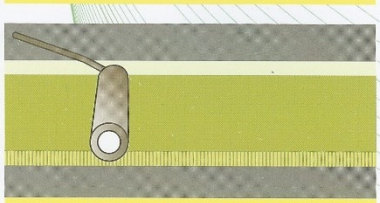

4.Roll resin gently into the 3D perform. Smooth surface and maximum height is achieved by fi-nishing with gently rolling in weft direction aga-inst the pile direction.

Appendix B: VUMAT to Evaluate Hashin 3D Failure Criteria

```
      subroutine vumat(
c Read only -
     1  nblock, ndir, nshr, nstatev, nfieldv, nprops, lanneal,
     2  stepTime, totalTime, dt, cmname, coordMp, charLength,
     3  props, density, strainInc, relSpinInc,
     4  tempOld, stretchOld, defgradOld, fieldOld,
     5  stressOld, stateOld, enerInternOld, enerInelasOld,
     6  tempNew, stretchNew, defgradNew, fieldNew,
c Write only -
     7  stressNew, stateNew, enerInternNew, enerInelasNew )
c
      include 'vaba_param.inc'
c
c 3D Orthotropic Elasticity with Hashin 3d Failure criterion
c
c The state variables are stored as:
c    state(*,1)   = material point status
c    state(*,2:7) = damping stresses
c
c User defined material properties are stored as
c  * First line:
c     props(1) --> Young's modulus in 1-direction, E1
c     props(2) --> Young's modulus in 2-direction, E2
c     props(3) --> Young's modulus in 3-direction, E3
c     props(4) --> Poisson's ratio, nu12
c     props(5) --> Poisson's ratio, nu13
c     props(6) --> Poisson's ratio, nu23
c     props(7) --> Shear modulus, G12
c     props(8) --> Shear modulus, G13
c
c  * Second line:
c     props(9)  --> Shear modulus, G23
c     props(10) --> beta damping parameter
c     props(11) --> "not used"
c     props(12) --> "not used"
c     props(13) --> "not used"
c     props(14) --> "not used"
c     props(15) --> "not used"
c     props(16) --> "not used"
c
c  * Third line:
c     props(17) --> Ultimate tens stress in 1-direction, sigu1t
c     props(18) --> Ultimate comp stress in 1-direction, sigu1c
c     props(19) --> Ultimate tens stress in 2-direction, sigu2t
c     props(20) --> Ultimate comp stress in 2-direction, sigu2c
c     props(21) --> Ultimate tens stress in 3-direction, sigu3t
c     props(22) --> Ultimate comp stress in 3-direction, sigu3c
c     props(23) --> "not used"
c     props(24) --> "not used"
c
c  * Fourth line:
c     props(25) --> Ultimate shear stress, sigu12
c     props(26) --> Ultimate shear stress, sigu13
c     props(27) --> Ultimate shear stress, sigu23
c     props(28) --> "not used"
c     props(29) --> "not used"
c     props(30) --> "not used"
c     props(31) --> "not used"
c     props(32) --> "not used"
c

      dimension props(nprops), density(nblock),
     1  coordMp(nblock,*),
     2  charLength(*), strainInc(nblock,ndir+nshr),
     3  relSpinInc(nblock,nshr), tempOld(nblock),
     4  stretchOld(nblock,ndir+nshr), defgradOld(nblock,ndir+nshr+nshr),
     5  fieldOld(nblock,nfieldv), stressOld(nblock,ndir+nshr),
     6  stateOld(nblock,nstatev), enerInternOld(nblock),
     7  enerInelasOld(nblock), tempNew(*),
     8  stretchNew(nblock,ndir+nshr), defgradNew(nblock,ndir+nshr+nshr),
     9  fieldNew(nblock,nfieldv), stressNew(nblock,ndir+nshr),
     1  stateNew(nblock,nstatev),
```

```
     2  enerInternNew(nblock), enerInelasNew(nblock)
*
      character*80 cmname
*
      parameter( zero = 0.d0, one = 1.d0, two = 2.d0, half = .5d0 )
*
      parameter(
     *     i_svd_DmgFiberLt   = 1,
     *     i_svd_DmgFiberLc  = 2,
     *     i_svd_DmgFiberTt  = 3,
     *     i_svd_DmgFiberTc  = 4,
     *     i_svd_DmgFiberZt = 5,
     *     i_svd_DmgFiberZc = 6,
     *     i_svd_statusMp   = 7,
     *     i_svd_dampStress = 8,
c     *     i_svd_dampStressXx = 8,
c     *     i_svd_dampStressYy = 9,
c     *     i_svd_dampStressZz = 10,
c     *     i_svd_dampStressXy = 11,
c     *     i_svd_dampStressYz = 12,
c     *     i_svd_dampStressZx = 13,
     *     i_svd_Strain   = 14,
c     *     i_svd_StrainXx = 14,
c     *     i_svd_StrainYy = 15,
c     *     i_svd_StrainZz = 16,
c     *     i_svd_StrainXy = 17,
c     *     i_svd_StrainYz = 18,
c     *     i_svd_StrainZx = 19,
     *     n_svd_required = 19 )
*
      parameter(
     *     i_s33_Xx = 1,
     *     i_s33_Yy = 2,
     *     i_s33_Zz = 3,
     *     i_s33_Xy = 4,
     *     i_s33_Yz = 5,
     *     i_s33_Zx = 6 )
*
* Structure of property array
      parameter (
     *     i_pro_E1    = 1,
     *     i_pro_E2    = 2,
     *     i_pro_E3    = 3,
     *     i_pro_nu12  = 4,
     *     i_pro_nu13  = 5,
     *     i_pro_nu23  = 6,
     *     i_pro_G12   = 7,
     *     i_pro_G13   = 8,
     *     i_pro_G23   = 9,
*
     *     i_pro_beta  = 10,
     *     i_pro_alpha = 11,
*
     *     i_pro_sigu1t = 17,
     *     i_pro_sigu1c = 18,
     *     i_pro_sigu2t = 19,
     *     i_pro_sigu2c = 20,
     *     i_pro_sigu3t = 21,
     *     i_pro_sigu3c = 22,
     *     i_pro_sigu12 = 25,
     *     i_pro_sigu13 = 26,
     *     i_pro_sigu23 = 27,
     *     i_pro_GFT = 28,
     *     i_pro_GFC = 29,
     *     i_pro_GMT = 30,
     *     i_pro_GMC = 31 )
* Temporary arrays
      dimension eigen(maxblk*3), strain(nblock, ndir+nshr)
*
* Read material properties
*
      E1 = props(i_pro_E1)
```

```
      E2 = props(i_pro_E2)
      E3 = props(i_pro_E3)
      xnu12 = props(i pro nu12)
      xnu13 = props(i pro nu13)
      xnu23 = props(i pro nu23)
      G12 = props(i_pro_G12)
      G13 = props(i_pro_G13)
      G23 = props(i_pro_G23)
*
      xnu21 = xnu12 * E2 / E1
      xnu31 = xnu13 * E3 / E1
      xnu32 = xnu23 * E3 / E2
*
*
* Compute terms of stiffness matrix
      gg = one / ( one - xnu12*xnu21 - xnu23*xnu32 - xnu31*xnu13
     *     - two*xnu21*xnu32*xnu13 )
      C11  = E1 * ( one - xnu23*xnu32 ) * gg
      C22  = E2 * ( one - xnu13*xnu31 ) * gg
      C33  = E3 * ( one - xnu12*xnu21 ) * gg
      C12  = E1 * ( xnu21 + xnu31*xnu23 ) * gg
      C13  = E1 * ( xnu31 + xnu21*xnu32 ) * gg
      C23  = E2 * ( xnu32 + xnu12*xnu31 ) * gg
*
      f1t = props(i_pro_sigu1t)
      f1c = props(i_pro_sigu1c)
      f2t = props(i pro sigu2t)
      f2c = props(i pro sigu2c)
      f3t = props(i pro sigu3t)
      f3c = props(i_pro_sigu3c)
      f12 = props(i_pro_sigu12)
      f13 = props(i_pro_sigu13)
      f23 = props(i_pro_sigu23)
*
      beta = props(i pro beta)
      alpha = props(i_pro_alpha)
*
      GFT = props(i_pro_GFT)
      GFC = props(i pro GFC)
      GMT = props(i pro GMT)
      GMC = props(i_pro_GMC)
*
* Assume purely elastic material at the beginning of the analysis
*
      if ( totalTime .eq. zero ) then
         if (nstatev .lt. n svd Required) then
            call xplb abqerr(-2,'Subroutine VUMAT requires the '//
     *           'specification of %I state variables. Check the '//
     *           'definition of *DEPVAR in the input file.',
     *           n_svd_Required,zero,' ')
            call xplb_exit
         end if
         call OrthoEla3dExp ( nblock,
     *        stateOld(1,i_svd_DmgFiberLt),
     *        stateOld(1,i_svd_DmgFiberLc),
     *        stateOld(1,i_svd_DmgFiberTt),
     *        stateOld(1,i_svd_DmgFiberTc),
     *        stateOld(1,i svd DmgFiberZt),
     *        stateOld(1,i svd DmgFiberZc),
     *        C11, C22, C33, C12, C23, C13, G12, G23, G13,
     *        strainInc,
     *        stressNew )
         return
      end if

*
*  Update total elastic strain
      call strainUpdate ( nblock, strainInc,
     *     stateOld(1,i_svd_strain), stateNew(1,i_svd_strain), strain )

*
* Stress update
```

```
      call OrthoEla3dExp ( nblock,
     *     stateOld(1,i_svd_DmgFiberLt),
     *     stateOld(1,i_svd_DmgFiberLc),
     *     stateOld(1,i_svd_DmgFiberTt),
     *     stateOld(1,i_svd_DmgFiberTc),
     *     stateOld(1,i_svd_DmgFiberZt),
     *     stateOld(1,i_svd_DmgFiberZc),
     *     C11, C22, C33, C12, C23, C13, G12, G23, G13,
     *     strain, stressNew )


      call characlength ( nblock, charachL, charLength(1))


*
* Failure evaluation
*
!      call copyr ( nblock,
!     *     stateOld(1,i_svd_DmgFiberLt), stateNew(1,i_svd_DmgFiberLt) )
!!      call copyr ( nblock,
!     *     stateOld(1,i_svd_DmgFiberLc), stateNew(1,i_svd_DmgFiberLc) )
!      call copyr ( nblock,
!     *     stateOld(1,i_svd_DmgFiberTt), stateNew(1,i_svd_DmgFiberTt) )
!      call copyr ( nblock,
!     *     stateOld(1,i_svd_DmgFiberTc), stateNew(1,i_svd_DmgFiberTc) )
!      call copyr ( nblock,
!     *     stateOld(1,i_svd_DmgFiberZt), stateNew(1,i_svd_DmgFiberZt) )
!      call copyr ( nblock,
!     *     stateOld(1,i_svd_DmgFiberZc), stateNew(1,i_svd_DmgFiberZc) )



      nDmg = 0
!      call eig33Anal ( nblock, stretchNew, eigen )

      call Hashin3d  ( nblock, nDmg,
     *     f1t, f2t, f3t, f1c, f2c, f3c, f12, f23, f13,
     *     stateNew(1,i_svd_DmgFiberLt),
     *     stateNew(1,i_svd_DmgFiberLc),
     *     stateNew(1,i_svd_DmgFiberTt),
     *     stateNew(1,i_svd_DmgFiberTc),
     *     stateNew(1,i_svd_DmgFiberZt),
     *     stateNew(1,i_svd_DmgFiberZc),
     *     stateNew(1,i_svd_statusMp),
     *     stressNew, eigen, strain, charachL,
     *     alpha,
     *     stateOld(1,i_svd_DmgFiberLt),
     *     stateOld(1,i_svd_DmgFiberLc),
     *     stateOld(1,i_svd_DmgFiberTt),
     *     stateOld(1,i_svd_DmgFiberTc),
     *     stateOld(1,i_svd_DmgFiberZt),
     *     stateOld(1,i_svd_DmgFiberZc),
     *     GFT, GFC, GMT, GMC )
*     -- Recompute stresses if new Damage is occurring
      if ( nDmg .gt. 0 ) then
         call OrthoEla3dExp ( nblock,
     *        stateNew(1,i_svd_DmgFiberLt),
     *        stateNew(1,i_svd_DmgFiberLc),
     *        stateNew(1,i_svd_DmgFiberTt),
     *        stateNew(1,i_svd_DmgFiberTc),
     *        stateNew(1,i_svd_DmgFiberZt),
     *        stateNew(1,i_svd_DmgFiberZc),
     *        C11, C22, C33, C12, C23, C13, G12, G23, G13,
     *        strain,
     *        stressNew )
      end if
*
* Beta damping
      if ( beta .gt. zero ) then
         call betaDamping3d ( nblock,
     *        beta, dt, strainInc,
     *        stressOld, stressNew,
```

```
     *        stateNew(1,i_svd_statusMp),
     *        stateOld(1,i_svd_dampStress),
     *        stateNew(1,i_svd_dampStress) )
      end if
*
* Integrate the internal specific energy (per unit mass)
*
!      call EnergyInternal3d ( nblock, stressOld, stressNew,
!     *   strainInc, density, enerInternOld, enerInternNew )
*
      return
      end


************************************************************
*   OrthoEla3dExp: Orthotropic elasticity - 3d             *
************************************************************
      subroutine OrthoEla3dExp ( nblock,
     *     dmgFiberLt, dmgFiberLc, dmgFiberTt, dmgFiberTc,
     *     dmgFiberZt, dmgFiberZc,
     *     C11, C22, C33, C12, C23, C13, G12, G23, G13,
     *     strain, stress )
*
      include 'vaba_param.inc'

*  Orthotropic elasticity, 3D case -
*
      parameter( zero = 0.d0, one = 1.d0, two = 2.d0)
      parameter(
     *     i_s33_Xx = 1,
     *     i_s33_Yy = 2,
     *     i_s33_Zz = 3,
     *     i_s33_Xy = 4,
     *     i_s33_Yz = 5,
     *     i_s33_Zx = 6,
     *     n_s33_Car = 6 )
*
      dimension  strain(nblock,n_s33_Car),
     *     dmgFiberLt(nblock), dmgFiberLc(nblock),
     *     dmgFiberTt(nblock), dmgFiberTc(nblock),
     *     dmgFiberZt(nblock), dmgFiberZc(nblock),
     *     stress(nblock,n_s33_Car)
*     -- shear fraction in matrix tension and compression mode
      parameter ( smt = 0.9d0, smc = 0.5d0 )
*
      do k = 1, nblock
*     -- Compute damaged stiffness
         dL = max(dmgFiberLt(k) , dmgFiberLc(k))
         dT = max(dmgFiberTt(k) , dmgFiberTc(k))
         dZ = max(dmgFiberZt(k) , dmgFiberZc(k))
*
         bL = one - dL
         bT = one - dT
         bZ = one - dZ
         bLT = ((2 * bL * bT)/(bL + bT + 0.001))**2
         bTZ = ((2 * bT * bZ)/(bZ + bT + 0.001))**2
         bZL = ((2 * bL * bZ)/(bL + bZ + 0.001))**2
*
         dC11 = (bL ** 2) * C11
         dC22 = (bT ** 2) * C22
         dC33 = (bZ ** 2) * C33
         dC12 = ( bL * bT ) * C12
         dC23 = ( bT * bZ ) * C23
         dC13 = ( bL * bZ ) * C13
         dG12 = bLT * G12
         dG23 = bTZ * G23
         dG13 = bZL * G13
*     -- Stress update
         stress(k,i_s33_Xx) = dC11 * strain(k,i_s33_Xx)
     *        + dC12 * strain(k,i_s33_Yy)
     *        + dC13 * strain(k,i_s33_Zz)
         stress(k,i_s33_Yy) = dC12 * strain(k,i_s33_Xx)
```

```
     *        + dC22 * strain(k,i_s33_Yy)
     *        + dC23 * strain(k,i_s33_Zz)
          stress(k,i_s33_Zz) = dC13 * strain(k,i_s33_Xx)
     *        + dC23 * strain(k,i_s33_Yy)
     *        + dC33 * strain(k,i_s33_Zz)
          stress(k,i_s33_Xy) = two * dG12 * strain(k,i_s33_Xy)
          stress(k,i_s33_Yz) = two * dG23 * strain(k,i_s33_Yz)
          stress(k,i_s33_Zx) = two * dG13 * strain(k,i_s33_Zx)
       end do
*
       return
       end

************************************************************
*   strainUpdate: Update total strain                      *
************************************************************
       subroutine strainUpdate ( nblock,
     *     strainInc, strainOld, strainNew, strain )
*
       include 'vaba_param.inc'
*
       parameter(
     *     i_s33_Xx = 1,
     *     i_s33_Yy = 2,
     *     i_s33_Zz = 3,
     *     i_s33_Xy = 4,
     *     i_s33_Yz = 5,
     *     i_s33_Zx = 6,
     *     n_s33_Car = 6 )
*
       dimension strainInc(nblock,n_s33_Car),
     *     strainOld(nblock,n_s33_Car),
     *     strainNew(nblock,n_s33_Car),
     *     strain(nblock,n_s33_Car)
*
       do k = 1, nblock
          strainNew(k,i_s33_Xx)= strainOld(k,i_s33_Xx)
     *                         + strainInc(k,i_s33_Xx)
          strainNew(k,i_s33_Yy)= strainOld(k,i_s33_Yy)
     *                         + strainInc(k,i_s33_Yy)
          strainNew(k,i_s33_Zz)= strainOld(k,i_s33_Zz)
     *                         + strainInc(k,i_s33_Zz)
          strainNew(k,i_s33_Xy)= strainOld(k,i_s33_Xy)
     *                         + strainInc(k,i_s33_Xy)
          strainNew(k,i_s33_Yz)= strainOld(k,i_s33_Yz)
     *                         + strainInc(k,i_s33_Yz)
          strainNew(k,i_s33_Zx)= strainOld(k,i_s33_Zx)
     *                         + strainInc(k,i_s33_Zx)
          strain(k,i_s33_Xx) = strainNew(k,i_s33_Xx)
          strain(k,i_s33_Yy) = strainNew(k,i_s33_Yy)
          strain(k,i_s33_Zz) = strainNew(k,i_s33_Zz)
          strain(k,i_s33_Xy) = strainNew(k,i_s33_Xy)
          strain(k,i_s33_Zx) = strainNew(k,i_s33_Zx)
          strain(k,i_s33_Yz) = strainNew(k,i_s33_Yz)

       end do
*
       return
       end


************************************************************
*   Hashin3d w/ Modified Puck: Evaluate Hashin 3d failure  *
*   criterion for fiber, Puck for matrix                   *
************************************************************
       subroutine Hashin3d ( nblock, nDmg,
     *     f1t, f2t, f3t, f1c, f2c, f3c, f12, f23, f13,
     *     dmgFiberLt, dmgFiberLc, dmgFiberTt, dmgFiberTc,
     *     dmgFiberZt, dmgFiberZc, statusMp, stress, eigen ,
     *     strain, L, alpha, OlddmgFiberLt,OlddmgFiberLc, OlddmgFiberTt,
     *     OlddmgFiberTc, OlddmgFiberZt, OlddmgFiberZc,
     *     GFT, GFC, GMT, GMC)
```

```
*
      include 'vaba_param.inc'

      parameter( zero = 0.d0, one = 1.d0, half = 0.5d0, three = 3.d0 )
      parameter(
     *     i_s33_Xx = 1,
     *     i_s33_Yy = 2,
     *     i_s33_Zz = 3,
     *     i_s33_Xy = 4,
     *     i_s33_Yz = 5,
     *     i_s33_Zx = 6,
     *     n_s33_Car = 6 )
*
      parameter(i_v3d_X=1,i_v3d_Y=2,i_v3d_Z=3 )
      parameter(n_v3d_Car=3 )
*
      parameter ( eMax = 1.00d0, eMin = -0.8d0 )
*
      dimension  dmgFiberLt(nblock), dmgFiberLc(nblock),
     *     dmgFiberTt(nblock), dmgFiberTc(nblock),
     *     dmgFiberZt(nblock), dmgFiberZc(nblock),
     *     stress(nblock,n_s33_Car),
     *     eigen(nblock,n_v3d_Car),
     *     statusMp(nblock), OlddmgFiberLt(nblock),
     *     OlddmgFiberLc(nblock), OlddmgFiberTt(nblock),
     *     OlddmgFiberTc(nblock), OlddmgFiberZt(nblock),
     *     OlddmgFiberZc(nblock), strain(nblock,n_s33_Car)
      Real:: L(nblock)
*
      f1tInv = zero
      f2tInv = zero
      f3tInv = zero
      f1cInv = zero
      f2cInv = zero
      f3cInv = zero
      f12Inv = zero
      f23Inv = zero
      f13Inv = zero
*
      if ( f1t .gt. zero ) f1tInv = one / f1t
      if ( f2t .gt. zero ) f2tInv = one / f2t
      if ( f3t .gt. zero ) f3tInv = one / f3t
      if ( f1c .gt. zero ) f1cInv = one / f1c
      if ( f2c .gt. zero ) f2cInv = one / f2c
      if ( f3c .gt. zero ) f3cInv = one / f3c
      if ( f12 .gt. zero ) f12Inv = one / f12
      if ( f23 .gt. zero ) f23Inv = one / f23
      if ( f13 .gt. zero ) f13Inv = one / f13
*
      do k = 1, nblock
         if ( statusMp(k) .eq. one ) then
*
         lFail = 0
*
         s11 = stress(k,i_s33_Xx)
         s22 = stress(k,i_s33_Yy)
         s33 = stress(k,i_s33_Zz)
         s12 = stress(k,i_s33_Xy)
         s23 = stress(k,i_s33_Yz)
         s13 = stress(k,i_s33_Zx)
*
         e11 = strain(k,i_s33_Xx)
         e22 = strain(k,i_s33_Yy)
         e33 = strain(k,i_s33_Zz)
         e12 = strain(k,i_s33_Xy)
         e23 = strain(k,i_s33_Yz)
         e13 = strain(k,i_s33_Zx)
*
         if ( s11 .gt. zero ) then

            rft = (s11*f1tInv )**2 + (s12*f12Inv )**2 + (s13*f13Inv )**2
```

```
            if ( rft .ge. one ) then

                XLT = L(k)*(((e11 + ABS(e11)) * 0.5)** 2
     *           + alpha * e12**2 + alpha * e13**2)**0.5
*
                sigLT= L(k)*((alpha*s12*e12) + (alpha*s13*e13)
     *              + ((s11+ABS(s11))*0.5 * (e11+ABS(e11))*0.5))/XLT
*
                XLT0 = XLT * (f1tInv**0.5)
                sigLT0 = sigLT * (f1tInv**0.5)
                XLTf = 2 * GFT/ sigLT0
                lDmg = 1
                dmgFiberLt(k) = XLTf * (XLT-XLT0) / (XLT*(XLTf-XLT0))
            end if
            ELT = OlddmgFiberLt(k) - dmgFiberLt(k)

            if ( ELT .gt. zero) then
                 dmgFiberLt(k) = OlddmgFiberLt(k)
            end if
*
         else if ( s11 .lt. zero ) then

            rfc = abs(s11) * f1cInv
            if ( rfc .ge. one ) then

                XLC = L(k)*(-e11 + ABS(-e11))*0.5
*
                sigLC= L(k)*(-e11 + ABS(-e11))*0.5
     *                * (-s11 + ABS(-s11))*0.5 / XLC
*
                XLC0 = XLC * (f1cInv**0.5)
                sigLC0 = sigLC * (f1cInv**0.5)
                XLCf = 2 * GFC/ sigLC0
                lDmg = 1
                dmgFiberLc(k) = XLCf * (XLC-XLC0) / (XLC*(XLCf-XLC0))
            end if
            ELC = OlddmgFiberLc(k) - dmgFiberLc(k)

            if ( ELC .gt. zero) then
                 dmgFiberLc(k) = OlddmgFiberLc(k)
            end if
*
         end if
*

         if ( ( s22 + s33 ) .gt. zero ) then

            rmt = ( s11 * half * f1tInv )**2
     *           + ( s22**2 * abs(f2tInv * f2cInv) )
     *           + ( s12 * f12Inv )**2
     *           + ( s22 * (f2tInv + f2cInv) )
            if ( rmt .ge. one ) then
                if(s22 .ge. zero) then
                    XTT = L(k) * (((e22 + ABS(e22)) * 0.5)** 2
     *                   + alpha * e12**2 + alpha * e23**2)**0.5
                    sigTT = L(k)*((alpha*s12*e12) + (alpha*s23*e23)
     *                  + ((s22+ABS(s22))*0.5 * (e22+ABS(e22))*0.5))/XTT
*
                    XTT0 = XTT * (f2tInv**0.5)
                    sigTT0 = sigTT * (f2tInv**0.5)
                    XTTf = 2 * GMT/ sigTT0
                    lDmg = 1
                    dmgFiberTt(k) = XTTf * (XTT-XTT0) /(XTT*(XTTf-XTT0))
                end if
                if(s33 .ge. zero) then
                    XZT = L(k) * (((e33 + ABS(e33)) * 0.5)** 2
     *                   + alpha * e23**2 + alpha * e31**2)**0.5
                    sigZT = L(k)*((alpha*s23*e23) + (alpha*s31*e31)
     *                  + ((s33+ABS(s33))*0.5 * (e33+ABS(e33))*0.5))/XZT
*
                    XZT0 = XZT * (f3tInv**0.5)
                    sigZT0 = sigZT * (f3tInv**0.5)
```

```
                    XZTf = 2 * GMT/ sigZT0
                    lDmg = 1
                    dmgFiberZt(k) = XZTf * (XZT-XZT0) /(XZT*(XZTf-XZT0))
                end if
                lDmg = 1
            end if
            ETT = OlddmgFiberTt(k) - dmgFiberTt(k)

            if ( ETT .gt. zero) then
                dmgFiberTt(k) = OlddmgFiberTt(k)
            end if
            EZT = OlddmgFiberZt(k) - dmgFiberZt(k)
            if ( EZT .gt. zero) then
                dmgFiberZt(k) = OlddmgFiberZt(k)
            end if
*
         else if ( ( s22 + s33 ) .lt. zero ) then
            rmc = ( s11 * half * f1tInv )**2
     *           + ( s22**2 * abs(f2tInv * f2cInv) )
     *           + ( s12 * f12Inv )**2
     *           + ( s22 * (f2tInv + f2cInv) )
            if ( rmc .ge. one ) then
                if(s22 .lt. zero) then
                    XTC = L(k)*(-e22 + ABS(-e22))*0.5
                    sigTC = L(k)*(-e22 + ABS(-e22))*0.5
     *                  * (-s22 + ABS(-s22))*0.5 / XTC
                    XTC0 = XTC * (f2cInv**0.5)
                    sigTC0 = sigTC * (f2cInv**0.5)
                    XTCf = 2 * GMC/ sigTC0
                    lDmg = 1
                    dmgFiberTc(k) = XTCf * (XTC-XTC0) /(XTC*(XTCf-XTC0))
                end if
                if(s33 .lt. zero) then
                    XZC = L(k)*(-e33 + ABS(-e33))*0.5
                    sigZC = L(k)*(-e33 + ABS(-e33))*0.5
     *                     * (-s33 + ABS(-s33))*0.5 / XZC
*
                    XZC0 = XZC * (f3cInv**0.5)
                    sigZC0 = sigZC * (f3cInv**0.5)
                    XZCf = 2 * GMC/ sigZC0
                    lDmg = 1
                    dmgFiberZc(k) = XZCf * (XZC-XZC0) /(XZC*(XZCf-XZC0))
                end if
               lDmg = 1
            end if
            ETC = OlddmgFiberTc(k) - dmgFiberTc(k)
            if ( ETC .gt. zero) then
                dmgFiberTc(k) = OlddmgFiberTc(k)
            end if
            EZC = OlddmgFiberZc(k) - dmgFiberZc(k)
            if ( EZC .gt. zero) then
                dmgFiberZc(k) = OlddmgFiberZc(k)
            end if
         end if
*
         eigMax=max(eigen(k,i_v3d_X),eigen(k,i_v3d_Y),eigen(k,i_v3d_Z))
         eigMin=min(eigen(k,i_v3d_X),eigen(k,i_v3d_Y),eigen(k,i_v3d_Z))
         enomMax = eigMax - one
         enomMin = eigMin - one
*
         if ( enomMax .gt. eMax .or.
     *        enomMin .lt. eMin .or.
     *        dmgFiberLt(k) .ge. one ) then
            statusMp(k) = zero
            nDmk = 1
         end if
*
         nDmg = nDmk + lDmg
*
         end if
*
      end do
```

```
*
      return
      end


*************************************************************
*   betaDamping: Add beta damping                           *
*************************************************************
      subroutine betaDamping3d ( nblock,
     *     beta, dt, strainInc, sigOld, sigNew,
     *     statusMp, sigDampOld, sigDampNew )
*
      include 'vaba_param.inc'
*
      parameter(
     *     i_s33_Xx = 1,
     *     i_s33_Yy = 2,
     *     i_s33_Zz = 3,
     *     i_s33_Xy = 4,
     *     i_s33_Yz = 5,
     *     i_s33_Zx = 6,
     *     n_s33_Car = 6 )
*
      dimension  sigOld(nblock,n_s33_Car),
     *     sigNew(nblock,n_s33_Car),
     *     strainInc(nblock,n_s33_Car),
     *     statusMp(nblock),
     *     sigDampOld(nblock,n_s33_Car),
     *     sigDampNew(nblock,n_s33_Car)
*
      parameter ( zero = 0.d0, one = 1.d0, two=2.0d0,
     *     half = 0.5d0, third = 1.d0/3.d0 )
      parameter ( asmall = 1.d-16 )
*
      betaddt =  beta / dt
*
      do k =1 , nblock
         sigDampNew(k,i_s33_Xx) = betaddt * statusMp(k) *
     *        ( sigNew(k,i_s33_Xx)
     *        - ( sigOld(k,i_s33_Xx) - sigDampOld(k,i_s33_Xx) ) )
         sigDampNew(k,i_s33_Yy) = betaddt * statusMp(k) *
     *        ( sigNew(k,i_s33_Yy)
     *        - ( sigOld(k,i_s33_Yy) - sigDampOld(k,i_s33_Yy) ) )
         sigDampNew(k,i_s33_Zz) = betaddt * statusMp(k) *
     *        ( sigNew(k,i_s33_Zz)
     *        - ( sigOld(k,i_s33_Zz) - sigDampOld(k,i_s33_Zz) ) )
         sigDampNew(k,i_s33_Xy) = betaddt * statusMp(k) *
     *        ( sigNew(k,i_s33_Xy)
     *        - ( sigOld(k,i_s33_Xy) - sigDampOld(k,i_s33_Xy) ) )
         sigDampNew(k,i_s33_Yz) = betaddt * statusMp(k) *
     *        ( sigNew(k,i_s33_Yz)
     *        - ( sigOld(k,i_s33_Yz) - sigDampOld(k,i_s33_Yz) ) )
         sigDampNew(k,i_s33_Zx) = betaddt * statusMp(k) *
     *        ( sigNew(k,i_s33_Zx)
     *        - ( sigOld(k,i_s33_Zx) - sigDampOld(k,i_s33_Zx) ) )
*
         sigNew(k,i_s33_Xx) = sigNew(k,i_s33_Xx)+sigDampNew(k,i_s33_Xx)
         sigNew(k,i_s33_Yy) = sigNew(k,i_s33_Yy)+sigDampNew(k,i_s33_Yy)
         sigNew(k,i_s33_Zz) = sigNew(k,i_s33_Zz)+sigDampNew(k,i_s33_Zz)
         sigNew(k,i_s33_Xy) = sigNew(k,i_s33_Xy)+sigDampNew(k,i_s33_Xy)
         sigNew(k,i_s33_Yz) = sigNew(k,i_s33_Yz)+sigDampNew(k,i_s33_Yz)
         sigNew(k,i_s33_Zx) = sigNew(k,i_s33_Zx)+sigDampNew(k,i_s33_Zx)
*
      end do
*
      return
      end


*************************************************************
*   EnergyInternal3d: Compute internal energy for 3d case   *
*************************************************************
```

```
      subroutine EnergyInternal3d(nblock, sigOld, sigNew ,
     *   strainInc, curDensity, enerInternOld, enerInternNew)
*
      include 'vaba_param.inc'
*
      parameter(
     *     i_s33_Xx = 1,
     *     i_s33_Yy = 2,
     *     i_s33_Zz = 3,
     *     i_s33_Xy = 4,
     *     i_s33_Yz = 5,
     *     i_s33_Zx = 6,
     *     n_s33_Car = 6 )
*
      parameter( two = 2.d0, half = .5d0 )
*
      dimension sigOld (nblock,n_s33_Car), sigNew (nblock,n_s33_Car),
     *     strainInc (nblock,n_s33_Car), curDensity (nblock),
     *     enerInternOld(nblock), enerInternNew(nblock)
*
      do k = 1, nblock
         stressPower  = half * (
     *        ( sigOld(k,i_s33_Xx) + sigNew(k,i_s33_Xx) )
     *        * ( strainInc(k,i_s33_Xx) )
     *        +       ( sigOld(k,i_s33_Yy) + sigNew(k,i_s33_Yy) )
     *        * ( strainInc(k,i_s33_Yy))
     *        +       ( sigOld(k,i_s33_Zz) + sigNew(k,i_s33_Zz) )
     *        * ( strainInc(k,i_s33_Zz))
     *        + two * ( sigOld(k,i_s33_Xy) + sigNew(k,i_s33_Xy) )
     *        * strainInc(k,i_s33_Xy)
     *        + two * ( sigOld(k,i_s33_Yz) + sigNew(k,i_s33_Yz) )
     *        * strainInc(k,i_s33_Yz)
     *        + two * ( sigOld(k,i_s33_Zx) + sigNew(k,i_s33_Zx) )
     *        * strainInc(k,i_s33_Zx) )
*
         enerInternNew(k) = enerInternOld(k) + stressPower/curDensity(k)
      end do
*
      return
      end

************************************************************
*   CopyR: Copy from one array to another                  *
************************************************************
      subroutine CopyR(nCopy, old, new )
*
      include 'vaba_param.inc'
*
      dimension old(nCopy), new(nCopy)
*
      do k = 1, nCopy
         old(k) = new(k)
      end do
*
      return
      end

************************************************************************
* eig33Anal: Compute eigen values of a 3x3 symmetric matrix analytically *
************************************************************************
      subroutine eig33Anal( nblock, sMat, eigVal )
*
      include 'vaba_param.inc'
*
      parameter(
     *          i_s33_Xx=1,
     *          i_s33_Yy=2,
     *          i_s33_Zz=3,
     *          i_s33_Xy=4,
     *          i_s33_Yz=5,
     *          i_s33_Zx=6,
     *          i_s33_Yx=i_s33_Xy,
```

```
*          i_s33_Zy=i_s33_Yz,
*          i_s33_Xz=i_s33_Zx,
*          n_s33_Car=6,
*          i_v3d_X=1,
*          i_v3d_Y=2,
*          i_v3d_Z=3,
*          n_v3d_Car=3)

*
      parameter ( zero = 0.d0, one = 1.d0, two = 2.d0,
     *     three = 3.d0, half = 0.5d0, third = one / three,
     *     pi23 = 2.094395102393195d0,
     *     fuzz = 1.d-8,
     *     preciz = fuzz * 1.d4 )

*
      dimension eigVal(nblock,n_v3d_Car), sMat(nblock,n_s33_Car)

*
      do k = 1, nblock
        sh  = third*(sMat(k,i_s33_Xx)+sMat(k,i_s33_Yy)+sMat(k,i_s33_Zz))
        s11 = sMat(k,i_s33_Xx) - sh
        s22 = sMat(k,i_s33_Yy) - sh
        s33 = sMat(k,i_s33_Zz) - sh
        s12 = sMat(k,i_s33_Xy)
        s13 = sMat(k,i_s33_Xz)
        s23 = sMat(k,i_s33_Yz)
*
        fac  = max(abs(s11), abs(s22), abs(s33))
        facs = max(abs(s12), abs(s13), abs(s23))
        if( facs .lt. (preciz*fac) ) then
          eigVal(k,i_v3d_X) = sMat(k,i_s33_Xx)
          eigVal(k,i_v3d_Y) = sMat(k,i_s33_Yy)
          eigVal(k,i_v3d_Z) = sMat(k,i_s33_Zz)
        else
          q = third*((s12**2+s13**2+s23**2)+half*(s11**2+s22**2+s33**2))
          fac = two * sqrt(q)
          if( fac .gt. fuzz ) then
            ofac = two/fac
          else
            ofac = zero
          end if
          s11 = ofac*s11
          s22 = ofac*s22
          s33 = ofac*s33
          s12 = ofac*s12
          s13 = ofac*s13
          s23 = ofac*s23
          r = s12*s13*s23
     *         + half*(s11*s22*s33-s11*s23**2-s22*s13**2-s33*s12**2)
          if( r .ge. one-fuzz ) then
            cos1 = -half
            cos2 = -half
            cos3 = one
          else if( r .le. fuzz-one ) then
            cos1 = -one
            cos2 = half
            cos3 = half
          else
            ang = third * acos(r)
            cos1 = cos(ang)
            cos2 = cos(ang+pi23)
            cos3 =-cos1-cos2
          end if
          eigVal(k,i_v3d_X) = sh + fac*cos1
          eigVal(k,i_v3d_Y) = sh + fac*cos2
          eigVal(k,i_v3d_Z) = sh + fac*cos3
        end if
      end do
*
      return
      end
```

```
*************************************************************
*               CharacteristicLength                        *
*************************************************************
      subroutine characlength ( nblock, Length, charlength )
*
      include 'vaba_param.inc'
      parameter ( zero = 0.d0, one = 1.d0, two = 2.d0)
*
      dimension   charlength(nblock)
      Real:: Length(nblock)
*
      do k = 1, nblock
*
        Length(k) = charlength(k)*one
*
      end do
*
      return
      end
```

Appendix C: Copyright Permissions

C.1 Copyright Permission for Chapter 3

October 3rd 2017

Journal of Composite Structures

I am preparing my Ph.D. thesis for submission to the Faculty of Graduate Studies at Dalhousie University, Halifax, Nova Scotia, Canada. I am seeking your permission to include a manuscript version of the following paper(s) as a chapter in the thesis:

[Zohreh Asaee, Shahin Shadlou and Farid Taheri, "*Low-velocity impact response of fiberglass/magnesium FMLs with a new 3D fiberglass fabric*", Composite Structures, 122, 155-165, 2015.]

Canadian graduate theses are reproduced by the Library and Archives of Canada (formerly National Library of Canada) through a non-exclusive, world-wide license to reproduce, loan, distribute, or sell theses. I am also seeking your permission for the material described above to be reproduced and distributed by the LAC(NLC). Further details about the LAC(NLC) thesis program are available on the LAC(NLC) website (www.nlc-bnc.ca).

Full publication details and a copy of this permission letter will be included in the thesis.

Yours sincerely,
Zohreh Asaee

ELSEVIER LICENSE
TERMS AND CONDITIONS

Oct 03, 2017

This Agreement between Dalhousie University -- Zohreh Asaee ("You") and Elsevier ("Elsevier") consists of your license details and the terms and conditions provided by Elsevier and Copyright Clearance Center.

License Number	4167671101175
License date	Aug 14, 2017
Licensed Content Publisher	Elsevier
Licensed Content Publication	Composite Structures
Licensed Content Title	Low-velocity impact response of fiberglass/magnesium FMLs with a new 3D fiberglass fabric
Licensed Content Author	Zohreh Asaee,Shahin Shadlou,Farid Taheri
Licensed Content Date	Apr 1, 2015
Licensed Content Volume	122
Licensed Content Issue	n/a
Licensed Content Pages	11
Start Page	155
End Page	165
Type of Use	reuse in a thesis/dissertation
Intended publisher of new work	other
Portion	full article
Format	both print and electronic
Are you the author of this Elsevier article?	Yes
Will you be translating?	No
Title of your thesis/dissertation	Low velocity impact response of a novel class of fiber metal laminates consisting of a 3D fiberglass fabrics
Expected completion date	Oct 2017
Estimated size (number of pages)	250
Requestor Location	Dalhousie University 1360 Barrington Street Halifax, NS B3H4R2 Canada Attn: Dalhousie University
Total	**0.00 CAD**
Terms and Conditions	

C.2 Copyright Permission for Chapter 4

October 3rd 2017

Journal of Composite Structures

I am preparing my Ph.D. thesis for submission to the Faculty of Graduate Studies at Dalhousie University, Halifax, Nova Scotia, Canada. I am seeking your permission to include a manuscript version of the following paper(s) as a chapter in the thesis:

[Zohreh Asaee and Farid Taheri, "*Experimental and numerical investigation into the influence of stacking sequence on the low-velocity impact response of new 3D FMLs*", Composite Structures, 40, 136-146, 2016.]

Canadian graduate theses are reproduced by the Library and Archives of Canada (formerly National Library of Canada) through a non-exclusive, world-wide license to reproduce, loan, distribute, or sell theses. I am also seeking your permission for the material described above to be reproduced and distributed by the LAC(NLC). Further details about the LAC(NLC) thesis program are available on the LAC(NLC) website (www.nlc-bnc.ca).

Full publication details and a copy of this permission letter will be included in the thesis.

Yours sincerely,
Zohreh Asaee

ELSEVIER LICENSE
TERMS AND CONDITIONS

Oct 03, 2017

This Agreement between Dalhousie University -- Zohreh Asaee ("You") and Elsevier ("Elsevier") consists of your license details and the terms and conditions provided by Elsevier and Copyright Clearance Center.

License Number	4167670999501
License date	Aug 14, 2017
Licensed Content Publisher	Elsevier
Licensed Content Publication	Composite Structures
Licensed Content Title	Experimental and numerical investigation into the influence of stacking sequence on the low-velocity impact response of new 3D FMLs
Licensed Content Author	Zohreh Asaee,Farid Taheri
Licensed Content Date	Apr 15, 2016
Licensed Content Volume	140
Licensed Content Issue	n/a
Licensed Content Pages	11
Start Page	136
End Page	146
Type of Use	reuse in a thesis/dissertation
Intended publisher of new work	other
Portion	full article
Format	both print and electronic
Are you the author of this Elsevier article?	Yes
Will you be translating?	No
Title of your thesis/dissertation	Low velocity impact response of a novel class of fiber metal laminates consisting of a 3D fiberglass fabrics
Expected completion date	Oct 2017
Estimated size (number of pages)	250
Requestor Location	Dalhousie University 1360 Barrington Street Halifax, NS B3H4R2 Canada Attn: Dalhousie University
Total	**0.00 CAD**
Terms and Conditions	

C.3 Copyright Permission for Chapter 5

November 9rd 2017

Journal of Sandwich Structures & Materials

I am preparing my Ph.D. thesis for submission to the Faculty of Graduate Studies at Dalhousie University, Halifax, Nova Scotia, Canada. I am seeking your permission to include a manuscript version of the following paper(s) as a chapter in the thesis:

[Zohreh Asaee and Farid Taheri, "*Enhancement of Performance of 3D Fiber Metal Laminates under Low Velocity Impact– A coupled Numerical and Experimental Investigation*", Journal of Sandwich Structures & Materials, 2017.]

Canadian graduate theses are reproduced by the Library and Archives of Canada (formerly National Library of Canada) through a non-exclusive, world-wide license to reproduce, loan, distribute, or sell theses. I am also seeking your permission for the material described above to be reproduced and distributed by the LAC(NLC). Further details about the LAC(NLC) thesis program are available on the LAC(NLC) website (www.nlc-bnc.ca).

Full publication details and a copy of this permission letter will be included in the thesis.

Yours sincerely,
Zohreh Asaee

C.4 Copyright Permission for Chapter 6

October 3rd 2017

Journal of Thin-walled Structures

I am preparing my Ph.D. thesis for submission to the Faculty of Graduate Studies at Dalhousie University, Halifax, Nova Scotia, Canada. I am seeking your permission to include a manuscript version of the following paper(s) as a chapter in the thesis:

[Zohreh Asaee, Mbarka Mohamed, Sadman Soumik and Farid Taheri, "*Experimental and numerical characterization of delamination buckling behavior of a new class of GNP-reinforced 3D fiber-metal laminates*", Thin-walled Structures, 112, 208-216, 2017.]

Canadian graduate theses are reproduced by the Library and Archives of Canada (formerly National Library of Canada) through a non-exclusive, world-wide license to reproduce, loan, distribute, or sell theses. I am also seeking your permission for the material described above to be reproduced and distributed by the LAC(NLC). Further details about the LAC(NLC) thesis program are available on the LAC(NLC) website (www.nlc-bnc.ca).

Full publication details and a copy of this permission letter will be included in the thesis.

Yours sincerely,
Zohreh Asaee

ELSEVIER LICENSE
TERMS AND CONDITIONS

Oct 03, 2017

This Agreement between Dalhousie University -- Zohreh Asaee ("You") and Elsevier ("Elsevier") consists of your license details and the terms and conditions provided by Elsevier and Copyright Clearance Center.

License Number	4167671182583
License date	Aug 14, 2017
Licensed Content Publisher	Elsevier
Licensed Content Publication	Thin-Walled Structures
Licensed Content Title	Experimental and numerical characterization of delamination buckling behavior of a new class of GNP-reinforced 3D fiber-metal laminates
Licensed Content Author	Zohreh Asaee,Mbarka Mohamed,Sadman Soumik,Farid Taheri
Licensed Content Date	Mar 1, 2017
Licensed Content Volume	112
Licensed Content Issue	n/a
Licensed Content Pages	9
Start Page	208
End Page	216
Type of Use	reuse in a thesis/dissertation
Intended publisher of new work	other
Portion	full article
Format	both print and electronic
Are you the author of this Elsevier article?	Yes
Will you be translating?	No
Title of your thesis/dissertation	Low velocity impact response of a novel class of fiber metal laminates consisting of a 3D fiberglass fabrics
Expected completion date	Oct 2017
Estimated size (number of pages)	250
Requestor Location	Dalhousie University 1360 Barrington Street Halifax, NS B3H4R2 Canada Attn: Dalhousie University
Total	**0.00 CAD**
Terms and Conditions	